Transactions of the ASME®

Transactions of the ASME, The Journal of Fluids Engineering (ISSN 0098-2202) is published quarterly (Mar., June, Sept., Dec.) for $95 per year by The American Society of Mechanical Engineers, 345 East 47th Street, New York, NY 10017. Second class postage paid at New York, NY and additional mailing offices. POSTMASTER: Send address changes to The Journal of Fluids Engineering, c/o THE AMERICAN SOCIETY OF MECHANICAL ENGINEERS, 22 Law Drive, Box 2300, Fairfield, NJ 07007-2300.
CHANGES OF ADDRESS must be received at Society headquarters seven weeks before they are to be effective. Please send old label and new address.
PRICES: To members, $27.00, annually: to nonmembers, $95. Add $12.00 for postage to countries outside the United States and Canada.
STATEMENT from By-Laws. The Society shall not be responsible for statements or opinions advanced in papers or . . . printed in its publications (B7.1, Par. 3).

INDEXED by Applied Mechanics Reviews and Engineering Information, Inc.

Journal of Fluids Engineering

Published Quarterly by The American Society of Mechanical Engineers

VOLUME 110 • NUMBER 2 • JUNE 1988

(Contents continued on page 122)

Contents (Continued)

An Explicit Non-Real Time Data Reduction Method of Triple Sensors Hot-Wire Anemometer in Three-Dimensional Flow

Y. T. Chew
Senior Lecturer,
Department of Mechanical and Production Engineering,
National University of Singapore,
Singapore

R. L. Simpson
Professor,
Department of Aerospace and Ocean Engineering,
Virginia Polytechnic Institute and State University,
Blacksburg, Virginia 24061.
Fellow ASME

An explicit non-real time method of reducing triple sensor hot-wire anenometer data to obtain the three mean velocity components and six Reynolds stresses, as well as their turbulence spectra in three-dimensional flow is proposed. Equations which relate explicitly the mean velocity components and Reynolds stresses in laboratory coordinates to the mean and mean square sensors output voltages in three stages are derived. The method was verified satisfactorily by comparison with single sensor hot-wire anemometer measurements in a zero pressure gradient incompressible turbulent boundary layer flow. It is simple and requires much lesser computation time when compared to other implicit non-real time method.

1 Introduction

For many years, the hot-wire anemometer has been the main tool for measuring velocities in highly turbulent flows. Before the advent of laser anemometry, it was the only means of making turbulence measurement. Numerous papers have been published on the techniques of using the hot-wire anemometer and on the results of its application during the past 40 years. While laser anemometry can provide measurements in certain unique situations like separated flows, very high temperature flows and flow highly sensitive to disturbances, the hot-wire anemometer still remains a useful tool because of the intrinsically discrete and discontinuous nature of laser anemometer signal, which is aggravated further by the flow seeding problem.

Unlike laser anemometry which measures the velocity vector, hot-wire anemometer responds only to the velocity magnitude since it involves the principle of heat transfer. Hence in using a single sensor hot-wire anemometer, the flow direction must be accurately known, a luxury which can be ill afforded in three-dimensional flows. However, if three sensors of the hot-wire anemometer can be arranged in such a way that they provide independent output signals, the three components of velocity can be measured and the velocity vector can be determined. One way of achieving this is by slanting a single sensor to provide optimum response to the flow and rotate the probe about its own axis into three different orientations, usually at 120° intervals [1–3]. If the six components of Reynolds stresses are also required besides the three components of the mean velocity, the single sensor probe must be rotated into at least six different orientations. This is because at three different orientations one can only obtain the six independent output signals of three mean voltages ($\bar{E}_1$, $\bar{E}_2$, $\bar{E}_3$) and three mean square voltages ($\overline{e_1^2}$, $\overline{e_2^2}$, $\overline{e_3^2}$). The cross correlations between fluctuating voltages ($\overline{e_1e_2}$, $\overline{e_1e_3}$, $\overline{e_2e_3}$) cannot be obtained since the signals are taken at different times. As such, another three different probe orientations are required to provide nine independent output signals for the solution of the three components of mean velocity and six components of Reynolds stresses. The disadvantages of this method become obvious since it is time consuming and difficult to keep the relative geometry of the sensors at six different orientations accurately. A slight off-axis rotation of the probe would introduce large uncertainties in the six components of Reynolds stresses [3]. Besides, there are many situations not amenable to the rotation of the probe, e.g., turbomachinery rotor passages.

One way of overcoming the disadvantages of a single sensor slant wire is to use a triple sensor hot-wire probe which is commercially available, e.g. DISA Type 55P91 or TSI Model 1294. In this type of probe, the three sensors are preset orthogonally. Rotation of probe during an experiment is not required since the cross-correlations between fluctuating voltages ($\overline{e_1e_2}$, $\overline{e_1e_3}$, $\overline{e_2e_3}$) can be obtained from the three simultaneous instantaneous output voltages of the triple sensors. Hence, geometric errors introduced by the alignment of the probe in an experimental setup is minimized. The errors caused by the deviation from orthogonality of the three sensors i.e., deviation from ideal internal geometry, has been investigated by Zank [4] and were found to be small, i.e., approximately 1 percent of the measured velocity per degree deviation. If the deviation from orthogonality is large, the probe can be realigned and rewired to better than 1 deg, measured by means of an optical comparator as was done by Frota and Moffat [5].

Contributed by the Fluids Engineering Division for publication in the JOURNAL OF FLUIDS ENGINEERING. Manuscript received by the Fluids Engineering Division April 2, 1986.

2 Triple Sensors Hot-Wire Equations

For incompressible flow, the heat loss from a constant temperature hot-wire sensor is proportional to the square of voltage input E. Since the heat loss from an infinite circular cylinder does not vary linearly with Reynolds number, King proposed that the voltage E may be related to the effective cooling velocity V_e by the following relationship

$$E^2 = E_0 + mV_e^n \tag{1}$$

where E_0 represents the heat loss through natural convection and conduction along the prongs at zero velocity and m, n are constants. For the measurement of large turbulence intensities, the assumption of a linear voltage variation over the range of a velocity fluctuation in order to relate $\overline{v_e^2}$ to $\overline{e^2}$ is not valid. Besides, m and n in equation (1) can vary substantially with velocity. Hence for greater accuracy and the ease of data reduction, a linearizing circuit is often employed to reduce equation (1) to

$$E = A + BV_e \tag{2}$$

where A and B are constants.

For a triple sensor hot-wire with linearized output, the corresponding equations for each sensor are

$$\begin{aligned} E_1 &= A_1 + B_1 V_1 \\ E_2 &= A_2 + B_2 V_2 \\ E_3 &= A_3 + B_3 V_3 \end{aligned} \tag{3}$$

For a single sensor hot-wire normal to the flow with its prongs parallel to the flow, the definition of the effective cooling velocity is unambiguous. However, for flow coming at an angle to the sensor, which is the case for a triple sensor hot-wire in a three-dimensional flow, there are contributions to the heat loss by the component of velocity along the wire and the component normal to the prongs-sensor plane. These can be accounted for by the introduction of the sensitivity coefficients K_T for the tangential velocity and K_N for the velocity component normal to the prongs-sensor plane. An orthogonal wire coordinates system is shown in Fig. 1, where the prongs-sensor planes for wires 1, 2, and 3 are along the x–y, y–z and x–z plane respectively. Assuming K_T and K_N are the same for each wire, the scalar equations relating the effective cooling velocity and the three velocity components are

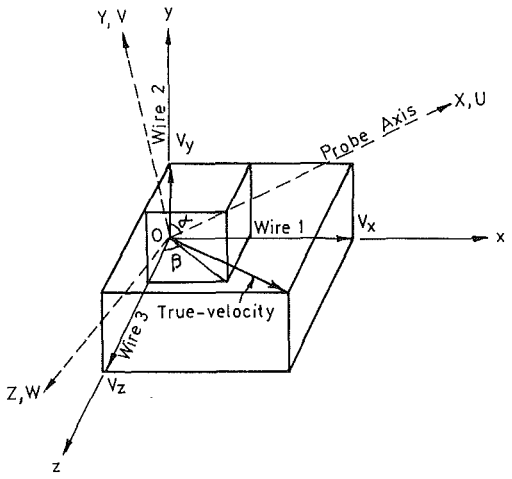

WIRE	1	2	3
PRONG - SENSOR PLANE	xy	yz	xz

Fig. 1 Wire coordinates and laboratory coordinates in relation to the probe

$$\begin{aligned} V_1^2 &= K_T^2 V_x^2 + V_y^2 + K_N^2 V_z^2 \\ V_2^2 &= K_N^2 V_x^2 + K_T^2 V_y^2 + V_z^2 \\ V_3^2 &= V_x^2 + K_N^2 V_y^2 + K_T^2 V_z^2 \end{aligned} \tag{4}$$

In matrix form, equation (4) becomes

$$\begin{vmatrix} V_1^2 \\ V_2^2 \\ V_3^2 \end{vmatrix} = M \begin{vmatrix} V_x^2 \\ V_y^2 \\ V_z^2 \end{vmatrix} \tag{5}$$

where

$$M = \begin{vmatrix} K_T^2 & 1 & K_N^2 \\ K_N^2 & K_T^2 & 1 \\ 1 & K_N^2 & K_T^2 \end{vmatrix}$$

or

Nomenclature

A_1, A_2, A_3 = hot-wire calibration constants
a_1, a_2, a_3 = elements of matrix M^{-1}
α = angle between probe axis and wire
B_1, B_2, B_3 = hot-wire calibration constants
b_1, b_2, b_3 = elements of matrix M^{-1}
β = bisector angle between wire no. 1 and 3
c_1, c_2, c_3 = elements of matrix M^{-1}
d_1, d_2, d_3 = elements of matrix N
δ = boundary layer thickness
E = hot-wire sensor output voltage
E_1, E_2, E_3 = instantaneous sensors output voltages of wire no. 1, 2, 3
$\bar{E}_1, \bar{E}_2, \bar{E}_3$ = mean sensors output voltages
e_1, e_2, e_3 = fluctuating sensors output voltages
f_1, f_2, f_3 = elements of matrix N
g_1, g_2, g_3 = elements of matrix N
K_T = sensitivity coefficient tangential to the wire
K_N = sensitivity coefficient normal to the prongs-sensor plane
M, N = transformation matrices
n = frequency in Hz
ρ = density
τ_w = shear stress at the wall
V_1, V_2, V_3 = instantaneous effective cooling velocities of wire no. 1, 2, 3
$\bar{V}_1, \bar{V}_2, \bar{V}_3$ = mean effective cooling velocities
v_1, v_2, v_3 = fluctuating effective cooling velocities
V_x, V_y, V_z = instantaneous velocities in wire coordinates
$\bar{V}_x, \bar{V}_y, \bar{V}_z$ = mean velocities in wire coordinates
v_x, v_y, v_z = fluctuating velocities in wire coordinates
U, V, W = instantaneous velocities in laboratory coordinates
$\bar{U}, \bar{V}, \bar{W}$ = mean velocities in laboratory coordinates
u, v, w = fluctuating velocities in laboratory coordinates
$\bar{U}_e$ = mean velocity at edge of boundary layer
U_τ = friction velocity, $(\tau_w/\rho)^{1/2}$
X, Y, Z = laboratory coordinates
x, y, z = wire coordinates

$$\begin{vmatrix} V_x^2 \\ V_y^2 \\ V_z^2 \end{vmatrix} = M^{-1} \begin{vmatrix} V_1^2 \\ V_2^2 \\ V_3^2 \end{vmatrix} \tag{6}$$

where

$$M^{-1} = \frac{1}{\Delta} \begin{vmatrix} K_T^4 - K_N^2 & K_N^4 - K_T^2 & 1 - K_T^2 K_N^2 \\ 1 - K_T^2 K_N^2 & K_T^4 - K_N^2 & K_N^4 - K_T^2 \\ K_N^4 - K_T^2 & 1 - K_T^2 K_N^2 & K_T^4 - K_N^2 \end{vmatrix}$$

and Δ is the determinant of matrix M given by

$$\Delta = K_T^6 + K_N^6 - 3\, K_T^2 K_N^2 + 1$$

The velocity components in the orthogonal wire coordinates x, y, and z can be transformed to any orthogonal coordinats if the direction cosines of the angles between the original and transformed axes are known. For the laboratory coordinates X, Y, and Z as shown in Fig. 1 where X represents the probe axis and wire 2 lies on the XY plane, the velocity components, U, V and W are given by

$$\begin{vmatrix} U \\ V \\ W \end{vmatrix} = N \begin{vmatrix} V_x \\ V_y \\ V_z \end{vmatrix} \tag{7}$$

where

$$N = \begin{vmatrix} \sin\alpha \sin\beta & \cos\alpha & \sin\alpha \cos\beta \\ -\cos\alpha \sin\beta & \sin\alpha & -\cos\alpha \cos\beta \\ -\cos\beta & 0 & \sin\beta \end{vmatrix} = \begin{vmatrix} \frac{1}{\sqrt{3}} & \frac{1}{\sqrt{3}} & \frac{1}{\sqrt{3}} \\ -\frac{1}{\sqrt{6}} & \frac{2}{\sqrt{6}} & -\frac{1}{\sqrt{6}} \\ -\frac{1}{\sqrt{2}} & 0 & \frac{1}{\sqrt{2}} \end{vmatrix}$$

when $\alpha = 54.74$ deg, $\beta = 45$ deg

3 Sensitivity Coefficients K_T and K_N

In order to solve equation (4) without any iteration, it is necessary to assume the sensitivity coefficients K_T and K_N to be constant so that equation (4) becomes a set of linear equations. The assumption of constant K_T and K_N has been a controversial issue [7]. Since K_T and K_N are merely empirical correction factors to account for the additional heat loss due to the tangential and normal to prongs-sensor plane components of velocity, they can be expected to vary with the magnitude and direction of velocity relative to the probe. However, the important issue is whether they are strong functions of the magnitude and direction of velocity, and whether their variations significantly affect the final results.

There are few reported values of K_T and K_N as functions of the magnitude and direction of velocity for a triple sensor hot-wire probe. Jørgensen [6] has conducted experiments to determine the directional sensitivity of Disa's single sensor hot-wire and hot-film probes. It was found that the values of K_T and K_N are higher for film probes and unplated wire probes than those for the gold-plated wire probe because of prong interference effects. Values of K_T varies significantly with the yaw angle, especially for the film probe and the unplated wire probe. For the gold-plated wire probe, K_T varies from 0.1 to 0.25 approximately. However, K_N remains almost constant at 1.02 to 1.05 for a pitch angle of 0 to 90 deg. Both K_T and K_N exhibit only a weak dependence on the magnitude of velocity within the approximate calibration range of 10-30 m/s. Saripalli and Simpson [3] also found that for a TSI model 1273-T 1.5 slant wire probe, K_T varies from 0.3 to 0.39 and K_N remains almost constant around 1.05 for the velocities ranging between 3 and 41 m/s. With increasing velocity, K_T was generally found to increase slowly and K_N was found to vary within a maximum of 1 percent. In most of the triple sensor hot-wire studies [5, 8], the values of K_T and K_N were based on experiments with single sensor probes.

To obtain K_T and K_N for a triple sensor hot-wire probe, each sensor can be calibrated individually by aligning the flow along the sensor and normal to the sensor-prongs plane of each sensor. While this method enables the determination of K_T and K_N individually for each sensor, it tends to introduce prong interference effects which are evidently more severe for a triple-sensor probe. In practice, triple sensor hot-wire probes are seldom used with the instantaneous flow angle greater than 35.26 deg to the probe axis and such that the flow is tangential to one of the sensors. Frota and Moffat [5] showed that when the third wire was placed in a plane parallel to the test wall, the mean velocity and Reynolds shear stress can be measured within 2 and 4.8 percent accuracy, respectively, only if the velocity vector lies within 20 deg of the probe axis, assuming K_T and K_N are constant. Butler and Wagner [7] found that by assuming K_T and K_N to be variable, the velocity magnitude and direction can be measured within 5 percent and 3 deg accuracy, respectively, if the velocity vector lies within approximately 30 deg of the probe axis. Therefore, unlike the laser anemometer, the flow direction of a three-dimensional flow must still be within a certain acceptable angle from the probe axis when using a triple sensor hot-wire probe. The ability of a triple sensor hot-wire to measure three-dimensional flows is restricted while that of a laser anemometer is not. In separated flows where flow reversal occurs, the laser anemometer must be used.

Another way of obtaining K_T and K_N is to calibrate the three sensors collectively. A set of calibration equation (3) can be obtained by mounting each wire normal to the flow along the sensor-prongs plane. The probe can then be positioned so that the flow of known magnitude is within the cone of operation and of known direction relative to the probe axis. The velocity can be resolved into V_x, V_y, and V_z components along the wire coordinates. With V_1, V_2, and V_3 obtained from the sensor output voltages using equation (3), K_T and K_N can be deduced by solving equations (4) simultaneously. With calibrations conducted at different magnitudes and directions of velocity, their influences on K_T and K_N can be investigated. The accuracy of the probe geometry, as depicted in equations (4), (7), and Fig. 1, can also be examined. Since there are three equations for the solution of K_T and K_N in the set of equation (4), the third equation can be used to check for closure. If closure is obtained, the assumptions of the same K_T and K_N for each sensor, the orthogonality of the sensors and their symmetry about the probe axis, are valid. Otherwise, the amount of residue would indicate the severity of the deviation.

4 Existing Methods of Data Reduction

When K_T and K_N are functions of the velocity magnitude and direction, equation (4) becomes nonlinear. Hirsch and

Kool [9] used a single slant sensor rotated into several orientations to measure the three-dimensional flow field behind an axial compressor. They allowed K_T to vary with velocity magnitude and direction, and the functional relationship was determined by extensive calibration. The set of nonlinear equations was solved by a relaxation method to yield the three components of mean velocity. Butler and Wagner [7] calibrated two TSI triple sensor hot-film probes over a range of flow direction and magnitude. The resulting calibration data were least-square fitted to quadratic polynomials to produce a calibration curve relating the velocity magnitude to the three linearized sensor output voltages and another calibration curve relating the velocity direction to the velocity magnitude, an effective velocity ratio and the sensor output voltages. The instantaneous sensor voltages were sampled in real time and converted into an instantaneous velocity vector with the aid of the calibration curves. Since measurements were taken behind a rotor in a large scale, low speed, axial flow research turbine, the velocity components were phase-lock ensemble-averaged over 100 successive revolutions. From the instantaneous velocity vector, the three components of mean velocity and six components of Reynolds stresses were then determined. As this is a calibration based method, the cone angle of flow within which the triple sensor probe can operate with good accuracy, is extended considerably, i.e., ± 30 deg approximately for 5 percent and 3 deg accuracy of the velocity magnitude and direction, respectively.

Since there are few reported values of K_T and K_N as a function of velocity magnitude and direction for a triple sensor hot-wire probe, it is natural to base K_T and K_N on Jϕrgensen's [6] experiments on single sensor probes. In light of Jϕrgensen's data, it is quite sufficient to assume K_T and K_N to be constant, especially for the DISA Type 55P91 triple sensors hot-wire probe, with gold-plated sensors that reduce prong interference effects. Gaulier [8] assumed $K_T = 0.15$ and $K_N = 1.02$ to determine the mean velocity and turbulence rate in the air stream emerging from domestic fuel burners. Lakshminarayana and Poncet [10] assumed a constant K_T and ignored and effect of K_N when making measurements of the mean and turbulent velocities inside an axial flow inducer. The instantaneous sensor voltages were sampled in real time using high speed phase locked sampler and converted to the instantaneous velocity vector.

Frota and Moffat [5], while investigating the effect of combined roll and pitch angles on the triple sensor hot-wire measurements of mean and turbulence structure, assumed constant K_T and K_N based upon previous experiments [6]. A Three-Dimensional Turbulent Flow Analyzer was used to solve equations (3), (6), and (7) by an analog computer technique. From the three linearized sensor voltages, three outputs were generated, each linearly related to U, V, and W. The desired turbulence correlations were then calculated by means of a Post-Processor Unit.

Andreopoulos [11], while examining the problems of nonorthogonality of the three wires and the variation of sensitivity coefficients K_T and K_N with the pitch and yaw angles, recorded the digitized outputs of the three wires real time on digital magnetic tapes, but the recorded data were analyzed non-real time using a Univac computer. The cooling velocities V_1, V_2, V_3 were converted to wire coordinate velocities V_x, V_y, V_z using equation (4), but with different K_T and K_N for each wire. The wire coordinate velocities were then converted to laboratory coordinate velocities U, V, W using equation (7). The three components of mean velocities and six components of Reynolds stresses can then be deduced frolm U, V, W. Based on the calculated $\bar{U}$, $\bar{V}$, $\bar{W}$, the flow direction was determined and the data reanalyzed with new K_T and K_N for each individual wire calibrated at this known flow direction. This iterative process of calculation continued until convergence occurred. In this way, he was able to examine the errors on the calculated results caused by assuming "overall" K_T and K_N instead of the actual K_T and K_N at that flow direction. He found that the effects on mean velocity profile is extremely small; and the combined nonorthogonality and K_T, K_N variation corrections affect $\overline{u^2}$ by not more than 5 percent even with pitching of the probe by as much as 30 deg. For zero pitch angle of the probe, the combined nonorthogonality and K_T, K_N variation corrections affect $\overline{v^2}$ by only about 5 percent. But for 15 deg or 30 deg pitch angle of the probe, the error increases to 20 percent. The effects on $\overline{w^2}$ is similar to those on $\overline{v^2}$. The experiment was conducted in a boundary layer with large turbulence intensities in the order of 20 percent such that the pitch and yaw angle variations of flow are considerable. Most of the large errors mentioned above occur near the wall where the turbulence intensities are high.

Besides the above methods where the sensor voltages are sampled real time digitally or analyzed real time through an analog computer technique, another method of processing the data is to use a non-real time averaging procedure to derive expressions for the three components of mean velocity and six components of Reynolds stresses in terms of the mean and mean square values of the sensor output voltages. Gorton and Lakshminarayana [12] assumed K_T = constant and $K_N = 1$ for all sensors when using a three sensor probe to measure the three-dimensional flow inside a rotating turbomachinery passage. The effective cooling velocities of each sensor, V_1, V_2, and V_3 were expressed in terms of the laboratory coordinate velocities, U, V, and W. By normalizing with the dominant mean stream velocity, carrying out a binomial expansion, and neglecting the higher order terms, the mean cooling velocities $\bar{V}_1$, $\bar{V}_2$, and $\bar{V}_3$ were expressed in terms of the mean velocities $\bar{U}$, $\bar{V}$, and $\bar{W}$. The mean square and cross-correlation of the fluctuating cooling velocities, $\overline{v_1^2}$, $\overline{v_2^2}$, $\overline{v_3^2}$, $\overline{v_1 v_2}$, $\overline{v_1 v_3}$, $\overline{v_2 v_3}$, were also expressed in terms of $\bar{U}$, $\bar{V}$, and $\bar{W}$ and the Reynolds stresses $\overline{u^2}$, $\overline{v^2}$, $\overline{w^2}$, $\overline{uv}$, $\overline{uw}$, $\overline{vw}$ by neglecting many of the small higher order terms such as $\overline{u^2 v}$, $\overline{u^2 v^2}$, etc. Since the mean, mean square and cross-correlation of fluctuating cooling velocities were related to the sensors output voltages of $\bar{E}_1$, $\bar{E}_2$, $\bar{E}_3$, $\overline{e_1^2}$, $\overline{e_2^2}$, $\overline{e_3^2}$, $\overline{e_1 e_2}$, $\overline{e_1 e_3}$, $\overline{e_2 e_3}$, a set of nine nonlinear equations for the nine unknowns (three mean velocity components and six Reynolds stresses) was derived. They also showed that the calculated mean velocities vary very little with a variation in K_T from 0 to 0.2. The error in mean velocity when assuming $K_N = 1$ instead of 1.03 (assuming a pitch angle of 45 deg) is about 1.5 percent.

5 Present Method of Data Reduction

With the exception of the method by Frota and Moffat [5] in which the sensor voltages are analyzed in real time with an analog computer technique, the other methods [7, 10, 11] of digitizing the sensor voltages in real time with a high speed analog to digital converter suffer from the disadvantage of a reduction in the digitizing accuracy of the fluctuating voltages. When the sensor voltages are digitized in real time, the mean and fluctuating components of the voltages cannot be separated prior to digitization. As the fluctuating component of voltage is usally small when compared to the mean component, its accurate digitization can only be achieved with a higher bit machine, e.g., a 16 bit machine. The situation is aggravated if the mean velocity and hence the sensor output voltages varies slowly in an unsteady flow, or the voltage range of digitization extends to the negative voltage e.g., ± 5 V or ± 10 V. In both cases, maximum utilization of the analog to digital converter resolution cannot be realized unless D.C. offset of the sensors voltages is made before amplification.

In the non-real time averaging procedure, the mean and

mean square of sensor output voltages, $\bar{E}_1$, $\bar{E}_2$, $\bar{E}_3$, $\overline{e_1^2}$, $\overline{e_2^2}$, $\overline{e_3^2}$, $\overline{e_1e_2}$, $\overline{e_1e_3}$, $\overline{e_2e_3}$, can be obtained through analog devices and the three components of mean velocity and the six components of Reynolds stresses computed later, either by computer or manually. If digitization by an analog to digital converter is required in order to obtain ensemble-averages in an unsteady flow, the fluctuating components of sensor voltages can be separated from the mean components by filtering and amplified separately in order to utilize the full range of digitization voltage and preserve the digitization accuracy. The mean and mean square values can be computed by the computer.

One of the major advantages of real time data analysis is the ability to obtain frequency information of the fluctuating velocities. However, as Moffat et al [13] pointed out, a sampling rate of 150 KHz is required to follow 10 KHz variations in each sensors output voltages. The sampling speed may not be beyond some high speed analog to digital converters, but the core memory required would be beyond most reasonably-sized computers. Hence, high frequency information of the fluctuating velocities will be lost. If the purpose of real time digitization of the sensor voltages is solely to obtain instantaneous velocity components U, V, and W for later determination of the mean velocity components and Reynolds stresses by time averaging, the frequency information is lost anyway. Thus there is no advantage over nonreal time method of time-averaging the sensor output voltages before deducing the mean velocity components and Reynolds stresses.

In Gorton and Lakshminarayana's [12] method of relating the mean velocities and Reynolds stresses to the mean and mean square sensors voltages, the probe axis must be quite closely aligned with the main flow so that the other two components of velocity are small. Otherwise the binomial expansion would be invalid. The velocity fluctuations must also be small when compared to the mean velocity components, especially since the sensor output voltages are not linearized. Another major disadvantage of their method is the implicit, nonlinear nature of the nine equations. As a result, successive iteration using a Newton-Raphson convergence scheme is required.

The present method overcomes the disadvantages by developing a set of nine explicit linear equations relating the mean velocity components and Reynolds stresses to the mean and mean square sensors output voltages. Unlike Gorton and Lakshminarayana's non-real time method which relates the cooling velocities to laboratory coordinates velocities directly, the present method divides it into three distinct steps, i.e., (*a*) triple sensor output voltages E_1, E_2, E_3 to cooling velocities V_1, V_2, V_3; (*b*) cooling velocities to orthogonal wire coordinates velocities V_x, V_y, V_z; (*c*) wire coordinates velocities to laboratory coordinates velocities U, V, W.

(*a*) Triple Sensor Output Voltages to Cooling Velocities. Representing the instantaneous voltage and cooling velocity by mean and fluctuating components, equation (3) becomes

$$\bar{E}_1 + e_1 = A_1 + B_1(\bar{V}_1 + v_1)$$

Taking the time mean: $\bar{E}_1 = A_1 + B_1\bar{V}_1$

$$\therefore e_1 = B_1 v_1$$

$$\overline{v_1^2} = \frac{1}{B_1^2}\overline{e_1^2}$$

$$\overline{v_1 v_2} = \frac{1}{B_1 B_2}\overline{e_1 e_2}$$

Since it is simpler to handle the sum and difference between two signals rather than their product electronically, $\overline{e_1e_2}$ can be expressed as

$$\overline{e_1e_2} = \frac{1}{4}[\overline{(e_1+e_2)^2} - \overline{(e_1-e_2)^2}]$$

Hence the cooling velocities are related to the sensor output voltages by the following nine equations.

$$\bar{V}_1 = \frac{1}{B_1}(\bar{E}_1 - A_1)$$

$$\bar{V}_2 = \frac{1}{B_2}(\bar{E}_2 - A_2)$$

$$\bar{V}_3 = \frac{1}{B_3}(\bar{E}_3 - A_3)$$

$$\overline{v_1^2} = \frac{1}{B_1^2}\overline{e_1^2}$$

$$\overline{v_2^2} = \frac{1}{B_2^2}\overline{e_2^2}$$

$$\overline{v_3^2} = \frac{1}{B_3^2}\overline{e_3^2}$$

$$\overline{v_1 v_2} = \frac{1}{4B_1B_2}[\overline{(e_1+e_2)^2} - \overline{(e_1-e_2)^2}]$$

$$\text{or } \frac{1}{2B_1B_2}[\overline{e_1^2} + \overline{e_2^2} - \overline{(e_1-e_2)^2}]$$

$$\overline{v_1 v_3} = \frac{1}{4B_1B_3}[\overline{(e_1+e_3)^2} - \overline{(e_1-e_3)^2}]$$

$$\text{or } \frac{1}{2B_1B_3}[\overline{e_1^2} + \overline{e_3^2} - \overline{(e_1-e_3)^2}]$$

$$\overline{v_2 v_3} = \frac{1}{4B_2B_3}[\overline{(e_2+e_3)^2} - \overline{(e_2-e_3)^2}]$$

$$\text{or } \frac{1}{2B_2B_3}[\overline{e_2^2} + \overline{e_3^2} - \overline{(e_2-e_3)^2}]$$

(*b*) Cooling Velocities to Orthogonal Wire Coordinate Velocities. The next step of the data reduction is to relate the nine components of velocity in wire coordinates x, y, and z to the nine components of cooling velocity given in equation (8). In the previous step, the nonlinearity of equation (1) can be overcome easily by electronic means because the equation contains only two variables. In the present step, each quadratic equation as represented in the set of equation (4) relates the cooling velocities V_1 or V_2 or V_3 to the three components of wire coordinate velocity V_x, V_y, V_z and as such cannot be easily linearized by electronic means. Simplification has to be made by using binomial expansion and neglecting smaller order terms. The transformation matrix required is M^{-1} given in equation (6). Representing the M^{-1} matrix as

$$M^{-1} = \begin{vmatrix} a_1 & a_2 & a_3 \\ b_1 & b_2 & b_3 \\ c_1 & c_2 & c_3 \end{vmatrix}$$

then

$$V_x^2 = a_1V_1^2 + a_2V_2^2 + a_3V_3^2$$

or

$$(\bar{V}_x + v_x)^2 = a_1(\bar{V}_1 + v_1)^2 + a_2(\bar{V}_2 + v_2)^2 + a_3(\bar{V}_3 + v_3)^2 \quad (a)$$

Expanding equation (*a*) and taking the time mean

$$\bar{V}_x^2 + \overline{v_x^2} = a_1(\bar{V}_1^2 + \overline{v_1^2}) + a_2(\bar{V}_2^2 + \overline{v_2^2}) + a_3(\bar{V}_3^2 + \overline{v_3^2})$$

Let $\bar{V}_{x0}^2 = a_1\bar{V}_1^2 + a_2\bar{V}_2^2 + a_3\bar{V}_3^2$

and $\overline{v_{x0}^2} = a_1\overline{v_1^2} + a_2\overline{v_2^2} + a_3\overline{v_3^2}$

$\therefore \overline{v_x^2} = \overline{v_{x0}^2} + \bar{V}_{x0}^2 - \bar{V}_x^2$

Rewriting equation (a) as

$$\bar{V}_x + v_x = (\bar{V}_{x0}^2 + 2\,a_1\bar{V}_1v_1 + 2\,a_2\bar{V}_2v_2 + 2\,a_3\bar{V}_3v_3 + a_1v_1^2 + a_2v_2^2 + a_3v_3^2)^{1/2}$$

Expanding and taking time mean, neglecting terms higher than v^2

$$\bar{V}_x = \bar{V}_{x0}\left[1 + \frac{1}{2}\frac{\overline{v_{x0}^2}}{\bar{V}_{x0}^2} - \frac{\Delta_x}{2\,\bar{V}_{x0}^4}\right] \tag{b}$$

where

$$\Delta_x = \sum_{j=1}^{3}\sum_{i=1}^{3} a_ia_j\,\bar{V}_i\bar{V}_j\,\overline{v_iv_j}$$

The neglect of terms higher than v^2 is justifiable because terms like $v_1v_2^2$ and $v_1^2v_2$ represent triple product of three small terms. Since the positive v_2^2 or v_1^2 terms are multiplied by another small term v_1 or v_2, the time mean of which is zero, $\overline{v_1v_2^2}$ and $\overline{v_1^2v_2}$ are expected to be small and can be neglected. Term like $\overline{v_1^2v_2^2}$ can also be neglected since it is the product of four small terms, although it is always positive. Besides, they are normalized by large mean term like $\bar{V}_{x0}$ of the same power and their effects are further diminished.

Also

$$(\bar{V}_x + v_x)^2(\bar{V}_y + v_y)^2 = [a_1(\bar{V}_1 + v_1)^2 + a_2(\bar{V}_2 + v_2)^2 + a_3(\bar{V}_3 + v_3)^2][b_1(\bar{V}_1 + v_1)^2 + b_2(\bar{V}_2 + v_2)^2 + b_3(\bar{V}_3 + v_3)^2] \tag{c}$$

Expanding the left-hand side of equation (c) and taking time mean, neglecting terms higher than v^2 for similar reasons as before,

$$\overline{(\bar{V}_x + v_x)^2(\bar{V}_y + v_y)^2} = \bar{V}_x^2\bar{V}_y^2 + \bar{V}_x^2\overline{v_y^2} + \bar{V}_y^2\overline{v_x^2} + 4\bar{V}_x\bar{V}_y\overline{v_xv_y}$$

Expanding the whole of equaton (c) and taking the time mean in a similar manner,

$$\therefore\ \bar{V}_x^2\bar{V}_y^2 + \bar{V}_x^2\overline{v_y^2} + \bar{V}_y^2\overline{v_x^2} + 4\bar{V}_x\bar{V}_y\overline{v_xv_y} = \sum_{j=1}^{3}\sum_{i=1}^{3} a_ib_j(\bar{V}_i^2\bar{V}_j^2 + \bar{V}_i^2\overline{v_j^2} + \bar{V}_j^2\overline{v_i^2} + 4\bar{V}_i\bar{V}_j\overline{v_iv_j})$$

Hence the three mean velocity components and six Reynolds stresses in the wire coordinates x, y, and z are related to the cooling velocities by the following nine equations.

$$\bar{V}_x = \bar{V}_{x0}\left[1 + \frac{1}{2}\frac{\overline{v_{x0}^2}}{\bar{V}_{x0}^2} - \frac{\Delta_x}{2\,\bar{V}_{x0}^4}\right]$$

$$\bar{V}_y = \bar{V}_{y0}\left[1 + \frac{1}{2}\frac{\overline{v_{y0}^2}}{\bar{V}_{y0}^2} - \frac{\Delta_y}{2\,\bar{V}_{y0}^4}\right]$$

$$\bar{V}_z = \bar{V}_{z0}\left[1 + \frac{1}{2}\frac{\overline{v_{z0}^2}}{\bar{V}_{z0}^2} - \frac{\Delta_z}{2\,\bar{V}_{z0}^4}\right]$$

$$\overline{v_x^2} = \overline{v_{x0}^2} + \bar{V}_{x0}^2 - \bar{V}_x^2$$

$$\overline{v_y^2} = \overline{v_{y0}^2} + \bar{V}_{y0}^2 - \bar{V}_y^2$$

$$\overline{v_z^2} = \overline{v_{z0}^2} + \bar{V}_{z0}^2 - \bar{V}_z^2$$

$$\overline{v_xv_y} = \left[\sum_{j=1}^{3}\sum_{i=1}^{3} a_ib_j(\bar{V}_i^2\bar{V}_j^2 + \bar{V}_i^2\overline{v_j^2} + \bar{V}_j^2\overline{v_i^2} + 4\bar{V}_i\bar{V}_j\overline{v_iv_j}) - \bar{V}_x^2\bar{V}_y^2 - \bar{V}_x^2\overline{v_y^2} - \bar{V}_y^2\overline{v_x^2}\right]\Big/4\bar{V}_x\bar{V}_y$$

$$\overline{v_xv_z} = \left[\sum_{j=1}^{3}\sum_{i=1}^{3} a_ic_j(\bar{V}_i^2\bar{V}_j^2 + \bar{V}_i^2\overline{v_j^2} + \bar{V}_j^2\overline{v_i^2} + 4\bar{V}_i\bar{V}_j\overline{v_iv_j}) - \bar{V}_x^2\bar{V}_z^2 - \bar{V}_x^2\overline{v_z^2} - \bar{V}_z^2\overline{v_x^2}\right]\Big/4\bar{V}_x\bar{V}_z$$

$$\overline{v_yv_z} = \left[\sum_{j=1}^{3}\sum_{i=1}^{3} b_ic_j(\bar{V}_i^2\bar{V}_j^2 + \bar{V}_i^2\overline{v_j^2} + \bar{V}_j^2\overline{v_i^2} + 4\bar{V}_i\bar{V}_j\overline{v_iv_j}) - \bar{V}_y^2\bar{V}_z^2 - \bar{V}_y^2\overline{v_z^2} + \bar{V}_z^2\overline{v_y^2}\right]\Big/4\bar{V}_y\bar{V}_z \tag{9}$$

where

$$\begin{vmatrix}\bar{V}_{x0}^2\\ \bar{V}_{y0}^2\\ \bar{V}_{z0}^2\end{vmatrix} = \begin{vmatrix}a_1 & a_2 & a_3\\ b_1 & b_2 & b_3\\ c_1 & c_2 & c_3\end{vmatrix}\begin{vmatrix}\bar{V}_1^2\\ \bar{V}_2^2\\ \bar{V}_3^2\end{vmatrix}$$

$$\begin{vmatrix}\overline{v_{x0}^2}\\ \overline{v_{y0}^2}\\ \overline{v_{z0}^2}\end{vmatrix} = \begin{vmatrix}a_1 & a_2 & a_3\\ b_1 & b_2 & b_3\\ c_1 & c_2 & c_3\end{vmatrix}\begin{vmatrix}\overline{v_1^2}\\ \overline{v_2^2}\\ \overline{v_3^2}\end{vmatrix}$$

$$\Delta_x = \sum_{j=1}^{3}\sum_{i=1}^{3} a_ia_j\bar{V}_i\bar{V}_j\overline{v_iv_j}$$

$$\Delta_y = \sum_{j=1}^{3}\sum_{i=1}^{3} b_ib_j\bar{V}_i\bar{V}_j\overline{v_iv_j}$$

$$\Delta_z = \sum_{j=1}^{3}\sum_{i=1}^{3} c_ic_j\bar{V}_i\bar{V}_j\overline{v_iv_j}$$

It should be noted that the three mean velocity equations and the three Reynolds normal stress equations in equation system (9) are expressed explicitly in terms of the cooling velocities and can be evaluated very easily. After calculating the mean velocity components and Reynolds normal stresses, the Reynolds shear stresses can also be determined explicitly using the last three equations of equation system (9).

(c) Wire Coordinate Velocities to Laboratory Coordinate Velocities. The most difficult portion of the whole exercise lies in relating the wire coordinate velocities explicitly to the cooling velocities undertaken in the previous step. In the present step, the nine values obtained in wire coordinates can be transformed to any other orthogonal coordinates if the direction cosines between the new and old coordinates are known. The transformation is simple since unlike the previous step, it does not involve the square of the velocity vectors in the linear transformation.

To obtain the mean velocity components and Reynolds stresses in laboratory coordinates as shown in Fig. 1, equation (7) can be used. Representing the N transformation matrix as

$$N = \begin{vmatrix}d_1 & d_2 & d_3\\ f_1 & f_2 & f_3\\ g_1 & g_2 & g_3\end{vmatrix}$$

it follows that

$$\begin{vmatrix} \bar{U} \\ \bar{V} \\ \bar{W} \end{vmatrix} = N \begin{vmatrix} \bar{V}_x \\ \bar{V}_y \\ \bar{V}_z \end{vmatrix}$$

and

$$\begin{vmatrix} u \\ v \\ w \end{vmatrix} = N \begin{vmatrix} v_x \\ v_y \\ v_z \end{vmatrix}$$

Squaring u and taking the time mean gives

$$\overline{u^2} = d_1^2\overline{v_x^2} + d_2^2\overline{v_y^2} + d_3^2\overline{v_z^2} + 2d_1d_2\overline{v_xv_y} + 2d_1d_3\overline{v_xv_z} + 2d_2d_3\overline{v_yv_z}$$

Multiplying u and v and taking time mean gives

$$\overline{uv} = d_1f_1\overline{v_x^2} + d_2f_2\overline{v_y^2} + d_3f_3\overline{v_z^2} + (d_1f_2 + d_2f_1)\overline{v_xv_y} + (d_1f_3 + d_3f_1)\overline{v_xv_z} + (d_2f_3 + d_3f_2)\overline{v_yv_z}$$

Hence, the three mean velocity components and six Reynolds stresses in laboratory coordinates X, Y, and Z are related to the corresponding values in wire coordinates x, y, and z explicitly by the following nine equations.

$$\begin{vmatrix} \bar{U} \\ \bar{V} \\ \bar{W} \end{vmatrix} = \begin{vmatrix} d_1 & d_2 & d_3 \\ f_1 & f_2 & f_3 \\ g_1 & g_2 & g_3 \end{vmatrix} \begin{vmatrix} \bar{V}_x \\ \bar{V}_y \\ \bar{V}_z \end{vmatrix}$$

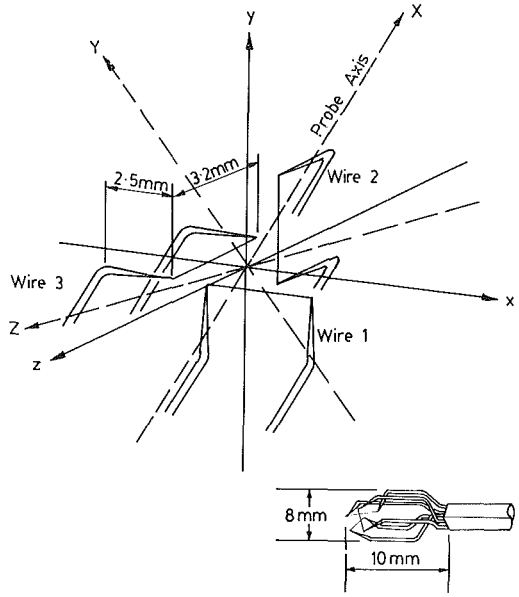

Fig. 2 Triple sensor probe geometry

where the sharp intersection 0 of the three wires points against the flow direction. For DISA Type 55P91 triple sensor probe where 0 points in the opposite direction, the flow velocity is along the negative OX axis and must be taken as negative in order to yield the Reynolds stresses of the correct sign.

The linearized triple sensor voltage signals E_1, E_2, E_3 were acquired by a DATA 6000 data acquisition unit with a data acquisition rate up to 100 KHz. The sum, difference and DC offset of signals were done in an analog way before the analog to digital data conversion, while the mean square computation, Fast Fourier Transform (FFT) were done digitally. Since the area under a FFT spectrum was equal to the mean square value of the fluctuating voltages, they could be used for cross-checking. Agreement within 2 percent was obtained except near the edge of the boundary layer where the fluctuating voltages were small and digitization, integration errors were large.

$$\begin{vmatrix} \overline{u^2} \\ \overline{v^2} \\ \overline{w^2} \\ \overline{uv} \\ \overline{uw} \\ \overline{vw} \end{vmatrix} = \begin{vmatrix} d_1^2 & d_2^2 & d_3^2 & 2d_1d_2 & 2d_1d_3 & 2d_2d_3 \\ f_1^2 & f_2^2 & f_3^2 & 2f_1f_2 & 2f_1f_3 & 2f_2f_3 \\ g_1^2 & g_2^2 & g_3^2 & 2g_1g_2 & 2g_1g_3 & 2g_2g_3 \\ d_1f_1 & d_2f_2 & d_3f_3 & (d_1f_2+d_2f_1) & (d_1f_3+d_3f_1) & (d_2f_3+d_3f_2) \\ d_1g_1 & d_2g_2 & d_3g_3 & (d_1g_2+d_2g_1) & (d_1g_3+d_3g_1) & (d_2g_3+d_3g_2) \\ f_1g_1 & f_2g_2 & f_3g_3 & (f_1g_2+f_2g_1) & (f_1g_3+f_3g_1) & (f_2g_3+f_3g_2) \end{vmatrix} \begin{vmatrix} \overline{v_x^2} \\ \overline{v_y^2} \\ \overline{v_z^2} \\ \overline{v_xv_y} \\ \overline{v_xv_z} \\ \overline{v_yv_z} \end{vmatrix} \quad (10)$$

6 Experimental Verification

To verify the above data reduction method, measurements were conducted in a zero pressure gradient incompressible turbulent boundary layer on the floor of a 0.91 m (3 ft) wide, 7.62 m (25 ft) long test section of the wind tunnel. The upper wall of the test section was adjusted so as to give a uniform freestream velocity of 21 m/s. The test floor boundary layer was tripped by the blunt leading edge of the plywood floor with a step height of 6.4 mm (1/4 in.). Boundary layer velocity profile measurements were taken with a DISA Type 55P91 triple sensor hot-wire and a single sensor hot-wire at X locations of 3.206 m, 4.255 m and 6.457 m measured from the leading edge of the test floor. The boundary layer thickness at the respective X locations are 38.9 mm, 49.4 mm, and 81.5 mm. The geometry of the triple sensor probe and its relation to the wire and laboratory coordinates is shown in Fig. 2. The three sensors are 3.2 mm long platinum-plated tungsten wires of 5 μm diameter. They are copper and gold plated at the ends to leav a sensitive length of 1.25 mm. The sensors are mutually perpendicular with the sensitive length inside a sphere of 3 mm diameter. It should be noted that the data reduction method described above adopts the sign convention as shown in Fig. 1 which is applicable to TSI Model 1294 triple sensor probe

Before data reduction, K_T and K_N must be determined. Although it was desirable to obtain K_T and K_N by calibrating the three sensors collectively as mentioned before, this method was not feasible with the present calibration set up. To determine K_T, K_N and obtain closure, the angles between the flow direction and each individual wires must be measured accurately; a condition beyond the capability of the present set up. However, the orthogonality of the sensors was checked by using a travelling microscope, and it was found to be accurate within 1 deg. The K_T and K_N were obtained by calibrating each sensor individually by aligning the flow along the sensor and normal to the sensor-prongs plane. Although this method may introduce prong interference effects, the results obtained

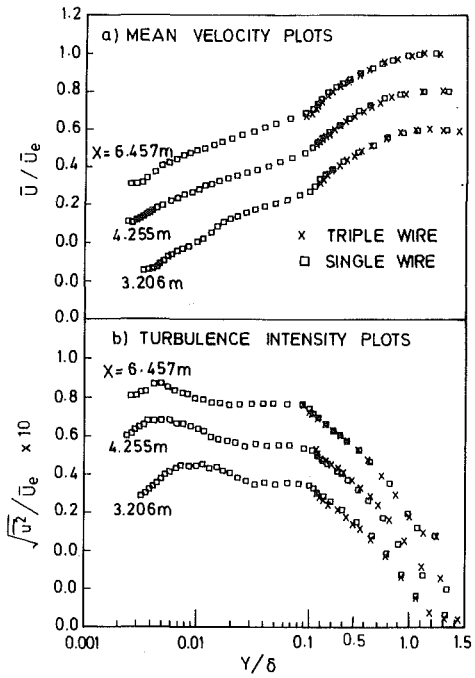

Fig. 3 Mean velocity and turbulence intensity at various X locations. Uncertainities: single wire, $\bar{U}/\bar{U}_e = \pm 0.01$, $\sqrt{u^2}/\bar{U}_e = \pm 0.001$; triple wire, $\bar{U}/\bar{U} = +0.02$, $\sqrt{\bar{u}^2}/\bar{U}_e = \pm 0.002$; $y/\delta = \pm 0.0005$.

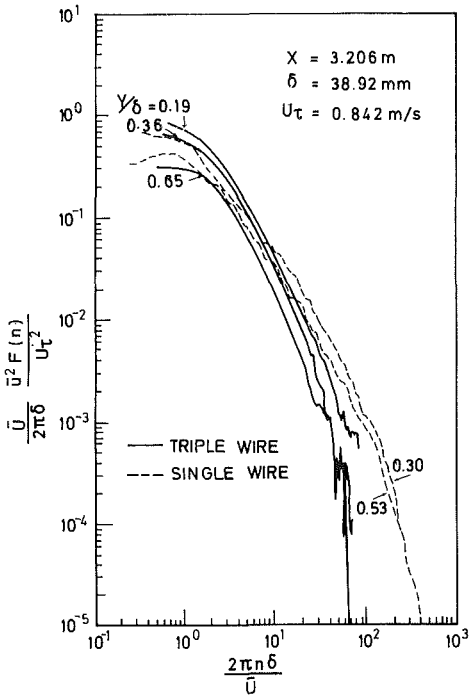

Fig. 4 Turbulence energy spectra at $X = 3.206$m. Uncertainties: ordinate, single wire $= \pm 10^{-4}$, triple wire $= \pm 10^{-3}$; abscissca $= \pm 0.01$.

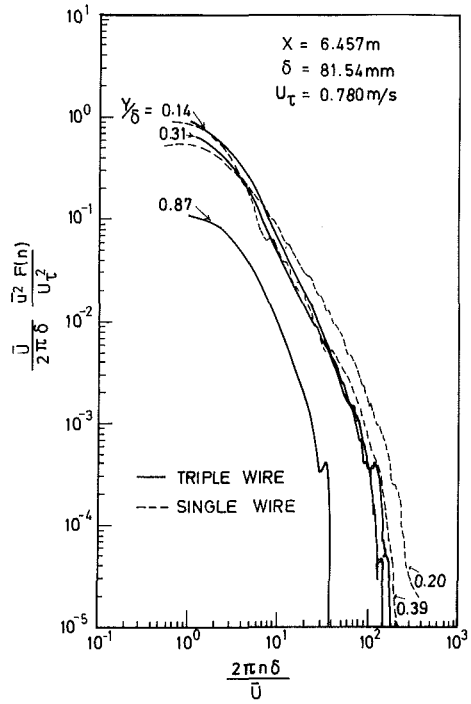

Fig. 5 Turbulence energy spectra at $X = 6.457$m. Uncertainties same as in Fig. 4.

were comparable to those obtained by Jϕrgensen [6] for gold-plated single wire since each individual wire of the DISA Type 55P91 triple-sensor probe is also gold-plated. For a calibration velocity range of 5–25 m/s, K_T and K_N for the three sensors were found to be 0.110–0.145 and 0.991–1.017, respectively. For final data reduction, $K_T = 0.13$ and $K_N = 1.02$ were chosen since most of the values of K_T and K_N were close to them. They were rounded to two places of decimal because of the experimental uncertainties.

If the flow was along the probe axis and the relative angles between the three sensors and probe axis were as shown in Fig. 1, α and β would be 54.74 and 45 deg, respectively. However, it was difficult to align the probe so that the flow was exactly along the probe axis in the wind tunnel, it was decided to compute α and β so that the conditions of $\bar{V} = \bar{W} = 0$, which are approximately the case in a two-dimensional zero pressure gradient boundary layer, were satisfied. The matrix N in equation (7) for transforming wire coordinate velocities to laboratory coordinate velocities was then computed.

The mean velocity profiles and u turbulence intensity measured by triple sensors and single hot-wire anemometer at various X locations are as shown in Fig. 3. Triple sensors data at Y/δ less than about 0.1 are not available because of the physical size limitation of the probe. The X coordinate is plotted as logarithmic scale up to $Y/\delta = 0.1$ and linear scale beyond that for clarity. The agreement between the triple sensors and single sensor hot-wire anemometer measurements is good and validates the above data reduction method.

To compute the energy spectra of u fluctuating velocity, the spectra of $\overline{e_1^2}$, $\overline{e_2^2}$, $\overline{e_3^2}$ etc are used. The computation is conducted at each individual frequency in the same way as before. It should be noted that $\bar{V}_x$, $\bar{V}_y$, $\bar{V}_z$ in equation system (9) are frequency dependent since they involve small correction terms like $\overline{v_{x0}^2}$, Δ_x etc which are fluctuating, frequency related quantities. In calculating the energy spectra at successive frequency, $\bar{V}_x$, $\bar{V}_y$, $\bar{V}_z$ are corrected only by small terms within the corresponding frequency bandwidth, whereas in calculating the overall Reynolds stresses, they are corrected by small terms covering the complete frequency range. To examine the extent of this inherent error, the area under the energy spectra curve of u fluctuating velocity was checked with the calculated $\overline{u^2}$. Agreement within 3 percent was obtained. Since part of this error is attributed to the discrepancies between the FFT of e_1, e_2, e_3 and their mean square values, the inherent error is small.

The energy spectra of a fluctuating velocity at $x = 3.206$ m and 6.457 m are presented in Figs. 4 and 5 for both triple sensors and single sensor measurements. The frictional velocity U_τ was obtained from Clauser's plot of single wire data. The agreement between the triple sensors and single sensor data is reasonable except at higher frequency where the tiple sensors data are lower. The high frequency attenuation by the triple

sensors probe is most probably due to the length scale effects. The three sensing elements of 1.25 mm length lie in a sphere of 3 mm diameter and true point measurement cannot be expected. High frequency eddies with length scale smaller than 3 mm would be attenuated since they cannot be resolved effectively. For single sensor probe of 5 μm wire diameter, the spatial resolution is much better. This high frequency attenuation due to scale effects is also evident when comparison is made between Fig. 4 and Fig. 5. At $X=6.457$ m where the boundary layer is more than twice the thickness of that at $X=3.206$ m, the high frequency attenuation by the triple sensors probe is smaller since the relative sizes of the eddies to the probe's spatial resolution are larger. The frequency sensed by the probe is directly related to the eddy size since the convection velocities $\bar{U}$ at corresponding Y/δ are equal for zero pressure gradient boundary layer.

It should be noted that the experimental verification of the present method does not consider the K_T, K_N variation corrections for each individual wire as suggested by Andreopoulos [11]. The present experimental data were measured in a turbulent boundary layer with maximum turbulence intensity less than 9 percent (as compared to 20 percent in Andreopoulos's experiment) and the pitch and yaw angle variations of instantaneous flow from a generally known mean direction were small. Based on Andreopoulos's results, the effects of K_T and K_N variation corrections on the present data would be very small. As mentioned earlier in section 4, these effects on $\overline{v^2}$ and $\overline{w^2}$ are only large when the probe is pitched by as much as 30 deg in highly turbulent flow. Andreopoulos also found that the effect of K_N variation correction on $\overline{v^2}$ and $\overline{w^2}$ is larger than that due to K_T variation. This may be due to the higher K_N of 1.10 to 1.14 used in his experiment. In the present experiment, $K_N=1.02$ was used which was more in line with that used by Gaulier [8], Frota and Moffat [5], and Lakshminarayana and Poncet [10] who assumed $K_N=1.00$. It is within the scatter of experiment data of K_N for single gold-plated wire obtained by Jørgensen [6]. The accuracy of measuring K_T and K_N depends strongly on the accuracy of determining the pitch and yaw angles of probe during calibration. These angles are needed to resolve the velocity into the normal and binormal or tangential components in order to calculate K_T and K_N. A small error in the measurement of these angles would bias the velocity towards one of the two resolved components, and increase or decrease the values of K_T and K_N significantly.

Although the present experimental verification does not include the K_T and K_N variation corrections, they can be easily incorporated into the present, non-real time data analysis method in highly turbulent flow. The same iterative scheme as proposed by Andreopoulos can be adopted.

7 Conclusions

The method of data reduction described above is explicit and requires no iteration. Hence unlike other methods, computation represented by the three sets of equations (8), (9), and (10) is simple and fast. The first stage of relating triple sensors cooling velocities to the sensors output voltages, represented by equation (8), and the third stage of relating the laboratory coordinates velocities to the wire coordinates velocities, represented by equation (10), are exact. The only simplification made is in the second stage of relating the wire coordinates velocities to the sensors cooling velocities, where the triple products and quadruple products of fluctuating velocities are neglected. These products, as explained before, are small.

From the three sensors output voltages, the nine voltages required $\bar{E}_1$, $\bar{E}_2$, $\bar{E}_3$, $\overline{e_1^2}$, $\overline{e_2^2}$, $\overline{e_3^2}$, $\overline{(e_1-e_2)^2}$, $\overline{(e_1-e_3)^2}$, $\overline{(e_2-e_3)^2}$ can be easily obtained from analog devices. The present method of relating the three mean velocity components and six Reynolds stresses to these voltages explicitly makes it possible to compute the results later manually using a simple calculator. If automatic data acquisition using a computer is required e.g., ensemble averaging of data in unsteady flow, the present method allows the separation of mean and unsteady components of voltages using a filtering technique before digitization, and hence maximizes the resolution of the analog to digital converter. As the number of arithmatic operations in calculating mean and mean square voltages is simple and few, their computations can be carried out simultaneously with data acquisition, especially when the computations are written in machine language. Hence, a small size computer can be used to sample data over a very long period without flooding the core memory.

In the present analysis, an ideal probe geometry is assumed. If the three sensors are orthogonal but not symmetrical about the probe axis, the deviation can also be easily incorporated into the matrix N.

The present method assumes constant K_T and K_N. If their variation affects the results significantly, an iterative calculation procedure same as that proposed by Andreopoulos [11] can be adopted. Based on the computed velocity vector, K_T and K_N can be determined from calibration data at different velocity magnitudes and directions and the computation repeated. The iteration procedure is not time consuming because of the explicit nature of equations and the weak dependence of the mean velocity compontnes and Reynolds stresses on K_T and K_N variation.

The present method also opens a way to obtain turbulence spectra of Reynolds stresses using non-real time method. For real time analysis, the conversion of E_1, E_2, E_3 to real time U, V, W for the extraction of turbulence spectra at high frequency is impossible digitally because of limitation in computer speed and storage. Hence, specially designed analog device is required [5]. In the present explicit non-real time method, turbulence spectra of Reynolds stresses can be calculated easily from the FFT of sensor output voltages which can be performed to the desired frequency resolutions. For the present Reynolds stresses calculation with 512 frequency data using a compiled basic program on an IBM PC XT micro-computer, the computation time is 4 min 10 s.

Acknowledgments

The authors wish to thank W. Devenport for useful discussion and S. K. Ahn for taking the single sensor hot-wire anemometer data.

References

1 Hoffmeister, M., "Using a Single Hot Wire Probe in Three Dimensional Turbulent Flow Fields," *DISA Information*, No. 13, 1972, pp. 26–28.

2 Fujita, H., and Kovasznay, L. S. G., "Measurement at Reynolds Stress by a Single Rotated Hot Wire," *Review of Scientific Instruments*, Vol. 39, 1968, p. 1351.

3 Saripalli, K. R., and Simpson, R. L., "Investigation of Blown Boundary Layers with an Improved Wall Jet System," NASA C. R. 3340, 1980.

4 Zank, I., "Sources of Errors and Running Calibration of Three-Dimensional Hot-Film Anemometers Especially Near the Sea Surface," *DISA Information*, No. 26, 1981, pp. 11–18.

5 Frota, M. N., and Moffat, R. J., "Effects of Combined Roll and Pitch Angles on Triple Hot-Wire Measurements of Mean and Turbulence Structure," *DISA Information*, No. 28, 1983, pp. 15–23.

6 Jørgensen, F. E., "Directional Sensitivity of Wire and Fiber Film Probes," *DISA Information*, No. 11, 1971, pp. 31–37.

7 Butler, T., and Wagner, J. H., "An Improved Method for Calibration and Use of a Three Sensor Hot Wire Probe in Turbomachinery Flows," AIAA paper 82-0195, 1982.

8 Gaulier, C., "Measurement of Air Velocity by Means of a Triple Hot-Wire Probe," *DISA Information*, No. 21, 1977, pp. 16–20.

9 Hirsch, C. H., and Kool, P., "Measurement of the Three-Dimensional Flow Field Behind an Axial Compressor Stage," ASME *Journal of Engineering for Power*, Vol. 99, 1977, p. 168.

10 Lakshminarayana, B., and Poncet, A., "A Method of Measuring Three-Dimensional Wakes in Turbomachinery," ASME JOURNAL OF FLUIDS ENGINEERING, Vol. 96, 1974, pp. 87–91.

11 Andreopoulos, J., "Improvements of the Performance of Triple Hot Wire Probes," *Rev. Sci. Instrum.*, Vol. 54, No. 6, 1983, pp. 733–739.

12 Gorton, C. A., and Lakshminarayana, B., "A Method of Measuring the Three-Dimensional Mean Flow and Turbulence Quantities Inside a Rotating Turbo-machinery Passage," ASME *Journal of Engineering for Power*, Vol. 98, 1976, pp. 137–146.

13 Moffat, R. J., Yavuzkurt, S., and Crawford, M. E., "Real Time Measurements of Turbulence Quantities with a Triple Hot-Wire System," *Proceedings of the Dynamic Flow Conference on Dynamic Measurements in Unsteady Flows*, 1978, pp. 1013–1035.

B. Lakshminarayana

R. Davino

Department of Aerospace Engineering,
The Pennsylvania State University,
University Park, PA 16802.

Sensitivity of Three Sensor Hot Wire Probe to Yaw and Pitch Angle Variation

The use of a three sensor hot wire probe for the measurement of three-dimensional flow field is increasing rapidly. This probe is very sensitive to yaw and pitch angle variations and existing laws for single sensor wires cannot be utilized to provide the correct hotwire response equations. A systematic study at various yaw and pitch angles (maximum values of ± 40 deg, nearly 220 different yaw and pitch angles) is carried out to determine the nature of response of a triple sensor hot wire probe. These results are analyzed to provide a correlation for the hot wire response equation which includes both pitch and yaw angles as variables.

1 Introduction

In three dimensional flows or when the direction of the incident flow-field is not known "a priori" it is necessary to determine the accuracy of the probe when it is yawed and pitched with respect to the calibration flow. However, many investigators are routinely employing the three-sensor probe to determine the characteristics of various three dimensional flows. A state-of-the-art review by Lakshminarayana[1] on the use of the triple sensor hot wire probe in three dimensional flow indicates that one of the major improvements in its use should come from an improved calibration technique to include the effects of yaw and pitch angles. The overall response of the probe is examined in this paper and sensitivity functions which compensate for the response of the three-sensor probe to varying angles of yaw and pitch are proposed.

2 Experimental Program

The investigation of three-sensor probe's response was performed in the potential core of a 30.5 cm diameter circular jet of very low turbulence intensity. The maximum jet velocity was 32.3 meters per second and maintained within an accuracy of ±0.1 percent. The temperature variation of the jet was limited to ±0.2 °C. The hot-wire probes were operated at a constant temperature employing three DISA Model 55M10 anemometer units. Overheat ratios of 0.5 were used. The probe sensors were of the copper coated tungsten type where the center section of the wire was etched to expose the sensing tungsten wire. Figure 1 shows the three-sensor hot-wire probe used for this investigation. Each sensor had a length-to-diameter ratio of 135 and a resistance of approximately 4.5 ohms.

3 Sensitivity of the Probe to Yaw and Pitch Angle Variation

The sensitivity of a three-sensor hot-wire probe to varying angles of yaw α and pitch β angle was investigated to determine the nature and magnitude of errors involved. In this way, a mapping of the individual sensor response was obtained for a range of ±40 degrees of yaw angle and ±30 degrees of pitch angle at 5 deg interval. Initially, each sensor of the probe had been individually calibrated with the calibration jet normal to the sensor using King's Law. The total incident velocity U_T sensed by the probe at various positions of yaw and pitch angle was derived using these calibrations. This velocity was then compared to the reference velocity U_{ref} of the calibration jet at its potential core which had a value of 30.5 m/s.

The probe response (Fig. 2) is given as the ratio of U_T-to-U_{ref} at various values of α and β. The left hand scale is the value of U_T/U_{ref} based upon the individual sensor calibration described above and the right hand scale is the value of U_T/U_{ref} based upon a combined sensor calibration which is described below. The difference in sensor response, based upon either calibration, is illustrated by reviewing the datum point of 0 deg yaw and 0 deg pitch. At this point, the ratio of U_T/U_{ref} should equal 1.0. However, the individual sensor calibration yields a value of 0.885, which represents an error of approximately 11 percent.

A combined sensor calibration was found to yield more cor-

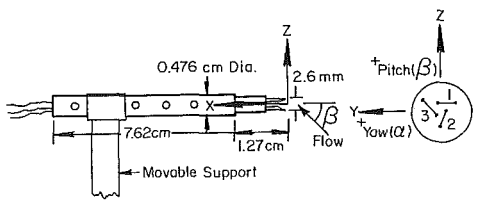

Fig. 1 Three-sensor hot-wire probe

Contributed by the Fluids Engineering Division for publication in the JOURNAL OF FLUIDS ENGINEERING. Manuscript received by the Fluids Engineering Division, October 15, 1986.

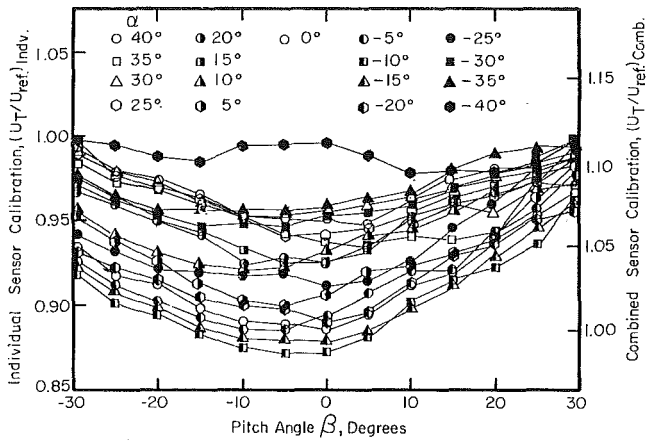

Fig. 2 Response of three-sensor hot-wire probe to varying angles of yaw and pitch angles

rect values of U_T. In this procedure, the probe was placed so that the calibration jet was aligned with the x axis of the probe (Fig. 1). The response of each sensor, at this probe position, was fit with the King's Law to the calibration jet velocity which was varied in magnitude. Using this method, all the three sensors were simultaneously calibrated at one probe position. This calibration procedure was found to determine, accurately, the incident velocity sensed by the probe, as indicated by Fig. 2.

The value of U_T was derived from the response of the three sensors, using a cosine law dependence only. The probe response is shown to be accurate at small values of yaw and pitch angles. However, at larger values of yaw and pitch angles, deviations as large as 12 percent of the reference velocity were measured. The two likely candidates causing asymmetry in the calibration curve are aerodynamic interference from the support prongs and the thermodynamic interference from the heated wakes of other sensors.

The error ϵ_T between the total velocity (based on a combined sensor calibration) sensed by the three-sensor hot-wire probe and the reference velocity is defined by:

$$\epsilon_T = \frac{U_T - U_{\text{ref}}}{U_T} \times 100$$

This error was plotted as a function of yaw and pitch angle and is shown in Fig. 3. The contours of error indicate that substantial asymmetric deviations from the cosine law occur as the probe is exposed to a directionally varying incident flow.

In addition, the probe configuration results in a greater yaw angle sensitivity which is probably due to the orientation of the three sensors. The increase in error at nonzero values of yaw and pitch is due mainly to the component of velocity parallel to the axis of the sensors. The maximum error is 12 percent over the yaw angle range of ±40 degrees. The error is less than 4 percent at values of yaw and pitch angle below 10 degrees.

Sensitivity of Individual Sensors in the Probe. The response of each sensor was investigated in an attempt to derive a more precise information on the nature of the variation in the probe response. The normalized cooling velocity of each sensor $(U_N)_i$, given by

$$(U_N)_i = \frac{(U_{\text{eff}})_i}{(U_{\text{ref}})_i}; i = 1,2,3 \qquad (1)$$

where i refers to an individual wire, was plotted as a function of the deviation (from the normal to the wire) angle λ for each sensor. The deviation angle λ was calculated from our knowledge of the sensor position relative to the probe axis and

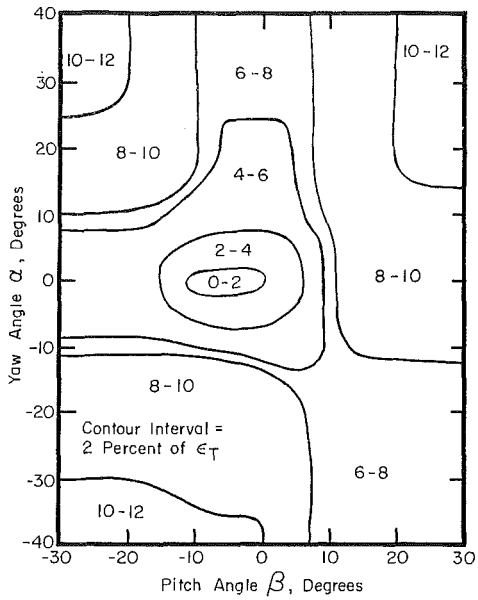

Fig. 3 Error of uncorrected three-sensor hot-wire probe response with yaw (α) and pitch angle (β) variation

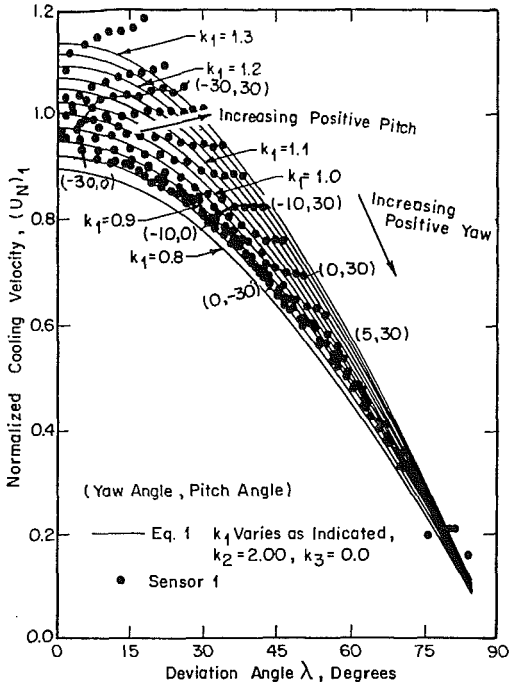

Fig. 4 Variation of deviation angle sensitivity function with deviation angle for sensor 1 and comparison with the data (uncertainty in the data ± 1 percent for U_N and ± 1 deg for angle)

the yaw and pitch angles. The normalized cooling velocity U_N was calculated from the response of the individual sensor (effective cooling velocity U_{eff}) and the normal component U_{ref} of the calibration velocity vector at each yaw and pitch angle. The resultant plot is given in Fig. 4 for sensor 1. Similar plots were produced for sensors 2 and 3. These data are plotted against the cosine law (solid line) for reference (K_1 = 1.0 in Fig. 4).Considerable deviations from the cosine law exist for each sensor and these deviations do not necessarily occur at the only high deviation angles. The deviation in the response of a sensor is a function of the yaw and pitch angle of the probe. For each sensor the data lie in a band whose width is

determined by yaw and pitch angle. The character of these data bands of the deviation from the cosine law indicates that it is necessary to consider the orientation of each sensor relative to the incident velocity field and the other sensors.

Technique for Incorporating the Yaw and Pitch Angle Effects. The error ϵ_T is given in Fig. 3 can now be interpreted as a combination of each individual sensor's deviation from the cosine law. A correction of the overall error of the three-sensor hot-wire probe, when it is subjected to varying angles of incidence with respect to the flow field, is obtained by first correcting the response of the individual sensors. This was achieved by correcting the normalized cooling velocity of each wire through the use of a deviation angle sensitivity function g(λ) given by:

$$U_{\text{eff}} = U_i g(\lambda) \tag{2}$$

The deviation angle λ, which is a function of the yaw and pitch angles of the probe, is the angle between the incident velocity and the normal to the wire.

By considering the behavior of the calibration data for each of the sensors (e.g., Fig. 4) a deviation angle sensitivity function of the form:

$$g(\lambda) = [k_1(\cos^{k_2}\lambda + k_3 \sin^2\lambda)]^{1/2} \tag{3}$$

is proposed. Figure 4 shows the family of curves generated by altering various parameters of the function for sensor 1, with k_1 varying for 0.8 to 1.3 in 0.05 increments, k_2 equal to 2.0, and k_3 equal to 0.0. This family of lines represents an accurate variation of the sensitivity function at various values of yaw and pitch angle for sensor 1. Parameters k_1, k_2, and k_3 for sensors 2 and 3 were similarly determined.

The sensitivity function given by Equation (3) was employed to calculate the total velocity sensed by the entire probe. The exact value of the parameters k_1, k_2, and k_3 were chosen to give the best fit between the data and the sensitivity functions of α and β (e.g. Fig. 4 for sensor 1). This procedure was employed for each of the three sensors. The corrected response of each sensor was then used with the direction cosines of the sensors to determine the total incident flow velocity U_T as a function of yaw and pitch angles. These values of U_T were compared to the reference flow velocity U_{ref} to derive the resultant error. This error ϵ_T is shown in Fig. 5 in the form of a contour plot for various yaw and pitch angles. The effect of employing the deviation angle sensitivity function is evident by comparing Figs. 3 and 5. Figure 3 shows that initially an error of 10 percent or greater occurred beyond a yaw or pitch angle of ±10 degrees. By employing the correction due to the deviation angle sensitivity function g(λ), this error is substantially reduced. Even at large angles of yaw and pitch, the maximum error is reduced to 8 percent. This is a substantial improvement in the total response of the probe.

In view of the results of this investigation, the following correction procedure is proposed. The response of the three-sensor probe should be determined for a variation of yaw and pitch angle which corresponds to a maximum flow angle deviation anticipated during the experimental investigation. For these values of yaw and pitch angle, figures similar to Fig. 2 can be derived for the total velocity U_T normalized by the jet velocity U_{ref} and the three components of velocity U_i (i = 1, 2, 3) normalized by the appropriate component of the calibration jet velocity $(U_{\text{ref}})_i$ (i = 1, 2, and 3). These figures will determine the probe sensitivity to yaw and pitch angles during the experimental investigation. At this stage, one can generate the empirical relationship (equation (3)) with k_1, k_2, k_3 as known functions of λ to correct the raw data for the error due to yaw and pitch angle. The probe can then be used to derive the corrected values of U_T and U_i (i = 1, 2, 3) of the flow field under investigation. The three components of velocity U_i determine the yaw and pitch angles of the probe. The process has to be iterated to convergence, as the pitch and yaw angles are not known a priori.

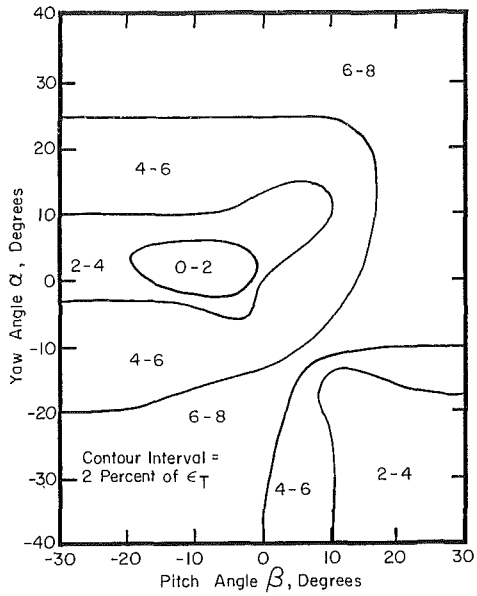

Fig. 5 Error of corrected triple hot-wire probe response with yaw and pitch angle variation

Reference

1 Lakshminarayana, B., "Three Sensor Hot Wire/Film Technique for Three Dimensional Mean and Turbulence Flow Field Measurement," *TSI Quarterly*, Vol. 8, No. 1, 1982, pp. 3–13.

The Dynamics of Small Annular Jets

José Meseguer
Associate Professor,
Laboratorio de Aerodinámica,
E.T.S.I. Aeronáuticos,
28040 Madrid, Spain

The experiments on small annular water jets performed by Hoffman et al. (1980) are analyzed by using a mathematical model similar to that developed by these authors. Such mathematical model has been modified to account for the difference in pressure between the region inside the annular jet and the atmosphere, the results obtained being in complete agreement with the experimental ones.

1 Introduction

In the last years several papers dealing with the dynamics of annular liquid jets have been published. Such fluid configurations are interesting because of the possibility of their use in some pulsed fusion reaction systems (Maniscalo and Meier, 1977) in which a first barrier for the products of the pulsed fusion reaction could be a self healing or renewable wall formed by an annular fall of lithium about 10 m in diameter and 0.5 m to 0.7 m thick, with an inlet flow velocity of about 5 $m.s^{-1}$. Although a theoretical analysis of such configurations is not too complicated (the only significant forces acting on an annular lithium fall are inertial and gravitational forces) the experimental verification of theoretical results would require an experimental apparatus with a size comparable to that of the pulsed reactor itself.

A different approach to the annular lithium fall problem is that presented by Hoffman et al. (1980) which consists in developing a mathematical model for annular inviscid liquid jets in which capillary terms are retained, in such a way that the validity of the model ranges from small annular capillary jets to large annular lithium falls. The following step followed in Hoffman et al. (1980) is to check the validity of the model by performing experiments with small size annular water jets, assuming that the correlation between theoretical and experimental data in this small annular jets case gives an estimation of the accuracy of the model in the whole range. However, such an assumption is not so clearly stated in further papers based on the work of Hoffman et al. (1980); for instance, from the paper of Esser and Abdel-Khalik (1984) one could get the idea that surface tension plays a significant role in full-scale annular lithium falls.

The aim of the experiments performed by Hoffman et al. (1980) is to determine the so-called convergence length (see Fig. 1), defined as the length to closure of the hollow region. Although these experiments are quite far from annular lithium falls (in Table 1 the different dimensionless parameters for the two configurations are compared) they have their own interest as a fluid mechanics problem in which two interfaces are involved (a similar configuration appears in the so-called compound jet printing technique, Hertz and Hermanrud (1983), Sanz and Meseguer (1985)).

The vertical annular jet was produced by using water as the working fluid, flowing through two concentric plexiglass

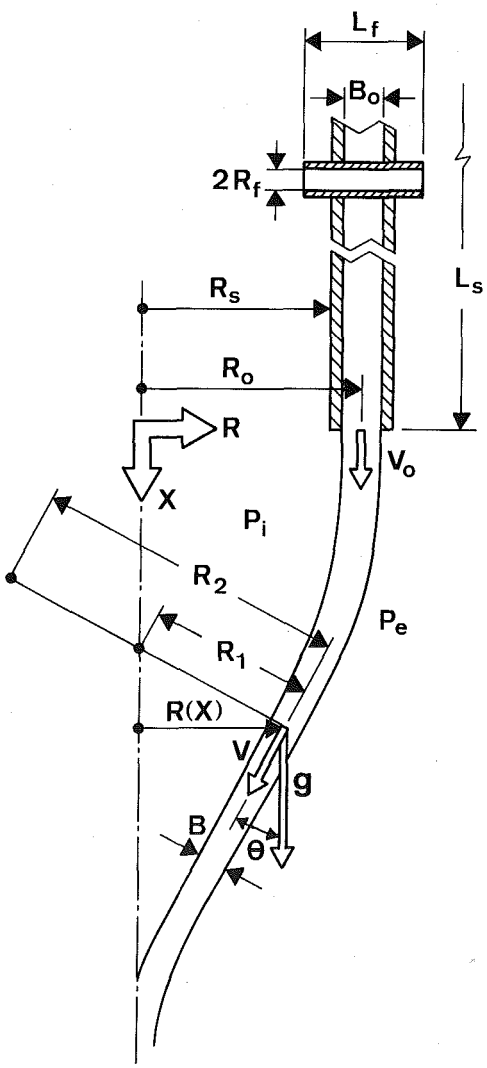

Fig. 1 Geometry and coordinate system for the annular capillary jet

Contributed by the Fluids Engineering Division for publication in the JOURNAL OF FLUIDS ENGINEERING. Manuscript received by the Fluids Engineering Division November 17, 1985.

Table 1 Lithium falls versus annular jets. Dimensionless parameters.

	Full-scale lithium falls	Small water annular jets ++
ρ_w[kg.m^{-3}]	515+	1000
σ[N.m^{-1}]	0.38+	0.07
B_0[m]	0.6	0.0064
R_0[m]	10	0.022
V_0[m.s^{-1}]	5	5
Froude number $V_0^2/(gR_0)$	0.25	116
Weber number $\rho_w B_0 V_0^2/(2\sigma)$	10^4	10^3
Bond number $\rho_w g B_0 R_0/(2\sigma)$	4×10^4	10

+ From Weast (1977).
++ Numerical values correspond to Hoffmann et al. (1980) experiments. To calculate dimensionless parameters a typical jet velocity $V_0 = 5$ m.s^{-1} has been considered.

tubes. A pressure equalizer vent tube was installed aiming at keeping the hollow region at ambient pressure. The experimental results obtained with this configuration (Run Series I) show that the convergence length increases with the jet velocity up to about 1.6 m.s^{-1}, and then the convergence length decreases with the jet velocity. Hoffman et al. (1980) hypothesized that the jet was acting as an ejector pump reducing the pressure inside the annular region in spite of the single pressure equalizer tube installed in the original apparatus. To test their hypothesis, they installed a second pressure equalizer vent tube (Run Series II), obtaining the same behavior, although the slope of the curve convergence-length versus jet velocity becomes negative at a higher value of the jet velocity. The apparatus was modified extensively, in such a way that the hollow region was entirely open to the atmosphere, and in this case (Run Series III) the closure length increases with jet velocity in the whole range of jet velocities tested.

The purpose of this paper is double. First, to clarify the differences between full-scale annular lithium falls and capillary water jets. Second, to revisite Hoffman et al. (1980) experiments. Such experiments are analyzed by using an improved version of the mathematical model used by these authors which accounts for inner to outer pressure difference effects. With this improvement theoretical results agree both qualitatively and quantitatively with experimental ones in the whole range of experimental results.

2 Theory for Convergence Length

Let us consider a vertical thin-walled annular liquid jet as sketched in Fig. 1. If the liquid thickness is small enough, $K = R_0/B_0 >> 1$, the equations governing the motion of a fluid particle will be, according to Hoffmann et al. (1980)

Continuity equation

$$BRV\cos\theta = B_0 R_0 V_0 \cos\theta_0, \tag{1}$$

Axial momentum equation

$$\frac{d^2X}{dT^2} = g - \frac{1}{\rho_w B}\left[2\sigma\left(\frac{1}{R_1}+\frac{1}{R_2}\right) - P\right]\sin\theta, \tag{2}$$

Radial momentum equation

$$\frac{d^2R}{dT^2} = -\frac{1}{\rho_w B}\left[2\sigma\left(\frac{1}{R_1}+\frac{1}{R_2}\right) - P\right]\cos\theta. \tag{3}$$

In the following we use the same dimensionless variables as in Hoffman et al. (1980), therefore, unless otherwise stated, all lengths are made dimensionless with R_0, time with V_0/g, velocities with $R_0 g/V_0$ and pressures with $\rho_w g^2 R_0^2/V_0^2$. Then, assuming the angle θ to be small enough and using lower case letters to denote dimensionless variables, after some calculations equations (1)–(3) become

$$brv = \frac{F}{K}, \tag{4}$$

$$\frac{d^2x}{dt^2} = F, \tag{5}$$

Nomenclature

a = parameter used in the definition of v_m
B = annular jet thickness [m]
b = B/R_0 = dimensionless annular jet thickness
$F = V_0^2/(gR_0)$ = Froude number
g = acceleration of gravity [m.s^{-2}]
L^* = convergence or closure length [m]
L_f, L_s = length of pressure equalizer tubes and inner plexiglass tube, respectively [m]
$P = P_i - P_e$ = difference between inner and outer pressures [Pa]
$p = PV_0^2/(\rho_w g^2 R_0^2)$ = dimensionless pressure difference
Q = air flow rate [m^3.s^{-1}]
R = annular jet radius, radial coordinate [m]
$\mathrm{Re}_j = Q/(\pi\nu_a R_j)$ = Reynolds number at duct j
R_f, R_s = inner radius of pressure equalizer tubes and inner plexiglass tube, respectively [m]
R_1, R_2 = principal radii of curvature [m]
r = R/R_0 dimensionless annular jet radius, dimensionless radial coordinate
T = time [s]
t = gT/V_0 = dimensionless time
V = jet velocity in the tangential direction [m.s^{-1}]
V_{0i} = jet velocity for which critical Reynolds number is reached at pressure equalizer tubes, see also § 3[m.s^{-1}]
v = $VV_o/(gR_o)$ = dimensionless jet velocity in the tangential direction
v_m = dimensionless mean jet velocity used to calculate the air flow rate
W = $\rho_w B_0 V_0^2/(2\sigma)$ = Weber number
X = vertical coordinate [m]
x = X/R_o = dimensionless vertical coordinate
θ = angle of the annular jet velocity vector from the vertical [degrees]
ν_a = kinematic viscosity of air [m^2.s^{-1}]
ρ_a, ρ_w = water and air density, respectively [kg.m^{-3}]
σ = surface tension coefficient [N.m^{-1}]

Subscripts

0 = conditions at the nozzle exit

Superscripts

* = conditions at the point where the hollow jet closes (or converges)

$$\left[1-\frac{r}{W(1+t)}\right]\frac{d^2r}{dt^2}+\frac{r}{W(1+t)^2}\frac{dr}{dt}$$

$$=\left(Kpr-\frac{F^2}{W}\right)(1+t). \tag{6}$$

Integration of equation (5) gives

$$x=Ft\left(1+\frac{1}{2}t\right). \tag{7}$$

On the other hand, once p is known, equation (6) can be numerically integrated and $r=r(t)$ obtained. Formally, the closure length is reached when the mean radius becomes equal to half the wall thickness, $r^*=b^*/2$ (an asterisk indicates magnitudes at the closure point). However, as it will be shown in the following, the best fitting to experimental data is obtained by assuming that the closure length is reached when the mean radius vanishes, $r^*=0$. In the former case equations (4) and (7) give

$$r^*=[2K(1+t^*)]^{-1/2}. \tag{8}$$

The time to convergence or closure is obtained by solving equation (8) together with $r^*=r(t^*)$ resulting from numerical integration of equation (6). Once t^* is known the convergence length directly results from equation (7)

$$L^*=Ft^*\left(1+\frac{1}{2}t^*\right). \tag{9}$$

In the second case the process is simpler, and the closure time t^* is directly obtained by integration of equation (6) until the mean radius vanishes.

To obtain the closure length, L^*, we still need to correlate the pressure jump p with the fluid mechanical magnitudes of the annular jet. The pressure jump occurs because the air in the hollow region is pumped away by the annular jet. Pumped air must enter the hollow region through the pressure equalizer tubes and the inner plexiglass tube; then the pressure difference is just the pressure losses in these ducts. To estimate the flow of pumped air we could study the growth of the boundary layer in the hollow region (a guide to this analysis can be found in the Appendix by Howarth enclosed in Taylor (1959)) and to postulate some pumping law in connection with the boundary layer growth. For our purposes it will be enough to assume that the air flow rate through the ducts, Q, is proportional to some mean jet velocity, $Q=Hv_m$, where H is a constant having the appropriate dimensions and the dimensionless mean velocity is defined as $v_m=aF+(1-a)v^*$, $0\le a\le 1$. The dimensionless pressure losses through duct "j" will be

$$p_j=C_j\mathrm{Re}_j^2 f(\mathrm{Re}_j) \tag{10}$$

where $C_j=(\rho_a\nu_a^2V_0^2L_j)/(16\rho_w g^2R_0^2R_j^3)$, and $f(\mathrm{Re}_j)$ is the friction factor. In calculations we assumed $f(\mathrm{Re})=64\mathrm{Re}^{-1}$ when $\mathrm{Re}\le\mathrm{Re}_{cr}$ (laminar flow), and $f(\mathrm{Re})=0.316\mathrm{Re}^{-1/4}$ when $\mathrm{Re}>\mathrm{Re}_{cr}$ (turbulent flow), Re_{cr} being the value of the Reynolds number for which the two expressions of the friction factor are equal, $\mathrm{Re}_{cr}\approx 1200$; no transitional regime has been considered, although some kind of transition is introduced by the method of calculation.

On the other hand, since the Reynolds number is proportional to air flow rate, it results

$$\mathrm{Re}_j=\frac{2H}{\pi\nu_a R_j}[aF+(1-a)v^*]. \tag{11}$$

Before pursuing this further it will be convenient to compare the pressure losses through the different ducts. For this purpose we consider the most unfavorable case assuming the flow regime to be laminar in the plexiglass tube as well as in the pressure equalizer tubes, then

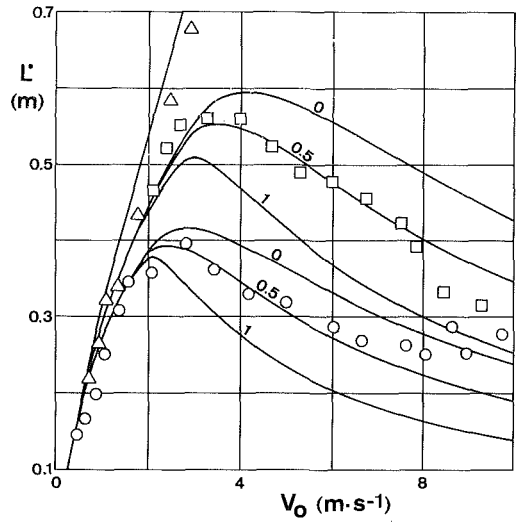

Fig. 2 Closure length L^* versus jet velocity at inlet V_0. The symbols correspond to experimental results from Hoffman et al. (1980) and indicate the different experimental conditions: one (○) or two (□) pressure equalizer tubes, or fully open (Δ). Continuous lines represent theoretical results corresponding to the case $r^*=b^*/2$, $V_{0i}=2.5$. Numbers on the curves indicate the value of parameter a.

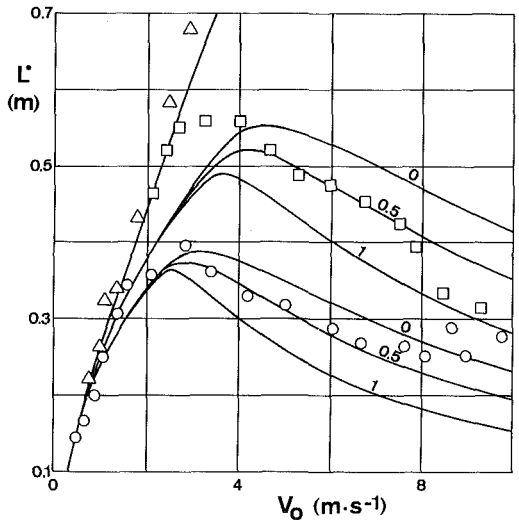

Fig. 3 Closure length L^* versus jet velocity at inlet V_0. The symbols correspond to experimental results from Hoffman et al. (1980) and indicate the different experimental conditions: one (○) or two (□) pressure equalizer tubes, or fully open (Δ). Continuous lines represent theoretical results corresponding to the case $r^*=0$, $V_{0i}=2.0$. Numbers on the curves indicate the value of parameter a.

$$\frac{p_f}{p_s}=\frac{L_fR_s^4}{L_sR_f^4}\sim 600, \tag{12}$$

where the subscripts f and s refer to pressure equalizer tubes and inner plexiglass tube, respectively; therefore, in the following only pressure losses through pressure equalizer tubes are considered.

3 Theoretical Results

The behavior of experimental results obtained by Hoffman et al. (the convergence length, L^*, increases with the jet velocity V_0 when V_0 is smaller than a certain value, and L^* decreases when V_0 is above this value) can be explained taking into account that pressure losses in pressure equalizer tubes are quite different depending on the air flow regime, laminar or turbulent, in these ducts. Based on this concept, the procedure to

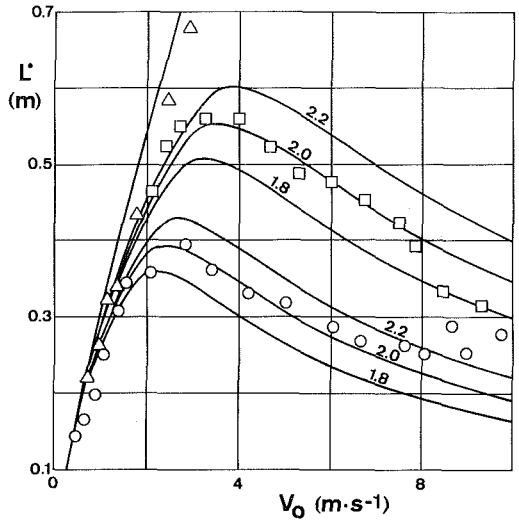

Fig. 4 Closure length L^* versus jet velocity at inlet V_0. The symbols correspond to experimental results from Hoffman et al. (1980) and indicate the different experimental conditions: one (○) or two (□) pressure equalizer tubes, or fully open (△). Continuous lines represent theoretical results corresponding to the case $r^* = 0$, $a = 0.5$. Numbers on the curves indicate the value of parameter V_{0i}.

calculate convergence lengths is as follows: since the formulation for the jet pumping effect here presented depends on two parameters, H and a, the first step is to guess suitable values for these two parameters. To estimate the value of H the procedure has been to select a value of jet velocity at inlet $V_0 = V_{0i}$ for which it is assumed that without any pressure difference ($p = 0$) the value $\mathrm{Re} = \mathrm{Re}_{cr}$ is reached at the pressure equalizer tube. Then, solving equation (6) as explained above,[1] a value of the velocity at the closure point v^* is calculated, and from equation (11), once the value of the constant a is fixed, the value of the constant H results.

Then, for each value V_0 the equation (6) is solved by iteration. In the first iteration it is assumed to be $p = 0$, then v_1^* is obtained and from equations (11) and (10) a new value $p = p_1$ results, with this new value of p a second iteration begins, and a new value $p = p_2$ is obtained, which in turn will be used in the following iteration. Calculations are stopped when the difference in dimensionless pressure between two consecutive iterations becomes smaller than a prefixed quantity, $|p_j - p_{j+1}| < 10^{-3}$. This explanation is valid only to analyze Run Series I data from Hoffman et al. (1980). In the Run Series II case we must take into account that there were two pressure equalizer tubes; therefore, for the same air flow rate it will be $\mathrm{Re}_{\mathrm{runII}} = 1/2\ \mathrm{Re}_{\mathrm{runI}}$ and, consequently, a factor equal to 1/2 must be included in equation (11). Finally, for Run Series III data, it is assumed that inner pressure is equal to ambient pressure ($p = 0$) regardless the value of V_0.

Theoretical and experimental results are compared in Figs. 2, 3, and 4. It must be pointed out that in these plots linear scales have been used instead of the logarithmic ones used by Hoffman et al. (1980) and Esser and Abdel-Khalik (1984). With this choice the difference between theoretical and experimental results can be appreciated at the same scale in the whole range of values of V_0.

Theoretical results presented in Fig. 2 have been obtained by assuming that the closure length is reached when the mean radius becomes equal to half the wall thickness ($r^* = b^*/2$) whereas the results shown in Figs. 3 and 4 correspond to the case $r^* = 0$. As it can be observed, the agreement between theoretical and experimental results is better in the case $r^* = 0$. The influence of the parameter a is analyzed in Figs. 2 and 3, in the cases $r^* = b^*/2$, $V_{0i} = 2.5$ and $r^* = 0$, $V_{0i} = 2.0$, respectively. In both cases the best fitting to experimental results from Hoffman et al. (1980) is obtained when $a \approx 0.5$ (that is, the air flow rate through pressure equalizer tubes is proportional to $(F + v^*)/2$). Finally, the influence of the parameter V_{0i} is shown in Fig. 4 ($r^* = 0$, $a = 0.5$).

4 Conclusions

The experiments on capillary annular liquid jets performed by Hoffman et al. (1980) have been explained by using the simplified mathematical model used by these authors in which a pressure difference term has been included. Theoretical results, obtained by assuming a very simple pumping law, are in complete agreement with experimental data presented by these authors, which seems to indicate that such simplified model is suitable to explain the behavior of capillary annular jet (in this sense, the agreement between Hoffman et al. (1980) theoretical results and those from Esser and Abdel-Khalik (1984)—Fig. 2 in the last paper—should be regarded as an indicator of the accuracy of the simplified model).

To conclude, it would be convenient to remember again that surface tension does not play a significant role in the behavior of large annular lithium falls. In effect, taking into account the dimensions for annular lithium falls suggested in Mansicalco and Meier (1977) one obtains values for both Weber and Bond number of the order of 10^4 (see Table 1), which indicate that, of course, surface tension acts in annular lithium falls, but its effects are negligible when compared with inertial and gravitational effects.

References

Esser, P. D., and Abdel-Khalik, S. I., 1984, "Dynamics of Vertical Annular Liquid Jets," ASME JOURNAL OF FLUIDS ENGINEERING, Vol. 106, pp. 45-51.

Hertz, C. H., and Hermanrud, B., 1983, "A Liquid Compound Jet," *Journal of Fluid Mechanics*, Vol. 131, pp. 271-287.

Hoffman, M. A., Takahashi, R. K., and Monson, R. D., 1980, "Annular Liquid Jet Experiments," ASME JOURNAL OF FLUIDS ENGINEERING, Vol. 102, pp. 344-349.

Maniscalco, J. A., and Meier, W. R., 1977, "Liquid-Lithium "Waterfall" Inertial Confinement Fusion Reactor Concept," *Transactions of the American Nuclear Society*, Vol. 26, pp. 62-63.

Sanz, A., and Meseguer, J., 1985, "One-Dimensional Linear Analysis of the Compound Jet," *Journal of Fluid Mechanics*, Vol. 159, pp. 55-68.

Taylor, G. I., 1971, *The Scientific Papers of Sir Geoffrey Ingram Taylor. Vol. IV. Mechanics of Fluids. Miscellanaeous Papers*, G. K. Batchelor Ed., Cambridge University Press, Cambridge, pp. 344-350.

Weast, R. C., 1977, *Handbook of Chemistry and Physics*, CRC Press, Cleveland, Ohio.

[1] Initial conditions are the same as in Hoffman et al. (1980): $r_o = 1$ $(dr/dt)_0 = 0$.

Development of the Reattached Flow Behind Surface-Mounted Two-Dimensional Prisms

J. Antoniou
Research Assistant.

G. Bergeles
Associate Professor.

Laboratory of Aerodynamics,
National Technical University of Athens,
Athens, Greece

Velocity and turbulence measurements are presented for the region after reattachment behind a two dimensional surface-mounted prism of varying length. The prism is mounted on the floor of an open circuit blow down wind tunnel and flow parameters for the developing boundary layer are deduced from the measurements; longitudinal integral time and length scales are estimated through autocorrelations. Reattchment on top of the prism, due to its increased length, affects the characteristics of the developing boundary layer; in this case the shear layer originating from the up-stream edge of the prism splits twice at reattachment points on top and behind the prism and the integral length scales of the turbulent eddies are found to be smaller due to the splitting.

Introduction

Flows including separation and reattachment occur frequently in many problems of engineering importance. Although there have been some theoretical investigations [1], the development of the boundary layer flow after reattachment has mainly been studied experimentally. Previous investigations are concerned with a variety of flow configurations; these include forward or rearward facing steps [2–7], surface mounted obstacles of different shapes [8–12], or flat plates of finite thickness and blunt leading edge immersed in a uniform airflow [13–15]. There is no concluding evidence of how the characteristics of the flow after reattachment are influenced by the geometry of the domain and the details of the upstream flow; obviously the characteristics of the flow at separation and the obstacle shape are the major factors affecting the relaxation of the reattaching flow. It is also possible for surface mounted obstacles, for the behavior of the flow, to be affected by the characteristics of the boundary layer before separation. For example, Castro [10] reports that reattachment, on top of a square section surface mounted obstacle, is promoted when the flow develops on rough surface, resulting in a higher turbulence intensity at obstacle height.

Existing numerical methods have difficulties in predicting accurately recirculating flows and hence the flow recovery in the relaxation region. The discrepancies between predicted and measured velocity field values are attributed both to difficulties in the accurate representation of the geometry domain and the assumptions related to the turbulence models used [16–18]. Thus experimental work, as the present one, promotes the understanding of such complicated flows and helps the improvement of calculation methods.

An experimental study of the length of the recirculation region behind a two-dimensional surface-mounted rectangular obstacle, as a function of its length to height ratio, has already been reported by Bergeles and Athanassiadis [19]; measurements of mean velocity on top of the obstacle are also presented there. The length of the recirculation region was found to decrease linearly with increasing obstacle length and then to remain constant once reattachment on top of the obstacle occured.

The present study examines the region behind a two-dimensional surface-mounted prism of varying length after reattachment. Measurements of mean velocity and turbulence intensity are presented, along with integral properties of the developing flow. Autocorrelation measurements of the turbulence fluctuating velocities have been made. Longitudinal integral time and length scales of the turbulent eddies have been estimated through the autocorrelations.

The flow configuration and the coordinate system used in the study are shown in Fig. 1(*a*) and 1(*b*). The flow separates

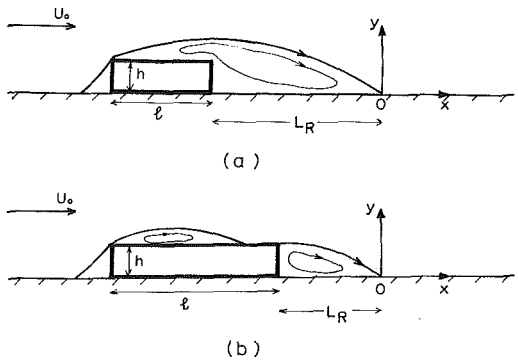

Fig. 1 Flow configuration and coordinate system: (*a*) $1/h < 4$; (*b*) $1/h > 4$; $\delta_0 = 0.7h$

Contributed by the Fluids Engineering Division for publication in the JOURNAL OF FLUIDS ENGINEERING. Manuscript received by the Fluids Engineering Division November 14, 1985.

from the upstream top corner, and depending on the value of the length to height ratio ($1/h \gtrsim 4$), reattaches on top or behind it.

Description of the Experimental Arrangement and Measuring Techniques

The experiments were performed in a low speed open circuit wind-tunnel of the blowdown type. The tunnel has a 8.5:1 contraction and a working section 400 mm wide, 230 mm high, and 1500 mm long. A slot of 20 mm height exists at the inlet of the test section through which the boundary layer, which develops on the bottom wall of the contraction, is sucked. For an empty working section the turbulence level of the free stream velocity, 230 mm from the inlet, is 0.4 percent and the variations of mean velocity over the width of the test section is less than 0.3 percent. Five prisms made of plexiglass, which spanned the width of the tunnel, were used in the present experiment. Four of them had a square cross section of 20 mm × 20 mm while the fifth one had dimensions 20 mm × 100 mm. Using combinations of these prisms the length to height ratio of the prism could be altered from 1 to 9. Care was taken for the prisms to have sharply cut edges in order to ensure that separation will always occur at the upstream leading edge. The presence of the prisms in the wind tunnel created a blockage of 8.7 percent, which could not be compensated by adjusting the roof of the test section. The forward face of the prism was located 500 mm from the entrance of the test section. All the measurements were made with a free stream velocity $U_0 = 15$ m s^{-1}, measured 230 mm from the inlet; this, along with a 20 mm long sand paper strip at the entrance of the test section which spanned the width of the tunnel, created in the empty tunnel and at 500 mm from the entrance a boundary layer $\delta_0 = 14$ mm (0.7h) thick. This was found to obey a 1./ 6.5 power law. The Reynolds number based on the height of the prism was 2×10^4. The boundary layer formed at prism position, in the absence of it, is turbulent. Thus according to Eaton and Johnston [6], although R_θ is relatively low ($R_\theta = 1420$), the results should not be Reynolds number dependent in any significant way.

Mean velocity and turbulence measurements were taken using a single wire constant-temperature anemometer. The calibration was done with the help of a pitot-tube connected to an electronic micromanometer. The output of the anemometer's bridge was fed to a signal conditioner which was used as a low-pass filter at 10KHz in order to reduce noise. Both wire and the pitot signals were then sent to the A/D converter of a Prime 450 minicomputer. Then through specially developed routines the constants of King's law were calculated. The hot-wire was calibrated in the range of 2 ms^{-1} to 20 ms^{-1}. The fitted calibration curve lay within 0.4 percent of the Pitot velocity measurements for the range of the velocities expected in the experiment (4 ms^{-1} to 16.5 ms^{-1}). The sampling rate was adjusted by a function generator. The software used allowed the on-line analysis of each data point before proceeding to the next. After a traverse was completed the wire was placed at a reference position 230 mm from the entrance, at $y = 130$ mm; if the readings differed more than 1.0 percent from the initial value of 15 ms^{-1} the traverse was rejected and was repeated again after recalibration of the wire. Thus the measurements suffered little from hot-wire contamination. Furthermore, room temperature during the measurements changed less than 1°C so that hot-wire drift was not experienced. At the end of each traverse, the integral parameters of the flow were calculated. Finally before calculating the autocorrelations of the longitudinal fluctuating velocity the hot-wire along with a linearizer and a real time FFT spectrum analyzer were used for a preliminary investigation of the frequencies present in the flow. The analysis range of the spectrum analyzer used (up to 10KHz) assured the absence of any significant energy content (distinguishable from noise level) for frequencies above 400 Hz. Thus the sampling rate was set at 1.5 KHz and the calculations were again performed on line through the minicomputer.

The length of the recirculation region L_R was measured in the same way as in [19]. First, L_R was determined visually by inspecting the direction of wool tufts attached to the floor. Second, the location where the output of a hot-wire, placed perpendicular to the mean flow .2mm from the floor, became minimum was regarded as the reattachment point. The recirculation lengths agreed with those found in [19] within ± .2h. It must be noted that the experimental arrangement in [19] ($\delta_0/h = 0.48$, $R_\theta = 1250$, $U_0 = 16$ ms^{-1}) is similar to the present one.

The prism aspect ratio is 20:1. This, along with the fact that the ratio of wind tunnel width is twice the length of L_R for $1/h = 1$ and increases to 6.6 for $1/h = 5$, provides an assurance of the two-dimensionality of the flow [24]. Spanwise measurements of L_R ±5h from the center line of the tunnel were also taken as a check of the two-dimensionality of the flow. These confirmed the uniformity of L_R over this width.

Presentation and Discussion of Results

Mean velocity and turbulence intensity measurements have been taken at five stations downstream of reattachment from $x/h = 5$ to $x/h = 25$ and for nine different length to height ratios of the prism; x is measured from the point of reattachment, Fig. 1. According to the length of the prism, as already stated, reattachment occurs behind it ($1/h < 4$, case (α)) or on top of it ($1/h > 4$, case (b)) in which case subsequently a new separation occurs at the rearward upper edge of the prism.

Figure 2 shows velocity profiles for both cases, at the first and the last stations of measurements. These profiles are representative of all the lengths of the prism examined; those not presented here were found to lie within the limits designated by them. It is noticed that in case (b) apart from the region near the wall in the most upstream station $x/h = 5$, the mean velocity profiles for the lengths studied coincide well. Thus it could be urged that, after the reattachment of the flow

Nomenclature

C_f = skin friction coefficient
G = Clauser parameter
h = prism height
H = shape factor
l = length of the prism
L_u = longitudinal integral length scale
L_R = length of the recirculation region
R_e = Reynolds number
R_{uu} = autocorrelation coefficient
T_{uu} = integral time scale of u
u = x-component of turbulent fluctuating velocity
U = x-component of velocity
U_m = free stream velocity outside boundary layer
U_0 = reference upstream velocity
U^* = wall shear velocity
x = distance from reattachment behind the prism
y = distance from bottom wall surface
ν = kinematic viscosity
δ = nominal boundary layer thickness
δ_0 = boundary layer thickness at prism position in the absence of the prism
θ = momentum thickness
τ = time lag
κ = von Karman constant

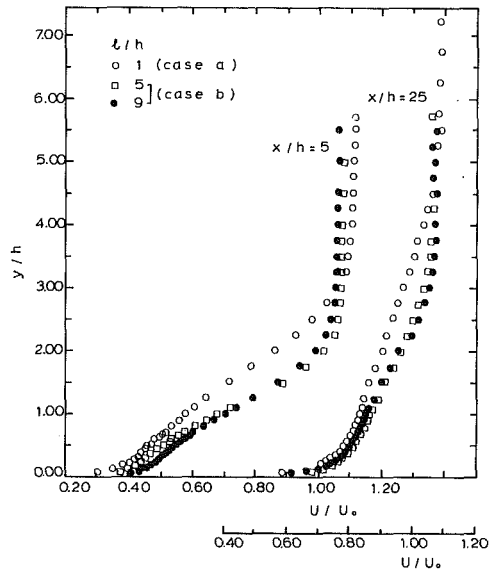

Fig. 2 Mean velocity distributions at $x/h = 5$ and $x/h = 25$. (Uncertainty in $U = 3$ percent in average; uncertainty in $y = 0.05$ mm; uncertainty in $x = 0.5$ mm.)

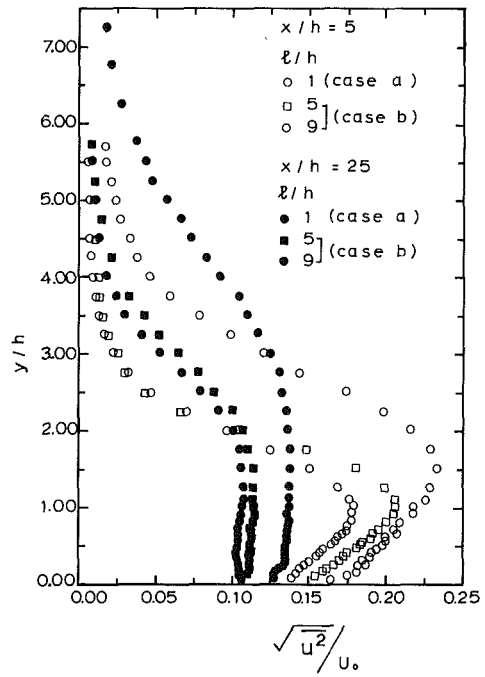

Fig. 3 Turbulent fluctuating velocities at $x/h = 5$ and $x/h = 25$. (Uncertainty in rms = 5 percent in average; uncertainty in $y = 0.05$ mm; uncertainty in $x = 0.5$m.)

on the top of the prism occurs, the rate of flow recovery is almost the same for all the lengths of the prism studied. Relaxation of the flow, to a profile typical of an ordinary boundary layer over smooth wall, seems to be faster in the near wall region than in the outer one. Due to the longer lifetime of the eddies in the outer part of the boundary layer, the relaxation of the flow there, takes a longer distance. This is obvious from the shape of the mean velocity profiles for both cases at $x/h = 25$. The existing deficit in the velocity profiles at $x/h = 5$, which is larger in case (α) relative to case (b), is still present at $x/h = 25$ and is seen at the outer part of the boundary layer.

The corresponding profiles of turbulence intensity are presented in Fig. 3. At $x/h = 5$ the turbulence intensities are seen to reach their maxima at different heights from the wall,

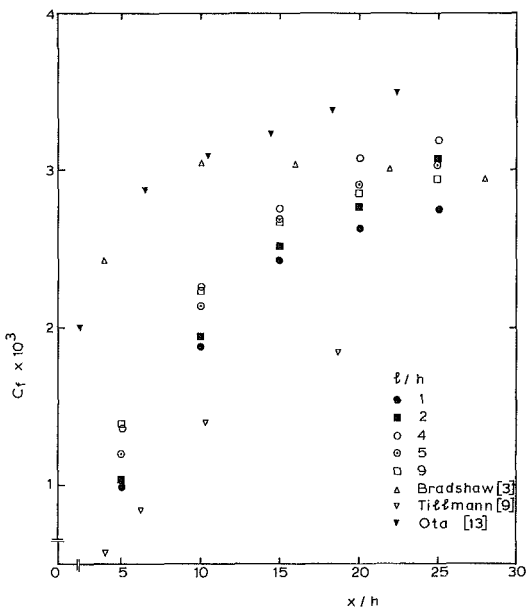

Fig. 4(*a*) Local skin friction coefficient versus x/h. (Uncertainty in C_f = 4 percent in average; uncertainty in $x = 0.5$ mm.)

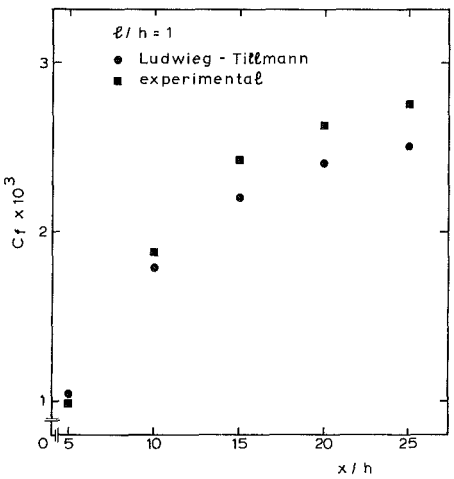

Fig. 4(*b*) Local skin friction coefficient versus x/h. For further information see the caption of Fig. 4(*a*).

depending on the case; these heights coincide with the locations where the velocity gradients $\partial U/\partial y$, estimated in the same way as in [5], assume their maxima. This height in case (a) is 1.5h while in case (b) it is 1h. At $x/h = 25$ it is seen that mixing and spreading of the shear layer has resulted in a more uniform distribution of the turbulence intensity. Turbulence values in case (b) are smaller than in case (a). Clearly in case (a) the recovery of turbulent characteristics, to those of a fully developed turbulent boundary layer over a flat plate, will require a longer distance than in case (b). As already shown in Fig. 2 (case (b)) the mean velocity profiles coincide well; for the same case, however, the effect of the longer length of the prism on the relaxation of the turbulent characteristics of the flow is evident in Fig. 3.

Figure 4(a) shows the skin-friction coefficient C_f for different lengths of the prism. The values of C_f were determined from mean velocity profiles under the assumption that the logarithmic law is valid in the region near the wall. To deduce C_f from the measurements a method similar to the one described by Coles and Hirst [20] was developed. C_f was first estimated from the Ludwieg-Tillman formula

$$C_f = 0.246 \times 10^{-0.678H} \left(\frac{U_m \theta}{\nu}\right)^{-0.268} \quad (1)$$

In the present experiment R_θ ranges from 8×10^3 to 1.4×10^4; hence equation (1) is valid. The value of U^* was accordingly deduced from the relation $C_f = 2(U^*/U_m)^2$, and the near wall velocity profile was fitted to the formula

$$\frac{U}{U^*} = \frac{1}{\kappa} \ln \frac{yU^*}{\nu} + C(\kappa = 0.41,\ C = 5.0) \quad (2)$$

This procedure was repeated in the range $0.01C_f$ to $2.0C_f$, in steps of $0.01C_f$. The value of C_f was selected as the one for which the corresponding value of U^* minimized the deviations of the points from a straight line in the range $100 < yU^*/\nu < 300$. As expected C_f increases sharply after reattachment and at $x/h = 25$ assumes values between 0.0027 and 0.0032. The trend is the same for both cases. Values of C_f especially in the near region after reattachment, are smaller than Bradshaw's [3] and Ota's [13] data. This may be attributed to the fact that in both those experiments the boundary layer at separation was considerably thinner than in the present experiment ($\delta_0 = 0.7h$). In the case of Tillman's [9] data, for the flow over a square section obstacle, the experimental values are generally lower. This may be due to the very thick boundary layer at separation that existed in Tillman's data ($\delta_0 = 3.3h$).

As a check on the log-law method C_f was also estimated from the Ludwieg-Tillman formula, equation (1). An example of this comparison is given in Fig. 4(*b*) for $1/h = 1$. Values at $x/h = 5$ almost coincide with values deduced from mean velocity profiles while at subsequent stations, equation (1) underestimates C_f. Yet agreement is considered to be acceptable.

Mean velocity profiles, plotted in semi-logarithmic coordinates, are presented in Fig. 5(*a*) and 5(*b*) for $1/h = 1$ and $1/h = 9$. These results are in accordance with those of Bradshaw and Wong [3] and Castro [10] who showed that the logarithmic region is quite limited in the early stages of development of the shear layer after reattachment. However even very close to reattachment the logarithmic law in the inner layer is well obeyed.

The variation of Clauser parameter

$$G = (2/C_f)^{1/2}(H-1)/H \quad (3)$$

is shown in Fig. 6. This parameter is known to be a meausre of the departure of a turbulent boundary layer from equilibrium. For a constant pressure turbulent boundary layer in equilibrium G is approximately 6.8. Included in the figure are the results of Tillman [9] and Bradshaw and Wong [3]. Following Bradshaw's and Wong's terminology, in accordance with the ratio h/δ_0, the present perturbation of the flow is a strong one ($h/\delta_0 = 0(1)$), while Bradshaw's and Wong's is an overwhelming one ($h/\delta_0 >> 1$) and Tillman's a weak one ($h/\delta_0 << 1$). From Fig. 3 of Bradshaw's and Wong's study [3] it is clear that, for the same distance from an obstacle divided by the obstacle height, values of G decrease as the ratio of h/δ_0 increases. Thus values of G for a strong perturbation should lie within values of a weak and an overwhelming one, in line with the present results. As Adams and Johnston [7] have shown, for the flow over a backward-facing step, values of G and hence the recovery to equilibrium are affected by the upstream boundary layer thickness. While in the present experiment δ_0/h remains the dominant factor for the behavior of G, clearly it is not the only one. The length of the prism and the appearance of reattachment on top of it are obviously two other factors that also affect the values of G, especially near reattachment. In both cases an increase of the length of the prism causes a decrease in the respective values of G, which is more rapid in case (*a*). Furthermore reattachment on top of the prism causes the values of G to increase. The return to equilibrium values seems however to be non-monotonic for both cases.

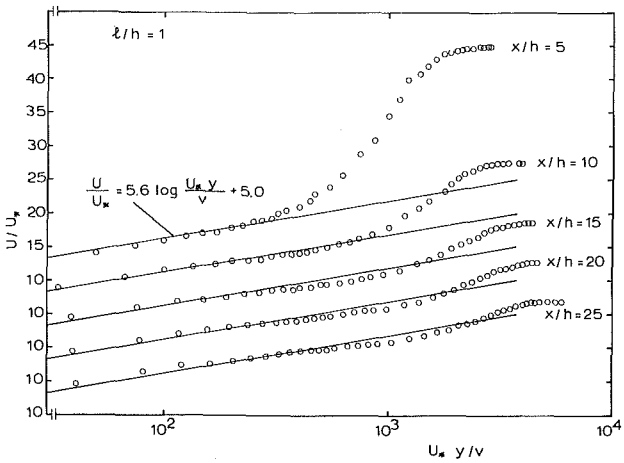

Fig. 5(*a*) Semi-logarithmic plots of mean velocity profiles. (Uncertainty in $U/U^* = 4$ percent in average.)

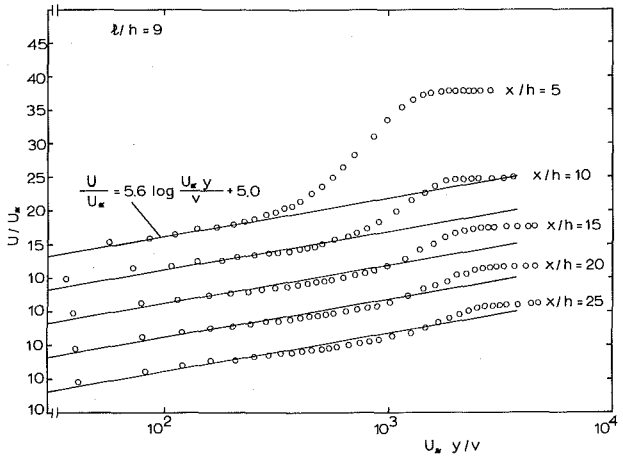

Fig. 5(*b*) Semi-logarithmic plots of mean velocity profiles; for further information see the caption of Fig. 5(*a*).

Estimation of Time and Length Scales. Assuming the validity of Taylor's hypothesis [21], the longitudinal integral time and length scales defined as

$$T_{uu} = \int_0^\infty R_{uu}(\tau)d\tau \quad (4)$$

$$L_u = U\int_0^\infty R_{uu}(\tau)d\tau \quad (5)$$

have been calculated from the measurements. R_{uu} is the autocorrelation coefficient defined as

$$R_{uu}(\tau) = \frac{\overline{u(t)u(t+\tau)}}{\overline{u^2}} \quad (6)$$

Integration was done up to the value of the time delay τ that R_{uu} reached zero. Figure 7 shows the integral time scales for $1/h = 2$ and $1/h = 3$ (case (*a*)) at three different stations. These have been nondimensionalized using the local boundary layer thickness and free stream velocity. The normalized values of T_{uu}, for both lengths at the corresponding stations, are comparable and the trend exhibited is the same. In the region near the wall values at $x/h = 5$ increase slightly until $y/\delta \cong 0.15$.

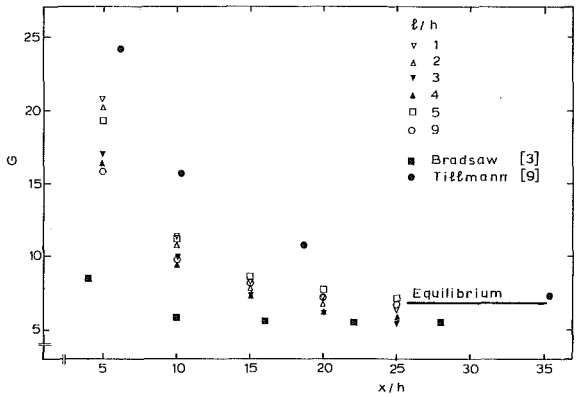

Fig. 6 Clauser parameter versus x/h. (Uncertainty in $G = 5$ percent in average; uncertainty in $x = 0.5$ mm.)

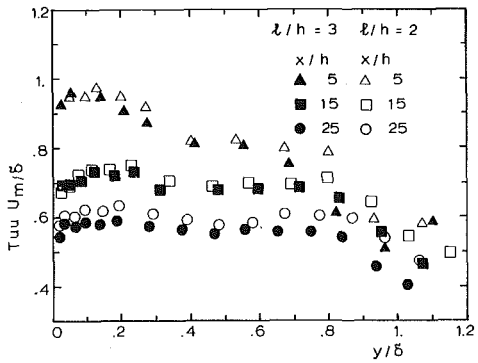

Fig. 7 Integral time scales of u versus y/δ (case (a)). (Uncertainty in $T_{uu} = 7$ percent in average; uncertainty in $y/\delta \simeq 1$ percent.)

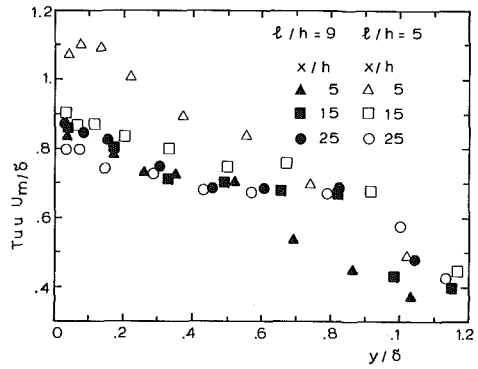

Fig. 8 Integral time scales of u versus y/δ (case (b)). For further information see the caption of Fig. 7.

Then they decrease and remain constant in the region $0.4 < y/\delta < 0.8$; finally at the edge of the boundary layer T_{uu} decreases to much lower values. At the two subsequent stations however, $x/h = 15$ and $x/h = 25$, the above changes in the values diminish and their distribution becomes more uniform throughout the boundary layer.

Figure 8 shows the integral time scales for $1/h = 5$ and $1/h = 9$ (case (b)) at the same stations as before. Discrepancies exist between values of T_{uu} at $x/h = 5$ while at subsequent stations T_{uu} values are in good agreement. It should be noticed that the trend at $x/h = 5$ is the same for both lengths of the prism ($1/h = 5$ and 9); T_{uu} shows an almost linear decrease up to $y/\delta = 1$. Nevertheless the different behavior of T_{uu} at $x/h = 5$ cannot be fully understood. At $x/h = 15$ and $x/h = 25$, T_{uu} remains constant in the region $0.3 < y/\delta < 0.8$ while at the

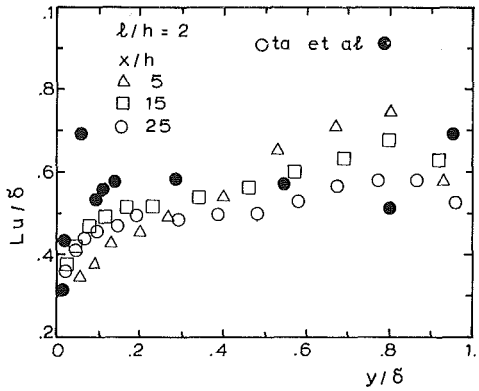

Fig. 9 Integral length scales of u versus y/δ. (Uncertainty in $L_u = 8$ percent in average; uncertainty in $y/\delta = 1$ percent.)

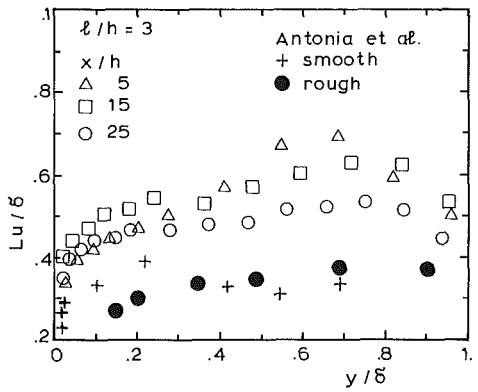

Fig. 10 Integral length scales of u versus y/δ. For further information see the caption of Fig. 9.

edge of the boundary layer decreases rapidly to much lower values. Figs. 7 and 8 suggest that the region where T_{uu} becomes more uniform expands as the distance from reattachment increases.

A comparison between the two cases examined here shows that except for $1/h = 9$ at $x/h = 5$, the normalized values of T_{uu} in case (a) are smaller than in case (b) at the corresponding stations. T_{uu} is known "to give a measure of the duration for which the turbulent fluctuations of various frequencies last, on average, before getting destroyed" [22]. Values of T_{uu} indicate a longer average lifetime for the eddies in case (b). Thus the more uniform distribution of T_{uu} in case (a) must be attributed to the smaller average lifetime of the eddies.

Figures 9 through 12 show the values of the integral length scales L_u for $1/h = 2$, 3, 5 and 9, representative of the two cases. Values have been normalized with the corresponding at each station boundary layer thickness. In Figs. 9 and 10 (case (a)) the distributions of L_u/δ at the corresponding stations are in good agreement taking into consideration the inevitable, for statistical quantities, experimental scatter. Values of L_u/δ decrease as the distance from the wall decreases. Furthermore as the distance from reattachment increases values of L_u/δ decrease for $y/\delta > 0.3$, while for $y/\delta < 0.3$ the values increase. Apparently in the region $y/\delta < 0.3$ the wall plays a dominant role on the size of the turbulent eddies. Antonia and Luxton [23] studied the distribution of the length scales across a self-preserving boundary layer over smooth and rough wall. Their results are shown in Fig. 10. It is interesting to notice that they also found that the presence of the wall, both smooth and rough wall cases, caused a reduction in the values of the length scales in the region $y/\delta < 0.3$ which was greater over the smooth wall. For $y/\delta > 0.3$ they found that L_u/δ was approximately constant and equal to 0.36. In the present case at

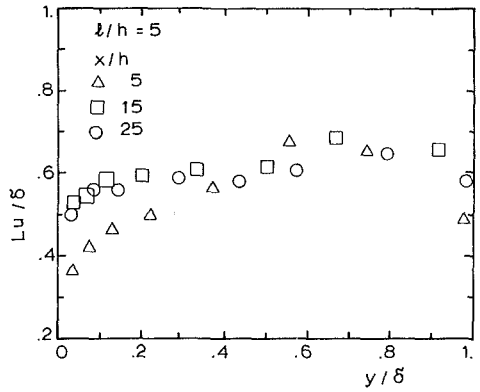

Fig. 11 Integral length scales of u versus y/δ. For further information see the caption of Fig. 9.

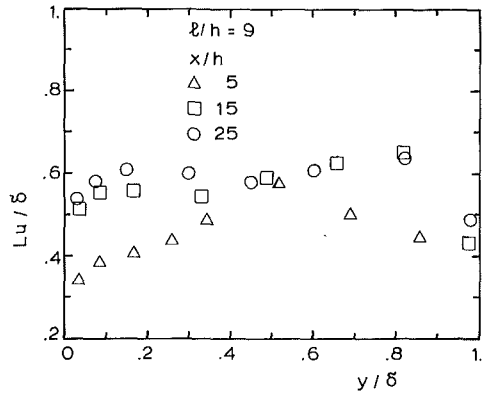

Fig. 12 Integral length scales of u versus y/δ. For further information see the caption of Fig. 9.

$x/h=25$ L_u/δ is, for both lengths of the prism, almost constant in the outer part of the boundary layer and equal to 0.53. This value is much larger than the value found by Antonia and Luxton [23] but comparable to the results of Ota and Motegi [15] (shown in Fig. 9) for the flow over a flat plate with blunt leading edge and for a distance of about $30h$ from reattachment. Apparently the originating eddies will need a large distance after reattachment in order to recover to the ordinary boundary layer scale.

Figs. 11 and 12 show the values of L_u/δ for $1/h=5$ and $1/h=9$ (case (b)). Values at $x/h=15$ and $x/h=25$ are comparable throughout the boundary layer for both lengths of the prism. However values at $x/h=5$ are comparable only in the near wall region, being smaller for $1/h=9$, while for the same prism length they are substantially lower in the outer part. In the present case only a small decrease of L_u/δ is observed for $1/h=5$ at the outer part as the distance from reattachment increases. At $x/h=25$, L_u/δ is approximately constant in the range $0.2<y/\delta<1$ and equal to 0.58. The corresponding value in case (a) is 0.53. The reduction of values observed is case (b) as well as in case (a) near the edge of the boundary layer is probably due as Antonia and Luxton [23] point out, to the influence of the intermittency in the signal on the correlation measurements.

The length scales of the originating turbulent eddies due to separation and reattachment are seen, even at the most downstream station $x/h=25$, to be much larger in magnitude than those found in a normal turbulent boundary layer over a flat plate. Hence they are expected to decrease in magnitude with increasing distance from reattachment. In the inner part of the layer ($y/\delta<0.3$) however, before this reduction in magnitude appears, an increase is observed. This initial increase in magnitude is a result of the mixing of the shear layer and is caused at the expense of the magnitude of the eddies in the outer part of the layer. Thus the decrease in magnitude of the eddies in the outer part ($y/\delta>0.3$), in the early stages of flow recovery, is both due to the aforementioned reason and the effect of increasing distance. In case (a) the expected decrease in magnitude is clearly observed at $x/h=25$, since values there are seen to be smaller than values at $x/h=15$.

This behavior of the eddies suggests that those in the region of the reattaching streamline, which after reattachment are found in the inner part of the layer, have suffered a decrease in magnitude relative to those in the outer part. The decrease must have been caused by the splitting of the eddies due to the bifurcation of the shear layer at reattachment. This supports the suggestions made by Bradshaw and Wong [3] that there is strong evidence of turbulence length scale decrease as the shear layer splits at reattachment. It also agrees with the indications found by Castro [10] that turbulence length scales are reduced as reattachment is approached. Furthermore values of L_u/δ at $x/h=5$ in the inner part of the layer are seen to be comparable for both cases. In the inner part of the layer the scale of the eddies is determined largely by their distance from the wall. Hence, they are not expected to scale on the boundary layer thickness. Since the boundary layer in case (a) is thicker than in case (b) by a factor of about thirty percent it follows that the size of the eddies in the inner part are larger in case (a). This more pronounced decrease of length scales in case (b) must be attributed to the fact that the shear layer splits twice due to the two separations and reattachments.

The above arguments concerning the splitting of the length scales at reattachment are offered as strong, rather than conclusive, evidence. In fact the distribution of L_u upstream of reattachment should be known in order to reach conclusions. Yet measurements in a recirculating region are difficult to make and due to the high intensity of turbulence suffer from large experimental uncertainties.

Conclusions

An experimental investigation of the flow field after reattachment behind a surface mounted prism of varying length has been conducted. Redevelopment of the flow takes a long distance, beyond the last downstream station presently studied. The redevelopment of the flow, demonstrated by the velocity measurements, at the same distance from reattachment is seen to be different for the two cases, case (a) and case (b). Results of C_f and G are in line with other experimental data and the nonmonotonic return of the Clauser parameter to equilibrium values is readily shown. The turbulent eddies are seen to be extremely large compared to those found in a normal smooth wall boundary layer. The integral length scales in the near wall region are reduced, a result that could be due to the splitting of the shear layer at reattachment. When reattachment on top of the prism occurs (case (b)) the integral length scales in the flow are reduced relative to those of the non-reattaching case (case (a)).

Acknowledgments

The authors want to thank Mr. J. Glekas for helpful discussions during the revision of this paper. Referees are also acknowledged for their comments which have led to improvement of the paper.

References

1 Counihan, J., Hunt, J. C. R., and Jackson, P. S., "Wakes Behind Two-Dimensional Surface Obstacles in Turbulent Boundary Layers," *Journal of Fluid Mechanics*, Vol. 64, 1974, pp. 529–563.

2 Bowen, A. J., and Lindley, D., "A Wind-Tunnel Investigation of the Wind Speed and Turbulence Characteristics Close to the Ground over Various

Escarpment Shapes," *Boundary-Layer Meteorology*, Vol. 12, 1977, pp. 259–271.

3 Bradshaw, P., and Wong, F.Y.F., "The Reattachment and Relaxation of a Turbulent Shear Layer," *Journal of Fluid Mechanics*, Vol. 52, 1972, pp. 113–135.

4 Troutt, T. R., Scheelke, B., and Norman, T. R., "Organized Structures in a Reattaching Separated Flow Field," *Journal of Fluid Mechanics*, Vol. 143, 1984, pp. 413–427.

5 Etheridge, D. W., and Kemp, P. H., "Measurements of Turbulent Flow Downstream of a Rearward-Facing Step," *Journal of Fluid Mechanics*, Vol. 86, pp. 545–566.

6 Eaton, J. K., and Johnston, J. P., "A Review of Research on Subsonic Turbulent Flow Reattachment," *AIAA Journal*, Vol. 19, No. 9, September 1981, pp. 1093–1100.

7 Adams, E. W., and Johnston, J. P., "Effects of the Upstream Boundary Layer Thickness and State on the Structure of Reattaching Flows," 5th Symposium on Turbulent Shear Flows, Cornell University, Ithaca, N.Y., Aug. 7–9, 1985.

8 Mueller, T.J., Korst, H. H., and Chow, W. L., "On the Separation, Reattachment and Redevelopment on Incompressible Turbulent Shear Flow," ASME *Journal of Basic Engineering*, Vol. 86, 1964, pp. 221–226.

9 Tillman, W., "Investigations of Some Particularities of Turbulent Boundary Layers on Plates," British Rep. and Transl. CGD-497, MAP-VG 34-T, 1946.

10 Castro, I. P., "Relaxing Wakes Behind Surface-Mounted Obstacles in Rough Wall Boundary Layers," *Journal of Fluid Mechanics*, Vol. 93, 1979, pp. 631–659.

11 Plate, E., and Lin, C. W., Colorado State University, Rept. CER-65-EJP-14, AD 614067, 1964.

12 Good, M. C., and Joubert, P. N., "The Form Drag of Two Dimensional Bluff Plates Immersed in Turbulent Boundary Layers," *Journal of Fluid Mechanics*, Vol. 31, 1968, pp. 547–582.

13 Ota, T., and Itasaka, M., "A Separated and Reattached Flow on a Blunt Flat Plate," ASME JOURNAL OF FLUIDS ENGINEERING, Vol. 98, 1976, pp. 79–86.

14 Ota, T., and Narita, M., "Turbulence Measurements in a Separated and Reattached Flow on a Blunt Flat Plate," ASME JOURNAL OF FLUIDS ENGINEERING, Vol. 100, 1978, pp. 224–228.

15 Ota, T., and Motegi, H., "Measurements of Spatial Correlations and Autocorrelations in Separated and Reattached Flow Over a Blunt Flat Plate," *J. Wind Eng. Ind. Aerodyn.*, Vol. 12, 1983, pp. 297–312.

16 Pope, S. E., and Whitelaw, J. H., "The Calculation of Near Wake Flows," *Journal of Fluid Mechanics*, Vol. 73, 1976, pp. 9–32.

17 Castro, I. P., "Numerical Difficulties in the Calculation of Complex Turbulence Flows," *Turbulent Shear Flows I*, 1979, p. 220, Springer-Verlag.

18 Gosman, A. D., Khalil, E. E., and Whitelaw, J. H., "The Calculation of Two-Dimensional Turbulent Recirculating Flows," *Turbulent Shear Flows I*, 1979, Springer-Verlag, p. 237.

19 Bergeles, G., and Athanassiadis, N., "The Flow Past A Surface-Mounted Obstacle," ASME JOURNAL OF FLUIDS ENGINEERING, Vol. 105, 1983, pp. 461–463.

20 Coles, D. E., and Hirst, E. A., *Proceedings Computation of Turbulent Boundary Layers – 1968*, AFOSR-IFP, Stanford Conference, Vol. 2.

21 Antonia, R. A., and Luxton, R. E., "The Response of a Turbulent Boundary Layer to a Step Change in Surface Roughness. Part 1. Smooth to Rough, *Journal of Fluid Mechanics*, Vol. 48, 1971, pp. 721–761.

22 Ramaprian, B. R., and Shivaprasad, B. G., "The Structure of Turbulent Boundary Layers Along Mildly Curved Surfaces," *Journal of Fluid Mechanics*, Vol. 85, 1978, pp. 273–303.

23 Antonia, R. A., and Luxton, R. E., "The Response of a Turbulent Boundary Layer to an Upstanding Step Change in Surface Roughness, *ASME Journal of Basic Engineering*, Vol. 93, 1971, pp. 22–32.

24 Ruderich, H., and Fernholz, H., "An Experimental Investigation of the Turbulent Shear Flow Downstream of a Normal Flat Plate with a Long Splitter Plate," *4th Symposium on Turbulent Shear Flows*, Karlsruhe, Sept. 1983.

Thermally Induced Flow in a Rotating Annulus Filled With a Compressible Fluid

M. A. Ortega

J. T. Sielawa

Instituto Tecnológico de Aeronáutica (ITA)
12225, São José dos Campos, SP, Brazil

The thermally induced flow field, in a rapidly rotating container consisting of a pair of coaxial cylinders bounded on the top and bottom by horizontal end plates, is considered. The top plate is heated and the bottom plate is cooled, both by small amounts, so that the thermal Rossby number is small, and the cylinders are supposed to be conductive. The induced velocity and temperature fields are determined by subdivision of the flow field; the equation for the central part, the inner core, is solved numerically as well as analytically.

1 Introduction

Sakurai and Matsuda (1974) were the first to solve the problem of the short-bowl centrifuge taking into account the compressibility of the fluid. They considered thermal convection in a bounded circular cylinder. After the work of Sakurai and Matsuda a number of papers followed, which explored certain variations of the boundary conditions. Among others, the following can be cited: Matsuda and Hashimoto (1976), Matsuda, Hashimoto and Takeda (1976), Matsuda and Hashimoto (1978), and Matsuda and Takeda (1978). Still in this area, Bark and Hultgren (1979) derived a solution without the assumption of a heavy gas made by Sakurai and Matsuda et al. Finally Brouwers (1976), properly using the aspect ratio of the machine, proposed a unification of the short and long bowl treatments.

The bicylindrical geometry is treated in a paper by Conlisk and Walker (1982), where the Boussinesq approximation is assumed. Conlisk, Foster, and Walker (1982) extend this treatment to a compressible fluid but, in spite of discussing thermal and mechanical induction, greatest attention is devoted to the mass transfer secondary flow field.

In what follows, an extension of the work of Sakurai and Matsuda (1974) for the case of two coaxial cylinders, is presented. In this respect, the study represents also the solution of the thermal problem as proposed by Conlisk, Foster, and Walker (1982). The inflow and outflow of material in a machine is undoubtedly one of the main factors. Nevertheless, our aim is to gain insight in the temperature field because, as it was pointed out by Sakurai and Matsuda (1974) and others, thermal convection is very important for centrifuges. In Section 2 the problem is stated and linearized equations are derived. The boundary layers solutions are presented in Section 3 and in Section 4 the inner core is analyzed in detail. Numerical results and a discussion are given in Section 5.

Contributed by the Fluids Engineering Division for publication in the JOURNAL OF FLUIDS ENGINEERING. Manuscript received by the Fluids Engineering Division November 26, 1985.

2 Formulation

2.1 Statement of the Problem. An inner cylinder of radius $\tilde{r}_i$ and an outer cylinder of radius $\tilde{r}_e$, bounded on the top and bottom by horizontal end plates, form a container which is filled with a gas (suffices "i" and "e" refer, respectively, to the inner and outer cylinders while tildes indicate dimensional quantities). The height of the machine is $2H$ and a system of cylindrical coordinates $(\tilde{r}, \theta, \tilde{z})$ is established. The whole apparatus is made to rotate with a high angular velocity Ω_0 around the common vertical axis $\tilde{z}$. The temperature of the top plate is $(\tilde{T}_0 + \Delta\tilde{T})$, the temperature of the bottom plate is $(\tilde{T}_0 - \Delta\tilde{T})$, where $\tilde{T}_0$ is the temperature at the middle of the container $(\tilde{z}=0)$ and $\Delta\tilde{T}$ is a positive, constant temperature difference such that $\Delta\tilde{T} << \tilde{T}_0$ ($\tilde{T}$ indicates absolute temperature). The cylinders walls are supposed to be thermally conductive with temperature distributions given by $\tilde{T}_i(z)$ and $\tilde{T}_e(z)$. Both functions $\tilde{T}_i(z)$ and $\tilde{T}_e(z)$ are considered to be antisymmetric relative to the midplane $\tilde{z}=0$ and to satisfy

$$\tilde{T}_i(\tilde{z}=H) = \tilde{T}_e(\tilde{z}=H) = \tilde{T}_0 + \Delta\tilde{T}, \qquad (2.1a)$$

$$\tilde{T}_i(\tilde{z}=-H) = \tilde{T}_e(\tilde{z}=-H) = \tilde{T}_0 - \Delta\tilde{T}, \qquad (2.1b)$$

The maximum absolute values of $[\tilde{T}_e(\tilde{z}) - \tilde{T}_0]$ and $[\tilde{T}_i(\tilde{z}) - \tilde{T}_0]$ are of the same order as $\Delta\tilde{T}$. It is considered that $\tilde{r}_i$, $\tilde{r}_e$, and $(\tilde{r}_e - \tilde{r}_i)$ are of the same order of magnitude and that $H/\tilde{r}_e$ is of order unity.

Under these conditions a secondary motion will be set up in the gas, which represents a small perturbation to a basic state of rigid body rotation with uniform temperature $\tilde{T}_0$. The aim of this paper is to work out a solution for this secondary motion.

2.2 Linearized Equations. The flow is assumed to be axisymmetric, the equation of state is taken to be the ideal gas law, and the viscosity and thermal conductivity are small and functions only of temperature. Gravitational effects are neglected when compared with the characteristic centrifugal ac-

celeration $\Omega_0^2\,\tilde{r}_e$ due to the high values of Ω_0. The thermal Rossby number is defined by $\epsilon=\Delta\tilde{T}/\tilde{T}_0$ and the following dimensionless variables are introduced

$$r=\tilde{r}/\tilde{r}_e,\quad z=\tilde{z}/\tilde{r}_e \tag{2.2a,b}$$

$$u=\frac{\tilde{q}_r}{\Omega_0\tilde{r}_e\epsilon},\quad v=\frac{\tilde{q}_\theta-\Omega_0\tilde{r}}{\Omega_0\tilde{r}_e\epsilon},\quad w=\frac{\tilde{q}_z}{\Omega_0\tilde{r}_e\epsilon}, \tag{2.2c,d,e}$$

$$p=\frac{\tilde{p}-\tilde{p}_{rb}}{\epsilon\tilde{p}_{rb}},\quad \rho=\frac{\tilde{\rho}-\tilde{\rho}_{rb}}{\epsilon\tilde{\rho}_{rb}},\quad T=\frac{\tilde{T}-\tilde{T}_0}{\epsilon\tilde{T}_0}, \tag{2.2f,g,h}$$

where $\tilde{q}_r$, $\tilde{q}_\theta$, and $\tilde{q}_z$ are the original velocity components in the cylindrical frame of reference, $\tilde{p}$ and $\tilde{\rho}$ are, respectively, pressure and density of the gas, and the suffix "rb" refers to the state of rigid body rotation. Neglecting terms of higher order in ϵ (observe that $\epsilon<<1$, as a result of the condition $\Delta\tilde{T}<<\tilde{T}_0$), one obtains linearized equations for a perturbation to the basic state:

$$\frac{\partial u}{\partial r}+(1+2Ar^2)\frac{u}{r}+\frac{\partial w}{\partial z}=0, \tag{2.3a}$$

$$-2v+rT+\frac{1}{2A}\frac{\partial p}{\partial r}=\frac{\mathrm{E}}{\beta}\left[\nabla^2 u-\frac{u}{r^2}+\frac{1}{3}\frac{\partial}{\partial r}(\vec{\nabla}\cdot\vec{\mathbf{q}}_p)\right] \tag{2.3b}$$

$$2u=\frac{\mathrm{E}}{\beta}\left[\nabla^2 v-\frac{v}{r^2}\right], \tag{2.3c}$$

$$\frac{1}{2A}\frac{\partial p}{\partial z}=\frac{\mathrm{E}}{\beta}\left[\nabla^2 w+\frac{1}{3}\frac{\partial}{\partial z}(\vec{\nabla}\cdot\vec{\mathbf{q}}_p)\right], \tag{2.3d}$$

$$-4Bru=\frac{\mathrm{E}}{\beta}\nabla^2 T, \tag{2.3e}$$

$$p=\rho+T, \tag{2.3f}$$

where

$$A=\frac{\Omega_0^2\tilde{r}_e^2}{2R\tilde{T}_0},\quad \mathrm{E}=\frac{\mu}{(\tilde{\rho}_e)_{rb}\Omega_0\tilde{r}_e^2},\quad \mathrm{Pr}=\frac{\mu c_p}{k}, \tag{2.4a,b,c}$$

$$\mathrm{B}=\frac{\gamma-1}{2\gamma}\mathrm{Pr}A,\quad \vec{\nabla}\cdot\vec{\mathbf{q}}_p=\frac{\partial u}{\partial r}+\frac{u}{r}+\frac{\partial w}{\partial z}, \tag{2.4d,e}$$

$$\beta=\exp[-A(r_e^2-r^2)],\quad \nabla^2=\frac{\partial^2}{\partial r^2}+\frac{1}{r}\frac{\partial}{\partial r}+\frac{\partial^2}{\partial z^2} \tag{2.4f,g}$$

In the relations above μ is the viscosity of the gas, c_p the specific heat at constant pressure, k the thermal conductivity, and γ is the ratio of specific heats, all assumed to be constant because the deviation from the basic state is small. A is the celerity factor, E the Ekman number, Pr the Prandtl number, and B is the Brinkman number (see Table 1 below for specific values of those parameters).

Boundary conditions can be obtained, considering the velocity and temperature of a particle of fluid in contact with a solid surface to be the same as those of the surface:

$$u=v=w=0,\quad T=j \text{ on } z=jh,\quad r_i\le r\le r_e, \tag{2.5a}$$

$$u=v=w=0,\quad T=T_k(z)=f_k(z) \text{ on } r=r_k,\quad -h\le z\le +h, \tag{2.5b}$$

where

$$h=H/\tilde{r}_e, \tag{2.6}$$

$$j=+1\rightarrow\text{upper plate},\quad j=-1\rightarrow\text{lower plate}, \tag{2.7a,b}$$

$$k\equiv e\rightarrow\text{outer cylinder},\quad K\equiv i\rightarrow\text{inner cylinder}. \tag{2.7c,d}$$

Table 1 Values of the celerity factor A, Ekman number E, and Brinkman number B for several values of the angular velocity and an outer radius $\tilde{r}_e=0.1$ m. The working fluid is UF_6 and the reference temperature and pressure are: $\tilde{T}_0=300$ K and $(\tilde{p}_e)_{rb}=8000$ N/m^2.

Ω_0(rad/s)	A	E	B
1000	0.71	1.5×10^{-6}	0.022
2000	2.82	7.5×10^{-7}	0.085
3000	6.35	5.0×10^{-7}	0.192
4000	11.29	3.7×10^{-7}	0.341

3 Boundary Layers Solutions

The smallness of E, which is basically a result of considering a fluid with small viscosity, permits obtaining an approximate uniform solution by subdividing the flow field into boundary layers at the end plates and cylinders, respectively, Ekman and Stewartson $(\mathrm{E}/\beta)^{1/3}$ layers, and a central part, or inner core. The approach to obtain simplified equations in those regions is the same as that used by former workers; for details the reader can refer, for example, to Soubbaramayer (1979) or Sakurai and Matsuda (1974).

The layers solutions are

$$u_\mathrm{E}=-jre^{-\sigma y}\sin(\sigma y)/2(1+\mathrm{B}r^2)^{1/2}, \tag{3.1a}$$

$$v_\mathrm{E}=-jre^{-\sigma y}\cos(\sigma y)/2(1+\mathrm{B}r^2), \tag{3.1b}$$

$$T_\mathrm{E}=j\mathrm{B}r^2e^{-\sigma y}\cos(\sigma y)/(1+\mathrm{B}r^2), \tag{3.1c}$$

$$T_S=\sum_{n=0}^{\infty}f_n(x)\cos\left[(2n+1)\frac{\pi}{2h}(z-h)\right], \tag{3.1d}$$

$$w_S=-\frac{th}{2\pi\mathrm{B}r_k\beta}\sum_{n=0}^{\infty}\frac{f'''(x)}{2n+1}\mathrm{sen}\left[(2n+1)\frac{\pi}{2h}(z-h)\right], \tag{3.1e}$$

where suffixes "E" and "S" denote quantities of order unity in the Ekman and Stewartson layers, respectively; $y=\mathrm{E}^{-1/2}(h-jz)$ and $x=t\mathrm{E}^{-1/3}(r_k-r)$ are stretched coordinates, $\sigma=\beta^{1/2}(1+\mathrm{B}r^2)^{1/4}$, primes denote differentiation with respect to x, $t=+1$ for the outer cylinder, $t=-1$ for the inner cylinder, and

$$f_n(x)=\frac{f_n(0)}{2}\left[e^{-\nu_n x}+\frac{2}{\sqrt{3}}e^{-\frac{\nu_n}{2}x}\cos\left(\frac{\sqrt{3}}{2}\nu_n x-\frac{\pi}{6}\right)\right], \tag{3.2a}$$

$$\nu_n=\left[\frac{\pi\beta}{h}(2n+1)\right]^{1/3}(1+\mathrm{B}r_k^2)^{1/6}, \tag{3.2b}$$

$$f_n(0)=\frac{\mathrm{B}r_k^2}{h(1+\mathrm{B}r_k^2)}\int_{-h}^{+h}f_k(z)\cos\left[(2n+1)\frac{\pi}{2h}(z-h)\right]dz. \tag{3.2c}$$

4 Solution for the Inner Core

An order of magnitude analysis in the inner core leads to an unique equation for T_N, the order-unity term for the temperature,

$$\frac{\partial^2 T_N}{\partial r^2}+\frac{1+3\mathrm{B}r^2}{1+\mathrm{B}r^2}\frac{1}{r}\frac{\partial T_N}{\partial r}+\frac{\partial^2 T_N}{\partial z^2}=0, \tag{4.1}$$

subjected to the following boundary conditions, which are obtained from the solutions of the layers,

$T_N=j/(1+\mathrm{B}r^2)$ at $z=jh$ and

$$T_N=f_k(z)/(1+\mathrm{B}r_k^2) \text{ at } r=r_k. \tag{4.2a,b}$$

Initially, the function $T_N(r,z)$ is written in the form of a sum

$$T_N(r,z)=\frac{z}{h(1+\mathrm{B}r^2)}+\sum_{n=1}^{\infty}T_n(r)\sin\left[n\pi\left(\frac{z}{h}+1\right)\right]. \tag{4.3}$$

The sine series in (4.3) can be differentiated with respect to z, term by term, because it vanishes for $z=jh$; the resultant series can also be differentiated term by term with respect to z (Churchill and Brown (1978)). Substituting (4.3) in (4.1) gives

$$\frac{d^2T_n}{dr^2}+\frac{1+3\mathrm{B}r^2}{r(1+\mathrm{B}r^2)}\frac{dT_n}{dr}$$

$$-\left(\frac{n\pi}{h}\right)^2T_n+\frac{8\mathrm{B}}{\pi n(1+\mathrm{B}r^2)^3}=0. \tag{4.4}$$

Boundary conditions for (4.4) are derived from (4.2*b*)

$$T_n(r_k)=\left(g_{kn}+\frac{2}{n\pi}\right)/(1+\mathrm{B}r_k^2),\quad n=1,2,3,\ldots, \tag{4.5}$$

where, due to the antisymmetry of $f_k(z)$ with respect to $z=0$:

$$g_{kn}=\frac{1}{h}\int_{-h}^{+h}f_k(z)\sin\left[n\pi\left(\frac{z}{h}+1\right)\right]dz. \tag{4.6}$$

4.1 Series Solution by Expansion in Terms of B, the Brinkman Number. In the case of $UF_6(\gamma=1.07)$, and in general for heavy gases, the Brinkman number B is a small parameter, what gets more accurate when the celerity factor A is of order unity (see equation (2.4*d*)). This suggests a method of solution (Sakurai and Matsuda (1974)) by expanding $T_n(r)$ in terms of B,

$$T_n(r)=T_{n0}(r)+\mathrm{B}T_{n1}(r)+\ldots \tag{4.7}$$

Retaining the first two terms of (4.7), substituting in (4.4) and applying boundary conditions (4.5), one obtains the functions $T_{n0}(r)$ and $T_{n1}(r)$ in the form

$$T_{n0}(r)=C_{1n}I_0\left(\frac{n\pi}{h}r\right)+C_{2n}K_0\left(\frac{n\pi}{h}r\right), \tag{4.8a}$$

$$T_{n1}(r)=C_{3n}I_0\left(\frac{n\pi}{h}r\right)+C_{4n}K_0\left(\frac{n\pi}{h}r\right)+[T_{n1}(r)]_P \tag{4.8b}$$

where I_0 is the modified Bessel function of first kind, order zero, K_0 is the modified Bessel function of second kind, order zero, C_{1n}, C_{2n}, C_{3n}, and C_{4n} are constants, and $[T_{n1}(r)]_P$ is a particular solution of the equation for $T_{n1}(r)$. K_0 is singular at the origin ($r=0$), but, as $r_i>0$, it has to be retained in (4.8*a*,*b*). The constants are given by

$$C_{1n}=D_{1n}/D_{n0},\quad C_{2n}=D_{2n}/D_{n0},$$

$$C_{3n}=D_{3n}/D_{n0},\quad C_{4n}=D_{4n}/D_{n0},$$

where

$$D_{1n}=\begin{vmatrix}\left(g_{en}+\frac{2}{n\pi}\right)&K_0\left(\frac{n\pi}{h}r_e\right)\\ \left(g_{in}+\frac{2}{n\pi}\right)&K_0\left(\frac{n\pi}{h}r_i\right)\end{vmatrix},$$

$$D_{2n}=\begin{vmatrix}I_0\left(\frac{n\pi}{h}r_e\right)&\left(g_{en}+\frac{2}{n\pi}\right)\\ I_0\left(\frac{n\pi}{h}r_i\right)&\left(g_{in}+\frac{2}{n\pi}\right)\end{vmatrix},$$

$$D_{3n}=\begin{vmatrix}\left\{-r_e^2\left(g_{en}+\frac{2}{n\pi}\right)-[T_{n1}(r_e)]_P\right\}&K_0\left(\frac{n\pi}{h}r_e\right)\\ \left\{-r_i^2\left(g_{in}+\frac{2}{n\pi}\right)-[T_{n1}(r_i)]_P\right\}&K_0\left(\frac{n\pi}{h}r_i\right)\end{vmatrix},$$

$$D_{4n}=\begin{vmatrix}I_0\left(\frac{n\pi}{h}r_e\right)&\left\{-r_e^2\left(g_{en}+\frac{2}{n\pi}\right)-[T_{n1}(r_e)]_P\right\}\\ I_0\left(\frac{n\pi}{h}r_i\right)&\left\{-r_i^2\left(g_{in}+\frac{2}{n\pi}\right)-[T_{n1}(r_i)]_P\right\}\end{vmatrix},$$

$$D_{n0}=\begin{vmatrix}I_0\left(\frac{n\pi}{h}r_e\right)&K_0\left(\frac{n\pi}{h}r_e\right)\\ I_0\left(\frac{n\pi}{h}r_i\right)&K_0\left(\frac{n\pi}{h}r_i\right)\end{vmatrix}.$$

An approximate form for $|T_{n1}(r)|_P$ was obtained, up to the term in r^6,

$$[T_{n1}(r)]_P=-(C_{qn}+C_n)-\left[12C_{pn}+12C_{qn}\ln\left(\frac{n\pi}{2h}r\right)\right.$$

$$\left.+(3+12\gamma_{\mathrm{E}})C_{qn}\right]-\left(\frac{n\pi}{2h}r\right)^2\left[12C_{pn}+12C_{qn}\ln\left(\frac{n\pi}{2h}r\right)\right.$$

$$\left.-(9-12\gamma_{\mathrm{E}})C_{qn}\right]-\left(\frac{n\pi}{2h}r\right)^4\left[\frac{5}{2}C_{pn}\right.$$

$$\left.+\frac{5}{2}C_{qn}\ln\left(\frac{n\pi}{2h}r\right)-\left(\frac{13}{4}-\frac{5}{2}\gamma_{\mathrm{E}}\right)C_{qn}\right]-\left(\frac{n\pi}{2h}r\right)^6$$

$$\left[\frac{1}{6}C_{pn}+\frac{1}{6}C_{qn}\ln\left(\frac{n\pi}{2h}r\right)-\left(\frac{5}{18}-\frac{\gamma_{\mathrm{E}}}{6}\right)C_{qn}\right],$$

with $C_{pn}=-2\left(\frac{h}{n\pi}\right)^2C_{1n}$, $C_{qn}=2\left(\frac{h}{n\pi}\right)^2C_{2n}$,

$C_n=-\frac{8h^2}{(n\pi)^3}$, and $\gamma_{\mathrm{E}}=0.577215\ldots$

is the Euler constant.

4.2 Series Solution by Expansion in Terms of r, the Radial Coordinate. In order to avoid the drawback of the condition $\mathrm{B}<<1$, a series solution by expansion in terms of r was developed. The solution of (4.4) is of the form:

$$T_n(r)=C_{5n}[T_n(r)]_1+C_{6n}[T_n(r)]_2+[T_n(r)]_P, \tag{4.9}$$

where $[T_n(r)]_1$ and $[T_n(r)]_2$ are two linearly independent solutions of the homogeneous equation, $[T_n(r)]_P$ is a particular solution of (4.4) and C_{5n}, C_{6n} are constants. To obtain $[T_n(r)]_1$ and $[T_n(r)]_P$ the series

$$(T_n)_{1P}=\sum_{l=o}^{\infty}\tilde{a}_lr^l \tag{4.10}$$

is substituted in (4.4). By standard procedures the coefficients $\bar{a}_l$ are determined and, as $\bar{a}_1 = \bar{a}_3 = \ldots = \bar{a}_{2l+1} = \ldots = 0$, one can write

$$(T_n)_{1P} = \sum_{m=0}^{\infty} \bar{a}_{2m} r^{2m}. \tag{4.11}$$

The coefficients $\bar{a}_{2m}$ are

$$\bar{a}_2 = -(\lambda_n \bar{a}_0 + G_n)/4, \tag{4.12a}$$

$$\bar{a}_4 = -[(16\mathrm{B} + \lambda_n)\bar{a}_2 + 3\mathrm{B}\lambda_n \bar{a}_0]/16, \tag{4.12b}$$

$$\bar{a}_6 = -[(56\mathrm{B} + \lambda_n)\bar{a}_4 + (20\mathrm{B}^2 + 3\mathrm{B}\lambda_n)\bar{a}_2 + 3\mathrm{B}^2\lambda_n \bar{a}_0]/36, \tag{4.12c}$$

$$\bar{a}_{2m} = -\Big\{\{[4(m-1) + 12(m-1)^2]\mathrm{B} + \lambda_n\}\bar{a}_{2(m-1)} + \{[8(m-2) + 12(m-2)^2]\mathrm{B}^2 + 3\mathrm{B}\lambda_n\}\bar{a}_{2(m-2)} + \{[4(m-3) + 4(m-3)^2]\mathrm{B}^3 + 3\mathrm{B}^2\lambda_n\}\bar{a}_{2(m-3)} + \mathrm{B}^3\lambda_n \bar{a}_{2(m-4)}\Big\}/(2m)^2, \quad m = 4,5,6, \ldots, \tag{4.12d}$$

where $\lambda_n = -\left(\frac{n\pi}{h}\right)^2$ and $G_n = \frac{8\mathrm{B}}{\pi n}$. (4.13a,b)

$[T_n(r)]_1$ and $[T_n(r)]_P$ are written as:

$$[T_n(r)]_1 = 1 + \sum_{m=1}^{\infty} a_{2m} r^{2m}, \quad [T_n(r)]_P = \sum_{m=1}^{\infty} c_{2m} r^{2m} \tag{4.14a,b}$$

and the coefficients a_{2m} and c_{2m} are given by

$$a_{2m} = \bar{a}_{2m}(\bar{a}_0 = 1;\ G_n = 0), \tag{4.15}$$

$$c_{2m} = \bar{a}_{2m}(\bar{a}_0 = 0;\ G_n). \tag{4.16}$$

Equation (4.15) means that a_{2m} are obtained from (4.12) by considering $\bar{a}_0 = 1$ and $G_n = 0$; c_{2m} are also obtained from (4.12) but with $\bar{a}_0 = 0$ and G_n given by (4.13*b*). Using such scheme, numerical values for the coefficients are easily calculated.

The second linearly independent solution is

$$[T_n(r)]_2 = [T_n(r)]_1 \ln(r) + \sum_{m=1}^{\infty} b_{2m} r^{2m}, \tag{4.17}$$

where the coefficients b_{2m} are

$$b_2 = -(2a_2 + \mathrm{B})/2, \tag{4.18a}$$

$$b_4 = -[8a_4 + 14\mathrm{B}a_2 + 4\mathrm{B}^2 + (16\mathrm{B} + \lambda_n)b_2]/16, \tag{4.18b}$$

$$b_6 = -[12a_6 + 26\mathrm{B}a_4 + 16\mathrm{B}a_2 + 2\mathrm{B}^3 + (56\mathrm{B} + \lambda_n)b_4 + (20\mathrm{B}^2 + 3\mathrm{B}\lambda_n)b_2]/36, \tag{4.18c}$$

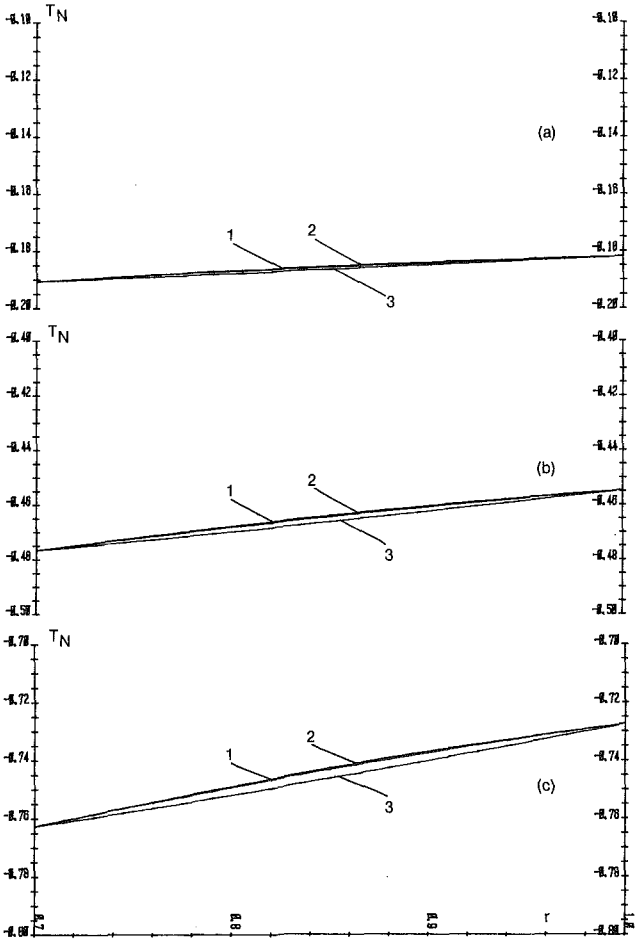

Fig. 1 Radial profile of inner core temperature for different values of the axial coordinate. Linear case; $B = 0.1$; (1) Series in B; (2) Finite differences; (3) Series in r; (*a*) $z = -0.20$ h; (*b*) $z = -0.50$ h; (*c*) $z = -0.80$ h.

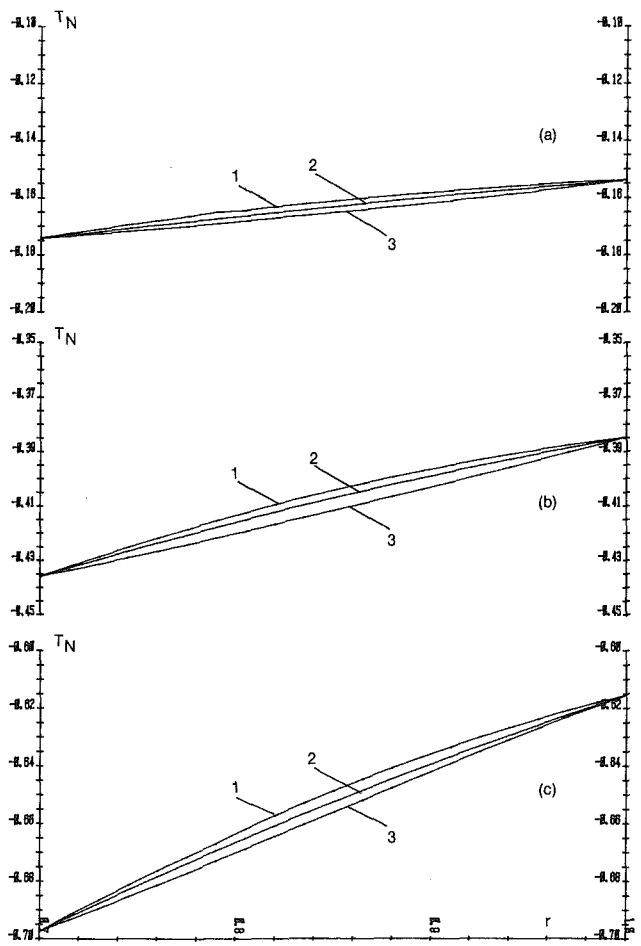

Fig. 2 Radial profile of inner core temperature for different values of the axial coordinate. Linear case; $B = 0.3$; (1) Series in B; (2) Finite differences; (3) Series in r; (*a*) $z = -0.20$ h; (*b*) $z = -0.50$ h; (*c*) $z = -0.80$ h.

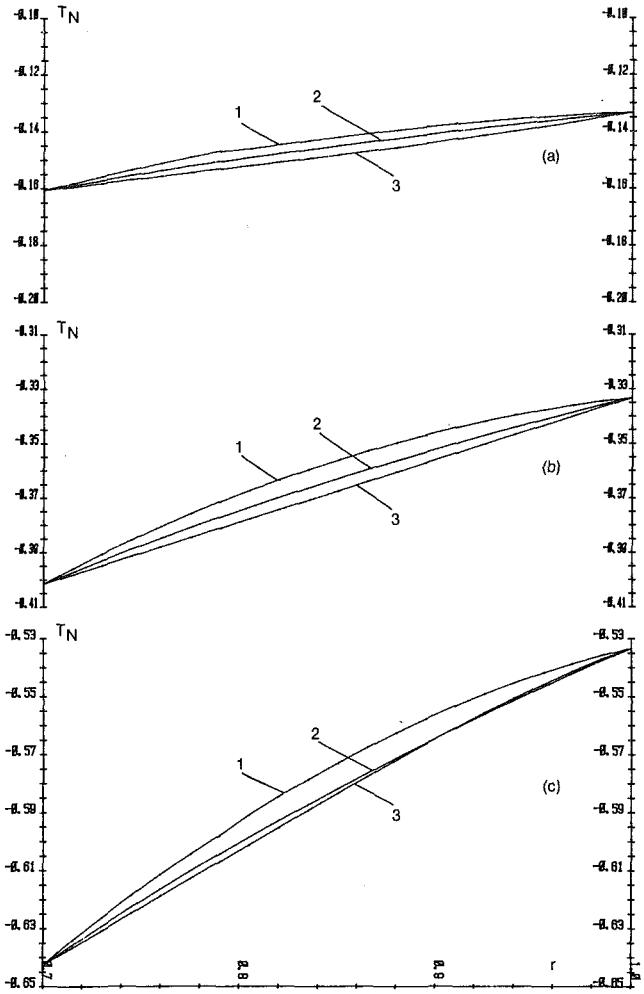

Fig. 3 Radial profile of inner core temperature for different values of the axial coordinate. Linear case; $B = 0.5$; (1) Series in B; (2) Finite differences; (3) Series in r; (a) $z = -0.20$ h; (b) $z = -0.50$ h; (c) $z = -0.80$ h.

$$D_{5n} = \begin{vmatrix} \left\{ \dfrac{g_{en} + \dfrac{2}{n\pi}}{1 + \mathrm{B}r_e^2} - [T_n(r_e)]_P \right\} & [T_n(r_e)]_2 \\ \left\{ \dfrac{g_{in} + \dfrac{2}{n\pi}}{1 + \mathrm{B}r_i^2} - [T_n(r_i)]_P \right\} & [T_n(r_i)]_2 \end{vmatrix}, \tag{4.20}$$

$$D_{6n} = \begin{vmatrix} [T_n(r_e)]_1 & \left\{ \dfrac{g_{en} + \dfrac{2}{n\pi}}{1 + \mathrm{B}r_e^2} - [T_n(r_e)]_P \right\} \\ [T_n(r_i)]_1 & \left\{ \dfrac{g_{in} + \dfrac{2}{n\pi}}{1 + \mathrm{B}r_i^2} - [T_n(r_i)]_P \right\} \end{vmatrix}, \tag{4.21}$$

$$D_n = \begin{vmatrix} [T_n(r_e)]_1 & [T_n(r_e)]_2 \\ [T_n(r_i)]_1 & [T_n(r_i)]_2 \end{vmatrix}. \tag{4.22}$$

4.3 Numerical Solution. The problem defined by equations (4.1) and (4.2*a*,*b*) was also solved numerically and served the important purpose of checking the two analytical methods (see Figs. 1, 2, and 3). A finite differences subroutine using the Gauss-Seidel iterative scheme was applied; to increase the convergence speed, the successive over-relaxation method was used with the relaxation parameter equal to 1.8. Due to the antisymmetry relative to the midplane $z = 0$, the calculation region consisted of only the upper or the lower half of the centrifuge depending upon the interest on a positive or negative z. As a check on convergence and accuracy several grid sizes were used, from a minimum of 9×9 to a maximum of 24×34 (24 points along r and 34 along z); in each coordinate direction the grid points were always equally spaced. Most cases were passed with a size of 19×19 and for a precision of 10^{-7} at each internal mesh point the number of iterations was about 80.

$$b_8 = -\frac{16a_8 + 36\mathrm{B}a_6 + 28\mathrm{B}^2a_4 + 6\mathrm{B}^3a_2 + (120\mathrm{B} + \lambda_n)b_6 + (64\mathrm{B}^2 + 3\mathrm{B}\lambda_n)b_4 + (8\mathrm{B}^3 + 3\mathrm{B}^2\lambda_n)b^2}{64}, \tag{4.18d}$$

$$b_{2m} = -\Big\{ 4ma_{2m} + [2 + 12(m-1)]\mathrm{B}a_{2(m-1)} + [4 + 12(m-2)]\mathrm{B}^2a_{2(m-2)} + [2 + 4(m-3)]\mathrm{B}^3a_{2(m-3)} + \{[4(m-1) + 12(m-1)^2]\mathrm{B} + \lambda_n\}b_{2(m-1)} + \{[8(m-2) + 12(m-2)^2]\mathrm{B}^2 + 3\mathrm{B}\lambda_n\}b_{2(m-2)} + \{[4(m-3) + 4(m-3)^2]\mathrm{B}^3 + 3\mathrm{B}^2\lambda_n\}b_{2(m-3)} + \mathrm{B}^3\lambda_n b_{2(m-4)} \Big\}/(2m)^2, \quad m = 5,6,7, \ldots . \tag{4.18e}$$

The constants C_{5n} and C_{6n} are determined from (4.5):

$$C_{5n} = D_{5n}/D_n, \quad C_{6n} = D_{6n}/D_n, \tag{4.19a,b}$$

with

5 Numerical Results and Discussion

The working fluid is UF_6 and $\tilde{r}_e = 0.1$ m; the dimensionless geometric parameters were taken as: $r_e = 1$, in view of (2.2), $r_i = 0.7$ and $h = 1$, in order to assure the short bowl model assumption. The main dimensionless parameters are shown in Table 1 for several values of the angular velocity.

Two types of temperature distribution for the cylinders were tested successfully: linear and sinusoidal. For presentation, the following linear functions were selected

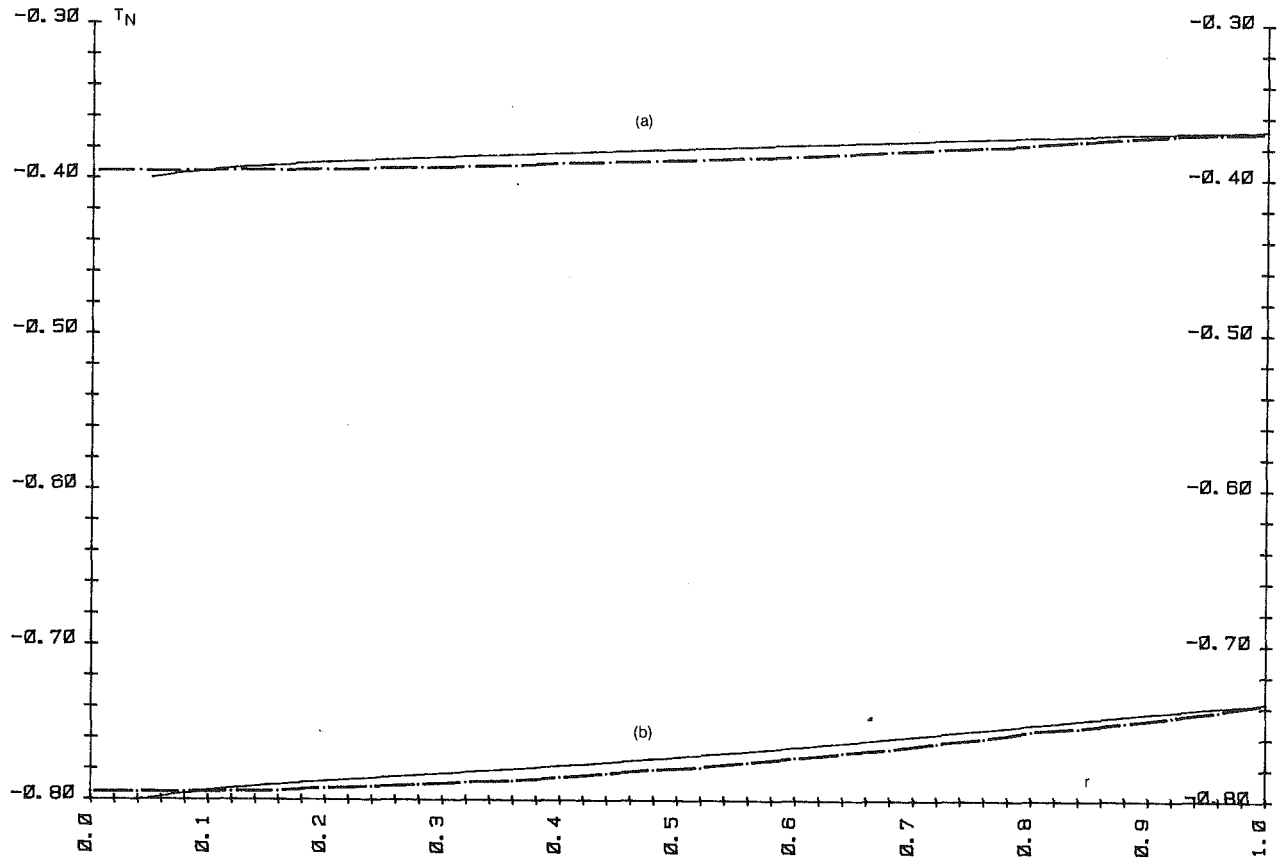

Fig. 4 Radial profile of T_N, the temperature in the inner core: comparison with the work of Sakuray and Matsuda (1974). Linear case; $B = 0.085$; $h = 1$; $r_i = 0.05$ (for the bicylindrical geometry); (*a*) $z = -0.40$ h; (*b*) $z = -0.80$ h; ____, present work; __.__, Sakurai and Matsuda (1974).

$$f_e(z) = f_i(z) = z/h, \tag{5.1}$$

which represent the case when the thermal conductivity of the cylinders material is sufficiently high when compared with that of the fluid. Inserting (5.1) into (3.2*c*) and (4.6) gives

$$f_n(0) = \frac{8}{(2n+1)^2\pi^2}\,\frac{\mathrm{B}r_k^2}{1+\mathrm{B}r_k^2}, \quad g_{en} = g_{in} = -\frac{2}{n\pi}.$$

Figures 1–3 illustrate, through the inner core temperature profiles, the three difference solutions in Section 4. One can see, clearly, that, as B grows, the error in the series in B solution grows. This shows the importance of the series in r solution, especially for greater values of Ω_0 or in cases of lighter gases (Bark and Hultgren (1979) has already worked without the assumption of heavy gases for the case of insulating boundaries).

The restrictions imposed on the above theory are due mainly to the "errors" introduced during the simplification of the equations for the different regions. The greatest of these errors, of order $\mathrm{E}^{1/3}/\beta$, is relative to the Stewartson layers equations. For high angular velocities and small values of r, the factor $\mathrm{E}^{1/3}/\beta$ may become of order unity and then, other terms would have to be retained in the inner sidewall layers equations. Then, for the sake of accuracy, A is restricted to order unity, (see equation (2.4*f*)), what, as can be seen in Table 1, falls within the practical range of modern centrifuges.

Finally, Fig. 4 shows a comparison with the work of Sakurai and Matsuda (1974). The main parameters are the same and calculations with the present theory were done considering $r_i = 0.05$. The idea was recovering the monocylindrical from the bicylindrical model in the limit $r_i \to 0$, what was practically accomplished in view that deviations are very small (of about 2 percent).

Acknowledgment

The authors wish to express their gratitude to Mr. Jadir Nogueira Gonçalves for his valuable assistance in the computer graphic plotting.

References

Bark, F. H., and Hultgren, L. S., 1979, "On The Effects of Thermally Insulating Boundaries on Geostrophic Flows in Rapidly Rotating Gases," *J. Fluid Mech.*, Vol. 95, p. 97.

Brouwers, J. J. H., 1976, "On The Motion of a Compressible Fluid in a Rotating Cylinder," PhD dissertation, Twente Univ. of Technology, Enschede, The Netherlands.

Churchill, R. V., and Brown, J. W., 1978, *Fourier Series and Boundary Value Problems*, McGraw-Hill, International Student edition.

Conlisk, A. T., Foster, M. R., and Walker, J. D. A., 1982, "Fluid Dynamics and Mass Transfer in a Gas Centrifuge," *J. Fluid Mech.*, Vol. 125, p. 283.

Conlisk, A. T., and Walker, J. D. A., 1982, "Forced Convection in a Rapidly Rotating Annulus," *J. Fluid Mech.*, Vol. 122, p. 91.

Matsuda, T. and Hashimoto, K., 1976, "Thermally, Mechanically or Externally Driven Flows in a Gas Centrifuge with Insulated Horizontal End Plates," *J. Fluid Mech.*, Vol. 78, p. 337.

Matsuda, T. and Hashimoto, K., 1978, "The Structure of the Stewartson Layers in a Gas Centrifuge. Part I. Insulated End Plates," *J. Fluid Mech.*, Vol. 85, p. 433.

Matsuda, T., Hashimoto, K., and Takeda, H., 1976, "Thermally Driven Flow in a Gas Centrifuge With an Insulated Side Wall," *J. Fluid Mech.*, Vol. 73, p. 389.

Matsuda, T., and Takeda, H., 1978, "The Structure of the Stewartson Layers in a Gas Centrifuge. Part 2. Insulated Side Wall," *J. Fluid Mech.*, Vol. 85, p. 443.

Sakurai, T., and Matsuda, T., 1974, "Gasdynamics of a Centrifugal Machine," *J. Fluid Mech.*, Vol. 62, p. 727.

Soubbaramayer, 1979, "Centrifugation," *Uranium Enrichment* (ed S. Villani) Springer, p. 183.

Effect of Free-Stream Turbulence on Characteristics of Fluctuating Forces Acting on Two Square Prisms in Tandem Arrangement

H. Sakamoto
Professor.

H. Haniu
Associate Professor.

Department of Mechanical Engineering,
Kitami Institute of Technology,
Kitami, 090, Japan

The effect of the addition of the turbulence intensity to the free stream on the characteristics of the bistable flow which takes place around two square prisms in tandem arrangement was studied experimentally at a Reynolds number of 3.32×10^4. A method of obtaining the fluid forces acting on two prisms in the bistable flow regimes where two flow patterns appear intermittently was introduced, and then the characteristics of the fluid forces, the Strouhal number, and the switching frequency of the switch phenomenon with the variation of the freestream turbulence intensity were investigated. Furthermore, the behavior of the fluid forces and the vortex shedding for other spacings between the two prisms were presented for the variation of the turbulence intensity.

1 Introduction

The interference between two closely placed cylindrical bodies with the separated flow (such as circular cylinders and square prisms) drastically changes the flow around them and produces unexpected forces and pressure distributions, and intensifies or suppresses vortex shedding. Especially, it is known that the discontinuity is caused by the abrupt change from one stable flow pattern to another (a so-called switch phenomenon) at the critical spacing (a bistable flow regime) for the cylindrical bodies in tandem arrangement [1–6]. In the case of two square prisms placed in the freestream with very low turbulence, it is reported that the switch phenomenon occurs only at $s/w = 3.0$ (s: spacing between two prisms, w: width of prisms) and the persistence of each flow pattern is very long [1]. However, in the case of the turbulent freestream which may be encountered often in engineering applications, the bistable flow regimes would be changed and the switching frequency of the switch phenomenon would be increased such as the case of the two circular cylinders in tandem arrangement placed in the turbulent freestream [7].

On the basis of these facts, the present study is intended to clarify the effects of the freestream turbulence on the characteristics of the bistable flow for two square prisms in tandem arrangement. Namely, the switching frequency of the switch phenomenon and the duration of one flow pattern with the variation of the freestream turbulence are clarified. Also, the characteristics of the fluid forces and the Strouhal number with the variation of the freestream turbulence in the bistable flow regimes are investigated. Furthermore, in addition to detailed measurements of the characteristics of the flow around the two prisms in the bistable flow regimes, the vortex shedding behavior and the aerodynamic forces at other spacings between the two prisms are presented.

2 Experimental Arrangement and Procedures

2.1 Experimental Facility and Equipment. The experiments were carried out in a closed-circuit wind tunnel which has a test section of rectangular shape with a height of 0.43 m, a width of 0.4 m, and a length of 4 m. The test bodies adopted in the present experiment were two square prisms with width w of 42 mm. The test prism was fitted with two load cells inside for measurement of fluid forces as will be illustrated in detail later. The free-stream velocity U_0 was kept constant at 12 m/s ($\mathrm{Re} = 3.32 \times 10^4$).

The spacing ratio between two prisms s/w (s: spacing between two prisms) was varied up to 6 as shown in Fig. 1. The prism for measuring the aerodynamic force is composed of two parts, namely an active cylinder and a dummy cylinder, and a load cell on which four semiconductor strain gages were attached was installed inside both cylinders. Load cell I attached in the active cylinder measured the combination of aerodynamic force and the force due to the vibration transmitted through the dummy cylinder, the load cell II attached in the dummy cylinder measured forces only due to the vibration transmitted from outside. Hence, by subtracting the output of load cell II from that of load cell I, the aerodynamic force acting on the active cylinder could be measured exclusively. Also, the natural frequency of the load cell I attached in the active cylinder was approximately 1050 Hz which was about 14 times of the maximum frequency 76 Hz of the fluctuating drag measured on the present study.

Contributed by the Fluids Engineering Division for publication in the JOURNAL OF FLUIDS ENGINEERING. Manuscript received by the Fluids Engineering Division May 26, 1987.

2.2 Turbulence-Producing Grids. The freestream turbulence was produced by a square grid composed of square prisms placed at the entrance of the test section as illustrated in Fig. 1. Grids composed of small circular wires were used for low turbulence intensity (Grid 1 in Table 1). The typical turbulence-producing grids and the turbulence properties adopted in the present study are shown in Table 1. The results of turbulence properties were measured at downstream distance $X = 684$ mm from the grids corresponding to the upstream prism location. The integral scale Lx was evaluated as the product of the freestream velocity U_0 and the integral time scale of the longitudinal velocity component. The power spectrum of the u-component of turbulence for the flow behind each of the grids agreed well with the spectrum calculated from von Karman's interpolation formula [8]. Accordingly, it was concluded that the grids produced approximately homogeneous turbulence. The intensity of turbulence was found to be uniform within the deviation of ± 3 percent over a range of -50 mm $< y, z <$ 50 mm at the test section.

2.3 Fluctuating Signal of Fluid Force and its Processing. All the detecting analog signals were digitized and processed by a microcomputer. Figure 2 shows examples of the fluctuating signals of fluid forces acting on the downstream prism in the bistable flow regimes. At any turbulence intensity studied in this experiment, two different patterns of fluctuating signals appear alternately at irregular time intervals. This is due to the presence of two flow patterns, which are indicated by the pressure distributions around the prisms and the vortex shedding measurements. This bistable phenomenon or the switch phenomenon, was confirmed by Zdravkovich [2]. The first flow pattern produces the quasi-steady flow formed between the two prisms, so that the vortex shedding behind the upstream prism is suppressed (defined as Mode 1 in the present study). The second flow pattern produces periodic vortex shedding behind both prisms because the flow which separates from the upstream prism does not reattach to the downstream prism and roll up within the gap between the two prisms (defined as Mode 2).

Accordingly, in the bistable flow regimes where the fluid forces switch, it is necessary to process separately the fluctuating signals with respect to the flow patterns of Mode 1 and Mode 2. To obtain several quantities such as time-mean and fluctuating fluid forces and the switching frequency of the switch phenomenon, signals were processed in sequence as shown in Fig. 3. The signal of the instantaneous lift as shown in Fig. 3(a) contains a portion of small amplitude of fluctuation (Mode 1) and of large amplitude of fluctuation (Mode 2). As defined in equation (1), the rms value $\hat{C}_{Lf}$ of C_L (fluctuating quantity of instantaneous lift coefficient) was calculated for a time interval corresponding to digitized N data counted from zero-crossing of ith data,

Table 1 Properties of grid-producing turbulence

Grid	Rod size (Shape) d (mm)	Mech size M (mm)	Intensity of turbulence $\sqrt{u^2}/U_0$ (%)	Scale of turbulence Lx/w
1	1·5 (○)	22	1·4	0·13
2	3·0 (□)	20	2·4	0·23
3	10 (□)	35	4·8	0·36
4	10 (□)	50	6·7	0·43
5	15 (□)	45	8·3	0·41

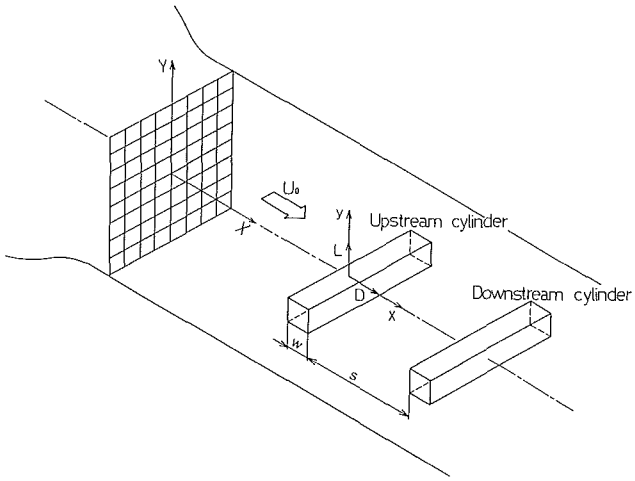

Fig. 1 Sketch of two prisms placed in wind tunnel, showing coordinate system and relevant parameters

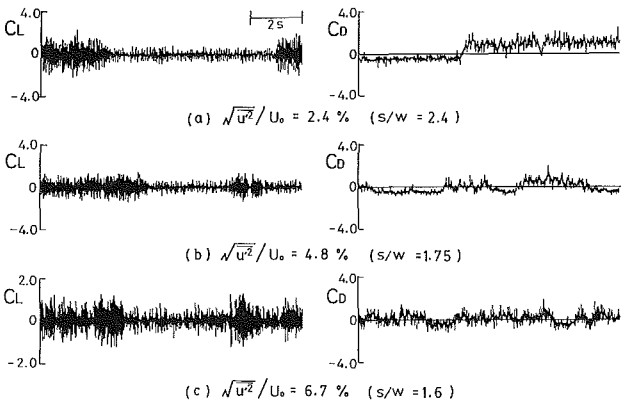

Fig. 2 Time-trace of fluctuating lift and drag for downstream prism in bistable flow regimes

$$\hat{C}_{Lf}(i,N) = \sqrt{\frac{1}{N}\sum_{j=i+1}^{i+N} C_L^2(j)} \tag{1}$$

Nomenclature

C_D = instantaneous drag coefficient
$\bar{C}_D$ = time-mean drag coefficient, see equation (5)
C_{Df} = rms drag coefficient, see equation (5)
$\hat{C}_D$ = time-mean drag coefficient over one period, see equation (4)
C_L = instantaneous lift coefficient
C_{Lf} = rms lift coefficient, see equation (5)
$\tilde{C}_{Lf}$ = local rms lift coefficient, see equation (2)
$\hat{C}_{Lf}$ = rms lift coefficient over one period, see equation (1)
$\bar{D}$ = time-mean drag
$D(t)$ = detection function, see equation (3)
D_f = fluctuating drag
E_r = rate of duration of flow pattern of Mode 2
F_r = switching frequency
L_f = fluctuating lift
S_J = range of spacing between two prisms occurring switch phenomenon
S_t = Strouhal number
U_0 = free-stream velocity
l = axial length of active prism
s = spacing between two prisms
u' = fluctuating velocity in streamwise direction
w = width of square prism
x = streamwise coordinate
y = lateral coordinate
ρ = density of fluid

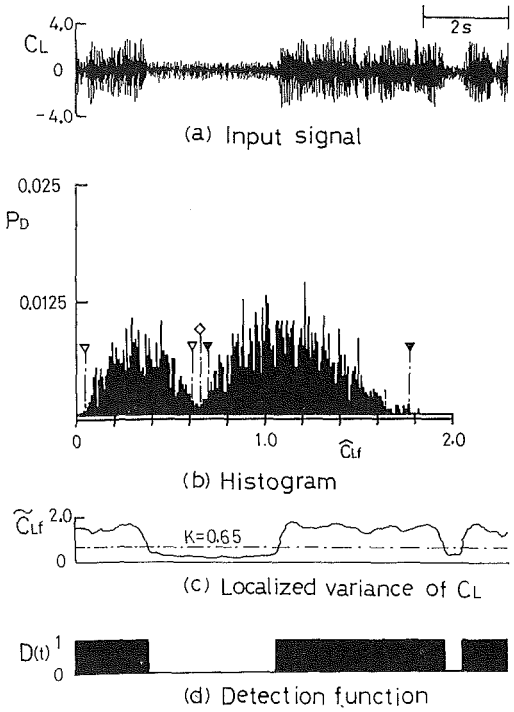

Fig. 3 Sequential diagram of detecting process for fluctuating lift in bistable flow regimes

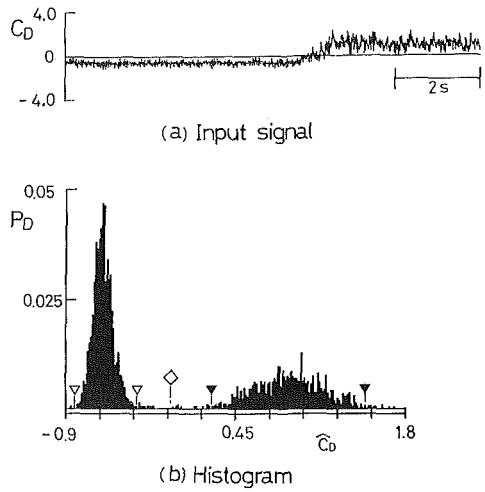

Fig. 4 Sequential diagram of detecting process for drag in bistable flow regimes

In this experiment the time interval is taken as one period of the fluctuation measured from a zero crossing to next zero crossing of the signal. To obtain zero crossing points of reasonable accuracy, low and high frequency noises were eliminated from digitally stored data by using nonrecursive digital band-pass filters while the original data were stored. Then, in order to separate these two different types of fluctuations, the rms values $\hat{C}_{Lf}$ for each period of fluctuation were classified in Fig. 3(*b*) as a probability density distribution P_D. It is clear from the figure that the probability density distribution is separated into Mode 1 (denoted by ▽) and Mode 2 (denoted by ▼), thus the value of $\hat{C}_{Lf}$ denoted by ◇ is the dividing value between Mode 1 and Mode 2. Consequently, by determining this dividing value as a threshold level K, a prerecorded input signal in the form of digital data into the memory can be portioned out into Mode 1 for $\hat{C}_{Lf} < K$ and Mode 2 for $\hat{C}_{Lf} \geqq K$ to evaluate the fluctuating lift separately. Figure 3(*c*) shows variation of local rms value $\tilde{C}_{Lf}$ defined in equation (2) as the instantaneous lift coefficient, presented in Fig. 3(*a*), centered at the *i*th data point (*i* is arbitrary),

$$\tilde{C}_{Lf}(i,M)=\sqrt{\frac{1}{M+1}\sum_{i-M/2}^{i+M/2} C_L^2(j)} \tag{2}$$

In this case number of data M for local averaging was chosen to be a number approximately corresponding to the duration 20 periods of the fluctuation (from consideration of each mode's persisting duration). From this result, a detecting function, defined in equation (3), is obtained and is shown in Fig. 3(*d*),

$$D(t)=\begin{cases}1: & \tilde{C}_{Lf}\geqq K\\ 0: & \tilde{C}_{Lf}<K\end{cases} \tag{3}$$

Hence from this detecting function, the switching frequency F_r from one mode to other mode and fraction of the duration E_r of the Mode 2 persisting in the bistable flow regimes can be calculated.

On the other hand, for obtaining time-mean and rms fluctuating drag from the signal of the instantaneous drag shown in Fig. 4(*a*), time-mean value $\tilde{C}_D$ defined in equation (4) of the instantaneous drag coefficient C_D evaluated for each period of the fluctuation is calculated,

$$\tilde{C}_D(i,N)=\frac{1}{N}\sum_{j=i+1}^{i+N} C_D(j) \tag{4}$$

Then from its probability density distribution P_D, the threshold level K dividing Mode 1 and Mode 2 (denoted by symbol ◇) is determined. Similarly to the case of fluctuating lift, a prerecorded input signal can be portioned out into Mode 1 for $\tilde{C}_D < K$ and Mode 2 for $\tilde{C}_D \geqq K$ to evaluate the time-mean and fluctuating drag separately.

2.4 Parameters Governing the Flow. Nondimensional parameters governing the flow around the two square prisms would be the Reynolds number Re ($=U_0 w/\nu$), the turbulence intensity $\sqrt{\overline{u'^2}}/U_0$ of the free-stream, turbulence length scale Lx/w and spacing ratio between the two prisms s/w. In this experiment the Reynolds number was kept constant at 3.32×10^4, and the turbulence length scale Lx/w was varied in a range of $0.13\sim0.43$. On the basis of the reports by Nakamura and Ohya [9] and Laneville and Williams [10] that the fluid force acting on a single square prism was not affected significantly by Lx in the range of $Lx/w<1$, the effects of the parameter Lx/w were not considered to be important in this experiment. Hence in this experiment, the effects of the other two parameters, $\sqrt{\overline{u'^2}}/U_0$ and s/w, on the fluid forces acting on the two prisms were investigated.

3 Results and Discussions

3.1 Switching Frequency and Rate of Duration. Figure 5 shows the switching frequency F_r of the switch phenomenon and the rate of duration Er for the flow pattern of Mode 2, when the free-stream turbulence intensity is varied. The ordinate F_r is nondimensionalized by its maximum frequency $F_{r\max}$ of each turbulence intensity. The abscissa S_X/S_J is defined as $S_X/S_J = (s-S_{\min})/(S_{\max}-S_{\min})$, where $S_{\min}$ is the spacing where the switch phenomenon starts to appear (defined as minimum spacing which is a datum point, hence $S_X=0$) and $S_{\max}$ is the spacing where the switch phenomenon vanishes (defined as maximum spacing, hence $S_X=S_J$ at the maximum spacing).

The switching frequency F_r shows maximum value in the vicinity of the mid point of the bistable flow regimes, and is very small at the starting and ending locations of the switch

(minimum spacing and maximum spacing, respectively) where each flow pattern is fairly stable. Regardless of change of the freestream turbulence intensity, $F_r/F_{r\max}$ collapses on a symmetric curve centered at $S_X/S_J = 0.5$. It is also noted that the rate of duration for both flow patterns is about 50 percent at the mid point $S_X/S_J = 0.5$.

Figure 6 shows the maximum switching frequency $F_{r\max}$ occurring in the vicinity of mid point $S_X/S_J = 0.5$ for the various freestream turbulence intensities (in order to obtain different values of the turbulence intensity, other kinds of grids beside those shown in Table 1 were used). Apart from some small scattering of distribution, $F_{r\max}$ increases stepwise as the free-stream turbulence intensity increases. These observations may be explained in the following manner. When turbulence is added to the freestream, the growth of inherent instabilities will induce the instabilities of the centrifugal force in the mean shear layers with curvature, so that the path taken by the shear layers from their point of origin at the front corners of the upstream prism to the vortex formation may alter easily. These instabilities induced in the shear layers may be attributable to movement of the position of the shear layers, and then the switch phenomenon increases with an increasing amount of turbulence. However, it is difficult to give some explanation for the stepwise jumps of the switching frequency with an increasing of the turbulence intensity since the mechanisms of the interaction between the free-stream turbulence and the shear layers in the present study are unclear.

Figure 7 shows the spacing ratio $(s/w)_{Fr\max}$ where the maximum switching frequency occurs for each turbulence intensity. It can be seen that $(s/w)_{Fr\max}$ decreases as the turbulence intensity increases. Hence it can be expected that the wake formed behind the upstream prism contracts as the freestream turbulence intensity increases. The addition of turbulence to the freestream causes the mean shear layers to thicken. This thickening may also provide that the centerline of the mean shear layer will be bent further inward toward the sides of the upstream prism. Hence, the result of adding turbulence to the free stream is contraction of the wake formed behind the upstream prism.

3.2 Time Mean and Fluctuating Fluid Forces Acting on Two Prisms. Figures 8 and 9 show the variation of time mean drag coefficient $\bar{C}_D$, rms fluctuating lift coefficient C_{Lf} and rms fluctuating drag coefficient C_{Df} of the upstream and downstream prism when both s/w and $\sqrt{\overline{u'^2}}/U_0$ are varied. Each quantity is defined as follows,

$$\{\bar{C}_D, C_{Lf}, C_{Df} = (\bar{D}, \sqrt{\overline{L_f^2}}, \sqrt{\overline{L_f^2}})/|(1/2)\rho U_0^2 wl|\}, \qquad (5)$$

Where $\bar{D}$, L_f, D_f are time mean drag, fluctuating component of lift and drag respectively, $l(l/w = 1.07)$ is the axial length of the active cylinder. As can be seen clearly from the figures, small fluid forces act on the two prisms in the regime where only the flow pattern of Mode 1 appears, small and large fluid forces act, respectively, on the two prisms in the bistable flow regime where flow patterns of Mode 1 and Mode 2 appear intermittently, and large fluid forces act on the two prisms in the regime where only the flow pattern of Mode 2 appears.

In the regime where the flow pattern of Mode 1 appears, the fluid forces acting on both prisms exhibit a much smaller value than that observed for a single prism because the separated shear layers from the upstream prism attach to the side surfaces of the downstream prism so that the regular vortex shedding associated with the high fluid forces is suppressed. Especially, it is noticed that the fluctuating lift acting on the upstream prism are nearly constant and very small regardless of change of the freestream turbulence intensity, due to the formation of the quasi-steady vortex region within the gap between the two prisms. Also, the fluctuating lift coefficient C_{Lf} of the downstream prism changes comparatively with the freestream turbulence intensity. Hence, it can be understood that the strength and location of roll up of the separated shear layer from the trailing edge of the downstream prism are affected significantly by the freestream turbulence intensity. However, the fluctuating lift of the downstream prism is small compared with that in other regimes, because any periodic rolling up of the separated shear layers from the trailing edge of the downstream prism into the region to its rear is very weak.

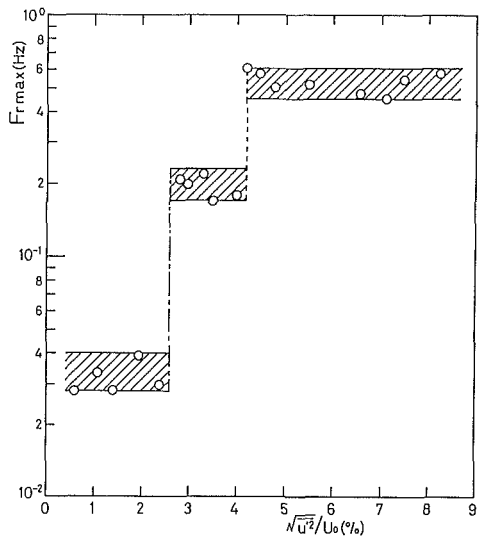

Fig. 6 Maximum switching frequency $F_{r\max}$ against various turbulence intensity. Uncertainty in $F_{r\max}$ is ±5 percent.

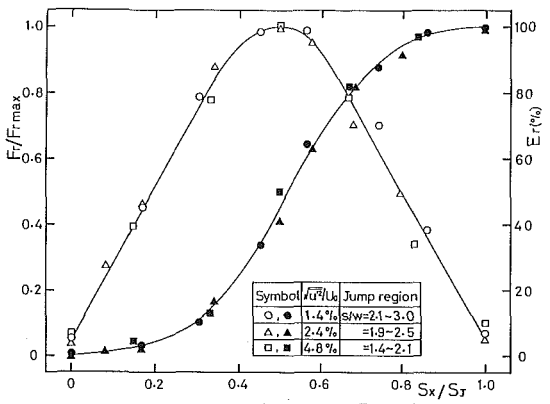

Fig. 5 Distribution of switching frequency F_r and rate of duration E_r for flow pattern of Mode 2. Uncertainty in $F_r/F_{r\max}$ is ±5 percent and in E_r is ±5 percent.

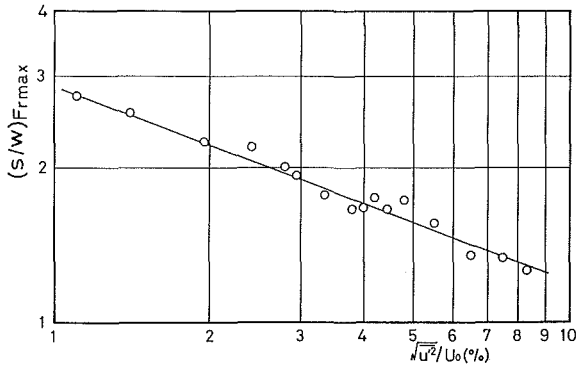

Fig. 7 Spacing ratio $(s/w)_{Fr\max}$ occurring maximum switching frequency. Uncertainty in $(s/w)_{Fr\max}$ is ±5 percent.

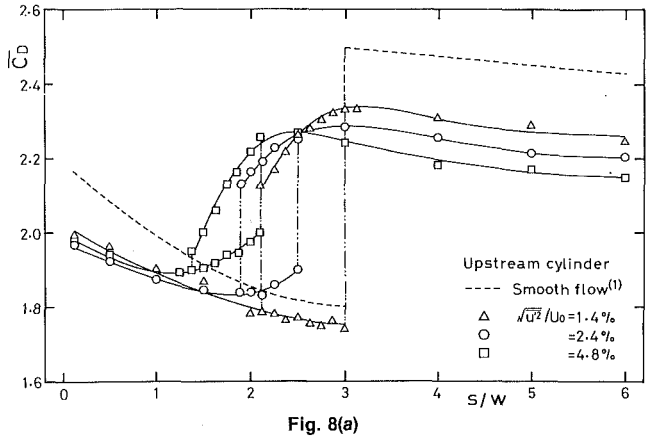

Fig. 8(a)

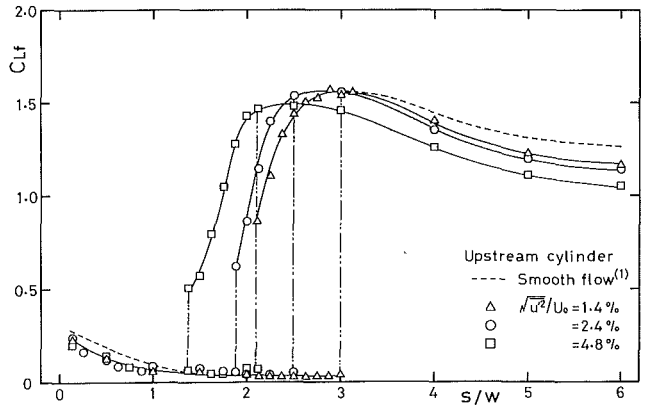

Fig. 8(b)

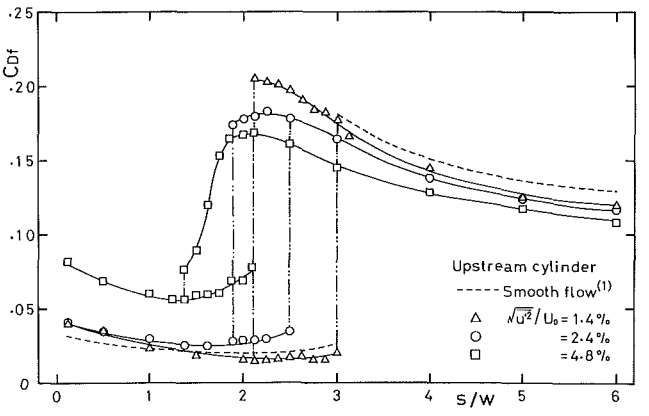

Fig. 8(c)

Fig. 8 Fluid forces acting on upstream prism. (*a*) is time-mean drag coefficient, (*b*) is rms fluctuating lift coefficient and (*c*) is rms fluctuating drag coefficient. Uncertainty in $\bar{C}_D$ is ±3 pecent, in C_{Lf} is ±3 percent and in C_{Df} is ±3 percent.

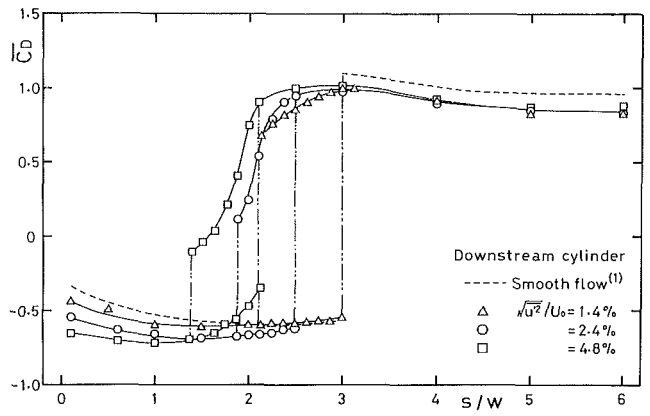

Fig. 9(a)

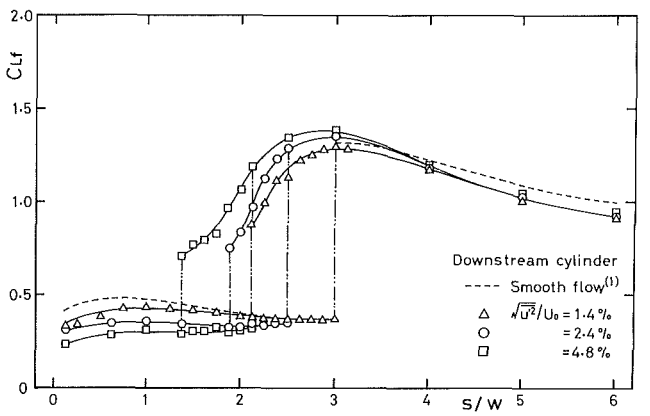

Fig. 9(b)

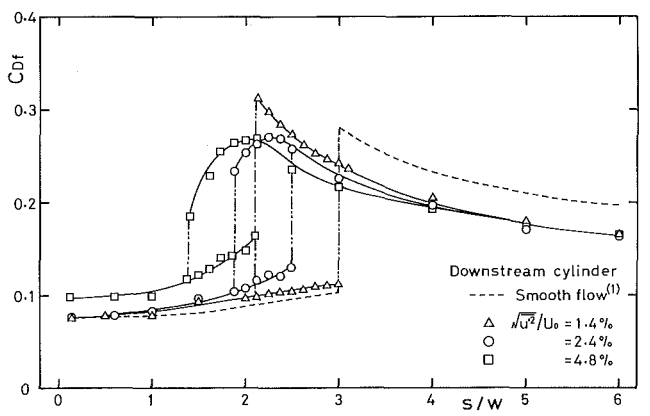

Fig. 9(c)

Fig. 9 Fluid forces acting on downstream prism. (*a*) is time-mean drag coefficient, (*b*) is rms fluctuating lift coefficient and (*c*) is rms fluctuating drag coefficient. Each uncertainty is same as in caption of Fig. 8.

In the bistable flow regime where the two flow patterns appear intermittently, the difference of the $\bar{C}_D$, C_{Lf}, C_{Df} values betweeen Mode 1 and Mode 2 becomes small as the turbulence intensity increases. This will be due to the fact that the flow patterns of both Mode 1 and Mode 2 occur simultaneously since a part of the separated shear layer from the upstream prism attaches to the side surface of the downstream prism and another part rolls up into its rear as the flow is disturbed by the increase of the turbulence intensity. Also, in the vicinity of the end of the bistable flow regimes where the switch phenomenon starts to vanish, $\bar{C}_D$ and C_{Lf} for both prisms exhibit the maximum values for each turbulence intensity. The generation of the maximum values of the fluid forces must be due to a synchronization in which the phase of the vortex shedding from the downstream prism is shifted by about 2π from the one from the upstream prism, and hence the flow around the two prisms fluctuates strongly with the same phase.

In the regime where the periodic vortices shed from both prisms, it can be seen that the $\bar{C}_D$, C_{Lf}, C_{Df} values of the upstream prism decrease with an increasing in the turbulence intensity, similar to those for a single prism in turbulent flow. The generally accepted explanation for this is that an increase in the mixing rate of the shear layers due to the turbulence can

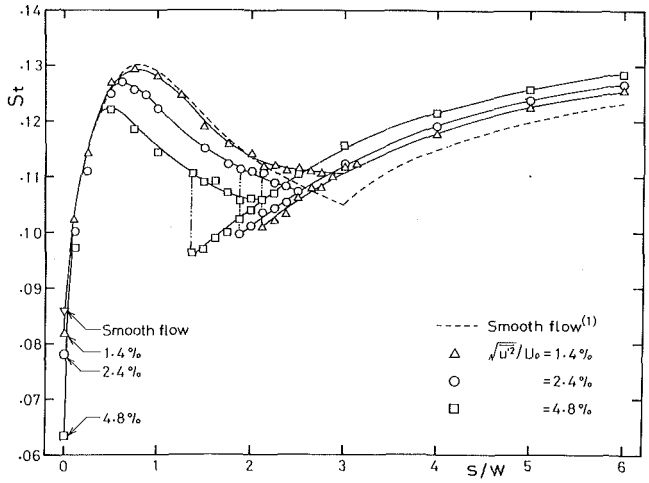

Fig. 10 Distribution of Strouhal number S_t versus spacing s/w between two prisms. Uncertainty in S_t is ± 3 percent.

make the shear layer thicker and closer to the side surfaces of the prism, resulting eventually in the reduction of the fluid forces [11]. On the other hand, each quantity for the downstream prism shows hardly any change with increase of the turbulence intensity. This is due to the fact that the downstream prism is exposed to a wake with a more highly turbulent flow induced by the upstream prism compared with the level of turbulence intensity in the freestream, so that the level of turbulence intensity adopted in the present study does not affect on the fluid forces acting on the downstream prism. Also, the fluctuating drag of the downstream prism shows much larger values than that for a single prism. This must arise from the fact that the downstream prism is situated in a strong turbulence intensity induced by the upstream prism. Therefore it can be concluded that the strong turbulence intensity induced by the upstream prism causes the generation of the large fluctuating drag, which may arise from the buffeting phenomenon occurring on the downstream prism.

3.3 Pattern of Vortex Shedding and Strouhal Number. The Strouhal numbers of the two prisms were obtained from spectral analysis of the instantaneous lift. Figure 10 shows the distributions of the Strouhal number S_t $(= w.f_c/U_0)$ of the downstream prism when the turbulence intensity $\sqrt{u'^2}/U_0$ is varied. Data for the upstream prism are not presented since the vortex shedding from the upstream prism occurs only for the flow pattern of Mode 2 and its frequency coincides with that of the downstream prism by synchronization.

As can be seen clearly from the figure, when the spacing between the two prism is very small, the Strouhal number in each turbulence intensity increases abruptly with an increasing of s/w, and reaches its maximum. It is well known that the Strouhal number of a single prism situated in a uniform flow suddenly increases at the critical values of B/H between 2.0 and 2.8 (B: width in the flow direction, H: width in the direction normal to the flow direction), and the increase of Strouhal number is due to the change of flow pattern from the detached to the reattached flow [12]. Accordingly, in the spacing where an abrupt increase in the Strouhal number curve occurs, it can be seen that the two prisms in a tandem arrangement are connected by the quasi-steady vortex regime and behave like one prism.

Beyond the regime of the spacing s/w where the Strouhal number rapidly increases, the flow pattern is that the shear layer separated from the upstream prism attaches on the side surface of the downstream prism, and then separates again from the trailing edge of the downstream prism to roll up periodically. In this flow pattern (Mode 1), the Strouhal number decreases owing to the broadening of the wake formed behind the downstream prism as s/w increases. Also, the addition of the turbulence to the free stream causes the formation of the wide wake behind the downstream prism with low frequency of the vortex shedding since the Strouhal number decreases with the increase of the turbulence intensity.

In the bistable flow regime, large value and small value of the Strouhal number which correspond to the flow pattern of Mode 1 and Mode 2, respectively, appear intermittently. It should be noted that the Strouhal number decreases with an increase of the turbulence intensity when the flow pattern of Mode 1 is occurring, while increasing when the flow pattern of Mode 2 is occurring.

Lastly, in the regime where the vortex shedding from the downstream prism synchronizes with that of the upstream prism, the vortex shedding frequencies of both prisms coincide completely. The Strouhal number increases with the increase of the turbulence intensity, thus the addition of the turbulence intensity causes the formation of the narrow wake behind the upstream prism with high frequency of the vortex shedding.

4 Conclusions

The effect of free-stream turbulence intensity on the fluid forces acting on two square prisms in tandem arrangement was investigated in detail with main attention to the regimes where the switch phenomenon occurs. The results led to the following conclusions:

(1) The bistable flow regime was found to shift toward lower values of s/w as the turbulence intensity increased. It was also found that the presence of the freestream turbulence intensity caused the formation of the wake behind the upstream prism to narrow.

(2) Flow around the two prisms becomes more instable by the instabilities induced in the shear layer as the intensity of the free-stream turbulence increases, thus the switching frequency was found to increase rapidly as the turbulence intensity increases.

(3) A method of obtaining the fluid forces in the bistable flow regimes where two flow patterns of Mode 1 and Mode 2 appear intermittently was introduced. In the bistable flow regimes, it was found that the difference of each fluid force value between Mode 1 and Mode 2 becomes small as the turbulence intensity increases. Also, the time-mean drag and the fluctuating lift for both prisms was found to exhibit their maximum values in the vicinity of the end of the bistable flow regimes where the switch phenomenon starts to vanish.

(4) The freestream turbulence intensity was found to have a significant effect on the vortex shedding frequency. In particular, it was found that the addition of the turbulence intensity to the freestream caused the Strouhal number to decrease in the regimes where the flow pattern of Mode 2 appears, while increasing it in the regimes where the flow pattern of Mode 2 appears.

Acknowledgment

The authors express their sincere thanks to Mr. Y. Obata, Department of Mechanical Engineering, Kitami Institute of Technology, for his assistance in the construction of the experimental apparatus.

References

1 Sakamoto, H., and Haniu, H., "Fluctuating Forces Acting on Two Square Prisms in Tandem Arrangement," *Journal of Wind Engineering and Industrial Aerodynamics*, Vol. 26, No. 1, 1987, pp. 85–103.

2 Zdravkovich, M. M., "Review of Flow Interference between Circular Cylinders in Various Arrangements," ASME JOURNAL OF FLUIDS ENGINEERING, Vol. 99, No. 4, 1977, pp. 618–633.

3 Okajima, A., "Flow around Two Tandem Circular Cylinders," *Bulletin of the JSME*, Vol. 22, No. 122, 1979, pp. 504–511.

4 Igarashi, T., "Flow Characteristics around Two Circular Cylinders in Tandem Arrangement," *Transaction of JSME*, Vol. 46, No. 406, 1980, pp. 1026–1036.

5 Moriya, M., Sakamoto, H., and Arie, M., "Fluctuating Pressure and Forces Acting on Two Circular Cylinders in Tandem Arrangement," *Transaction of JSME*, Vol. 49, No. 443, 1984, pp. 1364–1372.

6 Zdravkovich, M. M., and Pridden, D. L., "Interference between Two Circular Cylinder; Series of Unexpected Discontinuities," *Journal of Industrial Aerodynamics*, Vol. 2, 1977, pp. 255–270.

7 Sakata, I., and Kiya, M., "Fluctuation Acting on Two Circular Cylinders in Tandem Arrangement," *Transaction of JSME*, Vol. 49, No. 447, 1983, pp. 2618–2623.

8 Bearman, P. W., "Some Measurements of the Distortion of Turbulence Approaching a Two-Dimensional Bluff Body," *Journal of Fluid Mechanics*, Vol. 53, Part 3, 1972, pp. 451–467.

9 Nakamura, Y., and Ohya, Y., "The Effects of Turbulence on the Mean Flow Past Two-Dimensional Rectangular Cylinders," *Journal of Fluid Mechanics*, Vol. 149, 1984, pp. 255–273.

10 Laneville, A., and Williams, C. D., "The Effect of Intensity and Large-Scale Turbulence on the Mean Pressure and Drag Coefficients of 2D Rectangular Cylinders," *Proceedings of the 5th Int. Conf. on Winds Effects on Buildings and Structures*, Fort Collins, Color., 1979, pp. 397–404.

11 Lee, B. E., "The Effect of Turbulence on the Surface Pressure Field of a Square Prism," *Journal of Fluid Mechanics*, Vol. 69, Part 2, 1975, pp. 263–282.

12 Otsuki, Y., Washizu, K., Tomizawa, H., and Ohya, A., "A Note on the Aeroelastic Instability of a Prismatic Bar with Square Section," *Journal of Sound Vibration*, Vol. 34, No. 2, 1974, pp. 233–248.

Module Friction Factors and Intramodular Pressure Distributions for Periodic Fully Developed Turbulent Flow in Rectangular Interrupted-Plate Ducts

R. K. McBrien
Graduate Student.

B. R. Baliga
Associate Professor.
Mem. ASME

Department of Mechanical Engineering,
McGill University,
Montreal, Quebec, H3A 2K6, Canada

This paper presents detailed time-mean pressure measurements for periodic fully developed turbulent flows in straight interrupted-plate ducts of rectangular cross section. Several combinations of plate spacing and duct aspect ratio are investigated for Reynolds numbers, based on a module hydraulic diameter, in the range 5000 to 45000. The experiments undertaken in this work establish the existence of steady, time-mean, periodic fully developed flows for all flow rates and geometric configurations investigated. The results include graphical and tabular presentations of module friction factor versus Reynolds number data, and intramodular time-mean wall static pressure distributions. The physical implications of these results are also discussed.

Introduction

Rectangular flow passages with interrupted-surface configurations are often encountered in heat transfer equipment [1-5]. An example of such a flow passage, illustrated in Fig. 1(*a*), is the rectangular offset-fin configuration commonly employed in the cores of compact heat exchangers [6]. Another example is forced convection air cooling of an array of electronic modules deployed along circuit boards that are stacked in parallel [2-4], as illustrated in Fig. 1(*b*). The interruptions in such flow passages cause a continual restarting of the thermal boundary layers and thus lead to high heat transfer coefficients. This enhanced heat transfer performance is, however, accompanied by higher pressure drops than those encountered in uninterrupted configurations, due to the restarting of the velocity boundary layers. This paper presents detailed time-mean pressure measurements for turbulent flows in straight interrupted-plate ducts of rectangular cross section.

Experimental data on overall heat transfer and pressure drops in full-scale models of rectangular offset-fin heat exchanger cores are available in the literature [1, 6, 7]. The results of several laboratory investigations of fluid flow and heat transfer in rectangular interrupted-surface flow passages are also available [3, 5, 8-11]. However, there is little or no data available on intramodular pressure distributions, velocity distributions, and local heat transfer coefficients for flows in such geometries. The work presented in this paper is an effort to enhance the understanding of such flows and to fulfill a part of the aforementioned need for local data. It is limited to the experimental determination of module friction factors and intramodular wall static pressure distributions for periodic fully developed turbulent flow in rectangular interrupted-plate ducts. It complements and extends similar works by Cur and Sparrow [8, 9], Sparrow and Hajiloo [10], and Joshi and Webb [11].

Attention in this paper is focused on straight rectangular ducts with an interrupted-plate insert as illustrated in Fig. 2(*a*). These ducts are relatively simple geometrically, but they generate complexities in the flow similar to those produced by the interrupted-surface configuration shown in Fig. 1(*a*). In addition to enhancing the understanding of fluid flow in such flow passages, the data presented in this paper could be useful in the testing of numerical models of turbulent flows in rectangular interrupted-surface configurations.

A longitudinal cross section of an interrupted-plate rectangular duct, similar to the ones used in this work, is shown in Fig. 2(*b*). Turbulent flows in such ducts attain a spatially periodic behavior after a relatively short entrance length, which may extend at the most to eight ranks of plates [9, 12]. In the spatially fully developed regime, the flow repeats itself identically in successive geometrical modules, such as ABCDE in Fig. 2(*b*). Flow passages, such as those illustrated in Fig. 1, often have a large number of geometrically similar modules. In practice, it is sufficient to know the flow and heat transfer characteristics for a typical module in the periodic fully developed regime. Furthermore, it is possible to numerically

Contributed by the Fluids Engineering Division for publication in the JOURNAL OF FLUIDS ENGINEERING. Manuscript received by the Fluids Engineering Division January 30, 1987.

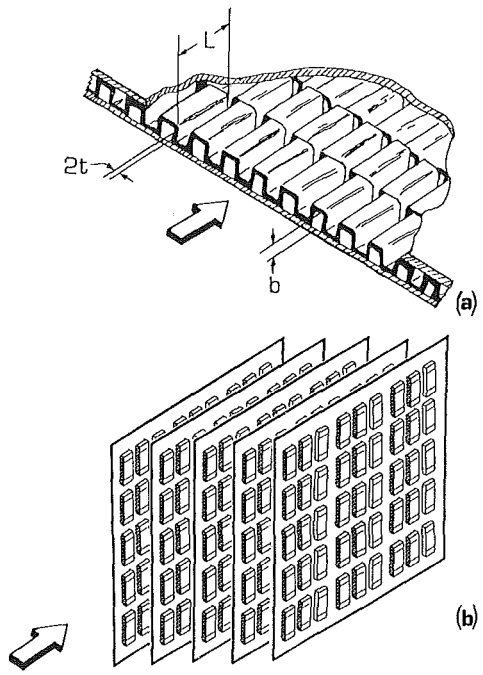

Fig. 1(*a*) Typical rectangular offset-fin arrangement in a compact heat exchanger core [6]; and (*b*) array of electronic modules deployed along circuit boards that are stacked in parallel

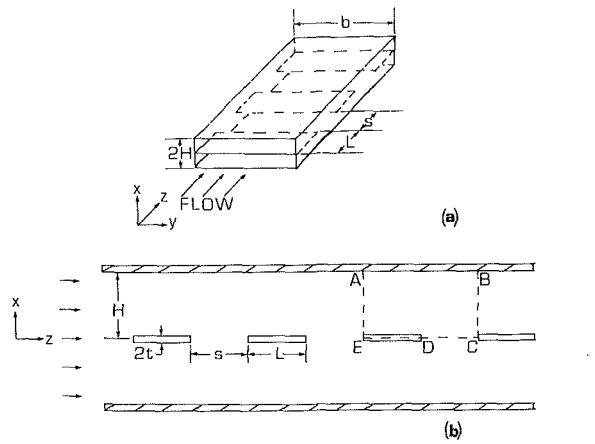

Fig. 2(*a*) Straight rectangular interrupted-plate duct; and (*b*) enlarged view of the cross section of a rectangular interrupted-plate duct, associated nomenclature, and representation of a geometrically similar module ABCDE

predict the flow in such a periodic fully developed module directly, without doing any entrance region computations [13, 14]. It is for these reasons that this experimental investigation is concentrated on the periodic fully developed regime.

Another important point to note at this stage is that vortex shedding from the plates in an interrupted-plate array has been studied in previous experimental investigations [15, 16]. Mochizuki and Yagi [15] found that for periodic fully developed flow in an interrupted-plate array, the Strouhal number ($\mathrm{St} = 2tn/\bar{W}$), based on mean flow velocity, plate thickness, and the frequency of vortex shedding, was essentially constant at a value of 0.13, independent of Reynolds number. Assuming this value for the Strouhal number, vortex shedding frequencies of 500 to 5000 Hz would be expected for the range of flow rates investigated in this work. If this

Nomenclature

ABCDE = geometrically similar module, Fig. 2(*b*)
b = width of a rectangular flow passage, Fig. 2(*a*)
d_h = module hydraulic diameter, equation (14)
D_h = hydraulic diameter of rectangular duct without interrupted-plate inserts, equation (3)
f = Darcy friction factor for rectangular duct without interrupted-plate inserts, equation (1)
f_m = module friction factor, equation (11)
H = half-height of rectangular ducts, Fig. 2
L = length of plate in interrupted-plate array, Fig. 2
L^* = nondimensional value of L ($=L/H$)
$\dot{m}$ = total mass flow rate in the duct
n = frequency of vortex shedding
$\tilde{p}$ = periodically varying part of P, equations (7) and (10)
P = time-mean static pressure
P_i = initial value of P in a module
P_o = value of P at a reference static pressure tap
P^*, P_i^*, P_o^* = nondimensional values of P, equation (15)
Re = Reynolds number for rectangular duct without interrupted-plate inserts, equation (2)
Re_m = module Reynolds number, equation (12)
Re* = laminar equivalent Reynolds number of Jones [22], equation (5)
s = interplate spacing, Fig. 2
s^* = nondimensional value of s ($=s/H$)
t = half-thickness of plates in the interrupted-plate array, Fig. 2(*b*)
t^* = nondimensional value of t ($=t/H$)
U = time-mean velocity component in the x direction
V = time-mean velocity component in the y direction
W = time-mean velocity component in the z direction
$\bar{W}$ = cross-sectional average value of W for *a* rectangular duct without interrupted-plate inserts ($=\dot{m}/(2\,H\,b\,\rho)$)
$\bar{W}_m$ = cross-sectional average value of W based on the nominal flow area of a module, equation (13)
x, y, z = Cartesian coordinate directions, Fig. 2(*a*)
z_i = initial value of z in a module
z_o = value of z at a reference static pressure tap
Z^*, Z_i^*, Z_o^* = nondimensional values of z ($=z/d_h$)
β = modular pressure drop per unit length, equations (7) and (9)
λ = aspect ratio of a module ($=b/H$)
μ = dynamic viscosity of the fluid
ρ = mass density of the fluid

relatively high-frequency vortex shedding is periodic, it could be treated in the same manner as flow turbulence, and by using an appropriate time-averaging procedure, steady time-mean flow values could be obtained. The experiments undertaken in this work did establish the existence of such steady time-mean flow values over the whole range of flow rates considered.

Six combinations of plate spacing, plate thickness, and duct aspect ratio were investigated. For each of these combinations, eight Reynolds numbers, based on average flow velocity and module hydraulic diameter, in the range of 5000 to 45000 were considered. In compact heat exchangers and current air cooling schemes for electronic components, the Reynolds number typically lies in the range of 500 to 10000, giving laminar, transitional, and turbulent flows [1-3]. However, Reynolds numbers greater than 10000 have been considered in enhanced gas cooling techniques for integrated circuit chips [3, 17]. The aforementioned Reynolds number range in this investigation was chosen to (i) obtain data that would be of fundamental interest in the study of fully turbulent flows in interrupted-plate rectangular ducts; and (ii) extend rather than duplicate currently available data [1, 8-11]. The results presented in this paper include the following: (i) overall pressure drop data presented in terms of module friction factor versus Reynolds number plots; and (ii) intramodular time-mean wall static pressure distributions.

Experimental Apparatus and Procedures

An experimental facility was specially designed and constructed for this work. A schematic representation of this facility is shown in Fig. 3. It consists of the following key elements: (i) a test section; (ii) a flow transition section; (iii) a flow metering section; (iv) a flow control, generation, and exhaust section; and (v) a data acquisition and processing system. Brief descriptions of some of these key elements are given in this section: Detailed descriptions of all sections are available in [18].

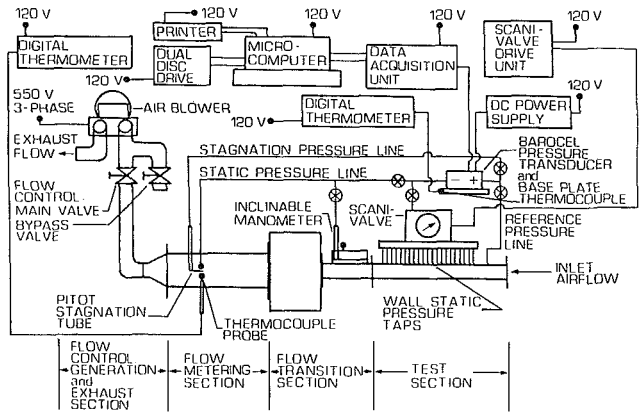

Fig. 3 Schematic of the overall experimental setup

Test Section. The test section of this facility was designed so that it could be easily detached, disassembled, reconfigured, and reattached to the rest of the flow circuit [18]. Six different interrupted-plate rectangular ducts were investigated. The cross-sectional and modular dimensions, and the corresponding nondimensional geometric parameters, of these six ducts, which will be referred to as Duct 1 to 6 in the remainder of this paper, are presented in Table 1, in terms of the nomenclature given in Fig. 2. The aspect ratios, λ, used in this work ensure essentially two-dimensional flow over the central region of the duct cross section; and the values of L^*, t^*, and s^* are representative of those found in compact heat exchangers [1]. The total length of each of the ducts was 1524 mm. This allowed each duct to be configured with at least 22 geometrically similar modules, such as ABCDE in Fig. 2(*b*). Thus periodic fully developed flow could be expected to prevail over at least 12 modules in each of the six ducts [9, 12]. The interrupted-plates were made of precision-ground steel and had blunt square edges, as shown in Fig. 2(*b*).

Axial pressure distributions were measured with the aid of 221 taps, each with a hole diameter of 0.5 mm, deployed along the centerline of the bottom plate of the test section. The first and the last of the holes for these pressure taps were drilled 63.5 mm from each end of the bottom plate, and the other holes were drilled at regular intervals, with a distance of 6.35 mm between the centers of adjacent holes. Further details on the design and construction of these pressure taps and the rest of the test section are available in [18].

Flow Metering Section. The main flow passage in this section was a 88.9 mm I.D. and 1244.6 mm long tube made of clear acrylic. The flow rates were obtained using stagnation pressure measurements from a traversing pitot tube and static pressure measurements from two taps in the flow tube wall. The pitot tube could be positioned to an accuracy of ± 0.2 mm. The ten-point log-linear method of Winternitz and Fischl [19] was used to determine volumetric flow rates. In order to minimize errors in the stagnation and static pressure measurements, the recommendations of Ower and Pankhurst [20] and Shaw [21] were followed as closely as possible in the design, construction, and assembly of the flow metering section: Details are available in [18].

Flow Control, Generation, and Exhaust Section. A centrifugal-type, constant-speed, air blower (Regenair R7100A), driven by a 10 HP AC motor with a rotor speed of 3450 rpm, was used in the suction mode to generate the air flow. The exhaust air coming out of the blower was passed to the outdoor environment to ensure that it did not disturb the air entering the test section. The use of two flow control valves, as shown in Fig. 3, made it possible to supply the air blower with an adequate supply of air over the whole range of test-section flow rates considered in this work.

Table 1 Cross-sectional and modular dimensions of the interrupted-plate rectangular ducts (Ducts 1-6)[+]

Duct No.	b (mm)	H (mm)	L (mm)	t (mm)	s (mm)	d_h (mm)	$\lambda = b/H$	$L^* = L/H$	$t^* = t/H$	$s^* = S/H$
1	152.40	13.07	25.42	0.39	12.64	24.08	11.66	1.945	0.030	0.9671
2	152.47	13.18	25.42	0.39	25.39	24.26	11.57	1.929	0.030	1.926
3	152.41	13.14	25.42	0.39	38.10	24.19	11.60	1.935	0.030	2.900
4	152.49	6.67	25.42	0.39	12.75	12.78	22.86	3.811	0.058	1.911
5	152.48	6.70	25.42	0.39	25.43	12.84	22.76	3.794	0.058	3.796
6	152.46	6.69	25.42	0.39	38.17	12.82	22.79	3.800	0.058	5.706

[+] 1. Refer to Fig. 2 for a description of the nomenclature.
2. The uncertainties in the measured dimensional quantities (b, H, L, t, and s) are less than ± 0.10 mm.

Pressure Measurement Instrumentation. All differential pressures greater than 1 kPa were measured using an inclinable reservoir-type manometer, accurate to ±1 percent. Differential pressures of less than 1 kPa were measured using an integral Barocel pressure transducer (Datametrics, Model 590-D-1kPa-2Q8-V1X-4D).

Data Acquisition and Processing System and Procedures. Most of the pressure measurements were recorded and processed using a microprocessor-based data acquisition unit (Hewlett-Packard, Model 34974). This data acquistion system was controlled by interfacing it to a desk-top scientific microprocessor (Hewlett-Packard, Model 86B).

Output signal fluctuations caused by electrical noise were minimized by using a very stable DC power supply to the Barocel transducer and by shielding all signal cables by several wraps of aluminum foil. Cyclical fluctuations in the Barocel output signal, caused by the inherent static pressure fluctuations in turbulent flows and flows generated by centrifugal blowers, and also by low-level 60 Hz AC noise and possible vortex shedding, were filtered out by using the following time-averaging procedure. For each measurement, the data acquisition system was programmed to take 60 discrete readings of the Barocel output over a period of 13 s, compute the arithmetic mean of these readings, and record this value. In test runs, it was established that this procedure provided a repeatability of better than $\pm 100\ \mu V$ of the mean value, which typically ranged from 0.1 V to 8 V.

Theoretical Considerations and Data Reduction

The experimental facility and procedures discussed in the last section were checked and validated by doing experiments on fully developed turbulent flow in uninterrupted rectangular ducts. In such ducts, fully developed flow is characterized by a time-mean velocity field which is invariant with the axial flow direction, z, and a time-mean static pressure, P, which drops linearly with z. It is customary to present pressure drop data for such flows in terms of Darcy friction factor, f, versus Reynolds number, Re, plots or correlations:

$$f = (-\partial P/\partial z) D_h/(\rho\ \bar{W}^2/2) \tag{1}$$

$$\mathrm{Re} = \rho\ \bar{W}\ D_h/\mu \tag{2}$$

where ρ is the mass density of the fluid, μ is the dynamic viscosity of the fluid, $\bar{W}$ is the cross-sectional average value of the time-mean axial velocity component, W, and D_h is the hydraulic diameter defined as follows:

$$D_h = 4\ b\ H/(2\ H + b) \tag{3}$$

Jones [22] has proposed a modified form of the Colebrook-White correlation [23] which expresses the Darcy friction factor as a function of Reynolds number for fully developed turbulent flow in straight, uninterrupted, smooth-walled, rectangular ducts. This modified correlation, which will be referred to as the Colebrook-White-Jones (CWJ) correlation in this paper, is the following [22]:

$$(1/\sqrt{f}) = 2.0\ \log_{10}(\mathrm{Re}^*\sqrt{f}) - 0.8 \tag{4}$$

where Re* is the "laminar equivalent Reynolds number" [22] and is related to the Reynolds number defined in equation (2) by the following equation:

$$\mathrm{Re}^* = \mathrm{Re}\left\{\frac{2}{3} + \frac{11}{24}\,(2\ H/b)[2 - (2\ H/b)]\right\} \tag{5}$$

The maximum deviation of the friction factors predicted by the CWJ correlation from the corresponding values obtained from the best of the published experimental data is about ±5 percent [22].

In interrupted-plate rectangular ducts, similar to that shown in Fig. 2(*a*), periodic fully developed turbulent flow is characterized by a time-mean velocity field which repeats itself identically in geometrically similar modules, such as ABCDE in Fig. 2(*b*). Thus:

$$U(x, y, z) = U(x, y, z+L+s) = U(x, y, z+2L+2s) = \ldots$$
$$V(x, y, z) = V(x, y, z+L+s) = V(x, y, z+2L+2s) = \ldots$$
$$W(x, y, z) = W(x, y, z+L+s) = W(x, y, z+2L+2s) = \ldots \tag{6}$$

As shown by Patankar et al. [13, 14], in the periodic fully developed regime, the variation of the time-mean static pressure can be expressed by the following equation:

$$P(x, y, z) = -\beta\ z + \tilde{p}(x, y, z) \tag{7}$$

The term $-\beta z$ is related to the overall mass flow rate in the duct, and $\tilde{p}(x, y, z)$ is related to the details of the local flow field in each geometrically similar module. With reference to Fig. 2(*b*), in the periodic fully developed regime, the difference in time-mean static pressures at adjacent (x, y) points, located a distance $(L+s)$ apart, will be the same throughout [13, 14]. As a result, the following equation applies:

$$\begin{aligned}[P(x, y, z) - P(x, y, z+L+s)] &= [P(x, y, z+L+s) - P(x, y, z+2L+2s)] \\ &= [P(x, y, z+2L+2s) - P(x, y, z+3L+3s)] \\ &= \ldots\end{aligned} \tag{8}$$

It follows from equations (7) and (8) that

$$\beta = \left\{\frac{P(x, y, z) - P(x, y, z+L+s)}{(L+s)}\right\} \tag{9}$$

and

$$\tilde{p}(x, y, z) = \tilde{p}(x, y, z+L+s) = \tilde{p}(x, y, z+2L+2s) = \ldots \tag{10}$$

The values of β were determined experimentally by (i) measuring time-mean values of the static pressure at the axial locations z, $(z+L+s)$, $(z+2L+2s)$, $(z+3L+3s)$, . . . , corresponding to a fixed (x, y) location on the wall of the duct; (ii) using the least-squares method to fit a straight line through these (P, z) points; and (iii) computing the slope of this straight line.

In this paper, the overall pressure drop data are presented in terms of module friction factors, f_m, versus module Reynolds numbers, Re_m, as defined by Patankar and Prakash [14]:

$$f_m = \beta d_h/(\rho\ \bar{W}_m^2/2) \tag{11}$$

$$\mathrm{Re}_m = \rho\ \bar{W}_m d_h/\mu \tag{12}$$

where β is as defined in equations (7) and (9), $\bar{W}_m$ is the average value of W based on the nominal flow area of a periodic module, and d_h is the module hydraulic diameter:

$$\bar{W}_m = (\dot{m}/2)/(b\ H\ \rho) \tag{13}$$

$$d_h = 4\ b\ H/(2H + 2b) \tag{14}$$

where $\dot{m}$ is the total mass flow rate, and ρ is the mass density of the fluid in the test section.

All uncertainties in the experimental data presented in this paper were estimated by the small-sample method of Kline and McClintock [24].

Results and Discussion

Initial Tests. Numerous initial tests were undertaken to determine the repeatability and accuracy of the measurements obtained with the experimental facility and procedures described earlier in this paper. This was done by conducting experiments on fully developed turbulent flow in straight rectangular ducts without interrupted-plate inserts and comparing the Darcy friction factor versus Reynolds number results of these experiments with the corresponding results in the

literature [22]. Details of these initial tests and the analyses of their results are given in [18]. In summary, it may be stated that these results agreed with those obtained from the CWJ correlation [22] to within ±5 percent.

Module Friction Factors. For each of Ducts 1 to 6, eight different module Reynolds numbers were considered in the range $5000 < Re_m < 45000$. Thus a total of 48 different combinations of interrupted-plate duct and flow rate were investigated. For each of these combinations, the time-mean wall static pressure measurements were converted into $(P_o^* - P^*)$ versus $(Z^* - Z_o^*)$ results:

$$P^* = P/(\rho\ \bar{W}_m^2/2) \tag{15}$$

$$Z^* = z/d_h \tag{16}$$

and the subscript, o, is used to denote quantities pertaining to a reference pressure tap located in the periodic fully developed region. These results for Duct 6 and $Re_m = 40880$ are presented in Fig. 4. Also shown in this figure are three sets of vertical lines which denote the leading edge (———), the center (— —), and the trailing edge (------) of each of the plates which constitute the interrupted-plate array in Duct 6. Plots similar to the one in Fig. 4 were obtained for each of the 48 cases investigated. Following that, for each case, a least-squares straight line was fittted to the $(P_o^* - P^*)$ versus $(Z^* - Z_o^*)$ data points corresponding to a set of periodically spaced pressure taps located above the leading edges of the plates in the interrupted-plate array. Then the slope of this straight line was used to obtain the module friction factor, f_m, defined in equation (11). In initial tests, for each case, module friction factors f_{mLE}, f_{mCT}, and f_{mTE}, corresponding to sets of periodically spaced data points over the leading edges, centers, and trailing edges of the plates, respectively, were calculated. It was established that, in all cases, f_{mCT} and f_{mTE} deviate from f_{mLE} by less than ±4 percent [18]. Thus only f_{mLE} values, without the subscript LE, are reported in this paper.

In addition, for each of Ducts 1 to 6, repeatability checks were done for the maximum and minimum Reynolds numbers [18]. In ten of these twelve cases, the deviations of the module friction factor, f_m, for the repeated run from that for the initial run, were less than ±3.92 percent. The corresponding deviations in Reynolds numbers were less than ±2 percent. For the other two cases, the deviations in f_m values were less than ±5.4 percent. This degree of repeatability in these measurements indicates that the experimental apparatus and procedure used were giving relatively steady time-mean flow values.

Graphical representation of the f_m versus Re_m results for Ducts 1, 2, and 3 are given in Fig. 5(*a*), and these results for Ducts 4, 5, and 6 are given in Fig. 5(*b*). A quantitative presentation of these results is given in Table 2. As can be seen from the duct dimensions given in Table 1, the aspect ratio ($\lambda = b/H$), the plate length ratio ($L^* = L/H$), and the plate thickness ratio ($t^* = t/H$) for Ducts 1, 2, and 3 are nearly equal, but the plate spacing ratio ($s^* = s/H$) for these ducts is different: $s^* = 0.9671$ for Duct 1; $s^* = 1.926$ for Duct 2; and $s^* = 2.900$ for Duct 3. Furthermore, λ, L^*, and t^* for Ducts 4, 5, and 6 are nearly equal, but their s^* values are different: $s^* = 1.911$ for Duct 4; $s^* = 3.796$ for Duct 5; and $s^* = 5.706$ for Duct 6. Thus, Figs. 5(*a*) and 5(*b*) not only allow a discussion of the f_m versus Re_m results for each of Ducts 1 to 6, but also enable a discussion about the effect of the spacing ratio, s^*, on these results. To facilitate this discussion, results for $s^* = 0$ are also plotted in Figs. 5(*a*) and 5(*b*). With $s^* = 0$, the plates in the colinear interrupted-plate array touch each other and divide

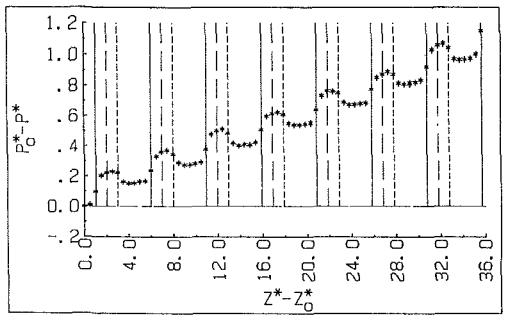

Fig. 4 Time-mean wall static pressure measurements for periodic fully developed turbulent flow in Duct 6 with $Re_m = 40880 \pm 815$. The maximum uncertainty in $(P_o^* - P^*)$ values is less than ±0.028. The maximum uncertainty in $(Z^* - Z_o^*)$ values is less than 3 percent of the reported values.

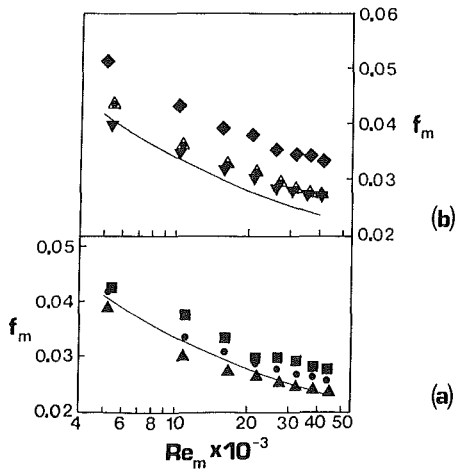

Fig. 5 Module friction factor versus Reynolds number results for (*a*) Duct 1 (■), Duct 2 (●), and Duct 3 (▲); and (*b*) Duct 4 (◆), Duct 5 (▲), and Duct 6 (▼). The uncertainty in each of the f_m and Re_m values is less than 5.4 and 2 percent of the reported values, respectively.

Table 2 Module friction factors and Reynolds numbers for periodic fully developed turbulent flow in Ducts 1–6 [+]

Duct 1		Duct 2		Duct 3		Duct 4		Duct 5		Duct 6	
$Re_m \times 10^{-3}$	$f_m \times 10^2$	$Re_m \times 10^{-3}$	$f_m \times 10^2$	$Re_m \times 10^{-3}$	$f_m \times 10^2$	$Re_m \times 10^{-3}$	$f_m \times 10^2$	$Re_m \times 10^{-3}$	$f_m \times 10^2$	$Re_m \times 10^{-3}$	$f_m \times 10^2$
43.43	2.773	43.96	2.571	44.12	2.336	40.68	3.343	40.23	2.783	40.88	2.721
38.06	2.816	37.71	2.644	38.11	2.381	36.71	3.454	36.68	2.777	36.08	2.773
32.30	2.912	32.31	2.657	32.52	2.447	31.75	3.476	31.90	2.819	31.13	2.804
26.83	2.980	26.93	2.757	27.33	2.508	26.23	3.534	27.13	2.940	26.21	2.847
21.28	2.962	21.64	2.888	22.27	2.625	20.93	3.819	21.52	3.132	21.00	3.005
16.36	3.338	16.10	3.090	16.75	2.754	15.54	3.913	16.27	3.278	15.69	3.195
10.95	3.713	11.11	3.310	10.88	3.005	10.27	4.336	10.69	3.604	10.49	3.474
5.521	4.257	5.271	4.197	5.287	3.897	5.152	5.125	5.441	4.353	5.332	3.976

[+] 1. The maximum uncertainty in each Re_m is less than ±2 percent of the reported value.
2. The maximum uncertainty in each f_m is less than ±5.4 percent of the reported value.

each of Ducts 1 to 6 into two identical rectangular ducts, each with a nominal aspect ratio equal to the module aspect ratio of the interrupted-plate duct. Thus the f_m versus Re_m curves for $s^* = 0$ in Figs. 5(*a*) and 5(*b*) were obtained from the Colebrook-White-Jones (CWJ) correlation [22] for rectangular ducts: Details of this correlation are given in equation (4).

In Figs. 5(*a*) and 5(*b*), the f_m versus Re_m results for each of Ducts 1 to 6 show the following variation: f_m drops with increasing Re_m. This trend can be explained by noting that the overall pressure drop in interrupted-plate rectangular ducts is required to overcome (i) wall friction, or shear forces at the walls of the duct; and (ii) the so-called inertial losses [10], which are proportional to $\bar{W}_m{}^2$ and occur in regions of separation and recirculation at the leading and trailing edges of the plates in the colinear interrupted-plate array. At low Reynolds numbers, there is a significant contribution of the wall friction to the overall pressure drop, and the module friction factor responds noticeably to changes in the Reynolds number. At high Reynolds numbers, however, the inertial losses dominate the wall-friction losses, and the module friction factor becomes less sensitive to changes in the Reynolds number.

In Fig. 5(*a*), the f_m versus Re_m curve for Duct 1 (■, $s^* = 0.9671$) lies above the corresponding curve for $s^* = 0$ (——). For a fixed total length of duct, the total (wall + plates) surface area for Duct 1 is less than that in a similar duct with $s^* = 0$. The interrupted plates in Duct 1, however, cause continual restarting of the velocity boundary layers on the plates. Thus the velocity gradients and shear stresses on the surface of the plates in Duct 1 are higher than those in the duct with $s^* = 0$. Furthermore, for the duct with $s^* = 0$ there are no inertial losses because there are no separation and recirculation zones at the leading and trailing edges of the plates, but these losses do occur in Duct 1. Therefore, despite the decrease in total area, for a given flow rate, or Reynolds number, the total static pressure drop, and hence f_m, for Duct 1 is higher than that for a similar duct with $s^* = 0$.

The arguments advanced in the previous paragraph can also be used to explain why, in Fig. 5(*a*), the f_m versus Re_m curve for Duct 2 (●, $s^* = 1.926$) is slightly higher than that for the duct with $s^* = 0$ (——). The f_m versus Re_m curve for Duct 2 is lower, however, than that for Duct 1 (■, $s^* = 0.9671$). For a fixed overall flow rate or Reynolds number, the larger plate spacing in Duct 2 would lead to a fuller redevelopment of the velocity profile in the wake regions than that in Duct 1. Thus the velocity gradients and shear stresses on the plate surfaces and the inertial losses in the separation zones at the leading edges of the plates would all be larger in Duct 2 than in Duct 1. However, for a fixed total length of duct, the total (wall + plate) surface area and the number of restartings of the velocity boundary layers on the plates are both less in Duct 2 than in Duct 1. Thus for a fixed Reynolds number, the results in Fig. 5(*a*) show that despite the aforementioned higher shear stresses and inertial losses per plate, the reductions in the total area and in the number of velocity boundary layer restartings lead to a lower module friction factor, f_m, for Duct 2 than that for Duct 1. Similar arguments can be used to explain why the f_m versus Re_m curve for Duct 3 (▲, $s^* = 2.900$) is lower than those for Duct 1 (■, $s^* = 0.9671$) and Duct 2 (●, $s^* = 1.926$).

In Fig. 5(*a*), the f_m versus Re_m curve for Duct 3 (▲, $s^* = 2.900$) is lower than that for a similar duct with $s^* = 0$ (——) for $Re_m < 3.0 \times 10^4$, but it is higher for higher Reynolds numbers. The f_m versus Re_m curves for Ducts 1 and 2, however, are higher than that for the duct with $s^* = 0$ for all Reynolds numbers considered in this investigation. For a fixed total length of duct, the total (wall + plates) surface area in Duct 3 is lower than the corresponding surface areas in Ducts 1 and 2, and considerably less than that in the duct with $s^* = 0$. Furthermore, the number of velocity boundary layer restartings is not as many in Duct 3 as those in Ducts 1 and 2. Thus for $Re_m < 3.0 \times 10^4$, where frictional losses contribute significantly to the overall pressure drop, the f_m versus Re_m curve for Duct 3 falls below that for the duct with $s^* = 0$. This behavior reverses for $Re_m > 3.0 \times 10^4$, however, because of the dominant inertial losses which exist in Duct 3 but are absent in the duct with $s^* = 0$.

The results in Fig. 5(*b*) can be explained by arguments similar to those already used to explain the results in Fig. 5(*a*). In Fig. 5(*b*), the f_m versus Re_m curves for Duct 4 (◆, $s^* = 1.911$), Duct 5 (▲, $s^* = 3.796$), and Duct 6 (▼, $s^* = 5.706$) are all higher than that for a similar duct with $s^* = 0$ (——). This is because the higher shear stresses and the inertial losses, caused by the interruptions of the velocity boundary layers on the plates, more than compensate for the lower total (wall + plate) surface areas of Ducts 4, 5, and 6 relative to that in the $s^* = 0$ duct. The f_m versus Re_m curve for Duct 4 lies above those for Ducts 5 and 6. This is because for a given length of duct, the total (wall + plates) surface area and the number of restartings of the velocity boundary layers on the plates in Duct 4 are both significantly larger than the corresponding values in Ducts 5 and 6. The f_m versus Re_m curve for Duct 6 is lower than that for Duct 5 for $Re_m < 10^4$, and for $Re_m > 10^4$, these curves are very close to one another. For the same length of duct, the total (wall + plates) surface area and the number of restartings of the velocity boundary layers on the plates in Duct 5 are both larger than the corresponding values for Duct 6. However, the interplate spacing in Duct 6 is larger, and hence the velocity redevelopment in the wake region is fuller, than that in Duct 5: Thus the shear stresses on the surface of the plates and the inertial losses in the leading edge separation zones are larger in Duct 6 than in Duct 5. The results in Fig. 5(*b*) show that for $Re_m < 10^4$, the overall static pressure drop is influenced more by changes in the total surface area and the number of restartings of the velocity boundary layers on the plates than by changes in the shear stresses and the inertial losses associated with each plate. For $Re_m > 10^4$, however, the overall static pressure drop is more or less equally influenced by these changes.

As is evident from the duct specifications given in Table 1, the width of the flow passage, b, the length of the interrupted plates, L, and the interplate spacing, s, for Duct 1 are almost the same as the corresponding values for Duct 4; these dimensions for Duct 2 are essentially the same as those for Duct 5; and these dimensions for Duct 3 are almost the same as those for Duct 6. The half-height, H, for Ducts 1, 2, and 3, however, is about twice that for Ducts 4, 5, and 6. Thus for the same overall flow rate, the average value of the time-mean axial velocity, $\bar{W}_m$, in Ducts 4, 5, and 6, is about twice that in Ducts 1, 2, and 3: Therefore, the shear stresses and frictional losses on the surfaces of the plates and the walls, and the inertial losses in the separated zones at the leading and trailing edges of the plates, for Ducts 4, 5, and 6 would be larger than the corresponding losses for Ducts 1, 2, and 3, respectively. Thus for the same overall flow rate and the same total length of duct, the overall time-mean pressure drops in Ducts 4, 5,

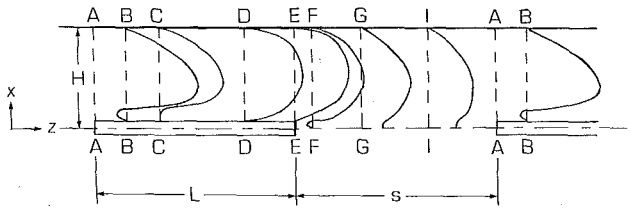

Fig. 6 Qualitative representation of axial time-mean velocity profiles expected in a periodic fully developed module

Table 3 Intramodular time-mean wall static pressure data for Duct 6[+]

$(Z^* - Z_i^*)$	$(P_i^* - P^*) \times 10^2$ $Re_m = 40.88 \times 10^3$	$Re_m = 31.13 \times 10^3$	$Re_m = 15.69 \times 10^3$	$Re_m = 5.332 \times 10^3$
0	0	0	0	0
0.4916	9.311	9.550	10.86	11.74
0.9898	12.52	12.96	15.40	18.26
1.487	12.28	12.99	16.32	21.16
1.970	11.20	11.76	15.64	21.97
2.478	5.007	5.539	8.721	16.02
2.966	3.324	3.927	5.972	11.26
3.468	3.629	4.164	6.001	9.727
3.957	4.072	4.673	6.466	9.528
4.448	4.551	5.263	7.169	10.74
4.955	13.50	14.07	15.84	17.88

[+] 1. The uncertainty in each $(P_i^* - P^*)$ value is less than ± 0.015.
2. The uncertainty in each Re_m is less than ± 2 percent of the reported value.
3. The uncertainty in each $(Z^* - Z_i^*)$ is less than ± 3 percent of the reported value.

and 6 would be larger than the corresponding pressure drops in Ducts 1, 2, and 3, respectively: The results in Table 2 and in Figs. 5(*a*) and 5(*b*) show that these increases in overall static pressure drops are so large that even the module friction factors, $f_m = \beta d_h/(\rho \bar{W}_m{}^2/2)$, for Ducts 4, 5, and 6 are, respectively, larger than the corresponding values for Ducts 1, 2, and 3.

Intramodular Wall Static Pressure Distributions. The presentation and discussion of the intramodular time-mean wall static pressure distributions is facilitated by reference to Fig. 6. This figure presents qualitative representations of axial velocity profiles expected in the longitudinal cross section of a typical periodic fully developed module. The velocity profiles in Fig. 6 were sketched after a careful examination of the numerical predictions of Patankar and Prakash [14] of laminar periodic fully developed flow in two-dimensional arrays of interrupted-plates, and the experimental results of Ota and Itasaka [25], pertaining to turbulent external flow over a blunt flat plate, and of Bellows and Mayle [26], pertaining to turbulent flow over a two-dimensional blunt body with a circular leading edge.

For each of Ducts 1 to 6, eight different Reynolds numbers were considered. The 48 intramodular time-mean wall static pressure distributions obtained from these experiments are available in [18]. In this paper, due to space restrictions, only samples of these results for Duct 6 are presented in Fig. 7. Quantitative representations of the data in this figure are given in Table 3. In Fig. 7, plots of $(P_i^* - P^*)$ versus $(Z^* - Z_i^*)$ are presented: P^* and Z^* are defined in equations (15) and (16), respectively, and the subscript, i, is used to denote quantities pertaining to the initial static pressure tap, located over the leading edge of the plate in the periodic fully developed module. In each of the Figs. 7(*a*) to 7(*d*), the first five data points (the first is located at $Z^* - Z_i^* = 0$) correspond to static pressure taps located above the plate, and the remaining data points correspond to static pressure taps located over the interplate gap. The vertical lines in these figures denote the locations of the leading edge (——), the center (— —), and the trailing edge (------) of the plate.

Consider the intramodular pressure distribution given in Fig. 7(*a*), which corresponds to Duct 6 with $Re_m = 40880$. With reference to the velocity profiles in Fig. 6, when the flow enters the periodic module, it undergoes separation, strong acceleration in the axial direction, and, as a result, transports increased momentum in the axial direction. All these features of the flow and the increase in the surface area caused by the presence of the plate, cause a steep drop in the time-mean static pressure: This is indicated by the sharp rise in $(P_i^* - P^*)$ over the first half of the plate. Downstream of the center of the plate, a mild recovery in the time-mean static pressure is indicated by the fourth and fifth data points. With reference

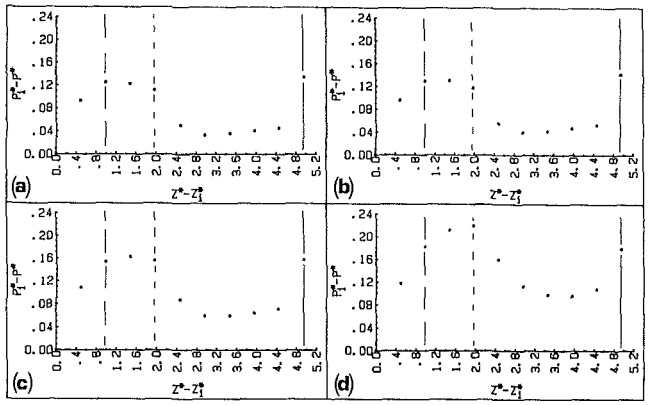

Fig. 7 Intramodular time-mean wall static pressure distributions for Duct 6: (*a*) $Re_m = 40880 \pm 815$; (*b*) $Re_m = 31130 \pm 620$; (*c*) $Re_m = 15690 \pm 310$; and (*d*) $Re_m = 5332 \pm 105$. The maximum uncertainty in each $(P^*_i - P^*)$ value is less than ± 0.015. The maximum uncertainty in each $(Z^* - Z_i^*)$ value is less than 3 percent of the reported value.

to the velocity profiles in Fig. 6, as the flow redevelops over the last half of the plate, it goes through velocity profiles similar to those at sections D-D and E-E which transport less axial momentum than the velocity profiles at section B-B and C-C. This lowering in the transport of axial momentum leads to an increase in the time-mean static pressure. The results in Fig. 7(*a*) show that this increase in static pressure is greater than the drop in static pressure needed to overcome frictional losses. Thus there is a net recovery of static pressure over the last half of the plate, as indicated by the fourth and fifth data points. Downstream of the trailing edge of the plate, there is a sharp rise in the static pressure, as indicated by the fifth and sixth data points. This recovery of static pressure is due to the following: (i) the axial momentum transported by velocity profiles similar to those in sections F-F and G-G in Fig. 6 is less than that transported by the velocity profile in section E-E, at the trailing edge of the plate; and (ii) the elimination of the plate surface leads to a sizable drop in frictional losses. Downstream of data point seven, the static pressure starts to drop again: This is because as the flow redevelopment in the interplate gap continues, the axial momentum transport starts to increase at the expense of a decrease in static pressure, and a static pressure drop is also needed to overcome frictional losses. Finally, as the flow hits the leading edge of the plate in the next periodic fully developed module, there is a sharp drop in the static pressure.

In Fig. 7(*a*), the overall drop in time-mean static pressure over the module, indicated by the $(P_i^* - P^*)$ value for the last data point, corresponds to the net static pressure drop which is needed to sustain an overall mass flow rate through the module. The ratio $(P_i^* - P^*)/(Z^* - Z_i^*)$ obtained from the last

data point for the module is equal to the module friction factor, f_m, defined in equation (11).

The intramodular time-mean wall static pressure distribution presented in Fig. 7(*d*) corresponds to Duct 6 with $Re_m = 5332$. This $(P_i^* - P^*)$ versus $(Z^* - Z_i^*)$ plot is similar to that presented in Fig. 7(*a*), except for one important difference. The time-mean wall static pressure drops steeply over the first half of the plate, and this drop continues, albeit mildly, all the way to the trailing edge of the plate. The recovery of static pressure starts only in the initial part of the wake region downstream of the trailing edge: In contrast, this static pressure recovery in Fig. 7(*a*) starts over the last half of the plate. This finding indicates that at the lower Reynolds number of 5332 pertaining to Fig. 7(*d*), compared to $Re_m = 40880$ for the plot in Fig. 7(*a*), the static pressure drop needed to overcome frictional losses dominates any static pressure recovery which may result because of the inertial effects of the flow redistribution over the plate.

Concluding Remarks

Time-mean wall static pressure measurements for periodic fully developed turbulent flows in six different interrupted-plate rectangular ducts have been presented and discussed in this paper. For the flow rates and geometric configurations investigated, the time-averaging procedure used in this work yields steady and repeatable time-mean wall static pressure measurements. This indicates that it may be possible to formulate numerical methods based on time-averaged steady-state models that can adequately simulate flows similar to those investigated in this work. To facilitate the use of the experimental data obtained in this work for the testing of such numerical prediction procedures, key results have been presented in both graphical and tabular forms, along with estimates of the uncertainties involved. In addition, explanations have been proposed for the module friction factor results and intramodular time-mean wall static pressure distributions, based on qualitative discussions of the flow in periodic fully developed modules.

Acknowledgments

Financial support of this work by the Natural Sciences and Engineering Research Council (NSERC) of Canada is gratefully acknowledged.

References

1 Kays, W. M., and London, A. L., *Compact Heat Exchangers*, 2nd ed., McGraw-Hill, New York, 1964.

2 Kraus, A., and Bar-Cohen, A., *Thermal Analysis and Control of Electronic Equipment*, Hemisphere Publishing Corp., Washington, D. C., 1983.

3 Chu, R. C., "Heat Transfer in Electronic Systems," *Proceedings of the Eighth International Heat Transfer Conference*, San Francisco, Calif., Vol. 1, 1986, pp. 293-305.

4 Sparrow, E. M., Niethammer, J. E., and Chaboki, A., "Heat Transfer and Pressure Drop Characteristics of Arrays of Rectangular Modules Encountered in Electronic Equipment, *Int. J. Heat Mass Transfer*, Vol. 25, 1982, pp. 961-972.

5 Sparrow, E. M., Vemuri, S. B., and Kadle, D. S., "Enhanced and Local Heat Transfer, Pressure Drop, and Flow Visualization for Arrays of Block-Like Electronic Components," *Int. J. Heat Mass Transfer*, Vol. 27, 1983, pp. 689-699.

6 Wieting, A. R., "Empirical Correlations for Heat Transfer and Flow Friction Characteristics of Rectangular Offset-Fin Plate-Fin Heat Exchangers," ASME *Journal of Heat Transfer*, Vol. 97, 1975, pp. 488-490.

7 London, A. L., and Shah, R. K., "Offset Rectangular Plate-Fin Surfaces-Heat Transfer and Flow Friction Characteristics," ASME *J. Engineering for Power*, Vol. 90, 1968, pp. 218-228.

8 Cur, N., and Sparrow, E. M., "Experiments on Heat Transfer and Pressure Drop for a Pair of Colinear, Interrupted Plates Aligned With the Flow," *Int. J. Heat Mass Transfer*, Vol. 21, 1978, pp. 1069-1080.

9 Cur, N., and Sparrow, E. M., "Measurements of Developing and Fully Developed Heat Transfer Coefficients Along a Periodically Interrupted Surfact," ASME *Journal of Heat Transfer*, Vol. 101, 1979, pp. 211-216.

10 Sparrow, E. M., and Hajiloo, A., "Measurements of Heat Transfer and Pressure Drop for an Array of Staggered Plates Aligned Parallel to an Air Flow," ASME *Journal of Heat Transfer*, Vol. 102, 1980, pp. 426-432.

11 Joshi, H. M., and Webb, R. L., "Heat Transfer and Friction in the Offset Strip-Fin Heat Exchanger," *Int. J. Heat Mass Transfer*, Vol. 30, 1987, pp. 69-84.

12 Sparrow, E. M., Baliga, B. R., and Patankar, S. V., "Heat Transfer and Fluid Flow Analysis of Interrupted-Wall Channels, with application to heat exchangers," ASME *Journal of Heat Transfer*, Vol. 99, 1977, pp. 4-11.

13 Patankar, S. V., Liu, C. H., and Sparrow, E. M., "Fully Developed Flow and Heat Transfer in Ducts Having Streamwise-Periodic Variation of Cross-Sectional Area," ASME *Journal of Heat Transfer*, Vol. 99, 1977, pp. 180-186.

14 Patankar, S. V., and Prakash, C., "An Analysis of the Effect of Plate Thickness on Laminar Flow and Heat Transfer in Interrupted-Plate Passages," *Int. J. Heat Mass Transfer*, Vol. 24, 1981, pp. 1801-1810.

15 Mochizuki, S., and Yagi, Y., "Characteristics of Vortex Shedding in Plate Arrays," in *Flow Visualization II* (Ed. W. Merzkirch), Hemisphere Publishing Corporation, 1982, pp. 99-103.

16 Mullisen, R. S., and Loehrke, R. I., "A Study of the Flow Mechanisms Responsible for Heat Transfer Enhancement in Interrupted-Plate Heat Exchangers," ASME *Journal of Heat Transfer*, Vol. 108, 1986, pp. 377-385.

17 Kishimoto, T., Saski, E., and Moriya, K., "Gas Cooling Enhancement Technology for Integrated Circuit Chips," *IEEE Trans.*, Vol. CHMT-7, 1984, pp. 286-293.

18 McBrien, R. K., "Pressure Measurements for Periodic Fully Developed Turbulent Flow in Interrupted-Plate Ducts, *M. Eng. thesis*, Department of Mechanical Engineering, McGill University, Montreal, Canada, 1986.

19 Winternitz, F. A. L., and Fischl, C. F., "A Simplified Integration Technique for Pipe-Flow Measurement," *Water Power*, June, 1957, pp. 225-234.

20 Ower, E., and Pankhurst, R. C., *The Measurement of Air Flow*, 4th ed., Pergamon Press, 1966.

21 Shaw, R., "The Influence of Hole Dimensions on Static Pressure Measurements," *J. Fluid Mechanics*, Vol. 7, 1960, pp. 550-564.

22 Jones, O. C., "An Improvement in the Calculation of Turbulent Friction in Rectangular Ducts," ASME JOURNAL OF FLUIDS ENGINEERING, Vol. 98, 1976, pp. 173-181.

23 Blevins, R. D., *Applied Fluid Dynamics Handbook*, Van Nostrand Reinhold Co., 1984.

24 Kline, S. J., and McClintock, F. A., "Describing Uncertainties in Single-Sample Experiments," *Mechanical Engineering*, Vol. 75, 1953, pp. 3-8.

25 Ota, T., and Itasaka, M., "A Separated and Reattached Flow on a Blunt Flat Plate," ASME JOURNAL OF FLUIDS ENGINEERING, Vol. 98, 1976, pp. 79-86.

26 Bellows, W. J., and Mayle, R. E., "Heat Transfer Downstream of a Leading Edge Separation Bubble," ASME *Journal of Turbomachinery*, Vol. 108, 1986, pp. 131-136.

A Simple Model for the Critical Swirl in a Swirling Sudden Expansion Flow

W. L. H. Hallett
Associate Professor,
Department of Mechanical Engineering,
University of Ottawa,
Ottawa, Canada K1N 6N5

A simple momentum integral model for estimating the minimum or "critical" swirl intensity required to produce central recirculation in a swirling sudden expansion flow is presented. An explicit equation is given for the critical swirl as a function of expansion ratio and inlet velocity profile shape, the latter expressed by the radius of the solid body vortex core and a parameter describing an axial velocity maximum or minimum on the axis. The model is tested against experimental data for expansion diameter ratios from 1.25 to 3.0 and a variety of inlet conditions, and found to give good predictions.

Introduction

Many fuel burners and combustors employ the central recirculation zone generated by a strongly swirling flow to enhance flame stability and mixing. Central recirculation or "vortex breakdown" sets in when the swirl exceeds a certain minimum or "critical" level, whose value is a function of geometry and inlet conditions. (The words "vortex breakdown" and "critical swirl" refer here to central recirculation only; other authors [1] use them in a wider sense for a number of related phenomena.) For design purposes, a knowledge of the critical swirl will allow good mixing and stability to be obtained without the large pressure losses associated with excessively high swirl levels. This paper presents a simple theory for estimating the critical swirl in a sudden expansion, a geometry which approximates many combustors, as a function of expansion ratio and inlet velocity profile shape.

A number of theories for vortex breakdown have been developed. Leibovich [1] and Hall [2] review several criteria for breakdown in "quasi-cylindrical" flows (slowly expanding flows with negligible axial derivatives), which identify breakdown variously as the onset of standing waves, as a singularity in the solution of the governing equations or as a critical streamline angle. For flow in a cylindrical tube, Chow [3] and Suematsu and Ito [4] present analytical solutions for several classes of breakdown phenomena, while Escudier and Keller [5] develop a simple theory and Escudier and Zehnder [6] a correlating parameter for the critical swirl. Bossel [7] presents a relationship between critical swirl and expansion ratio for inviscid flow in an expansion of unspecified shape based on an analytical solution of the equations for quasi-cylindrical flow. A simple criterion for breakdown of a free jet was postulated by Krüger [8], who equated the forward momentum of the flow on the axis with the radial pressure drop between the flow boundary and the axis at stagnation.

Contributed by the Fluids Engineering Division for publication in the JOURNAL OF FLUIDS ENGINEERING. Manuscript received by the Fluids Engineering Division August 14, 1987.

Momentum integral techniques have been widely used to solve for the flow field: simple functional forms are assumed for the radial variations of the velocities, allowing integration of the governing equations in the radial direction, and the resulting set of equations is then solved for the parameters defining the velocity profiles. Among these are the work of Mager [9] for a converging-diverging nozzle and the solutions of Morton [10] and Domkundwar et al. [11] for a conical diffuser. Krause [12] uses this method to assess the effects of velocity profile shape on stagnation on the axis. A more restrictive form of this technique, in which the variation of axial velocity in the axial as well as the radial direction is specified, has been used by Gore and Ranz [13] and Nakamura and Uchida [14] for unconfined flows.

Of the works reviewed above, only that of Bossel [7] is directly applicable to sudden expansions, and its validity is restricted to small expansion ratios because of the quasi-cylindrical approximation. The free jet theories of Krüger [8] and Gore and Ranz [13] do not account for the effects of expansion ratio in confined flow, while solutions for diffusers [9–11] are made inapplicable by the singularity associated with a step expansion. Complete solutions to swirling flow fields in sudden expansions have only been obtained with finite difference models, which have been applied to a variety of geometries and inlet conditions [15–19]. These would be capable of estimating critical swirl by a trial and error process, generating solutions at progressively higher swirls until recirculation appears. However, only Kubo and Gouldin [15] have actually used a finite difference model for this purpose, and their predictions have not been experimentally verified. There is, then, no simple, tested means of predicting the critical swirl in a sudden expansion.

Figure 1 gives a qualitative picture of a breakdown in a sudden expansion as observed experimentally [19–21]. The changes in the radial pressure distribution produced as the flow expands lead to axial pressure gradients opposing the forward flow [16, 22]. This effect is strongest at the axis, and at

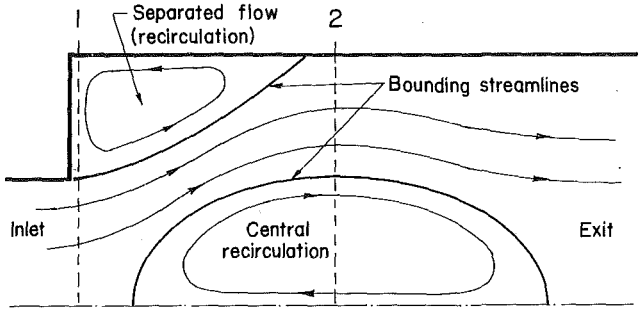

Fig. 1 Sketch of main features of a swirling sudden expansion flow with central recirculation

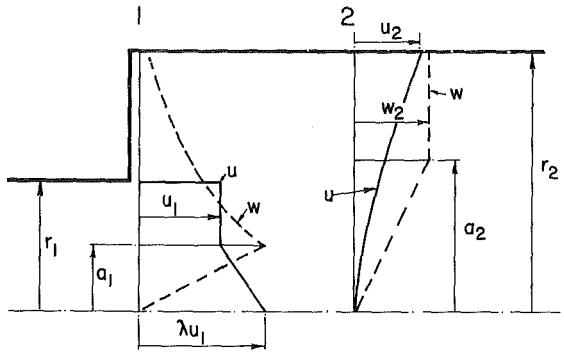

Fig. 2 Velocity profile assumptions used for the model

or above the critical swirl leads to a stagnation on the axis, which quickly expands into a backflow zone. Further downstream, the action of shear stresses and what Batchelor [23] has called the "elasticity" imparted to swirling flows by the Coriolis force closes the recirculation zone, leaving a wake-like forward flow downstream. At moderate swirl the backflow occupies roughly half the expansion diameter and has a length of about one expansion diameter [19-21]. The critical swirl is known to be a function of inlet velocity profile shape, in particular of the magnitude of the axial velocity on the axis where stagnation occurs and the diameter of the solid body vortex core [5, 8, 12, 22], as well as of expansion geometry. Experimental data [18, 20, 22] show that the critical swirl in a sudden expansion is independent of Reynolds number in a fully turbulent flow; in contrast, breakdown phenomena in a cylindrical or slowly diverging tube are known to be a function of Re [1, 2, 6].

Analysis

The present analysis uses a momentum integral method to solve for the critical swirl, in which the equations of motion are integrated over the control volume between Stations 1 and 2 (Fig. 1). The model assumes a state of flow in which breakdown is just beginning, then solves for the swirl intensity required to produce that flow field. Station 1 represents the inlet conditions; it is located just downstream of the step, as in the classical analysis for a non-swirling expansion flow, so that pressure forces on the end wall need not be accounted for. Section 2 is chosen at the plane of the greatest extent of the backflow, so that radial velocities become negligible. Under the additional assumptions of frictionless, incompressible flow and rotational symmetry, the following conservation equations apply:

Continuity:

$$\int_0^{r_2} urdr = \text{constant} \tag{1}$$

Axial Momentum Flux:

$$\int_0^{r_2} u^2 rdr + \int_0^{r_2} \frac{p}{\rho} rdr = \text{constant} \tag{2}$$

Angular Momentum Flux:

$$\int_0^{r_2} uwr^2 dr = \text{constant} \tag{3}$$

The radial momentum equation on integration yields the pressure distribution for insertion in equation (2):

$$p(r) = p_0 + \rho \int_0^r \frac{w^2}{r} dr \tag{4}$$

The velocity profile assumptions used to carry out these integrations are shown in Fig. 2. The upstream tangential velocity is represented by a Rankine vortex with core radius a_1:

$$w = \frac{\Gamma r}{a_1^2} \text{ for } 0 \le r \le a_1$$

$$w = \frac{\Gamma}{r} \text{ for } a_1 < r \le r_2 \tag{5}$$

while the axial velocity is described by

$$u = u_1 \left[\lambda - (\lambda - 1)\frac{r}{a_1}\right] \text{ for } 0 \le r \le a_1$$

$$u = u_1 \text{ for } a_1 < r < r_1$$

$$u = 0 \text{ for } r_1 < r \le r_2 \tag{6}$$

Note that the axial velocity profile ends at r_1, while the tangential profile continues to r_2. Experimental results [20, 21] show that rotation is present for $r > r_1$, caused by upstream transport of angular momentum by the corner recirculation (Fig. 1). These profiles were chosen to give a good approximation to those measured by Hallett and Toews [22]. The values of λ and a_1 are inputs to the model, and represent factors

Nomenclature

a = vortex core radius
A = see equation (12)
J_1 = Bessel function of the first kind, first order
$\dot{m}$ = mass flow
p = pressure
r = radius
r_1, r_2 = see Fig. 2
R_2 = see equation (12)
u = axial velocity
u_1, u_2 = velocity profile parameters, equations (6), (7)
w = tangential velocity
w_2 = velocity profile parameter, equation (8)
Γ = circulation/2π
λ = velocity profile parameter, equation (6)
ρ = density
ϕ = see equation (10)
ψ = see equation (11)
Ω = swirl parameter, equation (14)

Subscripts

cr = at critical swirl
0 = at axis
w = at wall
1,2 = stations 1, 2 (Fig. 1).

which are known to affect the critical swirl [5, 8, 12, 22], while the circulation required to produce breakdown is to be solved for.

The downstream profiles represent the state of the flow at the inception of breakdown, when the velocity on the axis has just been reduced to zero. No measurements are available at this state, but data taken at swirls somewhat in excess of the critical [19-21] suggest that axial velocities can be approximated by a parabola:

$$u = u_2(r/r_2)^2 \tag{7}$$

while the tangential velocity near the wall becomes flatter than a potential vortex and can be represented by

$$w = w_2(r/a_2) \quad \text{for} \quad 0 \le r \le a_2$$

$$w = w_2 \quad \text{for} \quad a_2 < r \le r_2 \tag{8}$$

The two sets of profiles are linked by the condition for stagnation of the flow on the axis, given by

$$p_{02} - p_{01} = \rho\lambda^2 u_1^2/2 \tag{9}$$

Krüger [8] has used a similar condition for an unconfined jet, except that the pressure difference was that between the flow boundary and the axis.

The integrals can now be evaluated at Station 1 and 2. Continuity yields

$$\frac{u_2}{u_1} = \phi = \frac{2}{R_2}\left[1 - \frac{A_1}{3}(1-\lambda)\right] \tag{10}$$

while equation (3) gives

$$\frac{w_2 r_2}{\Gamma_1} = \psi = \frac{1 + A_1\left(\frac{\lambda}{10} - \frac{3}{5}\right)}{\phi R_2\left(\frac{2}{5} - \frac{1}{15}A_2^{5/2}\right)} \tag{11}$$

where

$$A_1 = (a_1/r_1)^2;\ A_2 = (a_2/r_2)^2;$$

$$R_2 = (r_2/r_1)^2 \tag{12}$$

Equation (2) together with equations (4) and (9) then yields an explicit expression for the critical swirl:

$$\left(\frac{\Gamma_1}{u_1 r_1}\right)_{cr}^2 = \frac{1 - A_1\left(\frac{1}{2} - \frac{\lambda}{3} - \frac{\lambda^2}{6}\right) - \frac{\lambda^2}{2}R_2 - \frac{1}{3}\phi^2 R_2}{\psi^2\left(\frac{A_2}{4} - \frac{1}{2}\ln A_2\right) - \frac{R_2}{A_1} + \frac{3}{4} + \frac{1}{2}\ln\left(\frac{R_2}{A_1}\right)} \tag{13}$$

This is more conveniently expressed as a swirl parameter, defined here as the dimensionless angular momentum flux Ω:

$$\Omega = \frac{2\pi}{r_1 I}\int_0^{r_1} \rho u w r^2 dr \tag{14}$$

where I is an axial momentum flux based on the average inlet axial velocity $\bar{u}$:

$$I = \pi r_1^2 \rho \bar{u}^2$$

$$\bar{u} = \dot{m}/(\rho\pi r_1^2) \tag{15}$$

Using equations (5-6)

$$\Omega_{cr} = \left[\frac{\Gamma_1}{u_1 r_1}\right]\left[\frac{1 + A_1\left(\frac{\lambda}{10} - \frac{3}{5}\right)}{\left[1 + \frac{1}{3}A_1(\lambda - 1)\right]^2}\right] \tag{16}$$

It remains to find a suitable expression for the downstream core radius a_2. It was discovered that the downstream profile shapes used make the model quite insensitive to the value of a_2, so that a fairly arbitrary choice can be made. Experimental data [19, 20] show that a_2 grows with expansion ratio, while at the same time it seem likely that a_2 should also increase with upstream core size a_1. This suggests that the core expands in proportion to the rest of the flow, giving

$$A_2 = A_1 \tag{17}$$

Two other assumptions were tested, one with a constant core size ($a_2 = a_1$), which is physically unreasonable, the other setting $(a_2/r_2) = 0.5$. Predictions for the test data of Hallett and Toews [22] using the latter assumptions were inferior to those from equation (17), but differed from those with equation (17) by only 7 percent on average.

Other means of determining a_2 are available, but were not used here. A moment of axial momentum equation may be applied as an additional condition [10, 11]; however, its use requires knowledge of derivatives in the axial direction. An earlier version of the present model [24], which employed a Rankine vortex with zero axial velocity in the core at Station 2, used the results of an analysis by Strscheletzky [25], who applied the principle of least action to solve for the core radius of this particular profile. Similar to this are the assumptions of minimum kinetic energy used by Meldau [26] and Khalil et al. [27] and of minimum head loss used by Escudier [28] and others. As Escudier [28] remarks, there is no real theoretical justification for these assumptions; their use can also be objected to in the present context because they imply mechanical equilibrium, an assumption which is implausible in view of the large accelerations undergone by fluid particles in a breakdown flow.

Results

The model was tested against the data of Hallett and Toews [22], who measured inlet velocity profiles at the critical swirl for four different expansion ratios in fully turbulent flow. The swirl generator used in [22] allowed inlet profile shape and swirl to be varied independently, and measurements were made with four different sets of inlet conditions for each expansion, permitting the effects of (a_1/r_1) and λ as well as (r_2/r_1) in the present model to be tested. The model velocity profiles (a_1, λ) were fitted to the experimental data with a procedure which reproduced the measured centerline velocity, mass flow and angular momentum flux. To correct for the wall boundary layer, the outer boundary was moved inwards by the displacement thickness of the layer. The only arbitrary element in the fitting was the choice of the slope of the swirl velocity profile in the core, which influenced the value of (a_1/r_1) but had no significant effect on λ. However, the fitted values of (a_1/r_1) fell into the range from 0.78 to 0.96, a range in which the model showed Ω_{cr} to be only weakly dependent on (a_1/r_1) (see later discussion—Fig. 6), so that model predictions were quite insensitive to the exact slope chosen. Samples of fitted profiles are shown in Fig. 3.

Figure 4 compares measured and predicted critical swirls as a function of the fitted parameter λ. The model reproduces the trends of the data with (r_2/r_1) and with λ quite well, and predicts all experimental points to within an average error of 8 percent. For comparison, the experimental uncertainty is at most 5 percent of Ω_{cr}, this being roughly the range of swirl numbers over which the transition to breakdown occurred [22]. There is an obvious discrepancy in the trend predicted for $(r_2/r_1) = 1.25$ at low λ, and it appears that the unusual tangential velocity profile shape at the anomalous point (Fig. 3—$\Omega_{cr} = 0.414$) is not well enough fitted by the model. Apart from this, no correlation was observed between the goodness of fit of the inlet profiles and the accuracy of the predictions.

Figures 5-7 illustrate some general results of the model. The axial pressure gradient producing stagnation and breakdown can be considered to consist of a swirl-induced component

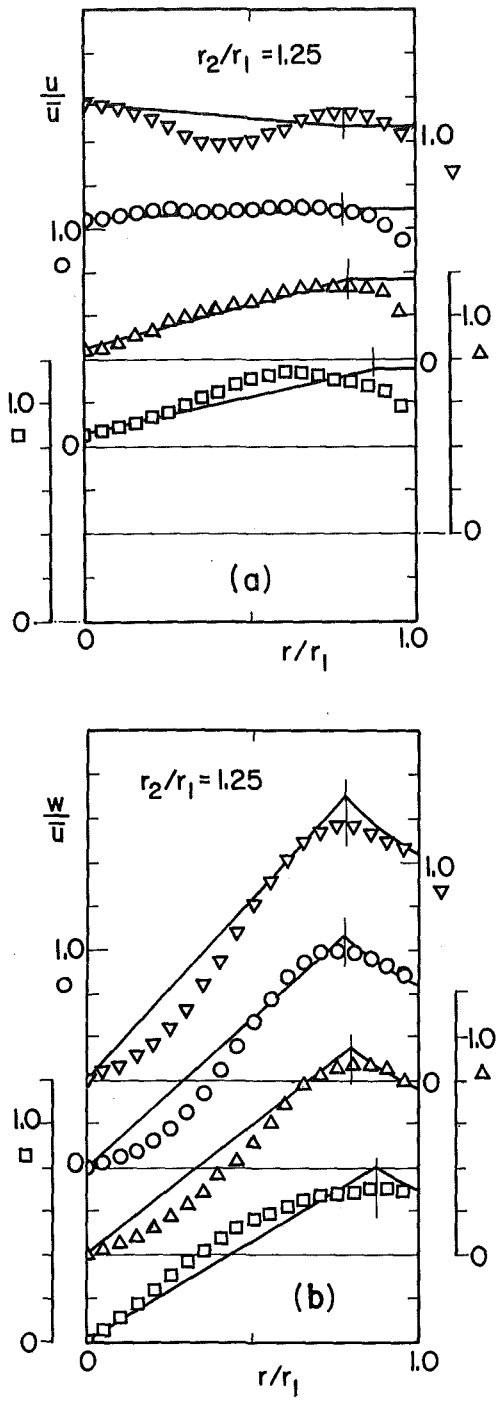

Fig. 3 Samples of fitted velocity profiles for $r_2/r_1 = 1.25$. (a) axial velocities; (b) tangential velocities.

▽ Ω = 0.660;	a_1/r_1 = 0.795;	λ = 1.105
○ Ω = 0.548;	a_1/r_1 = 0.784;	λ = 0.972
△ Ω = 0.491;	a_1/r_1 = 0.815;	λ = 0.734
□ Ω = 0.414;	a_1/r_1 = 0.874;	λ = 0.748

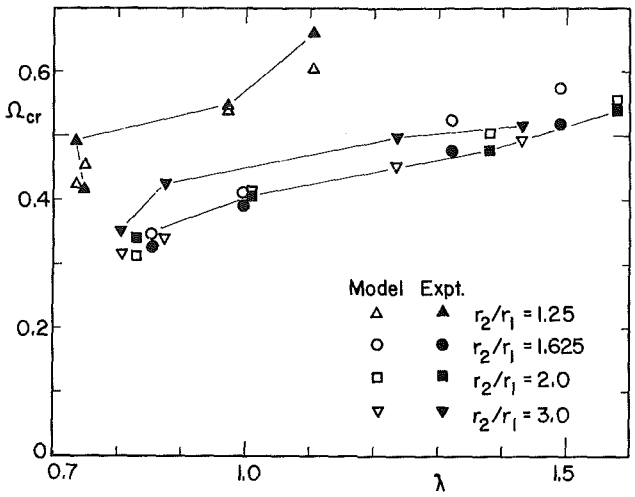

Fig. 4 Comparison of predicted Ω_{cr} with measurements of [22] as function of inlet profile parameter λ

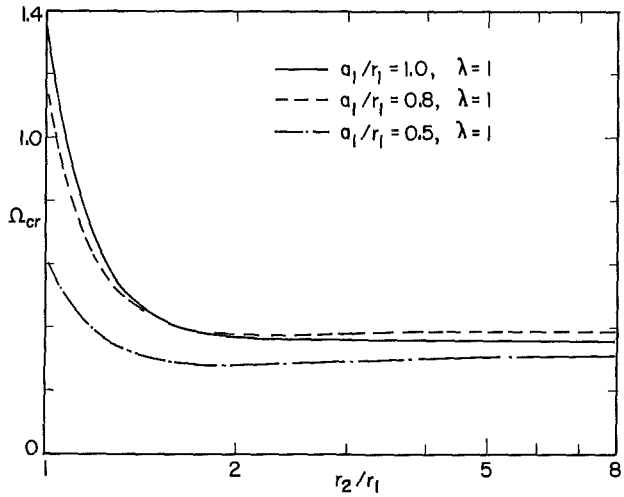

Fig. 5 Effect of expansion ratio on critical swirl

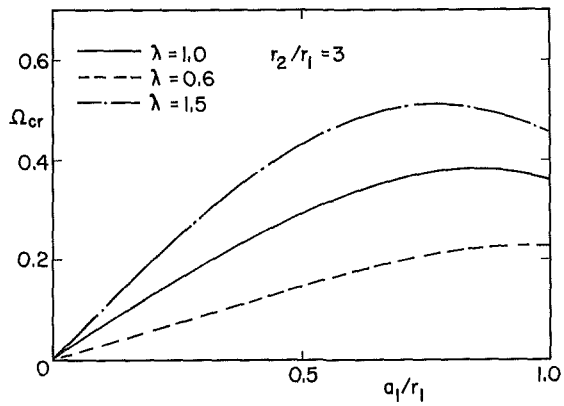

Fig. 6 Effect of inlet core radius on critical swirl for $(r_2/r_1) = 3$

superimposed on the pressure recovery due to axial velocity reduction. The latter, as in non-swirling flow, rises with increasing (r_2/r_1) to a maximum and falls to zero again for very large expansions. The swirl component arises from the coupling between the swirl velocity profile and the pressure difference $(p_w - p_0)$ between wall and axis. For Station 2, from equations (4) and (8)

$$p_{w2} - p_{02} = \rho w_2^2 \left[\frac{1}{2} + \ln\left(\frac{r_2}{a_2} \right) \right] \tag{18}$$

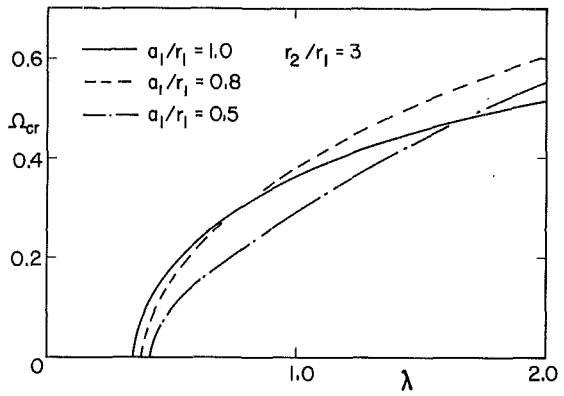

Fig. 7 Effect of centerline axial velocity parameter λ on critical swirl for $(r_2/r_1) = 3$

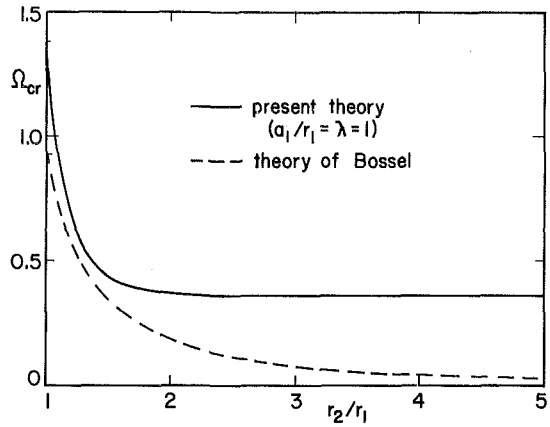

Fig. 8 Comparison of present model with that of Bossel [7], $a_1/r_1 = \lambda = 1$

For given upstream conditions a greater expansion ratio will reduce w_2 and hence increase p_{02} and the axial pressure gradient. The combined effect of axial velocity recovery and swirl will be a rapid drop in Ω_{cr} (= rise in gradient) up to a certain (r_2/r_1), after which, depending on the relative magnitudes of the two components, Ω_{cr} can either rise or fall to an asymptotic value at large expansion ratios. Both types of behavior can be seen in Fig. 5. It is tempting to regard predictions for large expansion ratios as equivalent to those for free jets. However, experiments in enclosed flows at large expansion ratios [20] show much larger recirculation zones than are found in free jets [29, 30], suggesting that a different model is required.

The effects of inlet core size are shown in Fig. 6. At Station 1

$$p_{w1} - p_{01} = \frac{\rho\Gamma^2}{r_2^2}\left[\left(\frac{r_1}{a_1}\right)^2\left(\frac{r_2}{r_1}\right)^2 - \frac{1}{2}\right] \qquad (19)$$

so that an increase in (a_1/r_1) causes p_{01} to rise relative to p_{w1}, tending to decrease the axial pressure gradient. This also increases the pressure force at Station 1, so that the pressure level at Station 2 must rise as well to conserve axial momentum. A further increase in p_{02} results from the expansion of the downstream core (equation (18)) since a_2 grows in proportion to a_1. Events at Station 2, therefore, tend to reduce the critical swirl (larger pressure gradient) as (a_1/r_1) grows, while those at Station 1 tend to increase it. At small inlet core radii equation (19) shows that p_{01} rises rapidly with (a_1/r_1), so that Ω_{cr} increases, while for large (a_1/r_1) pressure changes at Station 2 become significant, reducing the dependence on (a_1/r_1) and even reversing the trend in some cases (Fig. 6). A pure potential vortex ($a_1 = 0$), for which $(p_w - p_0)$ becomes infinite, has a critical swirl of zero. This agrees with the model of Krüger [8] for a free jet, whose predictions generally are very similar to those of Fig. 6, and is also implied by the analyses of Krause [12] and Escudier and Keller [5].

Figure 7 shows that a velocity peak on the axis increases the pressure gradient required to reverse the flow and hence the critical swirl. This is in agreement with predictions and measurements of others [8, 22]. The critical swirl falls to zero when the pressure recovery due to axial velocity reduction alone suffices to reverse the flow.

The present model is compared with that of Bossel [7] in Fig. 8. Bossel's analysis is restricted to inlet conditions of uniform axial velocity and solid body rotation $(a_1/r_1 = \lambda = 1)$, and gives the critical swirl implicitly as

$$\sigma - 2\sqrt{R_2}J_1(\sigma\sqrt{R_2})/(R_2 - 1) = 0 \qquad (20)$$

where the swirl parameter σ can be shown to be

$$\sigma = 4\Omega_{cr} \qquad (21)$$

The two theories agree best at $(r_2/r_1) \simeq 1.3$ and diverge away from this point. For large expansion ratios, Bossel's assumption of quasi-cylindrical flow is no longer valid, and his model yields the physically unreasonable result that a flow with infinite expansion ratio will break down at zero swirl. At very small expansion ratios $(r_2/r_1 < 1.25)$ the present model must be regarded as untested.

Conclusions

The model presented here has been shown to give predictions of critical swirl of sufficient accuracy for engineering design for at least the range of expansion ratios and inlet conditions tested here. Apart from the velocity profile assumptions themselves, the model contains only one arbitrary parameter—the downstream core size (a_2/r_2)—to which the model has been shown to be quite insensitive. As a caveat, it should be remarked that the solid body core size (a_1/r_1) produced by the swirl generator used in the experiments [22] seems to be unusually large; more typical values for vane swirlers appear to range from about 0.3 to 0.6 [29, 30]. Experiments on critical swirl with other types of swirler would be desirable to further test the model. Because the flow has been assumed inviscid, the model applies to high Reynolds number, fully turbulent flow.

Model results show that the swirl required for central recirculation can be reduced by producing an inlet flow with a small solid body core and/or a velocity deficit on the axis. By the same token, the momentum added by a central fuel injector or primary flow would increase the critical swirl. It is important in using the model that the input quantities (a_1/r_1) and λ accurately represent inlet conditions *at the critical swirl*, as many swirl generators produce a wide variation in profile shape with swirl intensity. Unfortunately, this requires more detailed knowledge of swirler characteristics than is generally available.

Acknowledgment

The author is grateful for the financial support of the Natural Sciences and Engineering Research Council of Canada.

References

1 Leibovich, S., "Vortex Stability and Breakdown: Survey and Extension," *AIAA Journal*, Vol. 22, Sept. 1984, pp. 1192-1206.

2 Hall, M. G., "Vortex Breakdown," *Annual Review of Fluid Mechanics*, Vol. 4, 1972, pp. 195-218.

3 Chow, C.-Y., "Swirling Flow in Tubes of Non-Uniform Cross-Sections," *Journal of Fluid Mechanics*, Vol. 38, 1969, pp. 843–854.

4 Suematsu, Y., and Ito, T., "Vortex Breakdown Phenomena in a Circular Pipe (1st Report, Modes of Stationary Breakdown)," *Bulletin of the JSME*, Vol. 24, 1981, pp. 1137–1144.

5 Escudier, M. P., and Keller, J. J., "Vortex Breakdown: A Two-Stage Transition," AGARD Conference Proceedings No. 342, *Aerodynamics of Vortical Type Flows in Three Dimensions*, Rotterdam, 1983, pp. 25-1–25-8.

6 Escudier, M. P., and Zehnder, N., "Vortex-Flow Regimes," *Journal of Fluid Mechanics*, Vol. 115, 1982, pp. 105–121.

7 Bossel, H. H., "Swirling Flows in Streamtubes of Variable Cross Section," *AIAA Journal*, Vol. 11, 1973, pp. 1161–1165.

8 Krüger, J., "Drehimpuls, Schub und innere Rückströmung bei Brennerstrahlen," *Gas Wärme International*, Vol. 22, 1973, pp. 497–504.

9 Mager, A., "Incompressible, Viscous, Swirling Flow through a Nozzle," *AIAA Journal*, Vol. 9, 1971, pp. 649–654.

10 Morton, H. L., "Effect of Swirl on Turbulent Flow in the Front End of Gas Turbine Main Burners," AIAA Paper No. 71-2, 1971.

11 Domkundwar, V. M., Sriramulu, V., and Gupta, M. C., "Analysis of Swirling Recirculating Reacting Turbulent Jets Passing Through Diffusers," *Combustion and Flame*, Vol. 33, 1978, pp. 241–249.

12 Krause, E., "A Contribution to the Problem of Vortex Breakdown," AGARD Conference Proceedings No. 342, *Aerodynamics of Vortical Type Flows in Three Dimensions*, Rotterdam, 1983, pp. 26-1–26-4.

13 Gore, R. W., and Ranz, W. E., "Backflows in Rotating Fluids Moving Axially through Expanding Cross Sections," *A.I.Ch.E. Journal*, Vol. 10, 1964, pp. 83–88.

14 Nakamura, Y., and Uchida, S., "Breakdown Condition of an Axisymmetric Swirling Flow," *AIAA Journal*, Vol. 19, 1981, pp. 1083–1085.

15 Kubo, I., and Gouldin, F. C., "Numerical Calculations of Turbulent Swirling Flow," ASME JOURNAL OF FLUIDS ENGINEERING, Vol. 97, 1975, pp. 310–315.

16 Grabowski, W. J., and Berger, S. A., "Solutions of the Navier-Stokes Equations for Vortex Breakdown," *Journal of Fluid Mechanics*, Vol. 75, 1976, pp. 525–544.

17 Narain, J. P., "Numerical Prediction of Confined Swirling Jets," *Computers and Fluids*, Vol. 5, 1977, pp. 115–125.

18 Rhode, D. L., Lilley, D. G., and McLaughlin, D. K., "On the Prediction of Swirling Flowfields Found in Axisymmetric Combustor Geometries," ASME JOURNAL OF FLUIDS ENGINEERING, Vol. 104, 1982, pp. 378–384.

19 Rao, A. N., Ganesan, V., Gopalakrishnan, K. V., and Natarajan, R., "Experimental and Theoretical Investigations of Vane-Generated Swirling Flows in a Circular Chamber," *Journal of the Institute of Energy*, Vol. 56, 1983, pp. 137–144.

20 Beltagui, S. A., and Maccallum, N. R. L., "Aerodynamics of Vane-Swirled Flames in Furnaces," *Journal of the Institute of Fuel*, Vol. 49, 1976, pp. 183–193.

21 Hallett, W. L. H., and Günther, R., "Flow and Mixing in Swirling Flow in a Sudden Expansion," *Canadian Journal of Chemical Engineering*, Vol. 62, 1984, pp. 149–155.

22 Hallett, W. L. H., and Toews, D. J., "The Effects of Inlet Conditions and Expansion Ratio on the Onset of Flow Reversal in Swirling Flow in a Sudden Expansion," *Experiments in Fluids*, Vol. 5, 1987, pp. 129–133.

23 Batchelor, G. K., *An Introduction to Fluid Dynamics*, Cambridge, 1967, pp. 555–557.

24 Hallett, W. L. H., "Prediction of the Onset of Central Recirculation in Swirling Flow using the Momentum Integral Method," Combustion Institute (Canadian Section) 1985 Spring Technical Meeting, pp. 18-1–18-4.

25 Strscheletzky, M., "Gleichgewichtsformen der rotationssymmetrischen Strömungen mit konstantem Drall in geraden, zylindrischen Rotationshohlräumen," *Voith Forschung und Konstruktion*, Vol. 5, 1959, pp. 1.1–1.19.

26 Meldau, E., "Drallströmung im Drehhohlraum," Dr.-Ing. Dissertation, Hannover, 1935.

27 Khalil, K. H., El-Mahallawy, F. M., and Moneib, H. A., "Effect of Combustion Air Swirl on the Flow Pattern in a Cylindrical Oil Fired Furnace," 16th Symposium (International) on Combustion, 1976, pp. 135–143.

28 Escudier, M., "Estimation of Pressure Loss in Ring-Type Exit Chambers," ASME JOURNAL OF FLUIDS ENGINEERING, Vol. 101, 1979, pp. 511–516.

29 Mathur, M. L., and Maccallum, N. R. L., "Swirling Jets Issuing from Vane Swirlers. Part 1: Free Jets," *Journal of the Institute of Fuel*, Vol. 40, 1967, pp. 214–225.

30 Sislian, J. P., and Cusworth, R. A., "Laser Doppler Velocimetry Measurements of Mean Velocity and Turbulent Stress Tensor Components in a Free Isothermal Swirling Jet," Report No. 281, University of Toronto Institute for Aerospace Studies, March, 1984.

Pressure-Driven Ranque-Hilsch Temperature Separation in Liquids

R. T. Balmer

Department of Mechanical Engineering,
University of Wisconsin—Milwaukee,
Milwaukee, Wis. 53201

The temperature separation phenomenon of the Ranque-Hilsch (vortex) tube is not limited to compressible gases and vapors. Theoretical analysis using the Second Law of Thermodynamics establishes that a net entropy producing temperature separation effect is possible when incompressible liquids are used in these devices. Experiments with liquid water in a commercial counterflow Ranque-Hilsch tube designed for use with air verify that significant temperature separation does in fact occur when a sufficiently high inlet pressure is used.

Introduction

The mechanism producing the temperature separation phenomenon as a gas or vapor passes through a Ranque-Hilsch vortex tube is not yet fully understood. This effect, which appears to depend upon generating a swirling vortex flow inside an open tube, was discovered with air in the early 1930s by Ranque [1] and was later popularized by Hilsch [2]. In this device the swirling action causes the gas to become very cold at the centerline and very hot at the tube wall, with temperature differences of 100°C not uncommon. When the core and wall flows are separated by a simple baffle arrangement, cold and hot outlet flows are produced and effective (though inefficient) refrigeration or heating can be done. Since the Ranque-Hilsch tube has no moving parts, it currently has commercial value primarily as an inexpensive cooling device for gases and vapors.

Though this phenomenon has been studied extensively during the past forty years, researchers today still do not agree on its underlying mechanism. Gortler vortices (Stephan et al. [3]), compressibility (Amitani et al. [4]), turbulent transfer of thermal energy (Linderstrom-Lang [5]), and acoustic streaming (Kurosaka et al. [6]) have all been proposed as possible mechanisms. Irregardless of the mechanism, this phenomenon is clearly a member of a growing class of energy driven order creating bifurcation phenomena [7].

Thus far Ranque-Hilsch vortex tube temperature separation experiments have been carried out only with gases and vapors, and consequently it is commonly believed that compressibility plays an important role in the mechanism. This paper reports the results of such a temperature separation experiment carried out with liquid water, which is essentially an incompressible fluid.

Theory

1 Thermal Mixing of Ideal Gases. In order to understand the operation of a standard vortex tube, we begin with an analysis of the reverse process, thermal mixing, and then move to the more complex subject of thermal separation. Consider the dual inlet, single outlet adiabatic thermal mixing shown in Fig. 1(*a*). There is no work input to this system (the mixing is done via turbulence). A single ideal gas at temperatures T_1 and T_2 is input at stations 1 and 2. The conservation of mass for this system is

$$\dot{m}_1 + \dot{m}_2 - \dot{m}_3 = 0 \tag{1}$$

Neglecting the potential energies of the flowstreams, the energy and entropy rate balances are

$$\dot{m}_1(h_1 + V_1^2/2) + \dot{m}_2(h_2 + V_2^2/2) - \dot{m}_3(h_3 + V_3^2/2) = 0 \tag{2}$$

and

$$\dot{m}_1 s_1 + \dot{m}_2 s_2 - \dot{m}_3 s_3 + (\dot{S}_p)_{\text{mixing}} = 0 \tag{3}$$

where the second law of thermodynamics requires that the entropy production rate be positive definite,[1] or

$$(\dot{S}_p)_{\text{mixing}} > 0 \tag{4}$$

Define the mass flow fraction, y, as

$$y = \dot{m}_1/\dot{m}_3 \tag{5}$$

and then equation (1) gives

$$\dot{m}_2/\dot{m}_3 = 1 - y \tag{6}$$

Since the flowstream kinetic energies are usually much smaller than the enthalpies in this process, they can be neglected and equations (2), (3), and (4) can then be written as

$$y(h_1 - h_2) + (h_2 - h_3) = 0 \tag{7}$$

$$(\dot{S}_p)_{\text{mixing}} = \dot{m}_3[y(s_2 - s_1) + (s_3 - s_2)] > 0 \tag{8}$$

The relevant equations of state for an ideal gas with constant specific heats are

$$h - h_o = c_p(T - T_o) \tag{9}$$

and

$$s - s_o = c_p \ln(T/T_o) - R\ln(p/p_o) \tag{10}$$

where the "o" subscript indicates an arbitrary reference state. For a simple turbulent thermal mixer, it is reasonable to

Contributed by the Fluids Engineering Division for publication in the JOURNAL OF FLUIDS ENGINEERING. Manuscript received by the Fluids Engineering Division August 17, 1987.

[1] We are ignoring the possibility of reversible mixing here.

assume that $p_1 = p_2 > p_3$, and then upon substituting equations (9) and (10) into equations (7) and (8) and combining the results we obtain

$$T_3/T_2 = 1 + y(T_1/T_2 - 1) \tag{11}$$

and

$$(\dot{S}_p)_{\text{mixing}} = \dot{m}_3 c_p \ln\left[\left(1 + y\left(\frac{T_1}{T_2} - 1\right)\right)\left(\frac{T_1}{T_2}\right)^{-y}\right] - \dot{m}_3 R \ln\left(\frac{p_3}{p_2}\right) > 0 \tag{12}$$

By setting the differential of equation (12) with respect to y equal to zero it can easily be shown that the entropy production rate of equation (12) is maximized when the mass flow fraction has a critical value given by

$$y_{\text{crit}} = \frac{(1 - T_1/T_2) + \ln(T_1/T_2)}{(1 - T_1/T_2)\ln(T_1/T_2)} \tag{13}$$

Since y crit produces the maximum amount of dissipation within the system, it would also presumably produce the most thorough mixing due to dissipation enhanced chaotic macroscopic motion.

2 Thermal Separation of Ideal Gases. Consider next the device shown in Fig. 1(*b*). It is similar to the thermal mixer shown in Fig. 1(*a*) except that all the flow directions are reversed, thus theoretically producing thermal separation rather than mixing without the need for an external work mechanism. Such a device does in fact exist, and is called a vortex or Ranque-Hilsch tube.

The conservation of mass and the energy rate balance equations and the associated assumptions are the same as for the thermal mixer, however the entropy rate balance equation and the Second Law of Thermodynamics are now given by

$$(\dot{S}_p)_{\text{separating}} = \dot{m}_3[y(s_1 - s_2) + (s_2 - s_3)] > 0 \tag{14}$$

A comparison of equations (8) and (14) reveals that

$$(\dot{S}_p)_{\text{separating}} = -(\dot{S}_p)_{\text{mixing}}$$

The significance of this result is only in the similarity of the algebraic forms of these two entropy production rate equations because the second law of thermodynamics requires that both of these entropy production rate terms be positive definite. Since these two entropy production rates cannot possibly have the same numerical values, the separation process must be sufficiently different from the mixing process so as to allow a completely different mechanism to dominate the internal entropy generation rate process. The most obvious difference between these two systems is the way in which the flowstream pressure is utilized. We get some feeling for this by recalling that thermal mixing can occur essentially isobarically (i.e., $p_1 = p_2 = p_3$), whereas thermal separation cannot (i.e., p_3 must be greater than p_1 and p_2). Assuming that $p_1 = p_2 < p_3$ for the thermal separation process, then equations (9), (10), (11) and (14) can be combined to give

$$(\dot{S}_p)_{\text{separating}} = \dot{m}_3 c_p \ln\left[\left(\frac{T_1}{T_2}\right)^{y}\left(1 + y\left(\frac{T_1}{T_2} - 1\right)\right)^{-1}\right] + \dot{m}_3 R \ln\left(\frac{p_3}{p_2}\right) \tag{15}$$

which will be positive if p_3 is sufficiently greater than p_2. Thus the thermal separation process for ideal gases is clearly pressure driven, and will not occur unless $(\dot{S}_p)_{\text{separating}} > 0$, or unless

$$(p_3/p_2)_{\text{separating}} > \left[\left(\frac{T_1}{T_2}\right)^{-y}\left(1 + y\left(\frac{T_1}{T_2} - 1\right)\right)\right]^{c_p/R} \tag{16}$$

3 Thermal Mixing and Separation of Incompressible Liquids. Equation (16) is the governing thermodynamic equation for the operation of a Ranque-Hilsch (vortex) tube using a constant specific heat ideal gas. In order to investigate the possibility of a similar thermal separation process using an incompressible liquid, we replace equations (9) and (10) with the equivalent equations of state for an incompressible liquid with a constant specific heat

$$u - u_o = c(T - T_o) \tag{17}$$

$$h - h_o = u - u_o + (p - p_o)/\rho = c(T - T_o) + (p - p_o)/\rho \tag{18}$$

and

$$s - s_o = c\ln(T/T_o) \tag{19}$$

Again neglecting the flowstream potential energies and assuming $p_1 = p_2$, the conservation of mass (equation (1)) and energy rate balance (equation (2)) can be combined with equations (17) and (19) to yield

$$\frac{T_3}{T_2} = 1 + y\left(\frac{T_1}{T_2} - 1\right) + \left(\frac{p_2 - p_3}{\rho c T_2}\right) - \left(\frac{V_3^2 - yV_1^2 - (1-y)V_2^2}{2cT_2}\right) \tag{20}$$

The amount of kinetic energy contained in the flowstreams was typically less than 1 percent of the driving pressure energy in the results presented here, so the kinetic energy terms in equation (20) can be dropped without a significant loss in accuracy. For thermal mixing ($p_1 = p_2 > p_3$) equations (8), (19) and (20) then yield

$$(\dot{S}_p)_{\text{mixing}} = \dot{m}_3 c \ln\left\{\left(\frac{T_1}{T_2}\right)^{-y}\left[1 + y\left(\frac{T_1}{T_2} - 1\right) + \left(\frac{p_2 - p_3}{\rho c T_2}\right)\right]\right\} \tag{21}$$

and for thermal separation ($p_1 = p_2 < p_3$) equations (14), (19), and (20) yield

$$(\dot{S}_p)_{\text{separating}} = \dot{m}_3 c \ln\left\{\left(\frac{T_1}{T_2}\right)^{y}\left[1 + y\left(\frac{T_1}{T_2} - 1\right) - \left(\frac{p_3 - p_2}{\rho c T_2}\right)\right]^{-1}\right\} \tag{22}$$

Equation (22) tells us that thermal separation with constant specific heat incompressible liquids is possible if $(\dot{S}_p)_{\text{separating}} > 0$, which will occur only if

$$p_3 > p_2 + \rho c T_2\left[1 + y\left(\frac{T_1}{T_2} - 1\right) - \left(\frac{T_1}{T_2}\right)^{y}\right] \tag{23}$$

[2] If the vortex tube exhausts to the atmosphere, then $p_1 = p_2 = p_{\text{atm}}$.

Nomenclature

c_p = constant pressure specific heat (gas)
c = specific heat (liquid)
h = enthalpy
$\dot{m}$ = mass flow rate
p = pressure
R = gas constant
s = specific entropy
$\dot{S}_p$ = entropy production rate
T = temperature
y = mass flow fraction

Subscripts

C = cold
H = hot
o = reference state
p = production
v = viscous
1, 2, 3 = see Figs. 1(*a*) and 1(*b*)
ρ = density

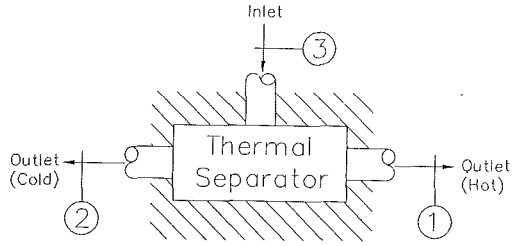

Fig. 1(*a*) Schematic of an adiabatic work-free thermal mixer

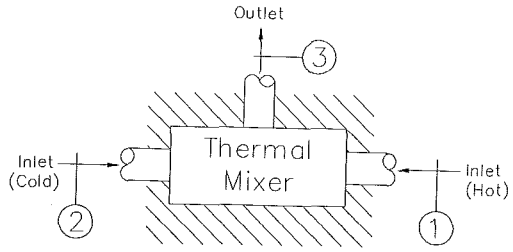

Fig. 1(*b*) Schematic of an adiabatic work-free thermal separator

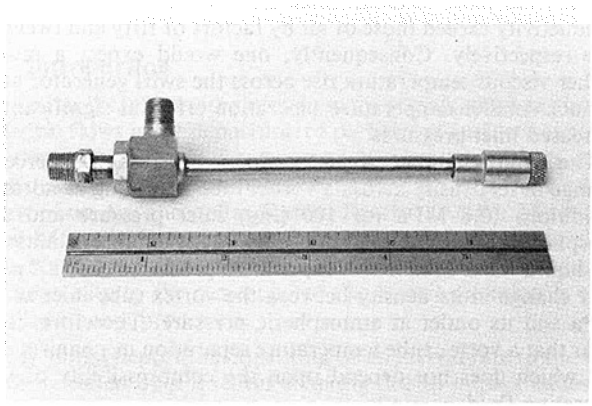

Fig. 1(c)Photograph of the Vortec Corp. Model 106 vortex tube

Thus, a Ranque-Hilsch (vortex) tube may work with an incompressible liquid if the inlet pressure is sufficiently high. For example, equation (23) predicts that for liquid water flowing through a vortex tube it would require more than 1.5 MPa to produce $T_1/T_2 = 1.1$ (or $T_1 - T_2 \approx 55°C$). Just how much more than 1.5 MPa would be required is not indicated by this equation since the actual value of the entropy production rate depends upon the amount of irreversibility within the vortex tube, and this in turn depends upon the level of viscous dissipation within the vortex tube. Note also that equations (22) and (23) suggest that compressibility need not be the governing mechanism in the Ranque-Hilsch temperature separation phenomena since they predict that $\dot{S}_p$ can be made to be greater than zero even for totally incompressible fluids.

Apparatus and Procedure

A commercially available counterflow Ranque-Hilsch (vortex) tube designed for use with air (Vortec Corp. Model 106 with 8-HG inserts, see Fig. 1(*c*)) was instrumented as shown in Fig. 2. The liquid water was supplied by a Tritan Plunger Pump rated at 8 gpm (30 lpm) at 15,000 psi (103 MPa). The inlet mass flow rate was obtained by closing the hot side outlet valve and then calibrating the entire Ranque-Hilsch (vortex) tube as a differential pressure flowmeter. A linear relationship was found between the inlet mass flow rate

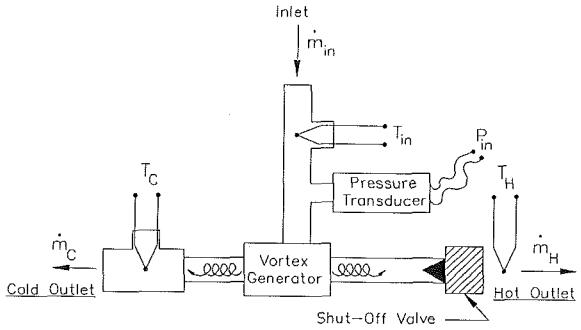

Fig. 2 Schematic of the instrumentation used on the commercial Ranque-Hilsch (vortex) tube (Vortec Corp. Model 106 with an 8-HG vortex generator) when high pressure liquid water was used as the working fluid. Temperature differences of 10 to 20 C were produced with inlet pressures of 20 to 50 MPa.

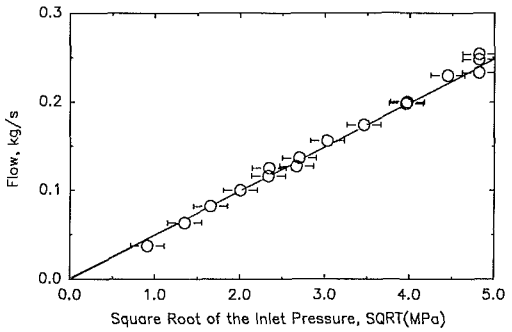

Fig. 3 The calibration curve for pressure drop vs mass flow rate of water through the vortex tube

and the square root of the inlet pressure (see Fig. 3). During testing, the hot side mass flow rate was collected in a beaker and timed while the inlet mass flow rate was determined from the inlet pressure via the previous calibration. Since virtually all of the vortex tube pressure drop occurs across the swirl generator, whether the hot side valve is open or not has no appreciable effect on the calibration curve shown in Fig. 3.

In this apparatus y was chosen to be the hot side mass fraction, so that station 1 is the hot (H) outlet and station 2 is the cold (C) outlet, then

$$y = \dot{m}_1/\dot{m}_{\text{in}} = \dot{m}_H/\dot{m}_{\text{in}} \tag{24}$$

Because of the small passages in the commercial vortex generator, the viscous temperature rise, ΔT_v, of an incompressible liquid passing through this device can be quite large. This temperature rise for an incompressible fluid of density ρ and specific heat c, with negligible changes in kinetic or potential energies and $p_3 = p_{in} >> p_2 = p_1 = p_H = p_C = p_{out}$, can be determined from equation (20) as

$$\Delta T_v = yT_1 + (1-y)T_2 - T_3 = yT_H + (1-y)T_C - T_{\text{in}}$$
$$= (p_3 - p_2)/(\rho c) = (p_{\text{in}} - p_{\text{out}})/(\rho c) \tag{25}$$

Since most of the viscous temperature rise results from the pressure dissipation across the vortex generator and not in the exit tubes, the temperature separation effect occurs relative to the swirl generator average exit temperature, T_G, where

$$T_G = T_{\text{in}} + \Delta T_v = yT_1 + (1-y)T_2 = yT_H + (1-y)T_C \tag{26}$$

Results and Conclusions

The calibration data of flow rate vs. pressure drop across the vortex tube with the hot side closed is shown in Fig. 3. It is seen that this data is quite linear, and the resulting correlation was used to determine $\dot{m}_{\text{in}}$ for all the remaining data. In the

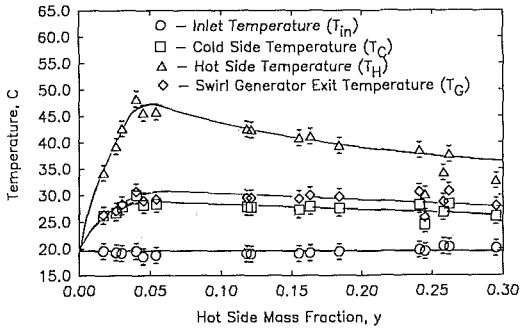

Fig. 4 Hot, cold, inlet and swirl generator exit temperatures vs hot side mass fraction (y)

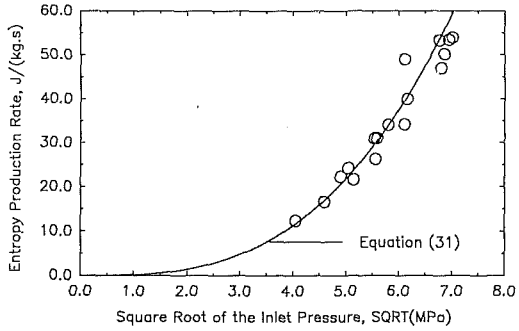

Fig. 5 The entropy production rate of a Ranque-Hilsch (vortex) tube using liquid water as the working fluid is seen to vary with the cube of $\sqrt{p_{in}}$ (or $\dot{m}_{in}$) and is independent of the flow split (y)

experiments reported here the measured cold side outlet temperature was always less than the vortex generator average exit temperature but was not less than the measured tube inlet temperature, that is, $T_{in} < T_C < T_G < T_H$, as shown in Fig. 4.

Since the magnitude of $\dot{S}_p$ is a measure of the irreversibilities within the vortex tube, it will reflect how efficiently the separation process takes place. Introducing the notation shown in Fig. 1(*b*) into equations (14) and (19) yields

$$\frac{\dot{S}_p}{\dot{m}_{in}c} = \ln\left[\left(\frac{T_H}{T_C}\right)^y \left(\frac{T_C}{T_{in}}\right)\right] \tag{27}$$

For the data presented here $1 \le T_H/T_C \le 2$, and equation (27) can be expanded in a power series as

$$\frac{\dot{S}_p}{\dot{m}_{in}c} = y\ln\left(\frac{T_H}{T_C}\right) + \ln\left(\frac{T_C}{T_{in}}\right)$$

$$\approx y\left[\left(\frac{T_H}{T_C}-1\right) - \frac{1}{2}\left(\frac{T_H}{T_C}-1\right)^2 + \ldots\right]$$

$$+\left[\left(\frac{T_C}{T_{in}}-1\right) - \frac{1}{2}\left(\frac{T_C}{T_{in}}-1\right) + \ldots\right] \tag{28}$$

and under these same assumptions equation (25) becomes

$$\Delta T_v = y(T_H - T_C) + (T_C - T_{in}) \tag{29}$$

Since the values of the data for T_H, T_C and T_{in} are all fairly close here, we can obtain a reasonably accurate result by using only the first term in each of the logarithmic expansions in equation (28). Inserting equation (29) into the truncated form of equation (28) gives

$$\dot{S}_p \approx \dot{m}_{in}c\left[\left(\frac{\Delta T_v}{T_C}\right) + \frac{(T_C - T_{in})^2}{T_C T_{in}}\right] \tag{30}$$

Assuming further that $p_{in} >> p_{out}$ and evaluating equation (25) for water with $c = 4186$ J/kg•K and $\rho = 998$ kg/m^3 gives $\Delta T_v = 0.239\ (p_{in})$, where ΔT_v is in K and p_{in} is in MPa. Also, the calibration of the vortex tube as a differential pressure flowmeter gave $\dot{m}_{in} = 0.051\sqrt{p_{in}}$ (correlation coefficient = 0.996), where $\dot{m}_{in}$ is in kg/s and p_{in} is in MPa. Inserting these results into equation (30) with $T_{in} = 293$ K and $T_C = 300$ K (both assumed constant here) gives

$$\dot{S}_p \approx 0.17(p_{in})^{3/2} + 0.12(p_{in})^{1/2} \tag{31}$$

where $\dot{S}_p$ is in J/(K•s) and p_{in} is in MPa. This equation predicts a cubic relationship between $\dot{S}_p$ and $p_{in}{}^{1/2}$ (or $\dot{S}_p$ and $\dot{m}_{in}$). Values of $\dot{S}_p$ calculated from equation (27) for various values of $(p_{in})^{1/2}$ are shown in Fig. 5. It is seen that there is good agreement between equation (31) (the solid line) and the data. The data do indeed seem to fall on a cubic curve independent of y. Thus, as one might expect, the losses and other irreversibilities within the vortex tube increase in a nonlinear way with increasing mass flow rate.

In conclusion, data generated with a commercial counterflow Ranque-Hilsch (vortex) tube using liquid water with inlet pressures in the 20 to 50 MPa range showed significant temperature separation of 10 to 20 C in the outlet flows. The physical properties of liquid water are considerably different from those of compressed air. Its viscosity and thermal conductivity exceed those of air by factors of fifty and twenty-five respectively. Consequently, one would expect a much higher viscous temperature rise across the swirl generator and a much smaller temperature separation effect at significantly increased inlet pressures.

The compressibility of air produces nearly a 700 percent change in its density across a vortex tube operating at normal conditions (0.8 MPa (or 100 psig) inlet pressure and atmospheric pressure at the outlet), while the compressibility of the liquid water used in this experiment produced only a 2 percent change in its density between the vortex tube inlet at 50 MPa and its outlet at atmospheric pressure. Therefore, it is clear that a vortex tube temperature separation mechanism exists which does not depend upon the compressibility of the operating fluid.

Considering the fact that these experiments were carried out with a device originally designed for use with air, it is conceivable that the Ranque-Hilsch effect in liquids could be enhanced by the development of a swirl generator designed specifically for use with liquids that would significantly reduce the viscous pressure losses.

References

1 Ranque, G. J., "Expriences sur la d tente giratoire avec productions simultan es d'un chappement d'air chaud et d'un chappement d'air froid," *J. Phys. Radium*, Paris, Vol. 4, 1933, pp. 112–114.

2 Hilsch, R., "Die Expansion von Gasen in Zentrifugalfeld als Klteproze," *Z. Naturforsch.*, Vol. 1, 1946, pp. 208–214.

3 Stephan, K., Lin, S., Durst, M., Huang, F., and Seher, D., "An Investigation of Energy Separation in a Vortex Tube," *Int. J. Heat Mass Transfer*, Vol. 26, 1983, pp. 341–348.

4 Amitani, T., Adachi, T., and Kato, T., "A Study on Temperature Separation in a Large Vortex Tube," *T. JSME*, Vol. 49, 1983, pp. 877–884.

5 Linderstrom-Lang, C. U., "The Three-Dimensional Distributions of Tangential Velocity and Total-Temperature in Vortex Tubes," *J. Fluid Mech.*, Vol. 45, 1971, pp. 161–187.

6 Kurosaka, M., Chu, J. Q., and Goodman, J. R., "Ranque-Hilsch Effect Revisited: Temperature Separation Effect Traced to Orderly Spinning Waves or 'Vortex Whistle'," paper number AIAA-82-0952, AIAA/ASME 3rd Joint Thermophysics, Fluids, Plasma and Heat Transfer Conference, June 7–11, 1982.

7 Prigogine, I., "Time, Structure, and Fluctuations," *Science*, Vol. 201, 1978, pp. 777–785.

Deposition and Resuspension of Gas-Borne Particles in Recirculating Turbulent Flows[1]

M. W. Reeks
D. Hall

Central Electricity Generating Board,
Berkeley Nuclear Laboratories, Berkeley,
Gloucestershire, GL13 9PB, U.K.

This paper proposes an integro-differential equation to describe the decay of particle gas-borne concentration in recirculating turbulent flows which are fully mixed. Its application to the decay of gas-borne concentration for particles injected into the primary circuit of an Advanced Gas Cooled Reactor is considered. The novel aspect of this work is the way the resuspension following initial deposition is modeled.

1 Introduction

An important consideration in many recirculating gas-borne particle flows is the deposition of particles at surfaces exposed to the flow. Of particular concern to the present authors is the accidental release of radioactive particulate into the coolant flow of an Advanced Gas Cooled Reactor (AGR). The retention of particulate by the reactor circuit reduces the level of gas-borne particulate and thus limits the potential release of radioactivity to the atmosphere. The circuit retention is controlled by two processes:

(*a*) initial deposition consisting of an arrival rate to the surface modified by a fraction adhering due to impact adhesion (particle bouncing),

(*b*) resuspension i.e., subsequent removal from the surface by local turbulence at the surface (turbulent bursting) after times greater than the timescale of the turbulence.

This paper proposes an integro-differential equation to describe the decay of particle gas-borne concentration in recirculating turbulent flows which are fully mixed. Its application to the decay in gas-borne concentration of particles injected into the primary circuit of an AGR is then considered.

The novel aspect of this work is the way the resuspension following initial deposition is modeled. It is based upon a statistical model recently reported which recognizes that resuspension from surfaces can be divided into two regimes, initial resuspension and longer term resuspension.

2 The Reeks, Reed and Hall Resuspension Model—A Brief Summary

This new approach to resuspension [1] illustrates a close analogy of particle motion in a turbulent flow with the behavior of thermodynamic systems [2],—in particular with the desorption of molecules from a surface, and with the escape of Brownian particles from a potential well.

The model for resuspension is based upon the view that an adhering particle and its substrate are deformed elastically by their surface adhesive forces (see Fig. 1). In static equilibrium (no external forces or flow) there is a balance between the adhesive force and an elastic restoring force. However, when a particle is exposed to a turbulent flow, there is a transfer of turbulent energy to the particle, which causes the particle and substrate to deform continually about their static equilibrium configuration (changing the area of contact). Particles in contact with the substrate are confined to motion within a surface adhesive potential well derived from the dependence of adhesive and elastic restoring forces upon particle-substrate deformation (see Fig. 2) i.e., absence of slip or rolling.

In this approach a particle is released from a substrate (resuspended) when it receives enough energy to escape from the adhesive potential well.

The transfer of energy takes place through the agency of fluid-induced lift forces where:

(*a*) the average component modifies the shape and height of the adhesive potential well,
and

(*b*) the random fluctuating component causes the particle and surface to deform in a random oscillatory fashion from their static equilibrium deformation (point of minimum potential, A in Fig. 2).

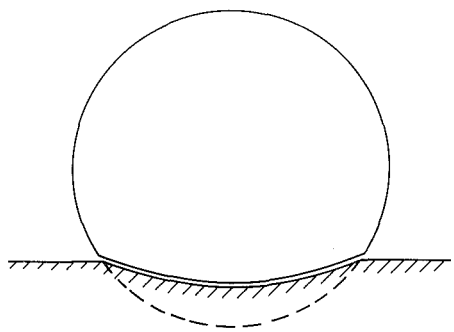

Fig. 1 The contact of an elastic sphere with an elastic flat surface (exaggerated)

[1]This paper is based on a Keynote Address presented at the ASME Gas-Solid Flows Symposium, Atlanta, Georgia, May 11–14, 1986.

Contributed by the Fluids Engineering Division for publication in the JOURNAL OF FLUIDS ENGINEERING. Manuscript received at the Fluids Engineering Division January 17, 1987.

The motion is represented by that of a very stiff lightly damped harmonic oscillator with a forcing term provided by the random fluctuations in aerodynamic lift force. Thus for a particle of mass m at time t with a deformation y about the point of mimimum potential,

$$\frac{dv}{dt}+\beta v+\omega^2 y=m^{-1}f_L(t);\ \frac{dy}{dt}=v, \tag{1}$$

where

(a) β is the fluid and mechanical damping term (particle inverse response time). The fluid damping is generally greater than its equivalent value based on Stokes drag, being dependent upon the frequency of vibration (vibrational damping). The mechanical damping corresponds to an energy loss due to elastic wave propagation in the solid substrate.

(b) ω is the natural frequency of the particle and substrate based on the harmonic approximation at the point of minimum potential. Using a model of adhesion by Johnson, Kendal and Roberts [JKR] [3], the stiffness $m\omega^2$, for zero applied load, has the form

$$m\omega^2=\frac{9}{10}\ (6\pi\Delta\gamma K^2R^2)^{1/3}, \tag{2}$$

for a particle of radius R on a surface where $\Delta\gamma$ is the adhesive surface energy per unit area and K an elastic constant given by

$$K=\frac{4}{3}\left[\frac{1-\sigma_1^2}{E_1}+\frac{1-\sigma_2^2}{E_2}\right]^{-1}, \tag{3}$$

where E_i, σ_i ($i=1$, 2) refer to the Young's modulus and Poisson's ratio of either substrate or particle materials. ω is typically $\sim 10^7$ Hz for a 10 μm diameter spherical particle on a flat surface.

(c) $f_L(t)$ is the fluctuating component (zero mean) of the aerodynamic lift force. The two most important statistical quantities associated with $f_L(t)$ in this model are its r.m.s., $<f_L^2>^{1/2}$, and its energy spectrum $E_L(\nu)$, where ν refers to the frequency of a Fourier component of $f_L(t)$.

If τ is the integral timescale of f_L, then for a stiff lightly damped oscillator

$$(\omega\tau)^2>>1;\ (\omega\tau)^2>>\beta\tau.$$

These conditions are satisfied in most practical cases of particle resuspension.

The transfer of turbulent energy eventually maintains some constant average potential energy $<$PE$>$ of particles within the surface potential well. It is considered that the balance of this energy with the height, Q, of the surface potential well is a more appropriate criterion than a force balance criterion for the initiation of resuspension. Consideration of the random motion of a particle in the well led to a simple formula for the probability per unit time of particle release from a surface (the rate constant), p, in situations where $<$PE$>/Q<<1$. This situation refers to long-term resuspension, meaning that the average lifetime of a particle on the surface is very much greater than both the timescale, τ, of the aerodynamic lift force, and the particle response time (β^{-1}). Explicitly

$$p=\frac{\omega_0}{2\pi}\exp\left[-\frac{Q}{2<\mathrm{PE}>}\right], \tag{4}$$

where ω_0 is the typical frequency of vibration.

It was noted that this formula has the same form as that for the rate constant associated with the desorption of molecules from a surface and many chemical activation processes. $<$PE$>$ was shown to depend upon β, the ratio of the r.m.s.

Nomenclature

A = region with both resuspension and deposition
a = constant for exponential decay in equation (22)
B = region with only deposition (perfect sink)
b = constant for resuspension in equation (22)
$C(t)$ = particle gas-borne concentration at time t
f_L = fluctuating aerodynamic lift force
f_R = fraction remaining after initial resuspension
E_i = Young's modulus for material i
$E_L(\nu)$ = energy spectrum of lift force
K = elastic constant defined in equation (3)
k_i = net mass transfer coefficient (including impact adhesion) for region i, $i=A$, B
n = exponent in equation (7)
$<PE>$ = average potential energy of particle in surface potential well
p = resuspension rate constant or probability per unit time of resuspension
Q = height of potential barrier
R = radius of spherical particle
r_a = adhesive radius $=\dfrac{r_1 r_2}{r_1+r_2}$
r_i = radius of curvature of adherent i at the point of contact, $i=1,2$
r_a' = normalized adhesive radius $=r_a/R$
$<r_a'>$ = adhesion reduction factor
r_0' = value of r_a' for $p=\omega_0 e^{-1}$
S_A = total area in A exposed to flow
s = time
$ds(\mathbf{x})$ = elemental area at $\mathbf{x}$
t = time
t_c = critical time for initial resuspension
t_0 = constant in equation (19)
v = particle velocity dy/dt
V = volume
$\mathbf{x}$ = position in recirculating flow
y = deformation
α = inverse time constant for exponential decay at position $\mathbf{x}$
α_i = inverse time constant for exponential decay in region i
β = damping constant
$\Delta\gamma$ = adhesive surface energy
ϵ = exponent for t in $\Lambda(t)=\xi/t^{\epsilon}$
ξ = resuspension constant for longer term resuspension in $\Lambda(t)=\xi/t^{\epsilon}$
$\Lambda(t)$ = fractional resuspension rate at time t
λ_i = surface to flow volume ratio in region i
ν = frequency
$\phi(r_a')$ = distribution density for r_a'
σ_a' = adhesion spread factor
σ_i = Poisson's ratio for material i
ω = natural frequency of surface potential well
ω_0 = typical frequency of vibration
$<>$ = ensemble average

Subscripts

A = region A
B = region B
AB = regions A and B

lift force to the force of adhesion, and $E_L(\nu)$ (especially upon its value near to the natural (resonant) frequency, ω). Estimates of p indicated that particles can be resuspended more easily from a surface than anticipated from a balance of adhesive and aerodynamic lift forces (see e.g., Cleaver and Yates [4]).

3 Resuspension Rates From Rough Surfaces

An important consideration appropriate to resuspension in recirculating turbulent flows is the form of the resuspension rate from rough surfaces exposed to the flow. Most surfaces in practice are rough i.e., they have a surface topography which can be characterized by a spread in the height and radius of curvature of surface asperities. This in turn gives rise to a spread in surface adhesive forces. The values of p in equation (4) is very sensitive to the value of the force of adhesion. Thus even when surfaces are nominally smooth the spread of adhesive forces can have a significant effect on the net resuspension from a surface.

These effects can be considered by first defining an effective adhesive radius r_a in terms of the local radii of curvature at the point of contact, and then normalizing this with respect to the radius R, of the particle (sphere). The effects upon resuspension are then considered in terms of a distribution $\phi(r_a')$ of nomalized adhesive radii r_a', where

$$r_a' = \frac{r_a}{R} . \tag{5}$$

Thus, if the average and spread of adhesive forces is proportional to particle radius R, then $\phi(r_a')$ will remain invariant to changes in R.

The fractional resuspension rate, $\Lambda(t)$, at time t, is therefore given by

$$\Lambda(t) = \int_0^\infty p(r_a')e^{-p(r_a')t}\phi(r_a')dr_a' . \tag{6}$$

The explicit dependence of p upon r_a' in equation (4) is of the form

$$p = \frac{\omega_0}{2\pi} \exp\left[-\left(\frac{r_a'}{r_0'}\right)^n\right], \tag{7}$$

where n is a positive number > 1, and r_0' a constant depending upon flow and particle size. For β independent of r_a, n has the value of two.

For $\omega_0 t >>> 1$ the values of r_a' for which the function pe^{-pt} (in the integrand of $\Lambda(t)$) is significantly different from zero is very sharply defined (see Fig. 3). The maximum value of pe^{-pt} is e^{-1}/t and occurs when

$$r_a' = r_0' \left(\ln \frac{\omega_0}{2\pi} t\right)^{\frac{1}{n}} . \tag{8}$$

Its width is of the order r_0'/n $[\ln \omega_0/2\pi\, t]^{(1-n)/n}$. Clearly the width changes on a much longer scale, $0[\ln \omega_0/2\pi\, t]^{(1-n)/n}$, than does the height, $0[t^{-1}]$. The value of Λ is thus typically

$$\Lambda \sim \frac{e^{-1}}{t} \cdot \frac{r_0'}{n} \left[\ln \frac{\omega_o}{2\pi} t\right] t^{\frac{1-n}{n}} \phi\left[r_0'\left(\ln \frac{\omega_0}{2\pi} t\right)^{\frac{1}{n}}\right]. \tag{9}$$

This suggests that the dependence of Λ on t is extremely close to t^{-1} in the limit of $\omega_0 t >>> 1$. Since $\omega_0 \gtrsim 10^7$ Hz such a dependence will exist for all practically observable times.

In view of these observations this relationship was investigated more thoroughly with a log-normal distribution for r_a'. Such distributions are typical of the distributions normally encountered with surface adhesive forces [5]. In this example therefore

$$\phi(r_a') = \frac{1}{\sqrt{2\pi} r_a' \ln\sigma_a'} \exp\left\{-\frac{1}{2(\ln\sigma_a')^2}\left[\ln\left(\frac{r_a'}{<r_a'>}\right)^2\right]\right\}. \tag{10}$$

Here $<r_a'>$ is the geometric average of r_a' and is a measure of the reduction in adhesion due to surface roughness (adhesion reduction factor). σ_a' is a measure of the spread of adhesive forces (adhesion spread factor). Typical values are $<r_a'> = .1$, and $\sigma_a' = 4$.

As an example Fig. 4 shows $\Lambda(t)$ numerically evaluated for the resuspension of 25 μm diameter glass spheres on a steel surface exposed to an air flow of 60 m s^{-1}. The calculations were performed for a log-normal distribution of normalized adhesive radii with roughness parameters $\sigma_a' = 4$, $<r_a'> = .1$.

It shows the variation of $\Lambda(t)$ naturally dividing into two regimes:

(*i*) A short "initial" resuspension (over times $\lesssim 10^{-2}$ seconds in this example) in which the resuspension rate is very high. Such resuspension is usually responsible for a significant fraction of the total resuspension from a rough surface. In the example chosen this fraction is of order 90 percent of the total resuspension.

(*ii*) A region of "longer term" resuspension in which the resuspension rate is seen to vary almost inversely with the time of exposure to the flow i.e.,

$$\Lambda(t) = \xi t^{-\epsilon}, \tag{11}$$

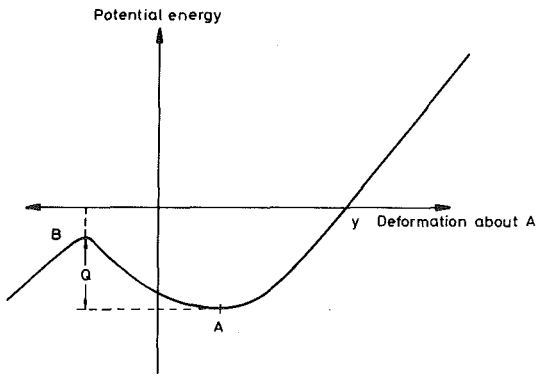

Fig. 2 The surface adhesive potential energy of a sphere on a surface with a constant applied lift force. Two positions of equilibrium. (A) stable and (B) unstable.

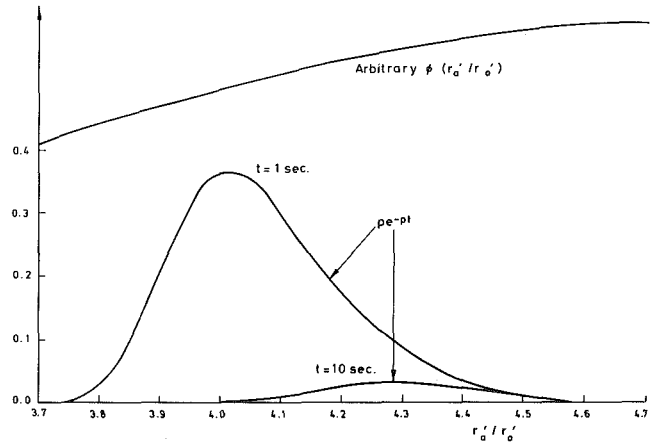

Fig. 3 The variation with (r_a'/r_0') of the terms contributing to the integrand of $\Lambda(t)$ in equation (6), using $n = 2$ for p in equation (7) with $\omega_0/2\pi = 10^7$ Hz

where ξ is a constant, and $\epsilon \simeq 1$. In this particular example $\epsilon = 1.1$. Figure 4 indicates that this inverse relationship is maintained over a wide range of exposure time (10^{-2} s $< t < 10^5$ s). This is also true of the longer term suspension rate for 50 μm particles shown also in Fig. 4. In fact, the numerical calculations show that this inverse relationship is extremely robust to wide variations in flow, particle diameter and surface roughness. It is of no significance to the inverse relationship that a log-normal distribution was chosen for the distribution of adhesive forces. [Note: For longer term resuspension in the example chosen, $\Lambda(t)$ for 50 μm particles is less than that for 25 μm particles.

4 Equation for the Decay in Concentration of Gas-Borne Particles in a Recirculating Turbulent Flow

Assume the flow is fully mixed. This means that the effects of concentration gradients along the direction of flow can be ignored. Further suppose that the surface area exposed to the flow is distributed uniformly throughout the flow continuum. To allow for the fact that there may be certain regions within this continuum which act as perfect sinks, let the surface area be composed of two parts:

(i) a region A where there is both deposition and resuspension; and

(ii) a region B where there is only deposition.

Let λ_A and λ_B be the surface area per unit volume for region A and B respectively, and k_A and k_B the associated mass-transfer coefficients for particulate deposition.

Thus in an elemental volume of flow, δV, the mass transfer of particles to the surface at time t, in a time δt, is

$$-(\lambda_A k_A + \lambda_B k_B) C(t) \delta t \delta V,$$

where $C(t)$ is the particle concentration at time t. For times $s \le t$ suppose $\Lambda(t-s)$ is the fractional resuspension rate [as defined in equation (6)] for the quantity of particles

$$C(s) \lambda_A k_A \delta s \delta V$$

deposited at time s in time δs in region A. These particles give a contribution

$$\Lambda(t-s) C(s) \lambda_A k_A \delta s \delta V$$

to the number of particles resuspended at time t.
Thus for mass conservation at time t, within δV

$$\frac{\partial C}{\partial t} = -(\lambda_A k_A + \lambda_B k_B) C(t) + \lambda_A k_A \int_0^t \Lambda(t-s) C(s) ds + S(t), \tag{12}$$

where $S(t)$ is the source strength per unit volume at time t.

In Section 3 it was demonstrated that over a wide range of surface roughness parameters, $\Lambda(t)$ can be approximated over times between 1 s and 10^5 s by

$$\Lambda(t) = \frac{\xi}{t^\epsilon}, \tag{13}$$

where ϵ is about 1.1.

For reasons already discussed we have considerable confidence in suggesting this form Λ in most practical cases. However, for the solution of equation (14) a form for Λ for all times less than t is required. In general for small times $\Lambda(t)$ does not follow the near inverse time relation of equation (13). *Define therefore a critical time, t_c, beyond which equation* (13) is valid and rewrite equation (12) as

$$\frac{\partial C}{\partial t} = -(\alpha_A + \alpha_B) C(t) + \alpha_A \int_{t-t_c}^t \Lambda(t-s) C(s) ds + \alpha_A \int_0^{t-t_c} \frac{\xi C(s)}{(t-s)^\epsilon} ds + S(t), \tag{14}$$

where $\alpha_A = \lambda_A k_A$, $\alpha_B = \lambda_B k_B$.

If t_c is sufficiently small that

$$t_c << (\alpha_A + \alpha_B)^{-1}, \tag{15}$$

then for $t - t_c < s < t$

$$C(s) \simeq C(t). \tag{16}$$

Thus equation (14) may be written as

$$\frac{\partial C}{\partial t} = -\alpha_{AB} C(t) + \alpha_A \int_0^{t-t_c} \frac{\xi C(s) ds}{(t-s)^\epsilon} + S(t), \tag{17}$$

where

$$\alpha_{AB} = \alpha_A + \alpha_B - \alpha_A \int_0^{t_c} \Lambda(s) ds = \alpha_B + \alpha_A \int_{t_c}^\infty \Lambda(s) ds = \alpha_B + f_R \alpha_A, \tag{18}$$

where f_R is the fraction remaining after a time t_c.

In short, the initial resuspension (i.e., in times less than t_c) is separated from the longer term resuspension by allowing the initial resuspension to modify the mass transfer coefficient to the surface. The contribution, seen as a reduction in the net mass transfer coefficient in equation (17), may be quite significant even though the value of t_c may be very small. From Fig. 4 it would be logical to choose $t_c = 10^{-2}$ s but the exact value is not critical so long as it is within the region where the resuspension rate is close to an inverse proportion in time, and for which $C(t - t_c) \simeq C(t)$ [equation (16)].

Equation (17) may in fact be fundamentally more correct than equation (12). $C(t)$, k_A and k_B refer to averages measured over times greater than the macro-scale of the turbulence. A measurement of the net mass transfer coefficient cannot therefore distinguish between mass transfer to the surface and resuspension. It is only the resuspension over times greater than the timescale of the turbulence that justifiably can be described in a manner different from a rate locally controlled by $C(t)$.

Equation (17) is not amenable to analytic solution. However, Please and Wilmott [6] have recently obtained an asymptotic solution to equation (12) for a kernel

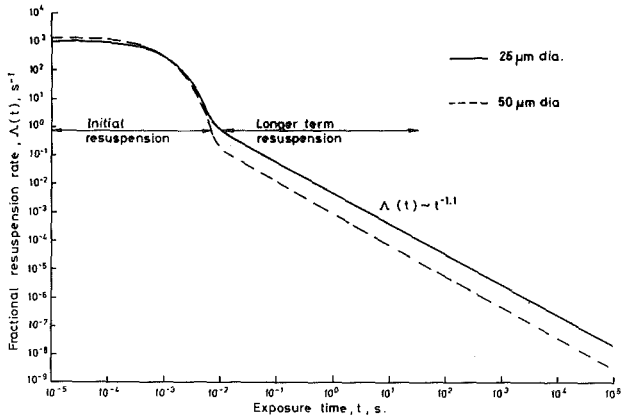

Fig. 4 The variation of the fractional resuspension rate $\Lambda(t)$ with exposure time t for glass spheres on a steel surface exposed to an air flow of 60 ms^{-1}, $\sigma_a' = 4$, $\langle r_a' \rangle \simeq 1$

$$\Lambda(t) = \frac{\xi}{(t+t_0)^{\epsilon}} . \tag{19}$$

This has identical properties to the general form of $\Lambda(t)$ for resuspension. For an instantaneous point source ($S(t)=\delta(t)$), they have shown that for $t \to \infty$:

(*a*)

$$C(t) \sim \frac{\Gamma(\epsilon)\Gamma(2-\epsilon)\sin[(\epsilon-1)\pi]\alpha_A \xi}{\pi(\epsilon-1)\left[\alpha_{AB} - \alpha_A \xi \int_{t_c}^{\infty} \frac{ds}{(s+t_0)^{\epsilon}}\right]^2} t^{-\epsilon}, \tag{20}$$

(*b*)

for $\alpha_B = 0$ and $\frac{\xi {t_0}^{1-\epsilon}}{\epsilon - 1} = 1$,

$$C(t) \sim \frac{(\epsilon-1)\sin[(\epsilon-1)\pi]}{\pi \alpha_A \xi} t^{\epsilon-2}. \tag{21}$$

These results are independent of t_0 if $t_0 << t_c$. This suggests that the asymptotic form given in equation (20) may be generally true of the asymptotic solution of equation (17) for $S(t)=\delta(t)$.

The case of $\alpha_B = 0$ is interesting in that even though resuspension and deposition occur together throughout the flow, equilibrium is never achieved. It is, as one might expect, a consequence of a distribution of adhesive forces. A particle resuspended is continually returned to the surface until it is located at a site where the adhesive force is large enough to bind it permanently to the surface. Thus, given sufficient time, the gas-borne concentration will decay eventually to zero. It has been demonstrated that it does so in a manner which is proportional to $t^{\epsilon-2}$ with ϵ close to unity. Significantly, both the resuspension rate and the decay in gas-borne concentration behave asymptotically in time in a similar manner.

5 Comparison With Measured Gas-Borne Concentration of Particles Injected Into the Coolant of an Advanced Gas Cooled Reactor (AGR)

The CO_2 coolant of an AGR is a highly turbulent recirculating flow (Reynolds numbers $\sim 10^5$). Particles have recently been injected into one of these reactors at full flow and measurements made of the decay in time of the particle gas-borne concentration.

The full details of this experiment have been described elsewhere [7]. The injected particles (2 μm, 5 μm and 17 μm in diameter) were labelled with radioactivity for identification. In observing the decay in gas-borne particulate (activity) concentration, (following an injection time, generally of one minute) measurements were made of sampled activity over a period of 1–200 min from the start of injection. However, for the 2 and 5 μm particles, only over a period of up to 1000 sec from injection was the activity concentration significantly above background particulate activity. For the 17 μm injected particles at full flow, an increase in concentration was observed 3000 sec after injection. Beyond this time use of the model equation (17) as it stands, is inappropriate. The increase of 17 μm particle concentration is attributed to flow perturbations. Sensitivity of resuspension to flow at low concentrations in fact means that very small changes in flow can affect the resuspension rate, and hence the gas-borne concentration of the 17 μm particles. This sensitivity of gas-borne concentration to a single flow increase will be more noticeable as time progresses: while the gas-borne concentration decreases with time, the amount of material available for resuspension remains little changed.

In view of previous comments, we are confident, even in a heterogeneous reactor, where there may be large spatial variations in flow and surface adhesion, that:

(*a*) the fractional resuspension rate over the duration of the measurements will vary almost inversely as the time that a particle is in contact with the surface;

(*b*) the decay in concentration as $t \to \infty$ will vary as $t^{-\epsilon}$ (see equation (20)) with ϵ close to unity.

Table 1 Values of a and b in equation (22) based on Least Squares Fit of Sampled Activity in AGR Particle Injection Experiments

Particle diameter, μm	ϵ	a, s^{-1}	b, $s^{\epsilon-2}$	Best fit, i.e., minimum mean sq. deviation
17	1.10	$5.96.10^{-3}$	$1.52.10^{-4}$	.175
	1.07	$6.52.10^{-3}$	$1.75.10^{-4}$	.105
	1.05	$6.82.10^{-3}$	$1.85.10^{-4}$	.08
	1.03	$7.00.10^{-3}$	$2.05.10^{-4}$	.06
	1.01	$7.41.10^{-3}$	$2.09.10^{-4}$	.05
5	1.1	$3.5.10^{-2}$	$1.38.10^{-3}$	.44
	1.05	$4.14.10^{-2}$	$1.44.10^{-3}$	.52
	1.01	$5.06.10^{-2}$	$1.72.10^{-3}$	.82
2	1.1	$3.47.10^{-2}$	$1.64.10^{-3}$	.102
	1.07	$4.05.10^{-2}$	$1.74.10^{-3}$	.15
	1.05	$4.03.10^{-2}$	$2.00.10^{-3}$	.18
	1.03	$4.28.10^{-2}$	$2.00.10^{-3}$	.18
	1.01	$4.6.10^{-2}$	$2.3.10^{-3}$	.24

It can be assumed therefore that the concentration $C(t)$ at time t is a solution of the equation

$$\frac{\partial C}{\partial t} = -aC(t) + b\int_0^{t-t_c} \frac{C(s)ds}{(t-s)^{\epsilon}} , \tag{22}$$

where a and b are constants and t_c is taken as one second. In this analysis a range of values of ϵ between 1.01 and 1.1 has been chosen (see Table 1). For each value of ϵ the solution of this equation can be fitted to the experimentally observed values of sampled activity to obtain best fit values for a and b for each of the three sizes of particles injected in the experiment.

The constants a and b, for each value of ϵ, are constants associated with the entire reactor circuit. If the reactor circuit were homogeneous with regard to both lift force and surface roughness a and b would have the same meaning as α_{AB} and $\alpha_A \xi$ implied in equation (17).

In general a and b represent spatially averaged quantities, taking into account variations in surface adhesion (σ_a' and $<r_a'>$) and flow throughout the entire reactor circuit. Thus if $\alpha(\mathbf{x})$ is the decay constant for deposition to an elemental surface at a position $\mathbf{x}$, and $f_R(\mathbf{x})$ the corresponding fraction remaining after initial resuspension, a and b are specifically

$$a = <f_R \alpha>_A + \alpha_B, \tag{23}$$

and

$$b = <\alpha \xi>_A . \tag{24}$$

where $<\ >$ denotes a spatial average. Thus for example

$$<f_R \alpha>_A = \frac{1}{S_A}\int_A f_R(\mathbf{x}, \ldots .)\alpha(\mathbf{x}, \ldots .)ds(\mathbf{x}), \tag{25}$$

where $ds(\mathbf{x})$ represents an elemental area at $\mathbf{x}$, forming part of the total surface area S_A in region A that is exposed to the flow. A similar expression exists for $<\alpha\xi>_A$. $(\mathbf{x}, \ldots .)$ denotes a dependence on several parameters which in turn are unspecified functions of $\mathbf{x}$ (most probably forming an infinite set of finite measure). It is likely that the most significant variations in f_R and α will be derived from variations in flow and surface roughness.

Equation (22) was solved numerically using an implicit technique in which a linear variation in concentration is assumed between time steps. Allowance for incomplete mixing during the initial stages of the injection have been made in the manner adopted by Wells et al., [7] using the same mixing curve. This accounts for the peak in concentration observed in Fig. 5.

Over the initial sampling time during the decay there was a significant variation in gas-borne concentration. The time integrated concentration was calculated using the same sampling times as in the injection experiment. These values were then compared with the experimental values corrected for background. By varying a and b, a least squares fit was performed based on the log of the concentration. The best fit values to the experimental results are displayed in Figs. 5–7.

On the basis of these calculations $\epsilon = 1.01$ would appear to give the best fit to 17 μm data at full flow and $\epsilon = 1.1$ the best fit for the 2 μm and 5 μm. However, it is believed that there is nothing statistically significant in the difference between these values of ϵ. No estimate of the errors in the experimental data points was given so equal weight has been attributed to all points in the least squares fit. It is more reasonable to suppose that experimentally the data are not sufficiently accurate to distinguish between any of the values of ϵ chosen in the data fit. However, values of ϵ significantly outside this range give unacceptably poor fits.

For $\epsilon = 1.1$, the corresponding fully mixed decay curves of gas-borne concentration for the 2 μm injected particles is shown in Fig. 8. Also shown for comparison is the decay arising from deposition and initial resuspension alone (i.e., no longer term resuspension). Of the two decays, that based on the integro-differential equation (with longer term resuspension) is clearly much more representative of the observed behavior. For completeness the asymptotic behavior given by equation (22) is also indicated.

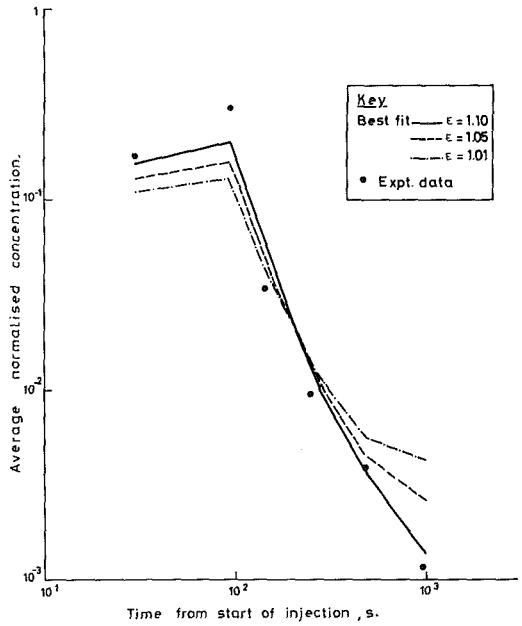

Fig. 5 The injection experiment results for 2μm iron oxide particles at full reactor flow

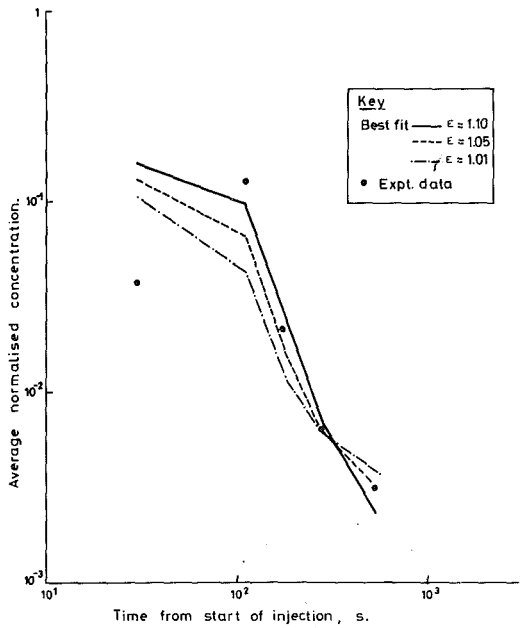

Fig. 6 The injection experiment results for 5μm iron oxide particles at full reactor flow

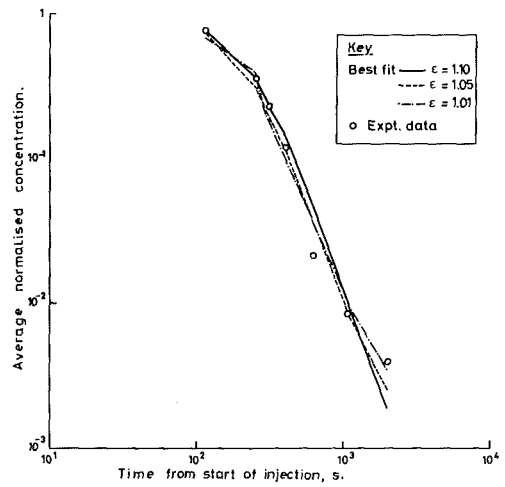

Fig. 7 The injection experiment results for 17μm aloxite particles at full reactor flow

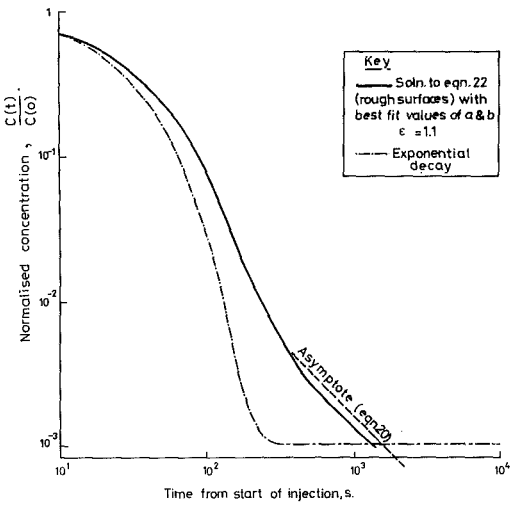

Fig. 8 Fully mixed decay curves for 2μm iron oxide particles at full reactor flow

6 Conclusions

The decay in gas-borne concentration of particles in a recirculating turbulent flow as observed e.g., in a Civil Advanced Gas-Cooled Reactor, is controlled by two processes:

—Initial decay (exponential) in which the mass transfer to surfaces is modified by initial resuspension (particles resuspended from a surface for up to one second exposure to the flow).
—Long term decay which varies asymptotically almost inversely with the decay time. This behavior is controlled by longer term resuspension (particles resuspended from a surface after being exposed to the flow for times between one second and the measured time). Such behavior is evidence for resuspension from a wide range of surface adhesion sites. For steady flows there is no equilibrium level of gas-borne concentration.

The observed decay is succesfully described by a Volterra Integro-differential equation in which:

(*a*) the effect of the initial resuspension is modeled by a reduced mass transfer coefficient;

(*b*) the effect on the longer term resuspension is modeled by an integral containing the history of the gas-borne concentration. The kernel of this integral is represented by a fractional resuspension rate varying almost inversely with time of exposure.

It is believed that the integro-differential equation used here to model the decay in gas-borne concentration is of general applicability. When used in conjunction with the resuspension model previously described [1] it will form an important basis for future predictions in recirculating flows.

Acknowledgment

We wish to thank Dr. Colin Please and Paul Wilmott of the University of Oxford, for the analysis they have performed on the integro-differential equation and for their assistance in its numerical solution. We are also grateful to Dr. Sean McKee, co-ordinator for UCINA, for initiating this co-operation. This work is published by permission of the Central Electricity Generating Board.

References

1 Reeks, M. W., Reed, J., and Hall, D., "On the Resuspension of Small Particles by a Turbulent Flow," *J. Physics D.*, Vol. 21, 1988, pp. 574–589.

2 Reeks, M. W., "On the Relationship between Brownian Motion and the Statistical Motion of Discrete Particles in a Turbulent Flow," *Symposium on Gas-Solid Flows*, ASME Meeting , New Orleans, La., 1984, pp. 9–14.

3 Johnson, K. L., Kendall, K., and Roberts, A. D., "Surface Energy and the Contact of Elastic Solids," *Proc. Roy. Soc.*, Vol. 324, 1971, pp. 301–313.

4 Cleaver, J. W., and Yates, B., "Mechanism of Detachment of Colloidal Particles from a Flat Substrate in a Turbulent Flow," *J. Colloid Interface Sci.*, Vol. 44, No. 3, 1973, pp. 464–474.

5 Böhme, G., Krupp, H., Rabenhorst, H., and Sandstede, G., "Adhesion Measurement Involving Small Particles," *Trans. Chem. Engrs.*, Vol. 40, 1962, pp. 252–259.

6 Please, C., and Wilmott, P., "The Deposition and Resuspension of Small Radioactive Particles in a Recirculating Flow in a Reactor," *Math. Eng. in Industry*, Vol. 1, No. 1, 1987, pp. 21–32.

7 Wells, A. C., Garland, J. A., and Hedgecock, J., "Techniques used in the Experimental Study of the Deposition of Aerosol Particles to Surfaces in the Coolant of a Commercial Carbon Dioxide Cooled Reactor," *Proc. of CSNI Specialist Meeting on Nuclear Aersols in Reactor Safety*, Karlsruhe, 1984, pp. 366–375.

An Experimental and Numerical Study of Flow and Convective Heat Transfer in a Freely Falling Curtain of Particles

J. Hruby
R. Steeper
G. Evans
C. Crowe

Sandia National Laboratories, Livermore, Livermore, Calif., Washington State University, Pullman, Wash.

The flow characteristics and convective heat transfer in a freely falling curtain of spherical particles with an average diameter of 650 μm has been studied experimentally and numerically. Both heated and unheated particle flows have been considered. This work is part of a larger study to determine the feasibility of using particles to directly absorb the insolation in a solar central receiver for high temperature applications. The particles of interest are Norton Master Beads™ which are primarily aluminum oxide. Measurements have been made of particle velocity in heated and unheated particle flows, and particle temperature and air temperature in heated particle flows. Comparison of the measurements with calculations has been made for two particle mass flow rates at room temperature and at two initial elevated particle temperatures. Excellent agreement between numerical and experimental results is obtained for particle velocity in the unheated flow. For the heated particles, both data and predictions show the same trends with regard to particle velocity, particle temperature, and air temperature. However, the calculations of these quantities overpredict the data. The results suggest that the drag coefficient in flows where the particles are hot compared to the air is larger than predicted using conventional methods to account for nonisothermal effects. The prediction of particle temperature and air temperature attained with a drag coefficient that is larger than the standard drag coefficient agrees well with the data.

Introduction

The flow characteristics and convective heat transfer in a freely falling curtain of particles have been investigated experimentally and numerically. This work is part of a larger study to determine the feasibility of using particles as direct absorbers of the insolation in a solar central receiver.

A solar central receiver system uses mirrors to reflect and focus sunlight onto a receiver located on top of a tower. By redirecting the sunlight in this manner, the solar flux at the receiver surface can be equivalent to hundreds of suns. A working medium heated in the receiver can be used to produce electricity, or incorporated into products as process heat. Currently, the working media in solar central receivers are gases or liquids which flow through tubes heated by the solar radiation. An example of such a system is the water/steam central receiver system located near Barstow, California, which produces electrical energy (Radosevich, 1985). Other common working fluids include molten salts, molten metals, and air.

The concept of interest here, termed the solid particle receiver, employs sand-size refractory particles which free-fall in a solar receiver and directly absorb the solar insolation (Martin and Vitko, 1982 and Hruby, 1986b). A conceptual design of a solid particle receiver is shown in Fig. 1. The solid particle receiver is being evaluated for high temperature (greater than 550°C) applications of solar energy. The advantages of a solid particle receiver over traditional fluid-in-tube receivers are: (1) the particles can directly absorb solar radiation eliminating thermal fatigue limitations on tube materials, and (2) the particles have high volumetric heat capacities and maintain their integrity at high temperatures. These advantages, coupled with the possibility that the particles can serve as the storage medium, could enable the solid particle receiver to be a cost effective means of high temperature solar energy utilization. High temperatures are attractive for fuels and chemicals production, industrial process heat applications, and Brayton cycle electricity generation.

In order to evaluate the performance of solid particles as the working media in a central receiver system, the behavior of freely falling particle curtains must be understood. The air-particle flow is expected to be dilute in the receiver. Dilute flow implies that the particle velocity is controlled by the aerodynamic drag and the gravitational force, not by particle-particle collisions. This report presents experimental data and

Contributed by the Fluids Engineering Division for publication in the JOURNAL OF FLUIDS ENGINEERING. Manuscript received by the Fluids Engineering Division January 28, 1987.

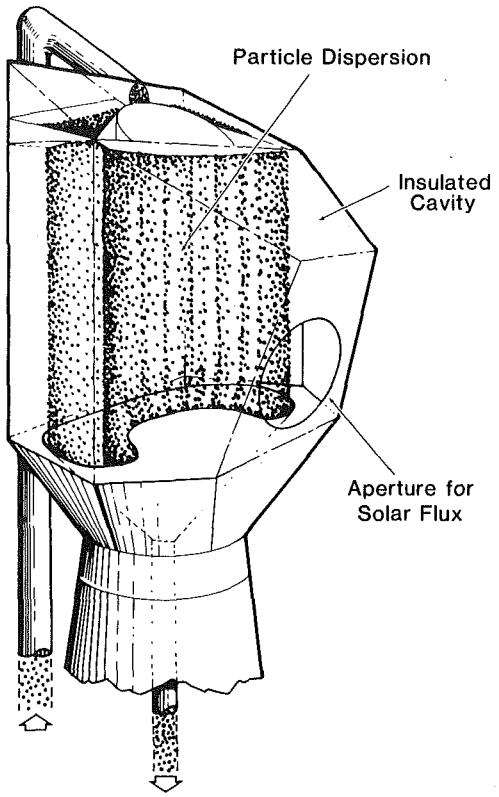

Fig. 1 Conceptual design of a solid particle central receiver

numerical predictions of the aerodynamic and thermal behavior of heated and unheated particles freely falling in initially quiescent air at room temperature. Other experimental studies of dilute freely falling particle curtains for the solid particle receiver project include the development of a particle velocity measurement system (Hruby and Burolla, 1984) and an experiment in which the particles were heated with a radiant flux (Burolla, Hruby, and Steele, 1984). Numerical work has focused on developing a model of a solid particle solar central receiver including radiative transfer within the particle cloud (Houf and Greif, 1985), and including the two phase flow and heat transfer of air and particles within the cavity receiver (Evans et al., 1986a). This model also accounts for convection and radiation from the walls of the cavity.

The numerical and experimental work performed previously has demonstrated the importance of two-way coupling between the particles and the air. Both measured and predicted velocities in the curtain were higher than the velocity of an isolated sphere in free-fall. The higher particle velocity is the result of entrainment of the surrounding air by the particle curtain, and can only be predicted with two-dimensional modeling and momentum coupling between the air and particle phase (Evans et al., 1986b). The previous work has also shown that coupling between momentum and energy is necessary for correct prediction of particle temperature. Momentum and energy coupling is important because the particle-air heat transfer can influence both particle velocity and particle temperature. The present experiment was designed to study particle velocity in both heated and unheated particle curtains, as well as particle temperature and air temperature in heated flows. The influence of initial particle temperature and mass flow rate was investigated.

Nomenclature

C_D = drag coefficient
F_p^x = drag force exerted on a single particle in the x-direction, N
$\dot{N}$ = particle number flow rate
Nu = Nusselt number $= hd_p/k$
P = pressure, N/m^2
Pr = Prandtl number
Q_p = heat transfer from a particle to air $=$ $\mathrm{Nu}k_f\,\pi d_p(T-T_p)$, W
Re = particle Reynolds number $= \rho d_p\,|\mathbf{u}_p-\mathbf{u}|/\mu$
$S_p^{x,y}$ = gas x, y momentum equation source term due to particles, N
S_p^T = gas energy equation source term due to particles, kg•K/s
T = temperature, K
T_g^* = dimensionless gas temperature $= (T_g-T_\infty)/(T_{po}-T_\infty)$
T_p^* = dimensionless particle temperature $= (T_p-T_\infty)/(T_{po}-T_\infty)$
T_{po} = initial particle temperature, K
T_∞ = ambient temperature, K
c_p = specific heat of air, J/(kg•K)
$c_{p_{part}}$ = specific heat of particle, J/(kg•K)
d_p = particle diameter, m or μm
g = acceleration due to gravity, m/s^2
h = convective heat transfer coefficient, W/(m^2•K)
k = thermal conductivity, W/(m•K)
n = particle number density, particles/m^3
t = time, s
Δt_i = particle transit time across a computational cell along the ith trajectory, s
u = vertical velocity, m/s
v = horizontal velocity, m/s
x = vertical position coordinate, m
y = horizontal position coordinate, m
Δx = vertical grid spacing, m
Δy = horizontal grid spacing, m
ϵ = particle emissivity or turbulent dissipation, m^2/s^2
κ = turbulent kinetic energy, m^2/s^2
σ = Stefan-Boltzmann constant = 5.669 E-08 W/(m^2•K^4)
ρ = density, kg/m^3
λ = ratio of $C_D/C_{D_{\mathrm{Stokes}}} = (\nu_f/\nu)\,(1+0.15\mathrm{Re}_f^{2/3})$
μ = dynamic viscosity, kg/(m•s)
ν = kinematic viscosity, m^2/s

Subscripts

eff = effective viscosity or conductivity
f = evaluated at the film temperature
g = gas phase
i = the ith trajectory
p = particle phase
s = surface
turb = turbulent quantity
n, s, e, w = values evaluated at north, south, east, or west faces of control volume
∞ = evaluated at ambient conditions

Superscripts

i = initial particle conditions
$*$ = nondimensional quantity
x, y = x- or y-direction

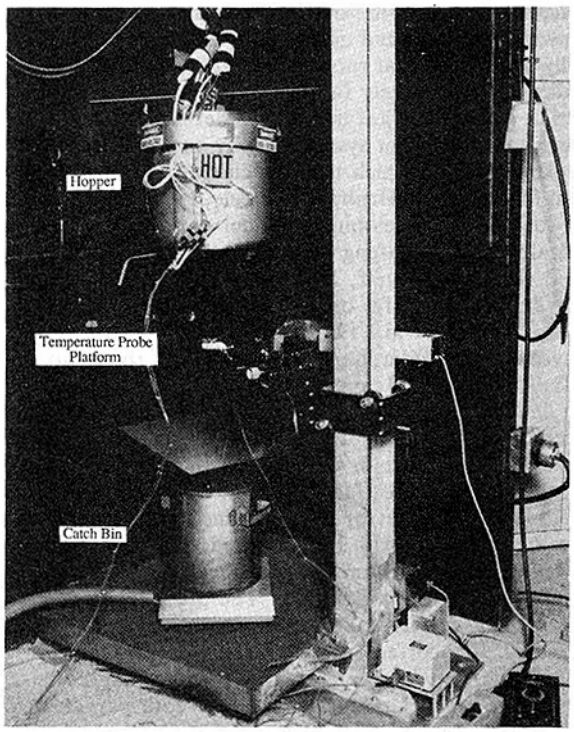

Fig. 2 Photograph of experimental apparatus identifying three assemblies: (1) hopper, (2) catch bin, and (3) temperature probe platform

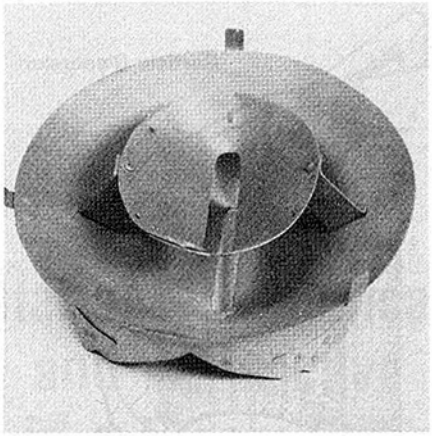

Fig. 3 Funnel-shaped inserts used in the hopper to provide a uniform temperature particle curtain at the hopper exit

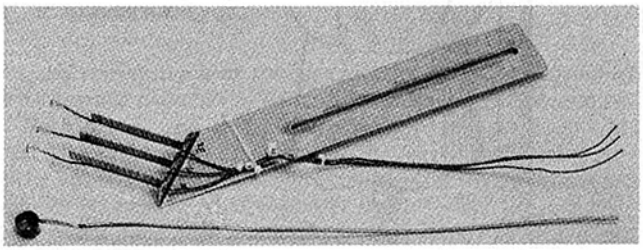

Fig. 4 Probes used to measure particle temperature and air temperature in the particle curtain

The calculations and experiments were performed using Norton Master Beads™ with an average size of 650 μm (94.6 percent between 417 and 710 μm and 5.4 percent between 250 and 417 μm). Master Beads™ are 86 percent aluminum oxide; the remaining 14 percent is comprised of near equal amounts of silica, iron oxide, and titania. Master Beads™ have been identified as particles that have high solar absorptivity, do not agglomerate at 1000°C, and have high fracture resistance (Hruby and Steele, 1986a).

Description of the Experiment

The experimental apparatus consisted of the following five assemblies: (1) hopper, (2) catch bin, (3) temperature probe platform, (4) laser Doppler velocimetry (LDV) system, and (5) data acquisition system. These assemblies are described in this section.

Hopper. The hopper (see Fig. 2) was a cylindrical, stainless steel receptacle that held 20 kg of heated Master Bead™ particles. The particles were discharged through an exit slit to form a steady, freely falling curtain. The hopper was suspended from a hoist and could be positioned from a few centimeters to 3.5 m above the catch bin assembly.

A uniform particle temperature at the hopper exit was obtained in the following manner. First, a convection oven was used to uniformly heat the particles prior to loading them in the hopper. Second, the hopper was ringed with band heaters controlled to maintain a constant interior wall temperature. Third, two funnel-shaped inserts (see Fig. 3) were stacked just above the exit slit to insure a uniform flow of particles within the hopper. It was observed that without these inserts, cooler particles from the top surface would funnel down the center and exit giving rise to a cool region within the curtain. Finally, three 1.6 mm shielded thermocouple probes were fixed vertically in the hopper with their tips 13 mm above the exit slit to record the temperature of the particles at this location.

The particle curtain was generated by a rectangular slit in the bottom plate of the hopper. The slit could be modified to provide two particle mass flow rates. For the low mass flow rate, the slit was covered with a 3.2 mm stainless steel screen. Slit dimensions in this case were 64 mm by 6.4 mm (aspect ratio of 10:1) and the particle mass flow rate was about 0.02 kg/s. For high mass flow rate, the screen was replaced with a single strand of 1.5 mm wire oriented longitudinally along the slit. With this arrangement, and slit dimensions of 51 mm by 5.1 mm, the particle mass flow rate was approximately 0.04 kg/s.

Catch Bin. The catch bin assembly, shown in Fig. 2, consisted of a funnel, an insulated receptacle, and an electronic scale platform. Falling particles were collected by the wide-mouthed funnel and channeled to the receptacle. The catch bin weight was successively measured by the scale to yield the particle mass flow rate.

Temperature Probe Platform. The probe platform, also shown in Fig. 2, was a moveable stage mounted on a vertical beam next to the particle curtain. It supported the temperature probes and could be positioned at any elevation from the hopper to the catch bin.

Two types of temperature probes, shown in Fig. 4, were used depending upon whether the particle temperature or air temperature was being measured. For measurement of particle temperature, a sampling cup consisting of a small, stainless steel foil cup fitted with a bare type K thermocouple junction was constructed. A hole was drilled in the bottom to allow a steady flow of particles past the junction when the cup was placed in the particle curtain. Several sizes and shapes were tried, the final choice being a short cylinder 10 mm high by 28 mm in diameter with a 3 mm hole in the bottom. Disturbance of the particle curtain by the sampling cup was small as shown in Fig. 5.

Air temperature was measured with a rake consisting of three bare type K thermocouples. The junction and last 7 mm of lead wire of each thermocouple were bent at right angles. When positioned in the curtain with the right angle section parallel to the flow and the junction downstream (see Fig. 6),

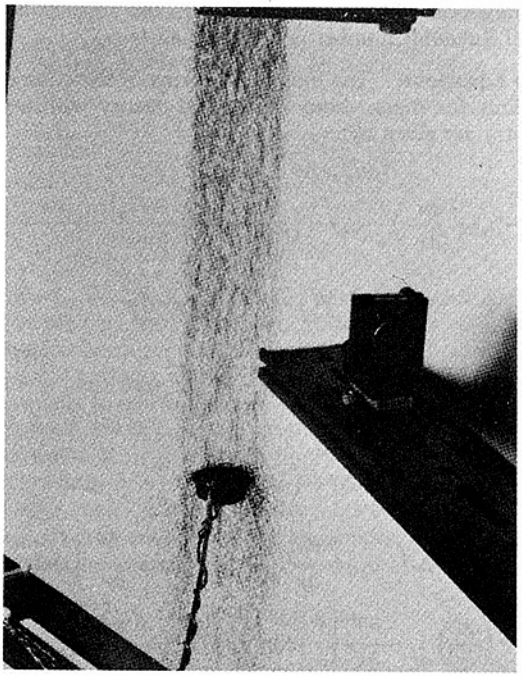

Fig. 5 Particle temperature sampling cup in the particle curtain during data collection

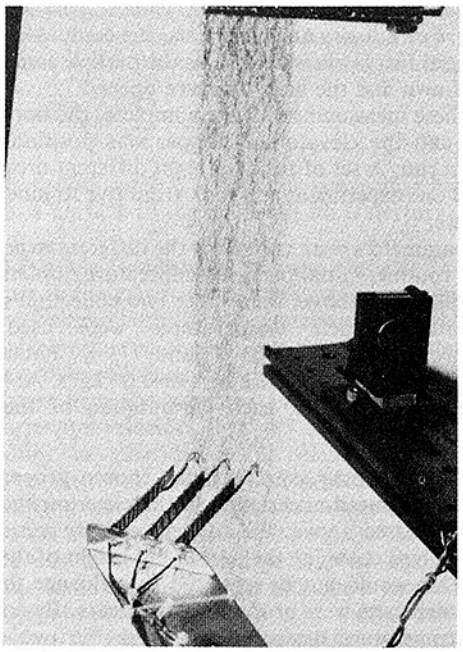

Fig. 6 Air temperature rake in the particle curtain during data collection

the thermocouples were shielded from contact with falling particles and so measured air temperatures. The three junctions were spaced 18 mm apart. The measurement of air temperature with thermocouple probes turned downstream has been performed successfully by others (Brewster and Seader, 1984).

A HeNe laser mounted on the elevator stage was used for visually positioning the stage with respect to reference marks on the wall. A linear position transducer was attached to the elevator to provide an accurate position measurement for the data acquisition system.

LDV System. Vertical particle velocities were measured with a TSI laser Doppler velocimetry system mounted on a fixed table. The system used a Lexel 4W argon ion laser tuned to 514.4 nm with optical components configured in a backscatter mode. The final lens had a focal length of 2.2 m allowing sufficient removal of the system from the hot particle curtain. This application of LDV was unconventional because of the large particle sizes, and attention to the diameter-to-fringe spacing ratio was required. A detailed discussion of the LDV system can be found in Hruby and Burolla (1984).

Data Acquisition System. The data required from this experiment were particle temperature, air temperature, particle velocity, and spread of the particle curtain, all as functions of fall height (the distance from the hopper discharge slit). A Hewlett Packard 9816 computer, 3497A scanner, and 3456A digital voltmeter were used to acquire most of this information. Data collected with the computer system included weights from the scale, voltages from the thermocouples, frequencies from the LDV counter, voltages from the position transducer, and time from the HP 9816 internal clock.

Particle curtain dimensions were acquired by taking still photographs of a roughly eight inch square region of the falling curtain at various drop heights. Both front and edge views of the curtain falling at high and low mass flow rates were filmed with the particles at room temperature (particle temperature was not expected to affect spread). Width and depth measurements were scaled from the photographs to give approximate spread-versus-fall height data.

Experimental Procedure

Preparation. Master Bead™ particles were heated in a convection oven at the selected temperature for a minimum of five hours prior to running an experiment. The hopper was preheated for a minimum of one hour. The hopper temperature was set slightly cooler than the temperature of the convection oven to compensate for heat loss in transferrring particles from the oven to the hopper. After the hopper was filled with particles and positioned, data collection began.

Data Collection. Experiments were run using one of two routines. For the first routine, the hopper was fixed at the top of its travel, about 3.5 m above the catch bin. The elevator stage with temperature probes was moved from top to bottom to sample at eight selected drop heights. Particle temperatures and air temperatures were measured using this routine.

Because the particle velocity measurement (LDV) system could not be traversed vertically, the second routine required moving the hopper rather than the elevator to acquire particle velocity as a function of height. For each run, the hopper was positioned to give the desired drop height between the hopper and the fixed position of the LDV laser. The temperature probe platform was also fixed at the LDV height, and a repeat set of particle temperature data was gathered along with velocity values.

The step-by-step procedure of the two routines was similar. First, the hopper and elevator were positioned. The hopper door was opened and the particle sampling cup was inserted and held centered in the particle curtain. About ten seconds was allowed for equilibration of the curtain and the various thermocouples; then the computer sampling program was triggered. Data from the digital scale, position transducer, clock, plus hopper slit and sampling cup thermocouples were collected in about two seconds. Eight values from each thermocouple were taken and averages and standard deviations were calculated.

Depending on the routine, either air temperature or particle velocity was measured next. For air temperatures, the thermocouple rake was inserted immediately after withdrawing the sampling cup. While the rake was held centered in the cur-

tain, the computer collected eight values from each thermocouple. For velocity measurements, the computer collected and averaged forty values as soon as the particle sampling cup was withdrawn and the laser aperture opened.

When these measurements were complete, the hopper door was shut and the elevator or hopper was positioned for a subsequent run. A set of runs for eight different drop heights comprised one experiment and took from five to nine minutes to complete.

Three parameters were varied for the different experiments: collection routine, initial particle temperature, and mass flow rate. As discussed above, there were two collection routines. Three initial particle temperatures were used: room temperature (isothermal), 603 K, and 773 K. Finally, mass flow rate was set at either 0.02 kg/s or 0.04 kg/s. At least two experiments were run at each permutation of these three parameters.

Uncertainty. Some aspects of the chosen procedure and apparatus introduced uncertainty in the experimental results. First, as discussed above, the particle velocity measurement routine involved changing the overall fall height of the particle curtain. This would not be expected to influence the results unless disturbances were propagated upstream. By comparing particle temperature measurements from the two different routines, it was shown that, in fact, altering the downstream conditions made no difference. Therefore, the only important length was the distance between the height of the hopper door and the elevation where the measurements were made; total fall heights and conditions below the measurement location were not important.

Another source of uncertainty with respect to particle temperature was the use of the particle sampling cup due to its thermal mass and possible flow disturbance. Thermal mass effects were shown to be negligible by good agreement of hopper exit temperatures with sampling cup temperatures taken just below the exit. Since the sampling cup disturbed only the downstream flow, this effect was negligible for the reasons discussed above.

Numerical Analysis

A model of dilute gas-particle flows with heat and mass transfer has been developed by Crowe et al. (1977). The model (PSI-Cell, i.e., Particle Source in Cell) includes two-way mass, momentum, and thermal coupling between the phases and has been applied to simulations of spray drying (Crowe, 1980), electrostatic precipitators (Eschbach and Stock, 1979), cyclone separators (Crow and Pratt, 1974), and combustion (El-Bainhawy and Whitelaw, 1980). The PSI-Cell code was modified for the present study by including buoyancy in the air and temperature dependent properties of the air and the particles. A single particle radiation model was also included in the particle energy equation. Briefly, the PSI-Cell code consists of a steady, two-dimensional planar or axisymmetric, elliptic, Eulerian description of the gas flow field coupled with a Lagrangian description of the particle flow field. The gas flow field is determined using TEACHT (Gosman and Pun, 1973), which solves the conservation equations on staggered control volumes with the pressure, density, and temperature evaluated at control volume centers and the velocities evaluated at the control volume faces. A two equation (κ-ϵ) model of turbulence is included with constants established for a forced flow (Launder and Spalding, 1972). Convection and diffusion of a dependent variable are combined into a single term, which when integrated over the control volume, represents the flux of that variable across the faces of the control volume. These terms are evaluated using hybrid differencing (Spalding, 1972). This differencing scheme is a combination of central differencing and upwind differencing, switching from central to upwind when the absolute value of the cell Reynolds number is greater than two.

Gas Equations. The integrated forms of the conservation equations for mass, momentum, and energy with a planar geometry are given by:

$$(\rho u)_w^e \cdot \Delta y + (\rho v)_s^n \cdot \Delta x = 0 \tag{1}$$

$$\left(\rho uu - \mu_{\text{eff}} \cdot \frac{\partial u}{\partial x}\right)_w^e \cdot \Delta y + \left(\rho vu - \mu_{\text{eff}} \cdot \frac{\partial u}{\partial y}\right)_s^n \cdot \Delta x$$

$$= (P_w - P_e) \cdot \Delta y + \rho g \cdot \Delta x \cdot \Delta y$$

$$+ \mu_{\text{eff}} \cdot \frac{\partial u}{\partial x}\bigg|_w^e \cdot \Delta y + \mu_{\text{eff}} \cdot \frac{\partial v}{\partial x}\bigg|_s^n \cdot \Delta x + S_p^x \tag{2}$$

$$\left(\rho uv - \mu_{\text{eff}} \cdot \frac{\partial v}{\partial x}\right)_w^e \cdot \Delta y + \left(\rho vv - \mu_{\text{eff}} \cdot \frac{\partial v}{\partial y}\right)_s^n \cdot \Delta x$$

$$= (P_s - P_n) \cdot \Delta x - \mu_{\text{eff}} \cdot \frac{\partial u}{\partial y}\bigg|_w^e \cdot \Delta y + \mu_{\text{eff}} \cdot \frac{\partial v}{\partial y}\bigg|_s^n \cdot \Delta x + S_p^y \tag{3}$$

$$\left[\rho uT - \left(\frac{k}{c_p}\right)_{\text{eff}} \cdot \frac{\partial T}{\partial x}\right]_w^e \cdot \Delta y + \left[\rho vT - \left(\frac{k}{c_p}\right)_{\text{eff}} \cdot \frac{\partial T}{\partial y}\right]_s^n \cdot \Delta x = S_p{}^T \tag{4}$$

where e, w, n, s indicate that the corresponding terms are to be evaluated at the east, west, north, and south faces of the control volume, and Δx and Δy are the control volume dimensions in the x and y directions, respectively. The reduction in the area of the gas phase on the control surface due to the presence of the particles is negligible. The dissipation term in the energy equation is small and has been neglected. The sign of the body force term for the x component of momentum is such that the coordinate system is oriented with the x direction aligned with gravity. The source terms, $S_p{}^x$, $S_p{}^y$, and $S_p{}^T$, refer to the momentum and energy added to the gaseous phase by the particles. Additional equations and relationships for the gas flow solution are:

(1) Pressure is determined using the SIMPLE procedure described by Patankar (1980) which is formulated to insure local continuity;

(2) Differential equations for turbulent kinetic energy, κ, and dissipation, ϵ, are solved as presented in Launder and Spalding (1972);

(3) Effective viscosity and conductivity are given by

$$\mu_{\text{eff}} = \mu + \mu_{\text{turb}} \tag{5}$$

$$\mu_{\text{turb}} = c_\mu \rho \kappa^2 / \epsilon, \quad c_\mu = 0.09 \tag{6}$$

$$\frac{k_{\text{eff}}}{c_p} = \mu_{\text{eff}}. \tag{7}$$

Equation (7) is the result of assuming that the effective Prandtl number is unity. The influence of the particles on the effective viscosity and conductivity of the air is neglected.

(4) An ideal gas equation of state is used and Sutherland law relationships for the dependence of viscosity and thermal conductivity on temperature are prescribed (White, 1974).

Particle Equations. The particle velocity is calculated assuming that the aerodynamic drag and the gravitational body force are responsible for the motion; that is, the flow is dilute. This assumption is justified based on the fact that the particle volume fraction is on the order of 10^{-2} at distances greater than 10 cm from the hopper exit slit, and the particle volume fraction decreases substantially as the particles accelerate and the curtain widens.

The particle momentum and energy equations are given by

$$\rho_p \cdot \frac{\pi d_p^3}{6} \cdot \frac{Du_p}{Dt} = 3\pi d_p \mu \lambda (u - u_p) + \rho_p \cdot \frac{\pi d_p^3}{6} \cdot g \tag{8}$$

$$\rho_p \cdot \frac{\pi d_p^3}{6} \cdot \frac{Dv_p}{Dt} = 3\pi d_p \mu \lambda (v - v_p) \tag{9}$$

$$\rho_p c_{p_{part}} \cdot \frac{\pi d_p^3}{6} \cdot \frac{DT_p}{Dt} = \mathrm{Nu} k_f \pi d_p (T - T_p) - \epsilon \sigma \pi d_p^2 (T_p^4 - T_\infty^4) \tag{10}$$

where $\lambda = C_D \mathrm{Re}/24$, and Re is the particle Reynolds number based on the free stream properties and relative velocity. The radiative loss term represents the radiative heat transfer from an isolated particle and is a conservative estimate of the radiative heat loss. The particle energy equation is based on a uniform particle temperature which is justified by the fact that the Biot number for particles in the experiment is less than 0.1 (Incropera and DeWitt, 1981).

The drag coefficient used in the model corresponds to the steady state drag coefficient for an isolated sphere. The empirical equation used is

$$C_D = \frac{24}{\mathrm{Re}_f}(1 + 0.15\mathrm{Re}_f^{2/3}) \tag{11}$$

where Re_f is the Reynolds number based on the film temperature (which is the average of the particle temperature and the bulk air temperature) and the relative velocity between the particle and the air. This equation was developed for isothermal conditions with Reynolds numbers up to 10^3 (Clift et al., 1978). The effects of pressure gradient and particle acceleration on the drag coefficient are negligible because the material density ratio between the air and particles is less than 10^{-3}. Tsuji et al. (1982) found that the drag of a particle is unaffected by neighboring particles if the particle separation distance is ten or more diameters. This condition is met over the greater portion of the particle's trajectory in the falling curtain. The effect of turbulence on drag coefficient is difficult to quantify because turbulence intensity data are unavailable. If it is assumed that the root mean square of the turbulence generated by the particle is the product of the particle diameter and vortex shedding rate, a relative turbulence intensity of 0.1 is calculated (Clift, et al., 1978). At this value and at the relative Reynolds number of the falling particles, the effect of turbulence on the particle drag coefficient is minimal. Thus the expression used for λ is equations (8) and (9) becomes

$$\lambda = (\nu_f/\nu)(1 + 0.15\mathrm{Re}_f^{2/3}) \tag{12}$$

where ν is the kinematic viscosity and the nonsubscripted value corresponds to free stream conditions.

The Ranz-Marshall correlation is used for the Nusselt number, namely (Bird et al., 1960)

$$\mathrm{Nu} = 2 + 0.6\mathrm{Re}_f^{1/2}\mathrm{Pr}_f^{1/3}. \tag{13}$$

The effect of neighboring particles on the Nusselt number is not included. There are no data available to assess this effect but it is presumed small because the effect of neighboring particles on the drag coefficient is small.

Gas Source Terms. The force in the x direction on the gas in the computational cell due to the particles is given by:

$$S_p{}^x = \sum_i F_{p,i}^x \dot{N}_i \Delta t_i \tag{14}$$

where $F_{p,i}^x = 3\pi dp\mu\lambda(u_p - u)$ is the aerodynamic force on the gas due to a particle, $\dot{N}_i$ is the particle number flow rate, and Δt_i is the particle transit time across the cell, all for the ith trajectory. The sum is applied over every trajectory passing through the computational cell for which the source term is being evaluated. A similar expression holds for the y direction source term. The energy equation source term for the gas is given by:

$$S_p{}^T = \sum_i (Q_{p,i}/c_p)\dot{N}_i \Delta t_i \tag{15}$$

where $Q_{p,i} = Nuk_f \pi d_p (T_p - T)$ is the convection heat transfer rate from a particle to the air in the ith trajectory.

Initial Particle Conditions. As the particles flowed from the hopper in the experiment, there was a component of the particle velocity in both the horizontal and vertical directions. The (small) horizontal component, which arose due to either particle-particle collisions within the hopper or the nature of the discharge from the hopper, was not measured. A range of initial horizontal velocities from 0.3 cm/s to 3.0 cm/s for the particle flow was provided in the calculation. This range in particle velocity was sufficient to reproduce the measured spread of the particle curtain (the measured spread was roughly 3 cm total at a 2 meter fall height). The particle mass flow rate was divided into ten parts, with each part representing the same fraction of the total flow rate. These parts were distinguishable only by different initial conditions on particle velocity. Each part was given an initial temperature corresponding to the measured temperature in the hopper just above the discharge slit. The particles were considered to be spherical, with a uniform size of 650 μm, density of 3130 kg/m^3, and a specific heat that was a function of temperature (1057 J/kgK at 603 K).

Calculational Procedure. The calculations were performed in a vertical cylinder or channel, depending upon whether axisymmetric or planar geometry was considered. Symmetry was assumed about the cylinder (channel) centerline with the solution obtained over half of the cylinder (channel). The cylinder (channel) was 1.5 meters in radius (half-width) and 4.0 meters high. The particles were introduced at the top of the cylinder (channel) near the centerline with initial downward velocity and temperature as given in the previous section. Although the experiment did not have confining walls, the convergence of the calculations and the specification of boundary conditions for the elliptic equations is aided by the addition of a solid boundary. The effect of the outer wall on the results for particle velocity and temperature when the radius (half-width) of the cylinder (channel) was varied from 1.0 to 2.0 meters was less than 5 percent. Slightly larger changes of approximately 10 percent occurred in the air temperature. The computational mesh consisted of 20 axial grid lines (in the direction of fall of the particles) and 16 lateral grid lines. The grid spacing was non-uniform in both directions with the smallest axial grid spacing (4 cm) at the top of the cylinder (channel) near the particle source and the smallest lateral grid spacing (2 cm) at the symmetry axis and within the particle curtain. Since the spread of the particle curtain was only a few centimeters, the computations did not yield detailed information on the distribution of the temperature and velocity of the air within the curtain nor was this information available from the results of the experiment. The sensitivity of the calculated results to the grid size was determined to be less than 1 percent for particle velocity and temperature and less than 5 percent for air temperature when the number of grid lines was doubled in both directions.

The calculations were initiated by assuming a stagnant air field. The particle trajectories were calculated and the source terms evaluated. The gas flow equations were solved incorporating the particle source terms which gave rise to motion in the gas flow field (entrainment). The particle trajectories were recalculated and the source terms re-evaluated. The gas flow field was calculated again and the cycle was continued until

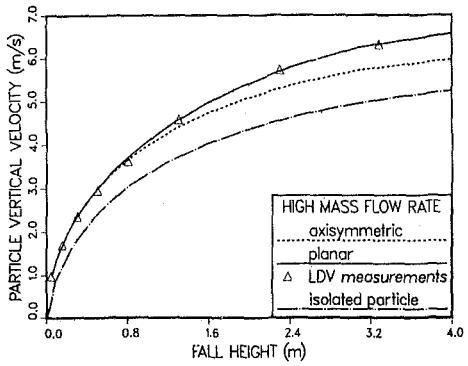

Fig. 7 Numerical prediction and experimental data of particle velocity in isothermal particle-air flow. (Uncertainty in velocity: ±0.25 m/s, Uncertainty in fall height: ±0.01 m at 20:1 odds.)

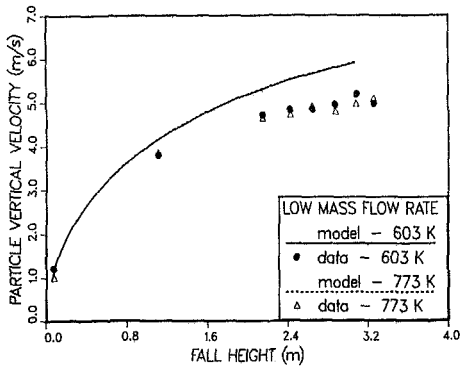

Fig. 8 Numerical prediction and experimental data of particle velocity in elevated particle temperature flow with low particle mass flow rate. The dashed and solid curves which represent the numerical results at different temperatures overlap. (Uncertainty in velocity: ±0.25 m/s, Uncertainty in fall height: ±0.01 m at 20:1 odds.)

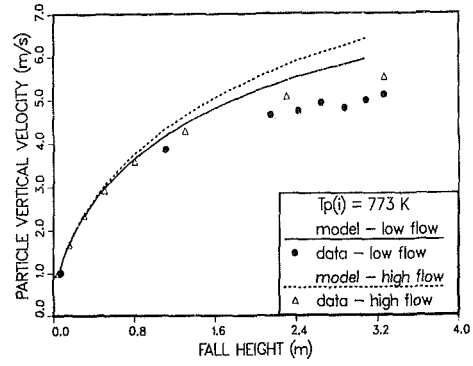

Fig. 9 Numerical prediction and experimental data of particle velocity in elevated particle temperature flow with two particle mass flow rates. (Uncertainty in velocity: ±0.25 m/s, Uncertainty in fall height: ±0.01 m at 20:1 odds)

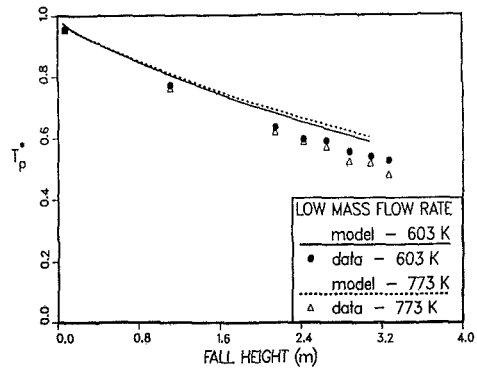

Fig. 10 Numerical prediction and experimental data of dimensionless particle temperature for low particle mass flow rate at two initial elevated particle temperatures. (Uncertainty in temperature: ±0.025 m/s, Uncertainty in fall height: ±0.01 m at 20:1 odds.)

convergence was achieved. This procedure took one to two minutes of computer time on the Cray-1.

Comparison of Experimental and Numerical Results

Unheated Flow Comparison. The geometry of the slit through which the particles exit the hopper was described earlier as being rectangular with an aspect ratio of 10:1. It was not clear that this aspect ratio was large enough to produce a purely two-dimensional, planar entrained air flow. Since the axisymmetric geometry allows for uniform air entrainment at a given distance from the axis of symmetry, both axisymmetric and planar geometries were used initially to determine which, if either, would result in acceptable agreement with particle velocity measurements made in the isothermal drop tests.

Figure 7 shows the results of the comparison between calculated and experimental vertical particle velocity as a function of distance from the hopper exit for the high mass flow rate of isothermal air-particle flow. Calculational results for both planar and axisymmetric geometries are shown. The results for the planar geometry are in excellent agreement with measurements whereas the axisymmetric results underpredict the data. Consequently, the planar geometry was used for all subsequent comparisons. Also shown in Fig. 7 is the result for a single isolated spherical particle falling in quiescent surroundings obtained by integrating equations (8)–(9) with air velocity components, u and v, set to zero. By comparison, particles in a curtain fall faster due to the entrainment of air which results in a downward component of air velocity in the curtain.

Heated Flow Comparison. Calculations of particle velocity and temperature, and air velocity and temperature have been made for the two mass flow rates and the two initial elevated particle temperatures. In this section, comparisons between calculations and experimental results are made for particle velocity, dimensionless particle temperature, and dimensionless air temperature. Although buoyancy effects for the air have been taken into account and a radiation heat loss term has been included in the particle energy equation, both of these effects are negligible for the conditions considered here.

Comparison of Particle Velocity. The calculated and measured vertical components of particle velocity as a function of distance from the hopper for the low mass flow rate and for the two initial particle temperatures (603 K and 773 K) are shown in Fig. 8. The effect of initial temperature on the predicted values is not discernible, and the effect on the measured values is small. The calculations overpredict the measured values of particle velocity.

Figure 9 shows the calculated and measured particle vertical velocity profiles for the two mass flow rates at the single initial particle temperature of 773 K. The calculations overpredict the velocity data for the high mass flow rate as well. The trend in both calculations and measurements toward higher particle velocities as the mass flow rate of particles increases is evident. The higher particle mass flow rate results in more air entrainment, increased downward air velocity in the curtain, and augmented particle fall velocities.

Comparison of Particle Temperature. For comparison

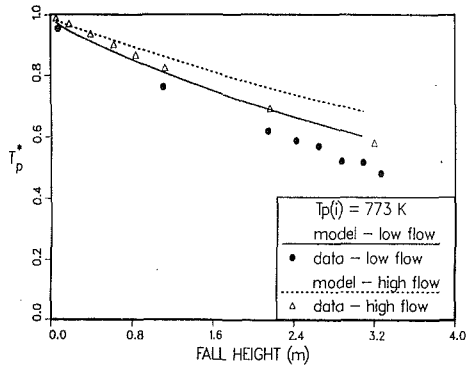

Fig. 11 Numerical prediction and experimental data of dimensionless particle temperature for two particle mass flow rates at an initial particle temperature of 773 K. (Uncertainty in temperature: ±0.025 m/s, Uncertainty in fall height: ±0.01 m at 20:1 odds.)

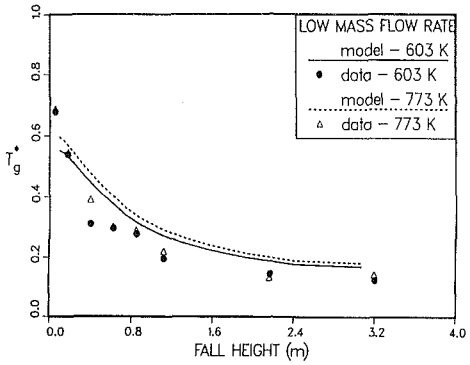

Fig. 12 Numerical prediction and experimental data of dimensionless air temperature for low particle mass flow rate at two initial elevated particle temperatures. (Uncertainty in temperature: ±0.07, Uncertainty in fall height: ±0.01 m at 20:1 odds.)

purposes, the particle temperature has been nondimensionalized: $T_p^* = (T_p - T_\infty)/(T_{po} - T_\infty)$. Dimensionless particle temperature is shown as a function of the distance from the hopper in Fig. 10 for the low mass flow rate case and for the two initial particle temperatures. The difference between the results for the two initial temperatures shown is quite small as a result of the nondimensionalization and the insignificance of radiative heat transfer. Calculations of particle temperature overpredict the measured values. This result indicates that the calculations underpredict the total heat transfer to the air.

Dimensionless particle temperature as a function of distance from the hopper for the two mass flow rates and for an initial particle temperature of 773 K is shown in Fig. 11. Both calculated and experimental results indicate that as the particle mass flow rate increases, the dimensionless particle temperature at a given fall height increases. The increase in dimensionless particle temperature at high mass flow rates is due to two factors; the increased particle concentration leads to a higher air temperature within the curtain and the increased relative particle velocity reduces the time available for heat transfer.

Comparison of Air Temperature. The measured and calculated dimensionless air temperature, $T_g^* = (T_g - T_\infty)/(T_{po} - T_\infty)$, is shown on Fig. 12 for the low mass flow rate case and for the two initial particle temperatures. The calculated air temperatures are higher than the measured values. The fact that the predicted air temperature is higher than measured does not necessarily imply that more energy was transferred to the air in the calculation; if this were true it would be inconsistent with the higher predicted than measured particle temperature. If the predicted air velocities are smaller than the experimental values, which were not measured, then the predicted air temperatures can be higher than those measured and still result in a smaller predicted than measured heat transfer to the air. As will be discussed in the next section, if the predictions were made with a particle drag coefficient that was too small then it is conceivable that predicted air velocities would be smaller than those in the experiment.

The variation of dimensionless air temperature as a function of distance from the hopper for the two mass flow rates and at the higher initial particle temperature is shown in Fig. 13. Both calculated and experimental values show an increase with increasing mass flow rate. This is expected since a higher mass flow rate of particles provides a larger source of heat to the surrounding air, and the air mass flow rate does not increase at the same rate as the particle mass flow rate.

Note that although both the particle and air temperature are decreasing as a function of distance from the hopper, it is not

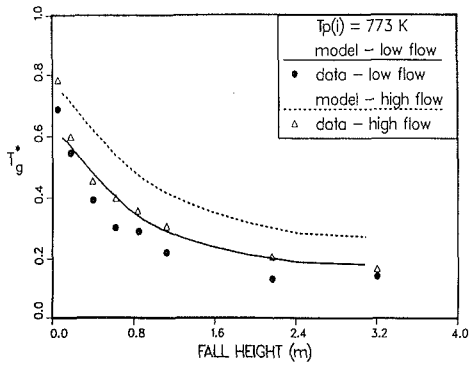

Fig. 13 Numerical prediction and experimental data of dimensionless air temperature for two particle mass flow rates at an initial particle temperature of 773 K. (Uncertainty in temperature: ±0.07 m/s, Uncertainty in fall height: ±0.01 m at 20:1 odds.)

true that the air is losing energy because a significant mass flow of air is occurring due to entrainment by the particles. For example, for the higher particle temperature and higher mass flow rate case, the downward mass flow rate of air at distances of 14, 89, and 191 cm from the hopper was calculated to be 0.054, 0.39, and 0.64 kg/s, respectively.

Drag Coefficient in Heated Flows

Because the calculations overpredict measured particle velocities in heated particle flows, the correlation used for the drag coefficient (equation (11)) needs to be examined in more detail. The calculations included the effect of hot particles by evaluating the Reynolds number of the film temperature in lieu of the bulk air temperature. This increased the calculated drag coefficient of a 650 μm particle at 773 K moving in air at 293 K with a relative velocity of 3 m/s by 70 percent from the value obtained assuming uniform air properties at 293 K. Still, the data suggest that the drag coefficient in hot particle flows is higher than predicted using the film temperature to determine the Reynolds number.

Very little information is available in the literature on the effect of surface-gas temperature difference on the particle drag coefficient. An analytic study by Kassoy et al. (1966) predicted that the drag coefficient of a particle in the Stokes flow regime would increase with increasing surface temperature and that the Nusselt number would decrease. The same trends result from the use of the film temperature to evaluate the air properties. There appears to be no analytic solution available for

temperature effects in the Reynolds number range of interest in this study ($10 < Re_f < 100$).

Some experimental studies have been reported in the Russian literature on the effect of particle surface temperature on particle drag coefficient. Babiy and Ivanova (1965) propose that the increased drag coefficient of burning particles is due solely to the increased surface temperature of the particle. They further propose that the drag coefficient should be correlated with a Reynolds number based on the surface temperature, not the average film temperature. They correlated a large volume of experimental data and proposed the following empirical relationships

$$C_D = \frac{52}{Re_s} (0 < Re_s < 50) \tag{16}$$

$$C_D = \frac{2}{Re_s^{0.2}} (Re_s > 50) \tag{17}$$

where Re_s is the Reynolds number evaluated using the kinematic viscosity of the gas at the particle surface temperature. This correlation leads to a lower drag coefficient than the one used in this study in the range $40 < Re_s < 120$. The particles falling in the curtain are in this range over the greater portion of their trajectory which leads to an even higher velocity if Babiy and Ivanova's correlation is used. Calculations were also done using Re_s instead of Re_f in the standard drag coefficient correlation given by equation (11) but the increase in drag was insufficient to account for the lower velocity observed in the experimental data.

Basina and Maksimov (1970) point out that the coal particles used in Babiy and Ivanova's correlations were not spherical and that the increased drag may partially be due to the asphericity. They carried out an experiment to measure the drag coefficient of a heated, 2.5 mm diameter spherical particle suspended in a horizontal stream of cooler air over a Reynolds number range of 1 to 150. They showed that the drag coefficient for heated particles was larger than the standard drag coefficient. The increase was as much as 45 percent for a particle at 723 K with a Reynolds number of 15, the effect decreasing with increasing Reynolds number to 26 percent at a Reynolds number of 40. This effect is attributed partially to increased viscous effects in the boundary layer as noted by Babiy and Ivanova, and partially to free convection effects. At low flow velocities they noted a vertical velocity component induced by free convection effects which probably had a significant effect on the measured drag coefficient. They point out that their data is only valid for a similar flow configuration (horizontal flow in a pipe). In the case of freely falling particles, the air velocities induced by free convection would increase the gas-particle relative velocity, and the effect of free convection on the drag coefficient would be greater.

Good agreement between the numerical and the experimental results for particle velocity in nonisothermal flows was obtained when the constant multiplying $Re^{2/3}$ in the drag coefficient of equation (11) was increased from 0.15 to 0.40, an increase of 166 percent. Because the calculated results for particle and air temperature also agreed well with the experimental results for particle and air temperature when the above change was made to the particle drag coefficient, the discrepancy between measured and predicted particle and air temperatures can be primarily associated with uncertainty in the particle drag coefficient and not the particle heat transfer correlation.

Conclusions

An experiment has been performed to determine the flow characteristics and the convective heat transfer in a curtain of freely falling particles. Measurements of particle velocity in heated and unheated flow at two mass flow rates have shown that the particles in a curtain fall faster than an isolated particle in free fall. Further, particle temperature measurements have shown that particle temperature at a given fall height is higher as the particle mass flow rate increases. Calculations using the PSI-Cell computer code, which accounts for the two-way momentum and thermal coupling between the particles and the air, are in excellent agreement with the particle velocity measurements in isothermal air-particle flow. The predictions show the same trends as the measurements for particle velocity, particle temperature, and air temperature in nonisothermal, heated particle flow. For the nonisothermal cases, these quantities are overpredicted. By using a larger drag coefficient, the predictions of particle velocity, particle temperature, and air temperature are in better agreement with experimental data. The data suggest that an increased drag coefficient should be used in flows where the particles are hot compared to the air. The convection coefficient for a single particle seems sufficient to describe the energy exchange in a dilute particle curtain when the local conditions are known.

Acknowledgment

This work was supported by the U.S. Department of Energy under contract DE-AC04-76DP00789.

References

Babiy, V. I., and Ivanova, I. P., 1965, "Aerodynamic Resistance of a Particle in a Nonisothermal Condition (in Russian)," Teploenergetika, Vol. 9, pp. 19–23.

Basina, I. P., and Maksimov, I. A., 1970, "Effect of Nonisothermicity on the Aerodynamic Drag of a Spherical Particle," *Heat Transfer-Soviet Research*, Vol. 2, No. 6, pp. 69–75.

Bird, R. B., Stewart, W. E., and Lightfoot, E. N., 1960, *Transport Phenomena*, Wiley, p. 409.

Brewster, B. S., and Seader, J. D., 1984, "Measuring Temperature in a Flowing Gas-Solids Suspension with a Thermocouple," *AIChE Journal*, Vol. 30, No. 4, pp. 676–679.

Burolla, V. P., Hruby, J. M., and Steele, B. R., 1984, "High Temperature Solar Thermal Energy Absorption with Solid Particles," *Proc. IECEC*, Vol. 3, pp. 1663–1668.

Clift, R., Grace, J. R., and Weber, M. E., 1978, *Bubbles, Drops and Particles*, Academic Press, New York.

Crowe, C. T., and Pratt, D. T., 1974, "Analysis of the Flow Field in Cyclone Separators," *Computers and Fluids*, Vol. 2, pp. 249–260.

Crowe, C. T., Sharma, M. P., and Stock, D. E., 1977, "The Particle-Source-in Cell (PSI-CELL) Model for Gas-Droplet Flows," ASME JOURNAL OF FLUIDS ENGINEERING, pp. 325–332.

Crowe, C. T., 1980, "Modeling Spray-Air Contact in Spray-Drying Systems," *Advances in Spray Drying*, Hemisphere Publishing, Chapter 3, pp. 63–99.

El-Bainhawy, V., and Whitelaw, J. H., 1980, "The Calculation of the Flow Properties of a Confined Kerosine-Spray Flame," *AIAA Journal*, Vol. 18, No. 12, pp. 1503–1510.

Eschbach, E. J., and Stock, D. E., 1979, "Optimization of Collection Efficiency by Varying Plate Spacing with an Electrostatic Precipitator," *Proceedings of the 2nd EPA Conference on Transfer and Utilization of Particulate Control Technology*, Denver.

Evans, G., Houf, W., Greif, R., and Crowe, C., 1986a, "Gas-Particle Flow Within a High Temperature Solar Central Receiver including Radiation Heat Transfer," *Journal of Solar Energy Engineering*, accepted for publication.

Evans, G., Houf, W., Greif, R., and Crowe, C., 1986b, "Numerical Modeling of a Solid Particle Solar Receiver," Sandia National Laboratories, SAND85-8249.

Gosman, A. D., and Pun, W. M., 1973, "Calculation of Recirculating Flow," Lecture Notes, Imperial College of Science and Technology, London, England.

Houf, W. G., and Grief, R., 1985, "Radiation Transfer in a Solar Absorbing Particle Laden Flow," *Radiation Heat Transfer*, ASME HTD-Vol. 43, eds. Armaly, B. F., and Emery, A. F., pp. 9–14.

Hruby, J. M., and Burolla, V. P., 1984, "Solid Particle Receiver Experiments: Velocity Measurements," Sandia National Laboratories, SAND84-8238.

Hruby, J. M., and Steele, B. R., 1986a, "A Solid Particle Central Receiver for Solar Energy," *Chemical Engineering Progress*, Vol. 82, No. 2, February, 1986.

Hruby, J. M., 1986b, "A Technical Feasibility Study of a Solid Particle Solar Central Receiver for High Temperature Applications," Sandia National Laboratories, SAND86-8211.

Incropera, F. P., and DeWitt, D. P., 1981, *Fundamentals of Heat Transfer*, Wiley, New York, p. 184.

Kassoy, D. R., Adamson, T. C., and Messiter, A. F., 1966, "Compressible Low Reynolds Number Flow Around a Sphere," *The Physics of Fluids*, Vol. 9, No. 4, pp. 671–681.

Launder, B. E., and Spalding, D. B., 1972, *Mathematical Models of Turbulence*, Academic Press.

Martin, J., and Vitko, J., 1982, "ASCUAS: A Solar Central Receiver Utilizing a Solid Thermal Carrier," Sandia National Laboratories, SAND82-8203.

Patankar, S. V., 1980, *Numerical Heat Tranfer and Fluid Flow*, McGraw-Hill.

Radosevich, L. G., 1985, "Final Report on the Experimental Test and Evaluation of the 10 MWe Solar Thermal Central Receiver Pilot Plant," Sandia National Laboratories, SAND85-8015.

Spalding, D. B., 1972, "A Novel Finite-Difference Formulation for Differential Expressions Involving Both First and Second Derivatives," *Int. J. of Numerical Methods Eng.*, Vol. 4, pp. 551–559.

Tsuji, Y., Morikwa, Y., and Terashima, K., 1982, "Fluid Dynamic Interaction Between Two Spheres," *Int. Journal of Multiphase Flow*, Vol. 8, No. 1, pp. 71–82.

Wallis, G. B., 1969, *One-Dimensional Two-Phase Flow*, McGraw-Hill.

White, F. M., 1974, *Viscous Fluid Flow*, McGraw-Hill.

Effect of Separation on Partial Cavitation[1]

C. Pellone
Research Scientist at CNRS.

A. Rowe
Research Scientist at CNRS.

Gentre de Recerches et d'Essais
de Machines, Hydrauliques de Grenoble
B.P.95 38402 St. Martin d'Hères, France

Partially cavitating flow around a hydrofoil in a confined two-dimensional flow is presented. The calculation method, based on the singularities technique combined with a minimisation method, is adapted to open configurations. With this extension, cavity wakes not necessarily merging with the upper-side of the foil can be treated. In the case of subcavitating flow, a boundary layer calculated is made, indicating a separation point downstream of which the flow becomes separated. In this area, an imaginary streamline (wake) is introduced to simulate the effect of separation. The choice of different forms of wake clearly shows the influence of wake form on the value of results. The process is extended to the case of cavitating flow for wakes developing behind the cavity. The method is applied to a test cavitating hydrofoil placed in a tunnel. Several cavity wakes progressively diverging from the foil were tested. The results obtained, compared with experimental results, show the great importance of achieving more accurate modelling of flow conditions behind cavities.

1 Introduction

Extensive literature is available dealing with the problem of modelling partially cavitating flow. However, even today, by far the greater part of this literature is based on older work carried out with analytical methods. During the sixties, various method were established [1, 2] to meet the requirements of technical developments considered at that time (for example: construction of high-speed ships or development of pumps with high rotation speed). These methods served as a basis for a wide range of subsequent studies, culminating perhaps in the work completed in 1980 by Furuya [3] who, used Tulin's single spiral vortex model in nonlinear theory to analyze partially cavitating cascade flows.

Analytical methods have a number of drawbacks: first, they are not flexible, i.e., it is difficult to adjust a given model for use in a field other than that for which it was established. Second, in nonlinear theory, which cannot reasonably be ignored today, the iterative methods proposed for solving the system of integral equations obtained through the formulation do not always give a convergent solution. This is notably the case when allowance has to be made for foil sections which do not have planar upper and lower sides, with a rounded leading edge. Finally, the extension of such methods to three-dimensional flow conditions is difficult, if not impossible, except within the restrictive framework of perturbation methods and lift line theory.

Today, analytical methods would appear to have lost even greater favor with the development of high-speed computers which can be used to take into account large matrices with a staggering reduction in calculation time. However, despite their decisive advantages, numerical models have not developed to any where near the extent of analytical models, possibly simply because the impetus given in the sixties started to fall off after 1970.

In the United States, Jiang, C. W., Leehey, P., and Golden, D. W., devised a simple model [4] applicable to the design of propellers [5] in nonsteady flow. However, the singularities are distributed over the propeller skeleton and not on the contour, and the thickness is considered in a simplified way.

In numerical analysis, the greatest efforts have perhaps been made in Japan, mainly by Yamaguchi, and Kato [6] and Ito and Nishiyama [7–9]. The Japanese models have a major drawback compared to Leehey's model: they are not well adapted to the case of foils of low relative thickness and, when subcavitating conditions develop, some of them degenerate into inoperative models (see refs. [10 and 11]).

For these reasons, it seems clear that numerical models must be developed which are not only flexible, simple and efficient, but also free from possible error when the relative foil thickness is small and when subcavitating conditions are set up.

With a view to achieving these objectives, and considering to the hypothesis of a perfect, incompressible fluid and irrotational flow, a combination of integral and minimisation methods can be used. This is the aim of the work presented in [12]. In this method, the cavity closure condition is modelled by assuming that a streamline forms a regular transition between the cavity and the upper-side of the foil. This model is referred to as a "closed model." Studies [3, 4, and 12] have shown that while this assumption is more or less acceptable in the case of short cavities, it does not hold true for longer ones. Here, the cavity and its wake are not closed in a regular fashion, and the assumption of a vanishing transition area on the upper side of the foil is not realistic.

[1]This study was co-funded by EdF (Electricité de France) under EdF agreement No. 2F0565.

Contributed by the Fluids Engineering Division for publication in the JOURNAL OF FLUIDS ENGINEERING. Manuscript received by the Fluids Engineering Division, April 30, 1986.

The present study concerns the effect of cavity wake modeling in the case of large deviations and confined flow. In order to do this, the closed model described in reference [12] is transformed into an "open model" which can be used to treat a wake behind the cavity which does not necessarily merge with the foil. The flow calculated by this procedure is fictitious and takes approximate account of the effect of separation to the rear of the cavity. The wake behind the cavity is determined on the basis of experimental results concerning the relationship Lc(K). Results of this kind were provided by Electricité de France, for a test cavitating hydrofoil placed in a confined two-dimensional flow.

The essential aim of the study is to show that in cases where an open wake is necessary, the adjustment of this wake can be rather tedious, and can be carried out only thanks to the flexibility of a numerical model. Compared to other techniques, the M.P.P.M. (minimization process panel method) has the advantage of minimizing the leak rate between control points and of not degenerating when subcavitating flow conditions are established. Moreover, it is possible to extend this method to treat three-dimensional cases. In view of the fairly localized character of the study presented, no comparison has been made with experimental results available in existing literature. Given the fact that the model allows precise adjustment of the Lc(K) law, such a comparison would be of interest only if it were to cover the shape of the pressure line, notably in the recompression zone. Such experimental results are apparently rare.

2 Theoretical Study

Initially, the cavity detachment point was displaced on the foil near the leading edge. The results of this initial calculation were inadequate for adjusting the Lc(K) curves to the experimental curves, and so a preliminary study was carried out in the case of subcavitating flow. Here, a boundary layer calculation indicates the existence of a separation point of the boundary layer on the upper-side of the foil and on the top of the tunnel. In order to represent the separation effect, the "surface-blowing" method is then used. This involves writing an "artificial" boundary condition which simulates the flow tangency condition on a displacement surface [11]. Strictly speaking, the idea of a displacement thickness becomes meaningless downstream of the separation point. However, in the study of an open cavity wake, in which the wake is generally represented by a displacement thickness, it is useful, and a priori not incoherent, to represent the separation effect by a displacement thickness. Since it is difficult to calculate a displacement thickness corresponding to the separation effect, a thickness variation law is imposed. This is adjusted so that the maximum velocity is obtained at the leading edge, equivalent to the experimental value obtained as the limit of the quantity $(1+K)^{1/2}$ when Lc tends toward zero.

In the case of cavitating flow, it is a well-known fact that the cavity detachment point is not where the pressure is minimum in subcavitating conditions. As demonstrated in § 3.2, the position of the cavity detachment point has a non-negligible effect on the value of the results obtained. Hence it is important to obtain a good approximation of the position of this point. The detachment criterion established in [13] for the supercavitating case [14] was therefore used for the present case. This detachment criterion proposed in study [13] takes into account the coupling between attached cavitation and boundary layer: it consists in connecting a cavitating potential-flow calculation and a boundary layer calculation. Among all the theoretically possible detachment points, the actual detachment point is chosen to be the one for which the calculation predicts a laminar separation just upstream the cavity. This involves displacing the detachment point along the foil near the leading edge. For each successive position, the position of the separation point is determined and compared with the position of the detachment point. The intersection with the first bisector in the plane (s separation, s detachment) gives the point.

With the position of the detachment point treated in this way and checked by comparison with experimental results, several wake configurations behind the cavity are tested. The study reveals the significant effect of wake deviation on the Lc(K) curves. The wake deviation is adjusted in order to obtain computation points in the experimental range.

2.1 Formulation of the Problem. A cartesian coordinate system (ω', X, Y) is defined on the foil with the X-axis positive from the leading edge to the trailing edge (Fig. 1). Another coordinate system $(0, x, y)$ on the top of the tunnel is such that the x-axis is positive downstream (the x-axis is parallel to the freestream velocity v0). The y-axis is deduced from the x-axis by means of a counter-clockwise rotation of $+\pi/2$. The foil is placed at an angle α with respect to the x-axis, with the leading edge at depth h. The depth of the tunnel is equal to H. It is assumed that a cavity develops near the leading edge ω',

Nomenclature

c = chord of the foil
$C_p = 2(p-p_0)/\rho\ V^2{}_0$ = pressure coefficient
Ds = displacement surface
h = submersion depth
H = tunnel height
$\bar{H} = H/c$ = nondimensional tunnel height
$K = 2(p_{CAV}-p_0)/\rho\ V^2{}_0$ = cavitation number
Lc = cavity length
$(o\ x\ y)$ = coordinate system of the tunnel
p = pressure
p_{CAV} = cavity pressure
p_0 = pressure at upstream infinity
s = curvilinear abscissa
V = modulus of vector $\mathbf{V}$
$\mathbf{V}$ = velocity
V_0 = modulus of vector $\mathbf{V}_0$
$\mathbf{V}_0$ = velocity at upstream infinity
α = angle of incidence
δ_M = gap between the foil and the streamline at point M
$\bar{\delta}_M = \delta_M/c$ = nondimensional gap
δ_t = gap between the top of the tunnel and the corresponding streamline characterizing the displacement thickness
$\bar{\delta}_t = \delta_t/c$ = displacement thickness characterizing the viscous effects in subcavitating conditions on the upper side of the foil
θ_M = fictitious displacement thickness characterizing the viscous effects in subcavitating conditions at point M downstream of the separation point
ϕ = velocity potential
$(\omega'\ X\ Y)$ = coordinate system of the foil
ρ = density of the liquid
∇ = gradient operator

beginning at a point ω and vanishing at point B′ via a transition area CB′ called the near wake. In this area, flow is mainly two-phase and unsteady. The model is made steady by representing the near wake as being limited by the fictitious streamline CB′. Downstream of point B′, it is assumed that there is a streamline B′A′, whose geometry is defined by all the points M′, such that $\mathbf{MM}' = \delta_M \mathbf{n}$. M travels along the curve BA of the foil, while δ_M is a positive or zero distance representing the gap between the cavity wake and the foil; $\mathbf{n}$ is the outward unit vector normal to the foil. When δ_B has a value other than zero, the model is referred to as an "open model" and B′A′ is the far wake boundary. If the value of δ_B is zero, then the model is "closed."

With a cavity length of fixed value, Lc, the pressure, p_{CAV}, within the cavity is an unknown. The assumptions made are those of a perfect, incompressible and irrotational fluid in a confined flow. The tunnel effect is taken into account by means of the images method. Velocity $\mathbf{V}$ due to the existence of the foil is derived from a harmonic potential ($\nabla\phi = 0$), such that:

$$\phi = V_0 x + \varphi;\ \mathbf{V} = \mathbf{V}_0 + \mathbf{v};\ \mathbf{v} = \nabla\varphi$$

where ϕ and $\mathbf{V}$ are the absolute potential and velocity fields, φ and $\mathbf{v}$ the perturbation potential and velocity. The boundary conditions are expressed as follows:

- Constant pressure on the cavity (ωC), expressed in terms of a tangential velocity condition:

$$M\epsilon(\omega C)\ \mathbf{v}\cdot\mathbf{t} = -V_0(1+K)^{1/2} - \mathbf{V}_0\cdot\mathbf{t} \qquad (1)$$

  In relation (1), $\mathbf{t}$ is a unit vector tangential to the contour, and K is the cavitation number: $K = 2(p_{CAV} - p_0)/\rho\ \mathbf{V}^2{}_0$, where p_0 is the pressure at upstream infinity and ρ the density of the liquid.
- Tangency condition on the wetted surface (A′B′) $\cup$ (ωA):

$$\mathbf{v}\cdot\mathbf{n} = -\mathbf{V}_0\cdot\mathbf{n} \qquad (2)$$

- A normal velocity behaviour relation is imposed on the transition surface (CB′) (near wake):

$$\mathbf{v}\cdot\mathbf{n} = f(s) \qquad (3)$$

where f represents a function of the curvilinear abscissa, which will be dealt with below.

Formulated in this way, the problem is an external one with boundary conditions of the mixed Neumann and Fourier type [15]. A general solution can be provided for the velocity field of this boundary problem, based on surface source distribution and doublicity distribution (normal doublets μ) on the contour A′ω′A, having respective densities, β and $\nu = d\mu/ds$ [16]. Boundary conditions (1), (2) and (3) result in the conventional integral equations:

$$P[C_M/2\text{-}f[-iC_M{}'k(z,z') + i\bar{C}_M{}'k(z,\bar{z}')]ds_M{}'] = g_M - V_0\ P(e^{i\alpha M}) \qquad (4)$$

z designates the complex coordinate of point M, z' the complex coordinate of point M'.

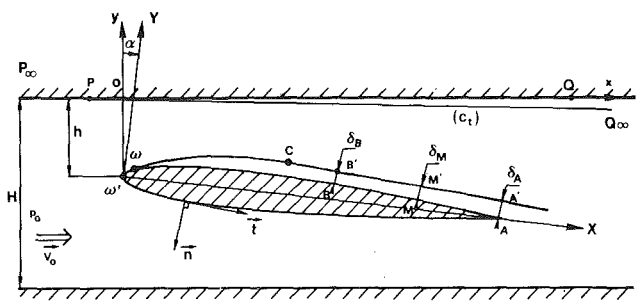

Fig. 1 Schematic representation

For M $\in$ ($A'C$) $\cup$ (ωA), P designates the imaginary part, $g_M = \tau_M f(s)$ (s is the curvilinear abscissa, with $\tau_M = 1$ when M is on the transition area B′C, or $\tau_M = 0$ *elsewhere*). For Mϵ ($C\omega$), P designates the real part, $g_M = -V_0\ (1+K)^{1/2}\ i$ is the complex number such that $i^2 = -1.C_M = \nu_M + i\ \beta_M$ represents the complex singularity density, with the overscore indicating that the complexes are conjugate. f designates the principal value of the integral according to Hadamard [17]. The complex function k is given by:

$$k(z,z') = (e^{i\alpha M}M/4H)\coth(\pi(z-z')/2H),$$

where α_M is the angle of the tangential vector to the contour in M with respect to the x-axis. This function represents the influence of an infinite series of sources or vortices regularly spaced at intervals of 2H and placed on a vertical passing through point M′. In the case of tunnel flow, the tangency condition must be satisfied on both walls. For this purpose, two conjugate series of the above type are used. The total influence of this double series is given by the complex kernel of the integral in relation (4). Thus, because of the two walls, a double infinity of images is used.

As the model is open, the inflow is compensated by locating a single sink at a relatively great distance downstream of the foil. In addition, in order to meet the fluid continuity condition (i.e., no flow-back) at points A′ and A, vorticity at these points has to be zero. It should be noted that when point B′ merges with point B (closed model), the sink intensity is automatically reduced to zero.

Relations (4) assume that the geometric shape of the cavity and its wake are known. To initialise the iterative procedure, at step (0), these shapes are merged with the foil. The gap $\mathbf{BB}' = \delta_B\ \mathbf{n}_B$ is imposed at the rear of the near wake. Using the solution found to this problem, all points M of curve BA are then displaced in order to obtain $\mathbf{MM}' = \delta_M\ \mathbf{n}_M$. At step (1), $\delta_B = \delta_M = 0$ is imposed. Iterations are performed until convergence is achieved. At each iterative step (j), the procedure is followed using the results obtained from iteration ($j-1$). If, during iteration (j), the gap imposed is $\delta^{(J)}$, the closure condition is given by the relation:

$$\int_\omega^B (\mathbf{V}\cdot\mathbf{n})^{(J)}/(\mathbf{V}\cdot\mathbf{t})^{(J-1)}ds_M = \delta^{(J)} = \begin{cases} \delta_B\ j=0 \\ 0\ j\geq 1 \end{cases} \qquad (5)$$

With step ($j-1$) assumed to be known, and $(\mathbf{V}\cdot\mathbf{n})^{(J)}$ being expressed as a linear function of the singularities used, relation (5) gives an additonal linear equation. Function f defined in (3) must tend toward zero during the iterations, in order to ensure the Neumann condition on the transition surface. This function meets the need to smooth the discontinuity in boundary conditions in the transition between the cavity and its wake. Function f is chosen as a linear function of the curvilinear abscissa, having the normal velocity value at the rear of the cavity and a zero velocity value at the rear of the near wake.

2.2 Discretization and Minimization Equations. The contour is discretized into N panels. On each panel the source density is taken to be constant and equal to β_n and the doublet density varies linearly. This doublicity distribution is equivalent to a vorticity distribution of constant density ν_n per panel, plus two point vortices located at the ends of the panel. When point A′ merges with point A, the total vorticity at this common point should be zero. In fact, the additional relation $\nu_1 + \nu_N = 0$ is introduced and retained even in the case of the open model (with different points A′ and A).

This scheme leads to doublet distribution with discontinuous values at the panel edges. At each control point, the vorticity ν_J is obtained by using a discrete representation of the relation $\nu = d\mu/ds$. This gradient is given by the slope of a quadratic passing through the μ value at the middle of the

panel of that of its neighbours. Thus, discretization of equations (4) and (5) gives rise to the matrix relation:

$$AX + CY = b \tag{6}$$

X is the matrix of the principal unknown source variables, to which is added the unknown $(1+K)^{1/2}$, while Y is the matrix of secondary unknown doublet variables. A and C are the corresponding influence matrices.

At this stage, the system of equations obtained is not closed. The methods generally used in subcavitating cases involve making an arbitrary choice vorticity distribution [15]. However, this choice affects the accuracy of the results obtained, on account of discretization of the equations [10]. Errors introduced by the discretization process are minimized by giving a minimum value to the modulus of a certain vector E, representative of the error in question. The vector E is a linear combination of X and Y, and the equations missing in (6) are obtained by giving a zero value to the differential of $\|\mathbf{E}\|$. In addition, in the cavitating case, the fact of not imposing an arbitrary vorticity law on the cavity leads to the resolution of a well-conditioned system. In this paper, the components of E represent the cyclic differences of the discrete values of the source and doublet distributions.

2.3 Study of the Boundary Layer and Wake Modelling. The perfect fluid model described above gives the velocity field on all the flow boundaries. A laminar boundary layer computation developed according to the CEBECI method [18] gives the displacement thickness ϵ existing as far as the separation point Ms, downstream of which the flow separates. Two methods are available for taking into account this displacement thickness [11, 19].

(*a*) **Deformation of the Boundary**. A displacement surface replaces the real surface for the inviscid part of the calculation, and this displacement surface is treated as a streamline of the inviscid flow; it is assumed that at "some distance" outside this displacement surface, this inviscid flow is the same as the real flow over the original surface. The method requires an iterative procedure, during which the streamline geometry changes, making it necessary to recalculate certain influence coefficients after each iterative step.

(*b*) **The "Surface-Blowing" Method**. This approach develops an inviscid flow calculation around the original real body with "artificial" boundary conditions which simulate the displacement surface as a streamline of the inviscid flow. A normal flow velocity is imposed across the surface of the foil (transpiration) where the boundary layer develops. This method is advantageous from the point of view of computation time, because singularities remain located on the real foil and their influence is unchanged during the iterations.

Subcavitating model: in this case, the surface-blowing method is applied for the laminar boundary layers occurring on the upper-side of the foil and on the top of the tunnel. The basic assumption is that the displacement surface is a flow streamline. Consequently, the boundary condition to be used in the potential computation is that the flow direction is tangential to the displacement surface, i.e.:

$$(\mathbf{V}\cdot\mathbf{n}/\mathbf{V}\cdot\mathbf{t})_{Ds} = d\epsilon/ds \tag{7}$$

where the subscript (Ds) designates the displacement surface.

The basis of the surface-blowing model is to replace this condition with an "artificial" boundary condition applied at the foil surface which simulates the flow tangency condition. For this purpose, the normal velocity is written on Ds as a series expansion of the velocity on the surface. Using the continuity equation, equation (7) to the first order gives the following relation:

$$\mathbf{V}\cdot\mathbf{n} = \mathbf{V}\cdot\mathbf{t}\ d\epsilon/ds \tag{8}$$

In relation (8), the gradient $d\epsilon/ds$ is calculated by a finite difference scheme.

On the upper side of the foil, upstream of the separation point Ms, the displacement thickness ϵ is calculated by the boundary layer program. From the separation point in the downstream direction, a fictitious linear displacement thickness θ_M is considered as far as the trailing edge after which a value of $\delta_A = AA'$ is imposed. The value of δ_A is adjusted so that velocity V_{MAX} near the leading edge of the foil is equal to that obtained experimentally (cf. § 3.2). Using the thickness relation $\delta_M = \theta_M$ thus obtained, the tangency condition ($\mathbf{V}\cdot\mathbf{n} = 0$) is replaced by condition (8) in the inviscid calculation with $\epsilon \equiv \epsilon$ for M ϵ ($A\omega'$Ms) and $\epsilon = \theta_M$ for Mϵ (Ms A). Because $\mathbf{V}\cdot\mathbf{t}$ is included in this condition, an iterative procedure must be used. It should be noted that during the iterations, the thickness θ_M is not recalculated, as the iterations involve simply recalculating $\mathbf{V}\cdot\mathbf{t}$ in the inviscid model.

The type (8) surface-blowing condition is achieved on the top of the tunnel by introducing a source distribution. In this case, it was assumed that the boundary layer occurs on the part (PQ_∞) of the top of the tunnel (curve c_t, Fig. 1). Consider the case of virtual flow in a tunnel of height 2H round the contour line comprising the following parts:

- the real foil and its symmetrical foil with respect to the top of the tunnel,
- the contour line (C_t) and its symmetrical line with respect to the top of the tunnel.

This virtual flow is symmetrical with respect to the x-axis. Consequently, the half straight line ($P_\infty P$) can be replaced by a solid surface. Thus, strict equivalence is achieved between the initial flow and the virtual flow.

Therefore, the images method (double infinity of images) is applied in the case of virtual flow with a source density along PQ calculated by the boundary layer method. In this way, allowance can be made for the wall effect in the initial flow configuration. For the example dealt with, calculations show that the influence of friction on the top and bottom of the tunnel and on the lower side of the foil may be ignored with respect to the separation effect on the upper side of the foil.

Cavitating model: here, in order to achieve results which agree with those obtained by experiment, the determining parameters are the position of the cavity detachment point and the geometric shape of the wake behind the cavity (cf. § 3).

The position of the detachment point being determined by the procedure described in § 2, the iterative cavity calculation initialises the computation, not with the geometry of the foil, but with the displacement surface obtained previously in the sub-cavitating model and characterized by the value δ_A at point A. The new geometry of the far wake is constructed in such a way that the imposed gap is $\delta_M = \theta_M + \nabla\delta_M$ MϵBA.

Joukovsky's condition: in viscous flow, the flow must leave the trailing edge smoothly and the real pressures on the upper and lower surfaces at the trailing edge must be equal. In the case of a simple boundary layer method, the pressure at the outer edge of the displacement thickness is assumed to be the same as that at the surface. Thus, the condition to control flow circulation should be that the pressures are equal on the displacement surfaces at the trailing edge [11]. This produces a relation of equal velocities on the displacement surface:

$$(\mathbf{V}\cdot\mathbf{t})^2_{\mathrm{EDS}} + (\mathbf{V}\cdot\mathbf{n})^2_{\mathrm{EDS}} = (\mathbf{V}\cdot\mathbf{t})^2_{\mathrm{IDS}} + (\mathbf{V}\cdot\mathbf{n})^2_{\mathrm{IDs}} \tag{9}$$

Subscript EDs designates the trailing edge of the displacement surface on the upper side and IDs the trailing edge on the lower side. Using the same properties as those which enabled equation (7) to be transformed into (8), equation (9) at the first order, gives an equivalent condition to be applied on the actual body surface:

$$(\mathbf{V}\cdot\mathbf{t})_\epsilon - (\mathbf{V}\cdot\mathbf{t})_1 = \{(\mathbf{V}\cdot\mathbf{n})^2{}_1 - (\mathbf{V}\cdot\mathbf{n})^2{}_E\} / \{(\mathbf{V}\cdot\mathbf{t})_E + (\mathbf{V}\cdot\mathbf{t})_1\} \tag{10}$$

Subscript E designates the trailing edge of the foil on the upper

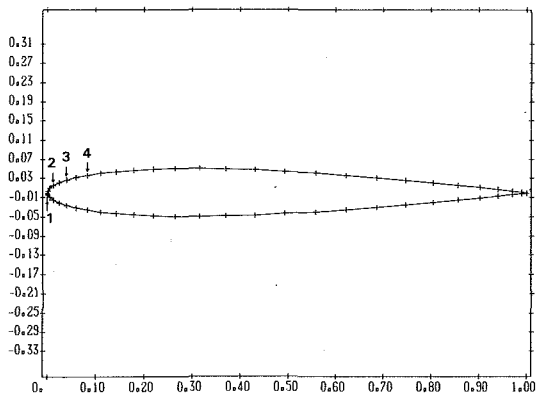

Fig. 2 NACA0010 hydrofoil

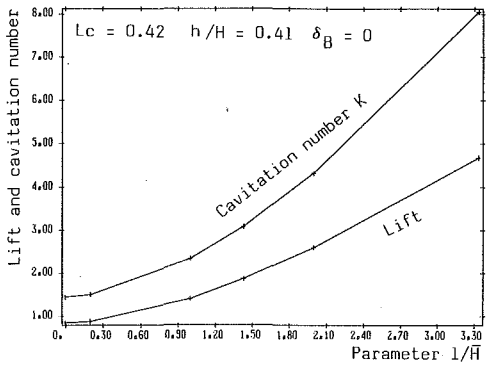

Fig. 3 Wall effect on lift and cavitation number

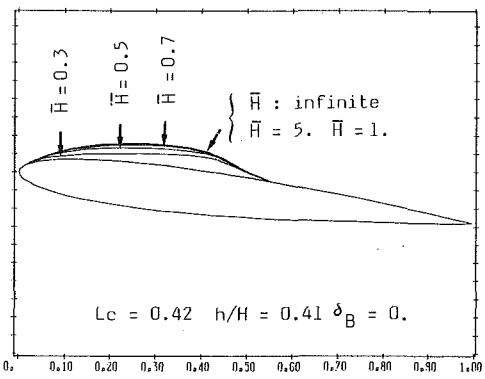

Fig. 4 Wall effect on cavity shape

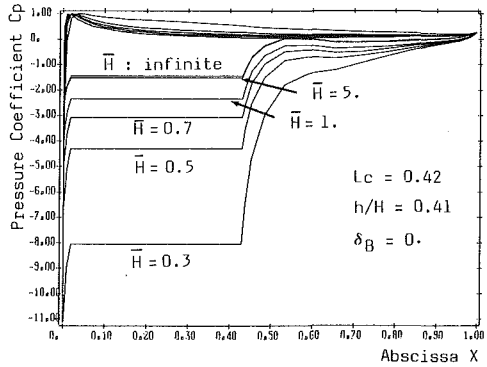

Fig. 5 Wall effect on pressure coefficient

side and I on the lower side. For the surface-blowing model, the normal velocity at point E is nonzero. Consequently, the right-hand side is updated iteratively.

3 Results and Comparison with Experimental Results

A comparison of the results obtained was undertaken using a test hydrofoil provided by Electricité de France (EdF). The foil is a symmetrical NACA0010 foil, with a relative thickness of 10 percent (Fig. 2). The chord of the foil (equal to 10 cm) is taken as reference length and basic unit throughout the study. The flow configuration is that used in the experiments: the foil is placed in a square test section of height 5 cm, at a depth h of 2.05 cm and with an angle of incidence $\alpha = 6°30'$. The velocity Vo at upstream infinity is 10 m/s.

The foil is discretized into $N = 54$ and 62 panels respectively in the subcavitating and cavitating models. In the latter case, the near wake CB′ consists of the four panels immediately downstream of point C. In order to ensure regular geometry and continuous singularity distributions, a finer computation mesh is required around point C. The panel size near the leading edge is of the order of 4×10^{-3} and that on the trailing edge of 4×10^{-2}. The cavity length Lc is defined as the distance ωB′ projected on the chord of the foil. The pressure coefficient is given by $C_p = 1 - V^2/V^2_0$. From the numerical point of view, convergence of the iterative procedure is obtained after seven iterations.

3.1 Wall Effect. To illustrate this effect, it is assumed that the cavity length is equal to 0.42. With the ratio h/H fixed at a value of 0.41, the closed model ($\delta_B = 0$) was used to treat five cases of tunnel height $\bar{H}$ ($\bar{H} = H/c$): 0.3, 0.5, 0.7, 1 and 5, plus the case of the infinite field of flow ($\bar{H}$ infinite). The last case uses the classic influence coefficients of the infinite field of flow. Figure 3 illustrates the decrease in lift coefficient and cavitation number with increase in tunnel height, the limit value of each being practically reached for a value of $\bar{H} = 5$. Figure 4 shows the variation in the shape of the cavitation pocket as a function of tunnel height. Noteworthy is the flattening out of the cavity caused by the proximity of the walls ($\bar{H} = 0.3$ and 0.5). For other values, the cavities obtained are more or less the same as that obtained in unconfined flow ($\bar{H}$ infinite). The significant effect of wall proximity on the value of relative pressure in the cavity shows that this factor is important for the validity of the results. For the case in question here ($\bar{H} = 0.5$), it is necessary to make strict allowance for the wall effect. This has been achieved by using the previously described image method.

3.2 Cavity Detachment Point. Before studying the effect of the wake behind the cavity, it is advantageous to examine the influence of the position of the cavity detachment point on the results. At the beginning of this study, the influence of the separation effect on the top of the tunnnel and above the foil was underestimated. Consequently, no provision had been made for evaluating the viscous effect on either the tunnel top and bottom or on the foil. For this reason, a preliminary calculation making no allowance for viscous effects was performed for the closed model case ($\delta_B = 0$).

For this case, Fig. 6 shows the influence of choice of cavity separation point on the Lc(K) curves. The various curves (C1, C2, C3, C4) correspond to the various detachment points indicated on Fig. 2. The experimental results are represented by an area bounded by two curves corresponding to the upper limit (Lc max) and lower limit (Lc min) of the results. The deviation obtained with respect to the experimental curves is significant. It is clear that, in order to obtain cavitation number values of comparable order of magnitude to the experimental values, unrealistic cavity separation points have to be chosen, located too far downstream of the leading edge (curves C3 and C4). In this case, the maximum flow velocity upstream of the point ω, although qualitatively experimentally verified, is much too high (Fig. 7).

The following remarks can be made concerning curves C2 and C3:

Within the validity limits of the calculation assumptions

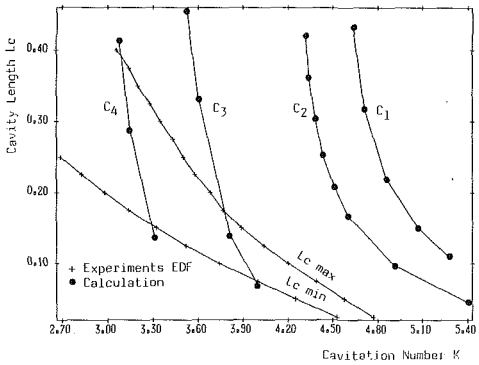

Fig. 6 Effect of the detachment point on the Lc(K) curves

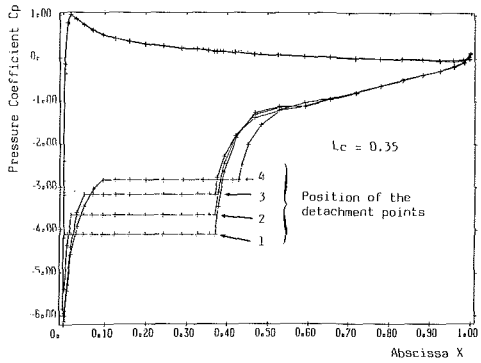

Fig. 7 Effect of the detachment point on the cavitation number (Lc = 0.35)

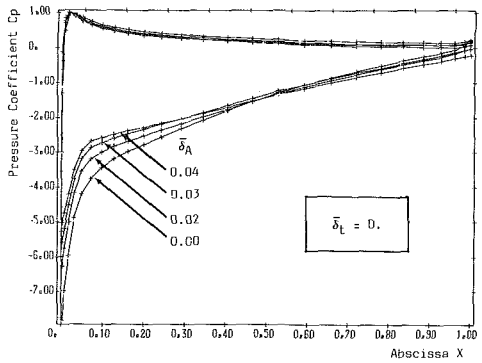

Fig. 8 Simulation of the separation effect on the upper side of the foil

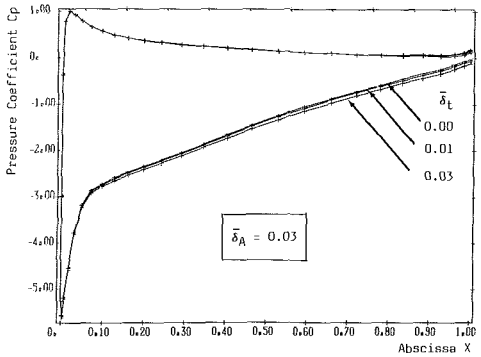

Fig. 9 Simulation of the separation effect on the top of the tunnel

made, the cavity detachment point should be located between positions 2 and 3. This position is probably too far downstream, compared with experimental observations. Moreover, even if this position is assumed to be correct, the cavity length varies too rapidly with cavitation number, and the maximum flow velocity on the cavity is much too high (excluding at the outset such cavity positions as 3 or 4). Such a difference can be explained only by assuming that the hypothesis of flow circulation around the foil is overestimated because separation takes place at the rear of the cavity.

For the above reasons, it was clear that a prior study of viscous effects on subcavitating flow was needed. As a first step, the flow was assumed to be nonviscous and unseparated from the tunnel top and bottom, and the effect of flow separation on the upper side of the foil was studied using the simplified method described previously. The idea of taking the separation effect into account by means of a displacement thickness is not improper here as the angle of attack of the foil is not too high. In order to estimate the influence of this displacement thickness, calculations were performed with arbitrary displacement thicknesses as follows: the boundary layer calculation indicates that separation occurs at point Ms on the 0.05 abscissa. Downstream of this point, as indicated in § 2.3, the deviation between the streamline and the foil is chosen arbitrarily as a linear function of the curvilinear abscissa. The wake deviation is thus characterized by the value $\bar{\delta}_A = \delta_A/c$ at the trailing edge. It is to be noted on Figure 8 that the viscous flow conditions on the upper side of the foil have a significant effect on the velocity value near the leading edge. On the other hand, they have only a minor effect on the pressure coefficient on the lower side. The value of $\bar{\delta}_A$ was determined in the following manner: from the experimental results Lc(K), the velocity corresponding to the $(1+K)^{1/2}$ limit when Lc tends toward zero is calculated.

Assuming Lc(K) to vary according to the average value between (Lc max) and (Lc min), this velocity is found to be 24 m/s. This limit value is no doubt a good approximation of the higher flow speed condition which occurs under subcavitating conditions. Since the experimental value of the cavitation number is not exactly equal to the corresponding pressure coefficient, due to the presence of dissolved gas in the cavity, the value of this number is at its maximum limit. A value of $\bar{\delta}_A = 0.03$ is taken, corresponding to a theoretical increased flow velocity Vmax close to 24 m/s ($V_{MAX} = (1+K-\Delta K)^{1/2}$, $\Delta K > 0$).

Assuming the displacement thickness to be fixed at a value of $\bar{\delta}_A = 0.03$, Fig. 9 shows that the viscous effect on the top of the tunnel is negligible under the following assumptions: negligible boundary layer thickness on the top of the tunnel opposite the leading edge, displacement thickness $\bar{\delta}_t$ on the top of the tunnel opposite the trailing edge equal to 0, 0.01 and 0.03. The values of $\bar{\delta}_t$ are made dimensionless by reference to the foil chord length.

The results of Figs. 8 and 9 show that the separation effect on the upper side of the foil predominates over the viscous effect on the top of the tunnel. In the lower part of the flow section, under the lower side of the foil, the boundary layer remains very thin. Consequently, in the remainder of the study, the viscous effect on the tunnel top and bottom and on the lower side of the foil will be ignored, and the separation effect on the upper side of the foil will be characterized by the value $\bar{\delta}_A = 0.03$.

It is then possible to repeat the calculations corresponding to Fig. 6 under more realistic conditions, at least subject to Lc remaining small. The results are illustrated in Fig. 10. A signficant shift is to be noted compared with Fig. 6. Using the detachment criterion previously described, the calculation demonstrates that the detachment point 2 is in fact a separation point. The effect of the cavity length on the position of this point is minimal. Indeed, calculation of the boundary layer shows that the separation point is practically independent of the cavity length. Therefore, in the remainder of the study, the cavity is considered to begin at this point.

3.3 Illustration of the Separation Effect under Cavitating Conditons

In the cavitating case, the foil is widened by $\bar{\delta}_A = 0.03$ at

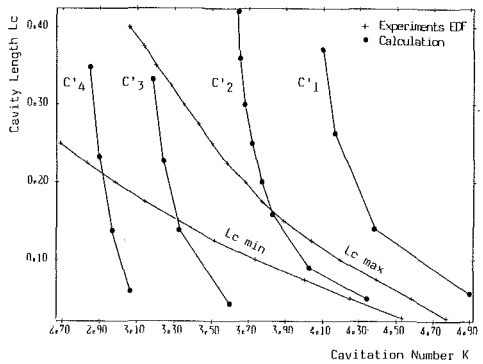

Fig. 10 Influence of the detachment point with separation effect ($\bar{\delta}_A$ = 0.03)

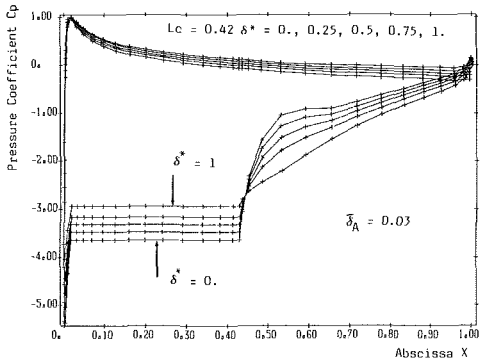

Fig. 12 Effect of the gap δ* on the pressure coefficient ($\bar{\delta}_A$ = 0.03).

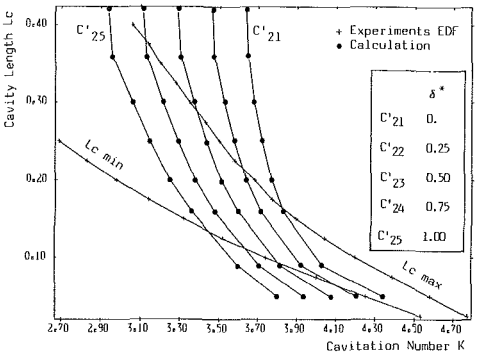

Fig. 11 Effect of the gap δ* on the Lc(K) curves ($\bar{\delta}_A$ = 0.03).

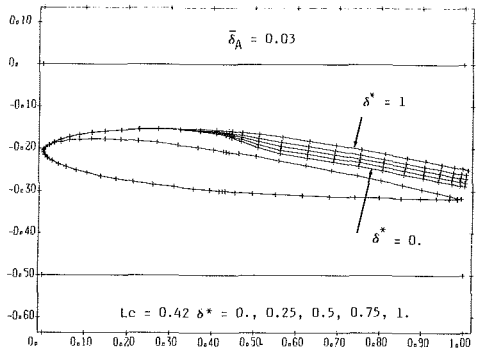

Fig. 13 Wakes corresponding to Fig. 12

the trailing edge. Figure 10 clearly shows that the separation effect in subcavitating conditions (Lc --> 0), characterized by the value $\bar{\delta}_A = 0.03$, is too small to be able to evaluate correctly the same effect under cavitating conditions. Initially, it is assumed that there is no wake deviation behind the near wake, but that δ_B is greater than θ_B (hence $\Delta\delta_M$ remains constant). The adimensional gap $\delta^* = \Delta\delta_B/CC_{MAX}$ is then defined, where C is the position of point C at iteration (0) and C_{MAX} the position of point C after convergence with no gap (taking into account the thickness effect $\bar{\delta}_A = 0.03$). Figure 11 shows the behavior of curves Lc(K) as a function of the adimensional gap δ*. Curves C'_{21} to C'_{25} are those obtained for values of δ* varying from 0 to 1, in 0.25 steps.

For a given cavity length, the effect of δ* on the pressure coefficient and the geometry of the streamlines is shown on Figs. 12 and 13, respectively. The velocity near the leading edge is directly affected. It is found that a far wake of constant relative thickness could possibly be used as a model to find the correct Lc(K) curve on condition that the δ* value chosen is dependent on cavity length.

This law is obtained in the following manner: the interaction of curves c'_{21} to c'_{25} (Fig. 11) with the mean experimental curve leads to a number of points which, for each cavity length value, characterize the corresponding gap δ*. The δ* (Lc) curve obtained in this way is approximated by the least-squares curve represented on Fig. 17, the equation for which is given by:

$$\delta^* = 0.98\ \mathrm{Ln}(\mathrm{Lc}/0.11) \qquad (11)$$

where Ln designates the Napierian logarithm.

By choosing a δ* value corresponding to this law, the recompression law behind the cavity is determined. This recompression law depends on the fact that there is no far wake deviation, which does not necessarily conform to reality. Characterizing the far wake by an angle of divergence, the δ* law can be modified so that the recompression behind the cavity is modified. Two parameters are then available for fixing the cavitation number and characterizing the recompression rate:

- the parameter δ* equal to the ratio of extra thickness behind the near wake to the extra thickness behind the cavity (thickness is measured with respect to the foil widened by $\bar{\delta}_A = 0.03$),
- a new value, $\bar{\delta}'_A$, of the parameter $\bar{\delta}_A$ characterizing the far wake divergence.

To study the practical possibility of such an adjustment, a large number of experimental results would be required, in particular to highlight the form of the recompression law behind the cavity. Unfortunately, very few investigations have been undertaken in this field.

Without anticipating subsequent developments, an example of how the two parameters can be adjusted is given hereafter for several cavities. For each cavity length, the values of $\bar{\delta}'_A$ and δ* are adapted to give the range of values obtained by experiment. Figure 14 shows that by taking values for $\bar{\delta}'_A$ and δ* which vary in accordance with cavity length, it is possible to obtain theoretical values which concur with those derived from experiments. Curve (L) is an example of this. The two laws $\bar{\delta}'_A$ (Lc) and δ*(Lc) obtained in this way are virtually straight lines and are shown on Fig. 17.

The parameters δ* and $\bar{\delta}'_A$ are adjusted in the following way: using the "closed model," the calculation is performed in the case of a widened foil, as under subcavitating conditions, but with a $\bar{\delta}'_A$ value greater than $\bar{\delta}_A = 0.03$ (value of the subcavitating case). In this way, the model now depends only on one degree of freedom, characterized by the $\bar{\delta}'_A$ (Lc) law (Fig. 17).

The previous results show that it is possible to vary the far wake deviation to a considerable extent when the cavity length varies within the limits of the experimental law Lc(K). In any case, the effect of flow separation is highlighted. Figures 15 and 16 show the pressure coefficients obtained in the case of curve (L) as well as the associated geometries.

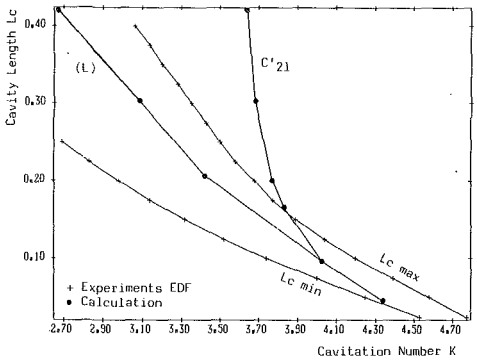

Fig. 14 Effect of the far wake deviation on the Lc(K) curves

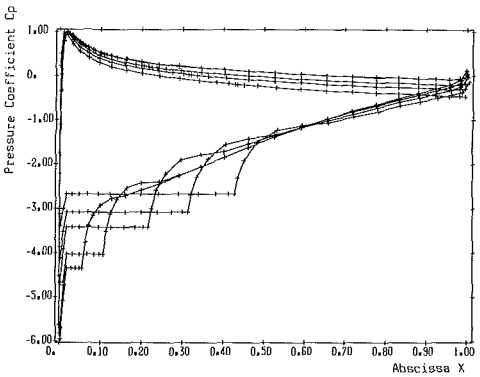

Fig. 15 Effect of cavity length on pressure coefficient, with wake deviation

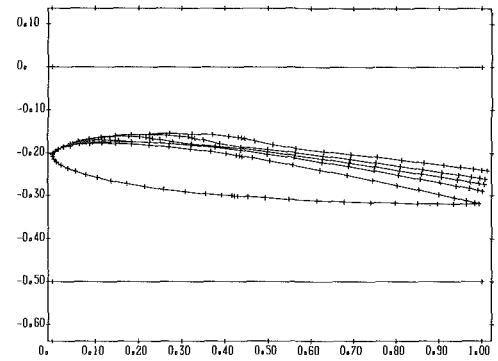

Fig. 16 Wakes corresponding to Fig. 15

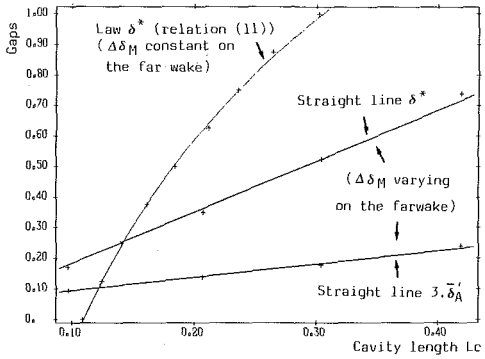

Fig. 17 Logarithmic law δ^* (with constant gap) and linear law δ^* (with variable gap). $\bar{\delta}_A$ law corresponding to the linear law δ.

4 Conclusions

This study shows that, in the case of partial cavitation where the confinement effect is dominant (walls near the cavity), the cavity wake is a determining factor for flow organization. The displacement thickness associated with the wake reduces the flow on the upper side. Consequently, the cavitation number is lower than the equivalent "closed model" number.

The numerical results show the major effect of the position of the detachment point on the Lc(K) curves (Fig. 10). A boundary layer computation reveals the existence of a separation point near the leading edge. Downstream of this point, the displacement thickness, simulating the wake effect, is chosen arbitrarily. To take into account viscous effects under subcavitating conditions, the foil is first widened by an initial displacement thickness. Then, the influence of an extra constant displacement thickness is examined (Figs. 12, 13, 14, and 15). Several cavity wakes diverging progressively from the foil were then tested. The near wake behind the cavity allows the different adjustments to be made efficiently and confers both flexibility and accuracy on the numerical model.

Provided that a suitable wake geometry is chosen the model produces results which fall within the range of those obtained experimentally. This analysis shows how important it is to have a precise understanding of how flow is organized behind the cavity. In order to achieve further progress, numerical models based on the concept of potential flow will probably have to introduce the notions of recompression and shear in addition to the previously used surface blowing concept.

References

1 Wu, T. Y. T., "Cavity and Wake Flows," *Annual Review of Fluid Mechanics*, Vol. 4, 1972, pp. 243–284.

2 Tulin, M. T., "Supercavitating Flows. Small Perturbation Theory," *Journal of Ship Research*, Vol. 13, No. 3, 1964, pp. 16–37.

3 Furuya, O., "Non-Linear Theory for Partially Cavitating Cascade Flows," I.A.H.R. 10th Symposium – Hydraulic Machinery and Equipment Associated with Energy Systems in the New Decade of the 1980s Tokyo, 28 Sept. – 2 Oct. 1980.

4 Golden, D. W., "A Numerical Method for Two Dimensional, Cavitating, Lifting Flows, M.I.T. Department of Ocean Engineering, Report No. 81512-1.

5 Chang-Sup Lee, "Prediction of the Transient Cavitation on Marine Propellers by Numerical Lifting Surface Theory," Thirteenth Symposium on Naval Hydrodynamics, Tokyo, Oct. 6–10, 1980.

6 Yamaguchi, H., Kato, H., "On Application of Non Linear Cavity Flow Theory to Thick Foil Sections," Second Conference on Cavitation, I.M.E. Edinburg, Sept. 6–9, 1983.

7 Nishiyama, T., and Ito, J., "Calculation of Partially Cavitating Hydrofoil by Singularity Method (Part 4, Experimental Explorations of the Optimum Partial Cavity Flow Model)," *Trans. J.S.M.E.*, Vol. 47, No. 420, Aug. 1981, pp. 1433–1438.

8 Nishiyama, T., and Ito, J., "Calculation of Partially Cavitating Hydrofoil by Singularity Method (Part 1, Two Dimensional Isolated Hydrofoil)," *Trans. J.S.M.E.*, Vol. 43, No. 370, July 1977, pp. 2165–2174.

9 Ito, J., "Calculation of Partially Cavitating Thick Hydrofoil and Examination of a Flow Model at Cavity Termination," *International Symposium on Cavitation*, April 1986, Sendai, Japan.

10 Hunt, B., "The Panel Method for Subsonic Aerodynamic Flows," Von Karman Institute for Fluid Dynamics, Lecture Series 1978-4, March 13–17, 1978.

11 Hunt, B., "Recent and Anticipated Advances in the Panel Method: the Key to Generalized Field Calculations," Von Karman Institute for Fluid Dynamics, Lecture Series 1980-5, March 24–28, 1980.

12 Lemonnier, H., Rowe, A., "Another Approach in Modelling Cavitating Flows," *Journal of Fluid Mechanics*. In press.

13 Franc, J. P., and Michel, J. M., "Attached Cavitation and the Boundary Layer: Experimental Investigation and Numerical Treatment," *Journal of Fluid Mechanics*, Vol. 154, 1985, pp. 63–90.

14 Pellone, C., and Rowe, A., "Supercavitating Hydrofoils in Non-Linear Theory," Third International Conference on Numerical Ship Hydrodynamics Paris, June 1981, Session VI.

15 Luu, T. S., and Goulmy, G., "Méthode des singularités à répartition discrétisée dans le domaine de l'hydro et l'aérodynamique," Laboratorie d'Informatique pour la Mechanique et les Sciences de l'Ingénieur (LIMSI), Orsay, France, 1975.

16 Hess, J. L., and Smith, A. M. O., "Calculation of Flows About Arbitrary Bodies, *Progress in Aeronautical Sciences*, Vol. 8, Pergamon Press, 1967.

17 Hadamard, J., *"Lectures on Cauchy's Problems in Linear Partial Differential Equations,"* New Hoven, Yale University Press, 1923.

18 Cebeci, T., and Bradshaw, P., "Momentum Transfer in Boundary Layers," McGraw-Hill Book Company, 1977.

19 Lighthill, M. J., "On Displacement Thickness," *Journal of Fluid Mechanics*, Vol. 4, 1958, pp. 383.

V. H. Arakeri
Visiting Associate Professor,
St. Anthony Falls Hydraulic Laboratory,
(on leave from IISC, India)

H. Higuchi
Assistant Professor,
Department of Aerospace Engineering and Mechanics.

R. E. A. Arndt
Director and Professor,
St. Anthony Falls Hydraulic Laboratory.

University of Minnesota,
Minneapolis, Minn. 55414

A Model for Predicting Tip Vortex Cavitation Characteristics

Introduction

Recently, Staufenbiel [1984] has presented a modified two parameter Lamb model for predicting the tangential velocity distribution in a fully rolled-up tip vortex. The two parameters are determined by satisfying both the dispersion and energy relationships. The agreement Staufenbiel has been able to obtain between the predicted values of the maximum tangential velocities based on his new model and those measured is far superior to the agreement based on the use of a simple one parameter Rankine or Lamb model. In the present work, the model proposed by Staufenbiel has been used to predict the minimum pressure coefficient in a fully rolled-up tip vortex. The model has also been extended to compute the radius of a developed tip vortex cavity. It is found that generally good agreement is found between the predictions based on the present model and the observations of Souders and Platzer (1981) on an elliptic planform hydrofoil.

The Model

The circulation distribution in the fully rolled-up tip vortex, following Staufenbiel [1984], is assumed to be of the form:

$$\Gamma/\Gamma_0 = q[1-e^{-\lambda r^2}] \quad 0<r\le r_c \tag{1}$$

$$\Gamma/\Gamma_0 = q[1-e^{-\lambda r^2}+ar] \quad r_c<r<r_k \tag{2}$$

$$\Gamma/\Gamma_0 = 0.99 \quad r\ge r_k \tag{3}$$

Here, Γ is the circulation in the vortex and all radii r, r_c, and r_k are non-dimensional with respect to the wing or hydrofoil semi-span, s. The above circulation distribution has a discontinuity at $r=r_c$; however, the magnitude of this being quite small, since a is the order of one and r_c is of the order of 0.02. To keep the model simple from a computational point of view this discontinuity is accepted. In any case, the present work is an extension of Stanfenbiel (1984) model and all the limitations in his model are retained here. The quantities q, a, λ, and r_k are parameters which need to be specified or determined. Γ_0 is related to the foil circulation distribution, which is given by

$$\Gamma_f/\Gamma_0 = f(\eta) \tag{4}$$

Here, Γ_f is the circulation on the foil at different spanwise locations, Γ_0 is the mid-span circulation and η is the non-dimensional distance along the span. It may be pointed out that in (1) above, r_c, the point of maximum tangential velocity which is also taken to be the core radius and the parameter λ are related by

$$\lambda r_c^2 = 1.255 \tag{5}$$

Therefore, it follows that

$$q = 1.4(\Gamma_c/\Gamma_0) \tag{6}$$

and thus q is a direct measure of the fraction of circulation at the core, Γ_c.

In the model, as presented above, there are four unknown parameters, namely: q, λ, a, and r_k. At this point, we will leave q as an unknown and the other three are determined by satisfying the following three conditions:

(*i*) This simply relates to the statement that

$$\Gamma/\Gamma_0 = 0.99 \text{ at } r=r_k \tag{7}$$

(*ii*) This relates to the conservation of the dispersion of vorticity and is expressed as

$$i^2 = \int_0^{r_k} \frac{d(\Gamma/\Gamma_0)}{dr} r^2 dr = \int_1^0 \frac{d(\Gamma_f/\Gamma_0)}{d\eta} (\eta-\bar{\eta}_1)^2 d\eta \tag{8}$$

where $\bar{\eta}_1$ is given by

$$\bar{\eta}_1 = \int_1^0 \frac{d(\Gamma_f/\Gamma_0)}{d\eta} \eta \, d\eta \tag{9}$$

Contributed by the Fluids Engineering Division for publication in the JOURNAL OF FLUIDS ENGINEERING. Manuscript received by the Fluids Engineering Division July 31, 1986.

(*iii*) This relates to the conservation of energy (per unit axial distance) and is expressed as

$$D_i/(\rho\Gamma_0^2/2\pi) = C_r + C_i \tag{10}$$

where D_i is the induced drag and C_r and C_i are given by

$$C_r = \int_0^{r_k} (\Gamma/\Gamma_0)^2 \frac{dr}{r} \text{ and } C_i = \frac{1}{2} \ln \frac{\sqrt{\bar{\eta}_1^2 + r_k^2} + \bar{\eta}_1}{\sqrt{\bar{\eta}_1^2 + r_k^2} - \bar{\eta}_1} \tag{11}$$

We might note here that the above conditions are the same as those proposed by Staufenbiel except that a more exact form for C_i [McCormick, 1962] is used here. By substituting the assumed circulation distribution, we obtain[1]

$$r_k = i\sqrt{3/(0.99-q)} \tag{12}$$

$$a = \frac{(0.99-q)}{q} \frac{1}{r_k} \tag{13}$$

and the following equation for computing λ,

$$q^2[0.5\ln\lambda r_k^2 - 0.058 + ar_k^2 + \frac{a^2}{4} r_k^4] + \frac{1}{2}\ln \frac{\sqrt{\bar{\eta}_1^2 + r_k^2} + \bar{\eta}_1}{\sqrt{\bar{\eta}_1^2 + r_k^2} - \bar{\eta}_1} = \frac{D_i}{\rho\Gamma_0^2/2\pi} \tag{14}$$

The minimum pressure coefficient, $Cp_{\min}$, is obtained by integrating

$$dp/dr = \rho v_\theta^2/r$$

to give

$$-C_{p\min} = \frac{p_\infty - p_{r=0}}{1/2\rho U_\infty^2} = \frac{2}{(2\pi)^2} \left[\frac{\Gamma_0}{U_\infty s}\right]^2 \int_0^\infty \frac{(\Gamma/\Gamma_0)^2}{r^3} dr \tag{15}$$

Here, P_∞ is the reference pressure far away from the vortex center, U_∞ is the free stream velocity and ρ is the liquid density. Evaluating the integral to the same approximations indicated earlier, we get

$$-C_{p\min} = \frac{2}{(2\pi)^2} \left[\frac{\Gamma_0}{U_\infty s}\right]^2 q^2 \left[\lambda \ln 2 + 3.37a\sqrt{\lambda} + a^2 \ln[0.9\, r_k\sqrt{\lambda}] - \frac{4a}{r_k} + \frac{1}{r_k^2}\left[\frac{0.49}{q^2} - 0.5\right]\right] \tag{16}$$

Here the first term[2] is so dominant that, to a very good accuracy, the above can be approximated as,

$$-C_{p\min} \cong \frac{2}{(2\pi)^2} \left[\frac{\Gamma_0}{U_\infty s}\right]^2 q^2 \lambda \ln 2 \tag{17}$$

Computations for Elliptic Planform Hydrofoil and Comparison With the Inception Data of Souders and Platzer

Recently, Souders and Platzer [1981] have presented tip vortex cavitation inception data for an elliptic planform hydrofoil with an aspect ratio, A of 2.55. They also included as part of their experimental program the measurement of lift and drag forces on the hydrofoil used for inception observations. From the classical lifting line theory of Prandtl, we expect elliptic load distribution on an elliptic planform hydrofoil; however, as pointed out by Kida and Miyai [1978][3], this is true only for large aspect ratio wings or hydrofoils. In particular, significant deviations are expected from the lifting line theory for a hydrofoil with an aspect ratio of 2.55. Thus, the induced drag magnitude required for present computations was obtained from the drag measurements of Souders and Platzer. It is well known in airfoil theory that the group of terms

$$\frac{\pi A C_{Di}}{C_L^2} = K_1 \tag{18}$$

has a constant value which depends only on the planform shape and aspect ratio; K_1, in fact, has a value of 1 for classical elliptical loading. In the above, C_L is the lift coefficient, C_{Di} the induced drag coefficient, and A the aspect ratio. For the hydrofoil in question, K_1 was evaluated by assuming that the measured total drag at the largest measured lift coefficient is the induced drag. This was based on the commonly observed fact that the induced drag becomes the dominant component of the total drag at large angles of attack. On the basis of this assumption and using the measured drag data of Souders and Platzer, K_1 was determined to be 1.25 and was used to evaluate $Di/(\rho\Gamma_0{}^2/2\pi)$. The other required parameters, i and $\bar{\eta}_1$, were obtained by assuming the classical elliptic load distribution since the solutions of Kida and Miyai, being singular at the tip, could not be used for this purpose. This was not a bad assumption, since the inferred value of $\bar{\eta}_1$, from the observed tip vortex cavity trajectory from the experiments of Souders and Platzer, was close to $\pi/4$, which is the classical theoretical value. Thus, the following values for i, $\bar{\eta}_1$ and $Di/(\rho\Gamma_0{}^2/2\pi)$ were finally used for the computations;

$$i = 0.223,\ \bar{\eta}_1 = \pi/4,\ Di/(\rho\Gamma_0{}^2/2\pi) = 3.084.$$

Assuming that inception of cavitation occurs as soon as vapour pressure is reached at the minimum pressure point, we can, from equation (16), express σ_i in the form

$$\sigma_i = kC_L{}^2 \tag{19}$$

where the relationship

$$\frac{\Gamma_0}{U_\infty s} = \frac{4}{\pi} \frac{C_L}{A}$$

has been used. Here, σ is the cavitation number defined as $(P_\infty - P_v)/(1/2\rho U_\infty{}^2)$ with P_v being the vapour pressure. The computed magnitude of k and other parameters as a function of q are shown in Table 1, and the former is also shown in Fig. 1.

It is clear that k is a very sensitive function of q and hence, for any direct comparison with experiments, a value for q has to be fixed. For this, the measured values of Γ_c/Γ_0 and equation (6) were used. Using the results of Fig. 2 of Uberoi [1979], we get a value of $q \cong 0.60$. More recent measurements of Takahashi et al. [1986] give a value of q which is approximately 0.70. Therefore, the average being $q \cong 0.65$ was selected for direct comparison with the results of Souders and Platzer. For $q = 0.65$, from Table 1, we find that

$$\sigma_i = 17.53\ C_L{}^2$$

whereas, the measurements of Souders and Platzer give

$\sigma_i = 14.7\ C_L{}^2$ for a Reynolds number of 2.5×10^6, and

$\sigma_i = 17.6\ C_L{}^2$ for a Reynolds number of 5.0×10^6.

Thus, the comparison is quite favorable. We might note that if the classical value for induced drag, namely $Di/(\rho\Gamma_0{}^2/2\pi) =$

[1] In giving these expressions, terms of the order of $1/\lambda$, $e^{-\lambda r_k^2}$, etc., have been neglected since λ is a very large number, like 1000, and r_k is of the order of 0.5.

[2] Evaluation of this term from the integral in (15) has been worked out in an appendix of the thesis by McCormick (1954).

[3] The authors would like to thank Professor Van Dyke of Stanford University for bringing this reference to their attention.

Table 1 Computed parameters for elliptic planform hydrofoil with $A = 2.55$

q	0.6	0.625	0.65	0.675	0.7	0.75
r_k	0.618	0.639	0.662	0.688	0.717	0.788
a	1.051	0.913	0.789	0.678	0.577	0.406
λ	10,940	6,879	4,495	3,058	2,179	1,154
r_c	0.0107	0.0135	0.0167	0.020	0.024	0.033
$k=\sigma_i/C_L{}^2$	36.1	24.72	17.53	12.88	9.79	5.99

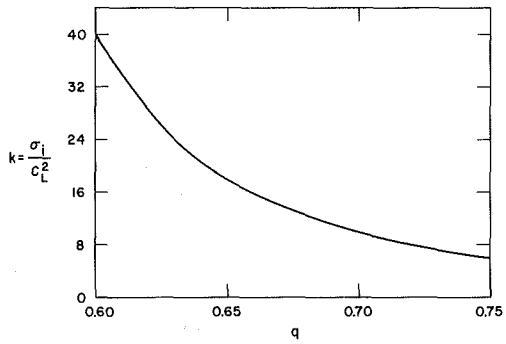

Fig. 1 Dependence of the coefficient $k=\sigma_i/C_L{}^2$ on the parameter q

$\pi^2/4$, was used in our computations, the result would have been

$$\sigma_i = 1.1\ C_L{}^2$$

Therefore, the predictions are very sensitive to the magnitude of $Di/(\rho\Gamma_0{}^2/2\pi)$, which, perhaps, is a weak point of this model. In addition, the observed Reynolds number dependence is not inherent in the model, except for what may appear through dependence of q or other parameters on the Reynolds number. However, using the present model, we can explain certain other findings by Souders and Platzer. In their experiments, it was found that roughening of the tip area very locally had a pronounced effect on the magnitude of σ_i. It may be conjectured physically that the roughening causes increased turbulence levels in the core, thus helping to diffuse the concentrated vorticity to outer regions. In our model, it is easy to show that the vorticity at the center, $\zeta_{r=0}$, is given by

$$\zeta_{r=0} = q\lambda(\Gamma_0/\pi s^2) \tag{20}$$

and, since λ decreases sharply with increase in q, the diffusion of vorticity away from the center is equivalent to the increase in q. In the present axisymmetric model, we may expect an upper limit for q which is given by the condition that

$$r_k = \bar{\eta}_1$$

in which case the two vortices will be touching each other. On this basis, an upper limit for q based on the results of Table 1 is close to 0.75 and the corresponding σ_i which is a minimum is given by

$$(\sigma_i)_{\min} = 5.99\ C_L{}^2$$

This again compares very favorably with the observations of Souders and Platzer, who found

$$(\sigma_i)_{\min} = 6.3\ C_L{}^2.$$

Extension of the Model to Two-Phase Analysis and Comparison with Observations

Experiments on tip vortex cavitation show that once σ is reduced sufficiently below σ_i, a well-defined tip vortex cavity is formed and the radius of this cavity, designated by r_0, increases with decrease in σ. The present model was extended to predict the magnitude of r_0 as a function of σ or σ/σ_i by assuming a modified circulation distribution of the form:

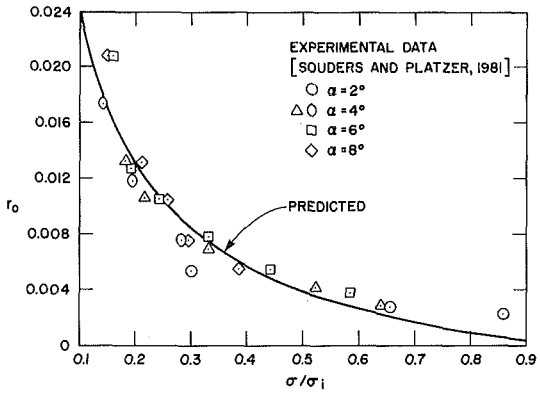

Fig. 2 Comparison of the predicted non-dimensional tip vortex cavity radius, r_0, with the observations by Souders and Platzer. α is the geometric angle of attack.

$$\Gamma/\Gamma_0 = 0.0 \quad 0 < r \le r_0 \tag{21}$$

$$\Gamma/\Gamma_0 = q[1 - e^{-\lambda(r-r_0)^2}] \quad r_0 < r \le r_c \tag{22}$$

$$\Gamma/\Gamma_0 = q[1 - e^{-\lambda(r-r_0)^2} + a(r-r_0)] \quad r_c < r < r_k \tag{23}$$

$$\Gamma/\Gamma_0 = 0.99 \quad r \ge r_k \tag{24}$$

Here again, all radii are non-dimensional with respect to the semi-span, s. This satisfies the conditions that the velocity and the shear stress at the cavity boundary ($r=r_0$) is zero. The condition of zero velocity at the cavity boundary ($r=r_0$) requires justification. This is based on the following argument. If the tangential velocity or circulation is nonzero in the region $0<r\le r_0$, then this circulation must account for some lift on the foil. However, at least in the initial stages of tip vortex cavitation development, the cavity barely touches the hydrofoil tip and per-say there is no vapor/gas flow on any part of the foil. Therefore, even with the presence of a tip vortex cavity, the foil flow is all liquid and the circulation conservation then would be expected to be limited only to the liquid region of the rolled up tip vortex. It is with this reasoning that the vapor/gas part of the tip vortex is assumed to be an inactive region. This, of course, must await experimental confirmation.

In addition, it was assumed that in equations (21) and (24) the basic parameters r_k, a, λ, and q are the same as those in single phase conditions ($r_0=0$). Then, for a given σ, the magnitude of r_0 can be computed to a very good accuracy from,

$$\frac{\sigma}{\sigma_i} = \frac{\displaystyle\int_{r_0}^{r_k} [1 - e^{-\lambda(r-r_0)^2}]^2 \frac{dr}{r^3}}{\displaystyle\int_0^{r_k} [1 - e^{-\lambda r^2}]^2 \frac{dr}{r^3}}. \tag{25}$$

Strictly speaking, some other terms should be included in the above; however, their ommission has very little effect on the final results. This is equivalent to approximating equation (16) by (17). In this sense, if r_k is assumed to be ∞, equation (25) could be obtained on the basis of the single parameter Lamb model. However, the magnitude of r_0 is quite sensitively dependent on the value of λ in this equation. The value of λ, if obtained on the basis of the single parameter Lamb model (see Stanfenbiel [1984]), is by an order of magnitude smaller than what is computed on the basis of the present modified Lamb model. The computed values of r_0, using equations (25) with $\lambda = 4{,}495$ ($q = 0.65$), are computed with the measured values of Souders and Platzer in Fig. 2. The agreement can be considered to be very good.

Summary

A modified Lamb model based on recent work of Staufenbiel has been used to predict the minimum pressure coefficient in a fully rolled-up tip vortex. The model has also been extended to compute the cavity radius of a developed tip vortex cavity. The predictions based on the model compare very favorably with many aspects of tip vortex cavitation observations made by Souders and Platzer on an elliptic planform hydrofoil. The weak point of the model is that the final predictions are very sensitive to small changes in certain parameters of the model.

Acknowledgments

This work was part of a project on hydroacoustics at the St. Anthony Falls Hydraulic Laboratory (SAFHL) sponsored by the Office of Naval Research. This support is gratefully acknowledged. The authors would also like to thank Dr. T. Ikohagi for many helpful discussions on the subject and the reviewers for helpful comments.

References

Kida, T., and Miyai, Y., 1968, "An Alternative Treatment of Lifting-Line Theory as a Perturbation Problem," *ZAMP*, Vol. 29, pp. 591–607.

McCormick, B. W., 1954, "A Study of the Minimum Pressure in a Trailing Vortex System," Ph.D. dissertation, Pennsylvania State University.

McCormick, B. W., 1962, "On Cavitation Produced by a Vortex Trailing from a Lifting Surface," ASME *Journal of Basic Engineering*, Sept. 1962, pp. 369–379.

Souders, W. G., and Platzer, G. P., 1981, "Tip Vortex Cavitation Characteristics and Delay of Inception of a Three-Dimensional Hydrofoil," DTNSRDC, Rpt. No. 81/007, DTNSRDC, Bethesda, MD.

Staufenbiel, R. W., 1984, "Structure of Lift-Generated Rolled-Up Vortices," *Journal of Aircraft*, Vol. 21, pp. 737–744.

Takahashi, R. K., and McAlister, K. W., 1986, "Preliminary Study of a Wing Tip Vortex Using Laser Velocimetry," USAAVSCOM TM-86-A-2, NASA TM 88343.

Uberoi, M. S., 1979, "Mechanisms of Decay of Laminar and Turbulent Vortices," *Journal of Fluid Mechanics*, Vol. 90, pp. 241–255.

Temperature Effects on Single Bubble Collapse and Induced Impulsive Pressure

A. Shima
Professor.
Mem. ASME

Y. Tomita
Research Associate.

Institute of High Speed Mechanics,
Tohoku University,
Sendai, Japan

T. Ohno
Engineer at Fuji Photo Film Co. Ltd.,
Tokyo, Japan

In relation to the temperature effect in cavitation damage, the collapse of a single bubble in water over a wide range of temperatures was experimentally studied. A spark-induced bubble was observed by using a high speed camera and the impulsive pressure caused by the bubble collapse was measured by means of a pressure transducer. As water temperature increases, the motion of a bubble tends to weaken owing to the increase in saturated vapor pressure of water, and the surface configuration of a bubble becomes highly irregular because of thermal instability. The impulsive pressure depends not only on the bubble size and its distance from a solid wall but also on the water temperature. When the water temperature approaches the boiling point of water, the impulsive pressure abruptly decreases with increasing water temperature. The evidence obtained seems to be associated with the known temperature effect on cavitation damage at high water temperature.

1 Introduction

In vibratory cavitation, there is unsolved and very interesting experimental evidence that the curve of weight loss of a material exposed to cavitation versus liquid temperature indicates a maximum at a certain intermediate temperature between the freezing and boiling points of liquid [1, 2]. Some ideas have been suggested for the explanation [2], however, the detailed mechanism is still an open question. Since a similar temperature dependence has been found for sonoluminescence [3], the above mentioned evidence must be related to a peculiar characteristic to the field in fluid.

Knapp [4] demonstrated the good correlation of damage pits with the collapse process of bubbles. Repeated attacks of impulsive pressures caused by individual bubble collapse on a material surface result in its deformation, fracture and finally removal [5]. One of the most important things to understand the mechanism of cavitation damage in detail, therefore, is knowing the mechanism of impulsive pressure generation, especially one caused by the collapse of a bubble cluster. Recently the collapse of an inertia-controlled bubble cluster has been investigated and an important finding has been obtained; that is a concerted collapse of bubble cluster which brings on the significant increase in pressure compared with that caused by a single isolated bubble [6, 7]. On the other hand, much research concerning thermal effects on the behavior of a spherical isolated bubble has been done theoretically [8–13] as well as experimentally [9, 14] until now. The problem has been recently developed by Chahine and Liu [15, 16] who investigated numerically the growth of a bubble cloud in a superheated liquid based on the singular-perturbation approach. However, the dynamics of the bubble cluster is involved even in the region of relatively low temperatures. Because air content in the liquid varies depending on the liquid temperature, it must be more complicated at high liquid temperature owing to the coupled liquid inertia and thermal effects. Viewing that cavitation damage is closely related to the impulsive pressure caused by the bubble collapse, the study of the single bubble collapse based on the pressure measurement, seems to be more important as a first step for the final goal. But, so far, very few papers have been reported on this kind of work [17].

The present study, therefore, deals with an experimental investigation of the bubble collapse and the induced impulsive pressure in a wide range of water temperature. As water temperature increases, the motion of a bubble weakens primarily because of the increase in saturated vapor pressure of water, and the irregularity of a bubble surface becomes evident owing to thermal instability. Further, the impulsive pressure depends not only on the bubble size and its distance from a solid wall but also on the water temperature at around the boiling point of water that is a qualitatively similar tendency to the known temperature effect on cavitation damage at the same region of water temperatures.

2 Experimental Equipment and Methods

A schematic diagram of the experimental setup including the optical system is shown in Fig. 1. A stainless steel cylindrical bubble chamber with dimensions of ϕ 100 × 150 mm is shown in Fig. 2. The outside surface of the chamber is surrounded by a coaxial heating wire and a cooling pipe, which are covered by adiabatic material for keeping the liquid temperature constant. The test liquid was tap water whose bulk temperature T_∞ measured by two thermocouples with an

Contributed by the Fluids Engineering Division and presented at the Cavitation and Multiphase Flow Forum, Atlanta, Ga., May 12–14, 1986 of THE AMERICAN SOCIETY OF MECHANICAL ENGINEERS. Manuscript received by the Fluids Engineering Division November 14, 1986.

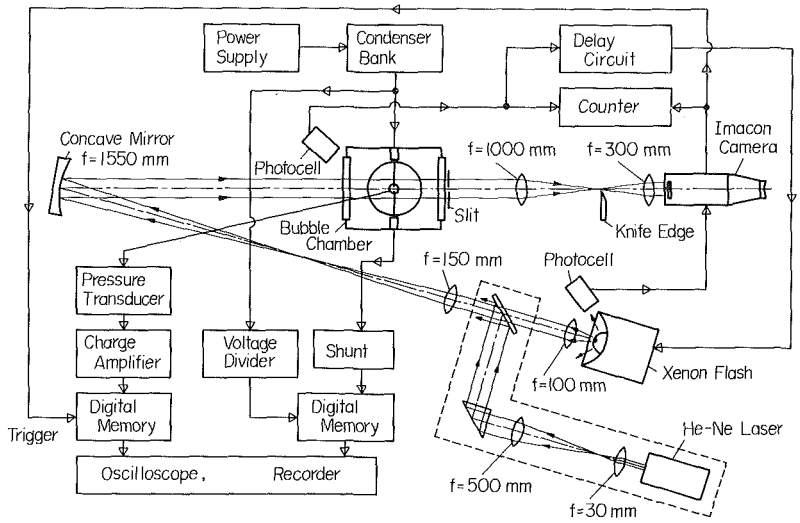

Fig. 1 Schematic diagram of experimental setup

accuracy of ±1K, was automatically adjusted by a temperature controller consisting of a heater and a refrigerator.

A bubble was produced by means of the underwater spark discharge as utilized before by several investigators [18–24]. In the present experiment, an energy E_c for creating a single bubble was determined by changing supply voltage V_c and keeping capacitance C constant ($=0.5\ \mu$F). The motion of the bubble was observed on films by an Imacon high speed camera (John Hadland 790) associated to a Xenon microflash with a duration of about 200 μs as a light source [25, 26]. The camera can be operated either in framing mode or in streaking mode with a slit width of 0.3 mm supplied onto the observation window. The maximum bubble radii R_{max} as well as the bubble collapse times T_c at various temperatures T_∞ were obtained by means of the streaking method. A partial optical system enclosed with a dashed line of Fig. 1, was used for determining distance from an underwater spark gap to a solid surface. Shock waves emitted from bubbles can be clearly seen by means of a schlieren method, which gives a change of the illumination in the image plane of the light source by providing a knife edge. For synchronization with the phenomena the output signal from a photocell receiving the light radiated at the instant of the underwater spark discharge was fed to the camera through a delay circuit. The impulsive pressure generated at bubble collapse was measured with a piezoelectric pressure transducer (Kistler 603B). The pressure transducer was mounted flush in a lucite wall below the electrodes. The impulsive pressure measurements were made for the following three cases, i.e., (1) constant maximum bubble radius (R_{max} = 3.5 mm), (2) constant distance from the electrodes to the solid surface (L = 4 mm) and (3) constant energy for producing a bubble (E_c = 3.3 J).

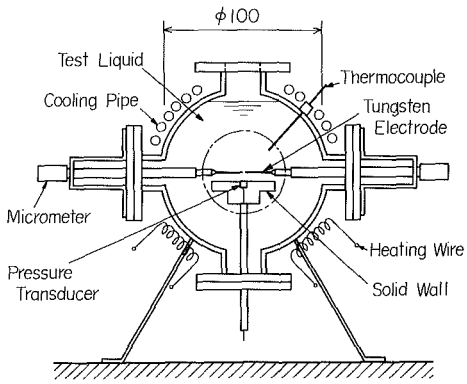

Fig. 2 Bubble chamber

3 Results and Discussion

3.1 Temperature Effect on Bubble Collapse. First, the relationship between R_{max} and T_∞ for various energies E_c was examined and the results are shown in Fig. 3. For constant E_c, the bubble radius becomes larger as liquid temperature increases, because the pressure differences between the inside and outside of a bubble tends to be reduced owing to the increase of saturated vapor pressure with increasing T_∞. Using these results, a bubble of R_{max} = 3.5 mm was produced in an infinite volume of water at various temperatures. Some typical photographs concerning (*a*) bubble behavior and (*b*) shock wave radiation at first collapse of these bubbles are shown in Fig. 4. For water temperatures below 333K, the bubble seems to be primarily controlled by the inertia of water. On the other hand, the collapse of the bubble becomes weak according as

Nomenclature

b = distance from solid surface to bubble center
b_{Rmin} = value of b at minimum bubble volume
$\dot{b}, \ddot{b}$ = db/dt, d^2b/dt^2
C = capacitance
C_∞ = sound velocity of liquid
E_c = charging energy
f = frequency
L = distance from underwater spark gap to solid surface
$p_a(t)$ = pressure in liquid surrounding bubble
p_A = pressure amplitude
p_{max} = maximum impulsive pressure
p_v = vapor pressure of liquid
p_∞ = pressure in unperturbed liquid at infinity
R = bubble radius
R_{max} = maximum bubble radius
R_0 = initial bubble radius
$\dot{R}, \ddot{R}$ = dR/dt, d^2R/dt^2
t = time
T_∞ = liquid temperature
V_c = supply voltage
γ = polytropic index
ω = angular frequency
μ = viscosity of liquid
ρ_∞ = liquid density
σ = surface tension of liquid

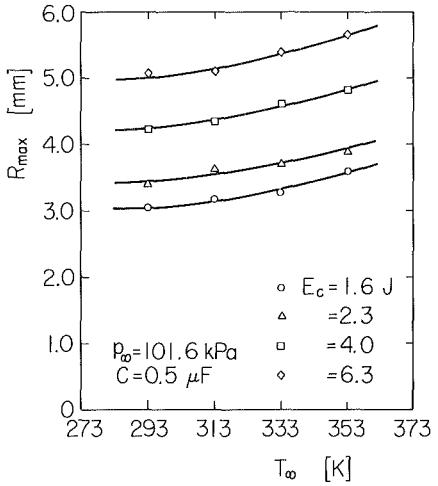

Fig. 3 Relation between maximum bubble radius R_{max} and water temperature T_∞ for various charging energy E_c

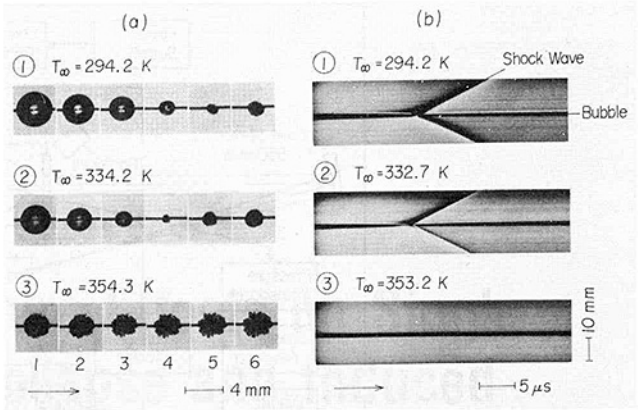

Fig. 4 Behavior of (*a*) a bubble and (*b*) a shock wave at a portion of the first collapse; $L\to\infty$, R_{max} = 3.5 mm, frame interval 10 μs

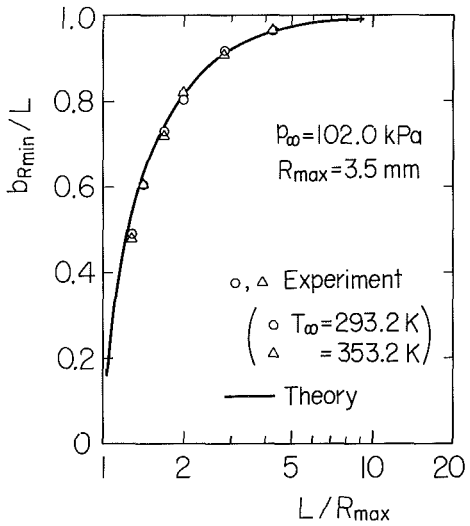

Fig. 5 Effect of water temperature T_∞ on the $b_{Rmin}/L - L/R_{max}$ curve

water temperature T_∞ rises. Because a saturated vapor pressure abruptly increases with increasing T_∞ in the region of high water temperatures, especially above 333K, the pressure difference between the inside and outside of the bubble suddenly drops down resulting in a very small inertia effect. Consequently, the shock wave disappears at T_∞ = 353K. For this condition, close to the so-called heat transfer controlled region [9], the bubble surface is disturbed due to the Taylor instability of the spherical shape [27] combined with the additional thermal instability [28], and finally divided into a large number of minute bubbles.

When a bubble collapses, near a solid wall, a translational motion toward it is induced in the final stage of collapse [29]. Figure 5 shows the relation between the position of the bubble center b_{Rmin} at minimum bubble volume and the dimensionless distance L/R_{max} compared with a previous theory [30]. b_{Rmin} is almost independent of water temperature within the temperature variation between T_∞ = 293K and T_∞ = 353K. This fact can be also confirmed from the good agreement between the experimental data and the theoretical curve, which was obtained out of consideration of thermal effect.

3.2 Temperature Effect on Induced Impulsive Pressure

3.2.1 Case of Constant Bubble Radius (R_{max} = 3.5 mm). The relation between the maximum impulsive pressure p_{max} generated at the first collapse of a bubble and the dimensionless distance L/R_{max} is shown in Fig. 6 for various water temperatures T_∞. For increasing values of L/R_{max}, $dp_{max}/d(L/R_{max}) = 0$ at $L/R_{max} \simeq 0.9$ for all temperatures but 353K as already indicated by the previous report [25] in which data only at room temperature were obtained. When water temperature increases the induced impulsive pressure goes down. For $L/R_{max} > 1.2$, p_{max} keeps the inverse drop-off with increasing L/R_{max} in the inertia controlled region. However, it departs from the L^{-1} dependency in water temperatures higher than 333K. The reason will be discussed in the end of this subsection.

Simultaneous records of bubble collapses and pressure histories at the points (II) and (III) (Fig. 6) are shown in Figs. 7 and 8. In the figures, two cases of temperatures (① T_∞ = 294K and ② T_∞ = 354K) were compared. A liquid microjet penetrates into the bubble interior and impacts on the solid wall. Subsequently, it turns outward as a high speed shear flow on the solid surface (see first frame of Fig. 7(*b*)). Thereafter, impulsive pressures occur. The liquid microjet may intensively impact on the solid wall at the point (III) [31]. However, no appreciable impulsive pressure can be detected owing to the characteristic of the transducer used here [26]. The resulting pressure history possesses a relatively low maximum impulsive pressure but a long duration.

Simultaneous records on streaking pictures and pressure histories at the points (III) and (IV) are shown in Figs. 9 and 10. In the region of (IV), the impact period of a liquid jet shifts to the collapse point of a bubble with decreasing L since the bubble shape becomes hemispherical. In this case, several impulsive pressures occur in an extremely short duration resulting from the interaction between the radial flow of a liquid jet and the contracting bubble surface near the solid wall [31]. The multiple shock waves probably originated through this phenomenon can be seen in the Schlieren pictures (Fig. 9(*b*) ①, ②) even at T_∞ = 352K where no shock waves appeared in $L\to\infty$ case. A steep increase on a pressure history exactly corresponds to the origin of shock waves. In general, a thermal boundary layer is formed during the bubble motion due to the temperature difference between the inside and outside of a bubble, especially it develops rapidly owing to a steep increase in temperature of the bubble interior in the later stage of the collapse [11]. If a bubble is relatively far from a solid surface, the thermal boundary layer is limited in a small region of water surrounding bubble. In this case, therefore, very little heat transfer will take place from the bubble to the solid wall. As water temperature increases, the driving force to collapse a bubble is reduced because of increasing saturated vapor pressure. As a result of the thermal instability as well as the slow moving of the bubble surface, a relatively low impulsive pressure is reached. On the other hand, when a bubble col-

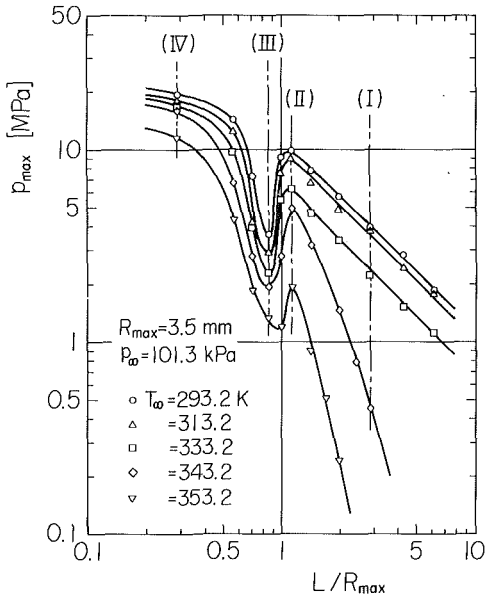

Fig. 6 Effect of water temperature T_∞ on the $p_{max} - L/R_{max}$ curve; R_{max} = 3.5 m

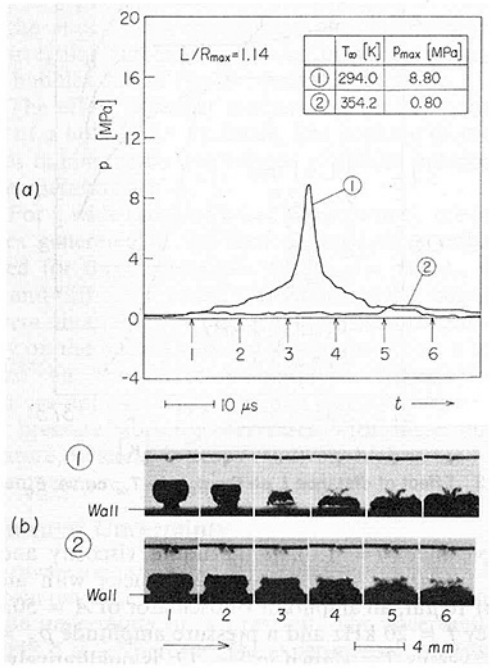

Fig. 7 Simultaneous records on (*a*) a pressure history and (*b*) a bubble collapse at a portion of the first collapse; R_{max} = 3.5 mm, L/R_{max} = 1.14, frame interval 10 μs; ① T_∞ = 294.0K, ② T_∞ = 354.2K

lapses in the neighborhood of a solid boundary, the following situation will be possible; i.e., a thermal boundary layer fully develops and entirely covers over the solid wall. In the later stage of the collapse, a bubble will be in high temperature state compared with the solid wall, so that some part of energy of the bubble dissipate through the solid wall by heat conduction resulting in the temperature reduction of water near the bubble surface.

3.2.2 Case of Constant Distance From the Underwater Spark Gap to a Solid Wall (L = 4 *mm*). Figure 11 shows the p_{max} versus L/R_{max} curve for various T_∞ and R_{max} which are obtained by keeping the distance L constant and changing the maximum bubble radius R_{max} by modifying the input charging energy E_c. The essential tendency is similar to that in Fig. 6 except for the case of T_∞ = 353.2K and for the steeper slope of

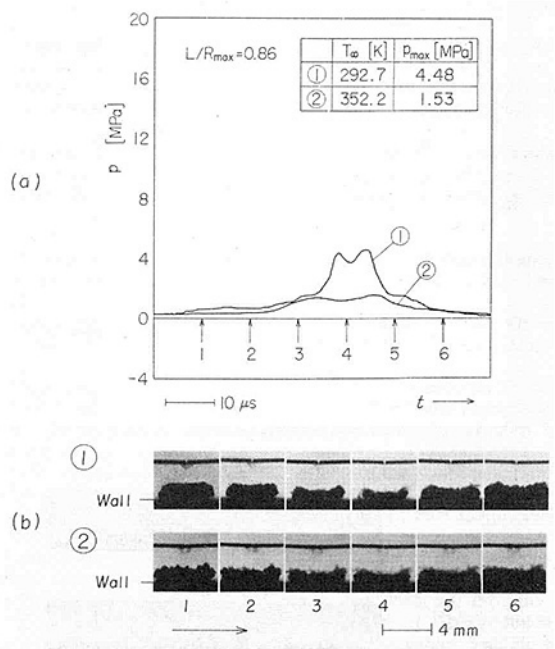

Fig. 8 Simultaneous records on (*a*) a pressure history and (*b*) a bubble collapse at a portion of the first collapse; R_{max} = 3.5 mm, L/R_{max} = 0.86, frame interval 10 μs; ① T_∞ = 292.7K, ② T_∞ = 352.2K

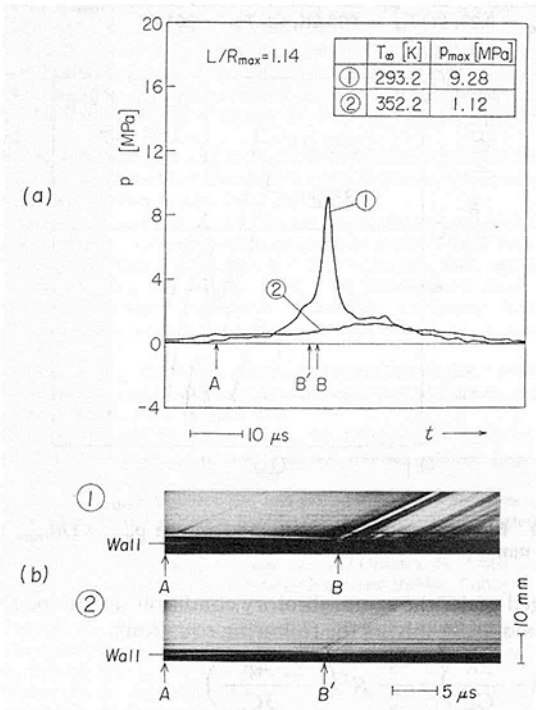

Fig. 9 Simultaneous records on (*a*) a pressure history and (*b*) a shock wave radiation at a portion of the first collapse; R_{max} = 3.5 mm, L/R_{max} = 1.14, ① T_∞ = 293.2K, ② T_∞ = 352.2K

this curve, which is caused by changeable input energy E_c at a constant water temperature. The results clearly indicate that the maximum impulsive pressure p_{max} depends not only on L/R_{max}, where L keeps constant and R_{max} is changeable, but also the water temperature T_∞.

3.2.3 Case of Constant Energy for Producing Bubble (E_c = 3.3 *J*). In this case, R_{max} monotonously increases with increasing T_∞ as already shown in Fig. 3. This experimental evidence is qualitatively similar to that obtained from vibratory cavitation test, in which water temperature is

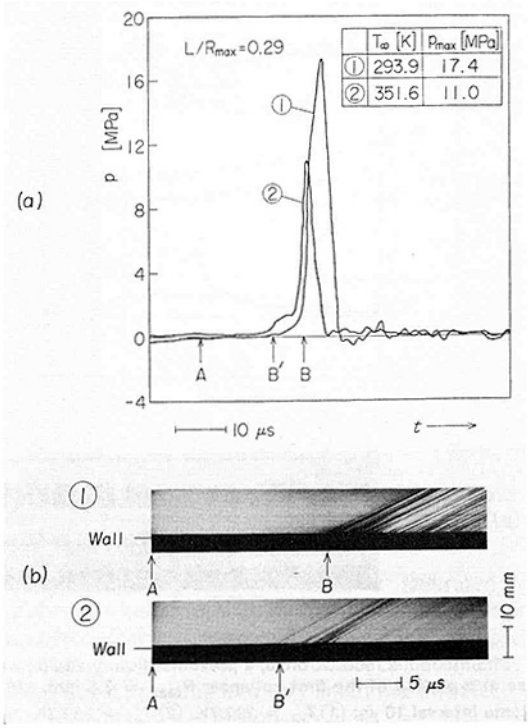

Fig. 10 Simultaneous records on (*a*) a pressure history and (*b*) a shock wave radiation at a portion of the first collapse; R_{max} = 3.5 mm, L/R_{max} = 0.29, ① T_∞ = 293.9K, ② T_∞ = 351.6K

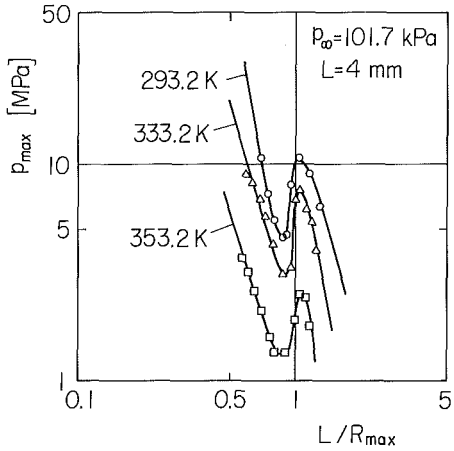

Fig. 11 Effect of water temperature T_∞ on the $p_{max} = L/R_{max}$ curve; L = 4 mm

changed under the same vibratory conditions as can be shown by numerically solving the following equations.

$$R\ddot{R}\left(1-\frac{2\dot{R}}{C_\infty}\right)+\frac{3}{2}\dot{R}^2\left(1-\frac{4\dot{R}}{3C_\infty}\right)+\frac{1}{\rho_\infty}\left\{p_a(t)-p_{r=R}+\frac{R}{C_\infty}(\dot{p}_a-\dot{p}_{r=R})\right\}=0 \quad (1)$$

where

$$p_a(t)=p_\infty-p_A\sin\omega t \quad (2)$$

$$\omega=2\pi f \quad (3)$$

$$p_{r=R}=p_v+\left(p_\infty-p_v+\frac{2\sigma}{R_0}\right)\left(\frac{R_0}{R}\right)^{3\gamma}-\frac{2\sigma}{R}-\frac{4\mu\dot{R}}{R} \quad (4)$$

where the bubble interior was assumed to be isothermal during its whole process and R is the bubble radius, p_∞ and ρ_∞ are the pressure and density in unperturbed liquid at infinity, p_v is the saturated vapor pressure, C_∞ the sound velocity of liquid, R_0 the initial bubble radius, σ the surface tension of liquid, γ the polytropic index (= 1.0), μ the liquid viscosity and ω the angular frequency. For a cavitation nuclei with an initial radius of 10 μm, an amplitude of oscillator of A = 50.8 μm, a frequency f = 20 kHz and a pressure amplitude p_A = 4 p_∞, R_{max}/R_0 versus T_∞, shown in Fig. 12, is qualitatively similar to the result of Fig. 3.

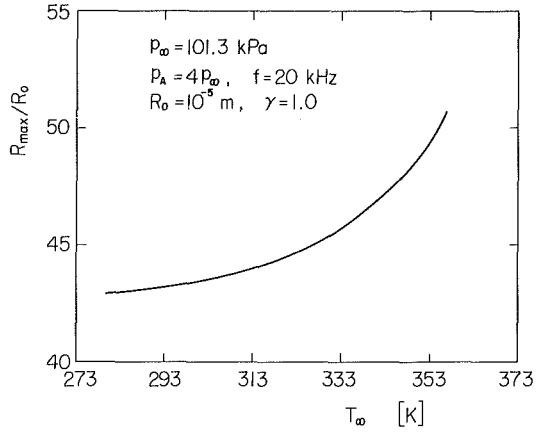

Fig. 12 Variation of a maximum bubble radius R_{max}/R_0 with water temperature T_∞; p_∞ = 101.3KPa, f = 20kHz, R_0 = 10^{-5}m

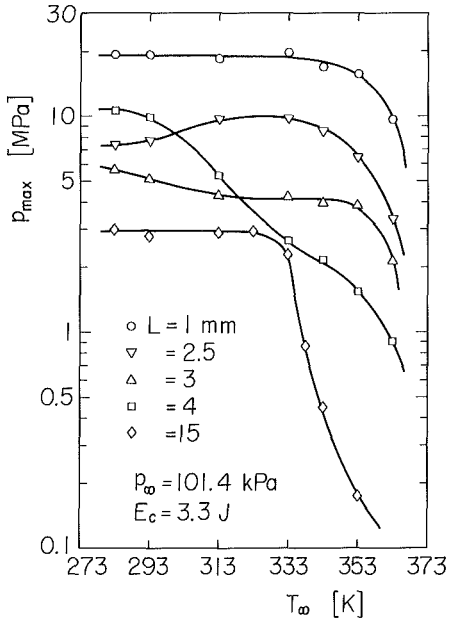

Fig. 13 Effect of distance L on the $p_{max} - T_\infty$ curve; E_c = 3.3J

Figure 13 shows the $p_{max} - T_\infty$ curve for various L while keeping E_c = 3.3J. It is obvious from this result that the induced impulsive pressure p_{max} strongly depends on the location of a bubble from a solid wall. When a bubble is located relatively far from a solid wall (L = 15 mm), the impulsive pressure p_{max} keeps constant up to about 323K, and it suddenly drops down for T_∞ > 333K. The similar tendency is appearing in the $p_{max} - T_\infty$ curve for L = 1 mm, but in this case p_{max} abruptly decreases at a higher water temperature. For the case where bubbles are located in near the solid wall (L = 2.5, 3 and 4 mm), the $p_{max} - T_\infty$ curves indicate various aspects. In particular, in case of L = 4 mm, the $p_{max} - T_\infty$ curve exhibits a transitional aspect which results from the change in the state of a bubble at the maximum expansion, especially its relative distance, L/R_{max}, from the solid wall when water temperature varies. Namely, in the region of low water temperatures, the bubble wall never touches a solid wall during its motion, but it comes near the wall and finally touches it at a certain water

temperature as increasing T_∞. For high temperature region, p_{max} always decreases with increasing T_∞, whenever a bubble collapses. This tendency is exceedingly similar to the temperature effect for cavitation weight loss at higher water temperature. On the other hand, for low water temperatures, the $p_{max} - T_\infty$ curve never drops down abruptly as decreasing T_∞. This is a quite different evidence from the known temperature effect on cavitation damage [1]. Viewing that a great number of cavitation bubbles are created in actual cavitation, for instance in vibratory cavitation [32], it is reasonable to consider that the behavior of the bubble cluster is closely related to cavitation damage. In general, the cluster is significantly influenced by air content which increases as decreasing T_∞. The increase of dissolved air for low water temperature will result in important bubble-bubble interaction contributing to remarkable decrease in impulsive pressure [26]. To clarify the temperature effect on cavitation damage in detail, therefore, the knowledge about interaction between bubbles, as well as the bubble-shock wave interaction, in the wide range of liquid temperatures, should be accumulated.

4 Conclusions

The results obtained are summarized as follows:

(1) The collapse of a bubble in an infinite volume of water becomes weaker with increasing water temperature T_∞ because of increasing saturated vapor pressure. When T_∞ = 353K, the shock wave disappears and the bubble surface makes irregular and finally divides into a large number of minute bubbles due to thermal instability.

(2) The effect of water temperature on the translational motion of a bubble is very small. The position of the bubble center at minimum bubble volume is almost independent of water temperature.

(3) For a wide range of water temperatures, the impulsive pressures generated at the first collapse of a bubble were measured for three cases, i.e., (i) R_{max} = const., (ii) L = const., and (iii) E_c = const. Consequently the following findings were obtained. The induced impulsive pressure depends not only on the bubble size and its distance from a solid wall but also on the water temperature. When the water temperature approaches the boiling point of water, the impulsive pressure abruptly decreases with increasing water temperature, whereas it keeps relatively high value for lower water temperature.

Experimental Uncertainty

Each open circle shown in the figures represents an averaged value from ten data points. The maximum bubble radii in Fig. 3 have an uncertainty of ±5 percent. The uncertainty of the data in Fig. 5 is ±8 percent. The experimental values shown in Figs. 6, 11, and 13 have the same order of uncertainty. In these cases, the relative maximum deviations from the averaged values fall within ±10 percent.

Acknowledgments

Finally, the authors wish to express their thanks to Professor K. Takayama of Tohoku University for his useful suggestions in this work. Assistance received from Mr. N. Miura, Miss M. Sekii, and Miss N. Inomata is acknowledged with thanks.

References

1 Plesset, M. S., "Temperature Effects in Cavitation Damage," ASME *Journal of Basic Engineering*, Vol. 94, No. 3, Sept. 1972, pp. 559-566.

2 Garcia, R., and Hammitt, F. G., "Cavitation Damage and Correlations with Material and Fluid Properties," ASME *Journal of Basic Engineering*, Vol. 89, No. 4, Dec. 1967, pp. 753-763.

3 Taylor, K. J., and Jarman, P. D., "The Temperature Dependence of Sonoluminescence from Water," *British Journal of Applied Physics* (*J. Phys. D*), Vol. 1, 1968, pp. 653-655.

4 Knapp, R. T., "Recent Investigations of the Mechanics of Cavitation and Cavitation Damage," *Trans. ASME*, Vol. 77, 1955, pp. 1045-1054.

5 Knapp, R. T., Daily, J. W., and Hammitt, F. G., *Cavitation*, McGraw-Hill, New York, 1970.

6 Hansson, I., and Mørch, K. A., "The Dynamics of Cavity Clusters in Ultrasonic (Vibratory) Cavitation Erosion," *Journal of Applied Physics*, Vol. 51, No. 9, Sept. 1980, pp. 4651-4658.

7 Chahine, G. L., "Pressure Generated by a Bubble Cloud Collapse," ASME, Cavitation and Polyphase Flow Forum, St. Louis, 1981, pp. 27-31.

8 Plesset, M. S., and Zwick, S. A., "A Nonsteady Heat Diffusion Problem with Spherical Symmetry," *Journal of Applied Physics*, Vol. 23, No. 1, Jan. 1952, pp. 95-98.

9 Florschuetz, L. W., and Chao, B. T., "On the Mechanics of Vapor Bubble Collapse," ASME *Journal of Heat Transfer*, Vol. 87, No. 2, May 1965, pp. 209-220.

10 Prosperetti, S., and Plesset, M. S., "Vapour-Bubble Growth in Superheated Liquid," *Journal of Fluid Mechanics*, Vol. 85, Part 2, Mar. 1978, pp. 349-368.

11 Tomita, Y., and Shima, A., "The Effect of Heat Transfer on the Behavior of a Bubble and Impulse Pressure in a Viscous Compressible Liquid," *Zeitschrift fur angewandte Mathematik und Mechanik*, Bd. 59, Heft 7, July 1979, S.297-306.

12 Fujikawa, S., and Akamatsu, T., "Effects of the Non-Equilibrium Condensation of Vapour on the Pressure Wave Produced by the Collapse of a Bubble in a Liquid," *Journal of Fluid Mechanics*, Vol. 97, Part 3, Apr. 1980, pp. 481-512.

13 Matsumoto, Y., and Beylich, A. E., "Influence of Homogeneous Condensation Inside a Small Gas Bubble on Its Pressure Response," ASME JOURNAL OF FLUIDS ENGINEERING, Vol. 107, No. 2, June 1985, pp. 281-286.

14 Dergarabedian, P., "The Rate of Growth of Vapor Bubbles in Superheated Water," ASME *Journal of Applied Mechanics*, Vol. 20, No. 4, Dec. 1953, pp. 537-545.

15 Chahine, G. L., and Liu, H. L., "Collective Effects on the Growth of Vapor Bubbles in a Superheated Liquid," ASME JOURNAL OF FLUIDS ENGINEERING, Vol. 106, No. 4, Dec. 1984, pp. 486-490.

16 Chahine, G. L., and Liu, H. L., "A Singular-Perturbation Theory of the Growth of a Bubble Cluster in a Superheated Liquid," *Journal of Fluid Mechanics*, Vol. 156, July 1985, pp. 257-279.

17 Board, S. J., and Kimpton, A. D., "Spherical Vapour Bubble Collapse," *Chemical Engineering Science*, Vol. 29, 1974, pp. 363-371.

18 Harrison, M., "An Experimental Study of Single Bubble Cavitation Noise," *Journal of Acoustical Society of America*, Vol. 24, Nov. 1952, pp. 776-782.

19 Jones, I. R., and Edwards, D. H., "An Experimental Study of the Forces Generated by the Collapse of Transient Cavities in Water," *Journal of Fluid Mechanics*, Vol. 7, Part 4, Apr. 1960, pp. 596-609.

20 Naudé, C. F., and Ellis, A. T., "On the Mechanism of Cavitation Damage by Nonhemispherical Cavities Collapsing in Contact with a Solid Boundary," ASME *Journal of Basic Engineering*, Vol. 83, No. 4, Dec. 1961, pp. 648-656.

21 Shutler, N. D., and Mesler, R. B., "A Photographic Study of the Dynamics and Damage Capabilities of Bubbles Collapsing Near Solid Boundaries," ASME *Journal of Basic Engineering*, Vol. 87, No. 3, Sept. 1965, pp. 511-517.

22 Gibson, D. C., "Cavitation Adjacent to Plane Boundaries," *Proceedings of 3rd Australasian Conference on Hydraulics and Fluid Mechanics*, Institution of Engineer, Sydney, 1968, pp. 210-214.

23 Kling, C. L., and Hammitt, F. G., "A Photographic Study of Spark-Induced Cavitation Bubble Collapse," ASME *Journal of Basic Engineering*, Vol. 94, No. 4, Dec. 1972, pp. 825-833.

24 Chahine, G. L., Courbière, P., and Garnaud, P., "Correlation Between Noise and Dynamics of Cavitation Bubbles," *Proceedings of 6th Conference on Fluid Machinery*, Budapest, Hungary, Sept. 1979, pp. 200-210.

25 Shima, A., Takayama, K., Tomita, Y., and Ohsawa, N., "Mechanism of Impact Pressure Generation from Spark-Generated Bubble Collapse Near a Wall," *AIAA Journal*, Vol. 21, No. 1, Jan. 1983, pp. 55-59.

26 Tomita , Y., Shima, A., and Ohno, T., "Collapse of Multiple Gas Bubbles by a Shock Wave and Induced Impulsive Pressure," *Journal of Applied Physics*, Vol. 56, No. 1, July 1984, pp. 125-131.

27 Plesset, M. S., and Mitchell, T. P., "On the Stability of the Spherical Shape of a Vapor Cavity in a Liquid," *Quarterly of Applied Mathematics*, Vol. 13, 1955, pp. 419-430.

28 Hsieh, D. Y., "On the Dynamics of Nonspherical Bubbles," ASME *Journal of Basic Engineering*, Vol. 94, No. 3, Sept. 1972, pp. 655-665.

29 Cole, R. H., *Underwater Explosions*, Princeton Univ. Press, Princeton, N.J., 1948.

30 Shima, A., Tomita, Y., and Takahashi, K., "The Collapse of a Gas Bubble Near a Solid Wall by a Shock Wave and the Induced Impulsive Pressure," *Proceedings of the Institution of Mechanical Engineers*, Vol. 198C, No. 8, 1984, pp. 81-86.

31 Tomita, Y., and Shima, A., "Mechanisms of Impulsive Pressure Generation and Damage Pit Formation by Bubble Collapse," *Journal of Fluid Mechanics*, Vol. 169, Aug. 1986, pp. 535-564.

32 Sanada, N., Ikeuchi, J., Takayama, K., and Onodera, O., "Generation and Propagation of Cavitation Induced Shock Waves in an Ultrasonic Vibratory Testing," *Proceedings of the 14th International Symposium on Shock Tubes and Shock Waves*, edited by R. D. Archer and B. E. Milton, New South Wales University Press, Sydney, 1983, pp. 405-412.

Comparison of Holographic and Coulter Counter Measurements of Cavitation Nuclei in the Ocean

T. J. O'Hern[1]

L. d'Agostino

A. J. Acosta

Department of Engineering and Applied Sciences, California Institute of Technology, Pasadena, Calif. 91125

Holographic and Coulter Counter detection techniques were jointly used to measure the concentration density distribution of cavitation nuclei in the ocean. Comparison of the two techniques indicates that Coulter Counter analysis measures particulate contents up to an order of magnitude smaller than indicated by the holographic method and may also produce a distorted concentration density distribution. Several possible explanations of the observed discrepancies are proposed and discussed, including fundamental differences between the in situ holographic samples and the collected samples examined with the Coulter Counter, differences between the unknown electrical conductivity of the measured particles in the sea water samples and the non-conductive polystyrene spheres used to calibrate the Coulter Counter, the rupture of aggregate particles in the flow through the Coulter Counter orifice, the effect of electronic noise on the Coulter Counter signal, and the influence of statistical sampling error. The particle number concentration density distributions decrease approximately with the fourth power of the particle radius in the observed size range of 10 to 50 μm radius. Both sets of data indicate an increase in particle concentration near the bottom of the thermocline, and the holographic bubble concentrations also indicate a similar behavior. Much higher concentrations of particles were detected in the ocean, according to the holographic analysis, than in typical cavitation test facilities. Consideration of the static mechanical equilibrium of individual air bubbles suggests that the average tensile strength of the ocean waters examined in this study is not larger than about 2000 Pa and occasionally as low as about 100 Pa.

1 Introduction

The maximum tensile stress of liquids is considerably reduced by the presence of weak spots, generically called nuclei, which act as preferential sites for the occurrence of liquid rupture. These nuclei have been the subject of considerable research effort, yet their exact nature and origin have not been firmly established. However, it has been recognized that bubbles, some kinds of solid particles and gas pockets inside crevices and cracks on the surface of particulates suspended in the liquid can act as cavitation nuclei and that their effect usually dominates that of the nuclei located at the liquid boundaries.

The presence of nuclei is particularly important in technical applications because they control the onset and the development of cavitation, which is a generally undesirable phenomenon due to the severe limitations it imposes on the performance of hydraulic machinery. The liquid characteristics which affect the occurrence of cavitation through their influence on the nuclei population are collectively called liquid quality. For the purpose of cavitation research the concentration of nuclei in the liquid and their dynamic behavior when exposed to a change of pressure are thought to be of special importance in trying to predict cavitation inception and to deduce scaling laws capable of correlating the results of model tests to full-scale operation. Not all the nuclei respond in the same way to a change of the surrounding pressure. The dynamic properties of gas bubbles in mechanical equilibrium can be directly related to their size, so in this case the liquid quality is adequately described by the nuclei concentration distribution as a function of bubble size. Traditionally the concentration density distribution has also been used in the literature to characterize the liquid quality even when the main source of nuclei is represented by particles, whose dynamic behavior cannot be directly related to their geometry. In this case the size measurements of particulates contained in liquids still provides an upper limit for the concentration of potentially active cavitation nuclei. Significant efforts have been made to develop suitable methods of nuclei detection in liquids, based on various physical principles. In general the results obtained using these methods are in substantial qualitative agreement, but they often differ significantly under the quantitative point of view.

Ocean waters are known to contain the above nucleation

[1]Present address: Fluid and Thermal Sciences Department, Sandia National Laboratories, Albuquerque, New Mexico 87185.

Contributed by the Fluids Engineering Division for publication in the JOURNAL OF FLUIDS ENGINEERING. Manuscript received by the Fluids Engineering Division January 28, 1987.

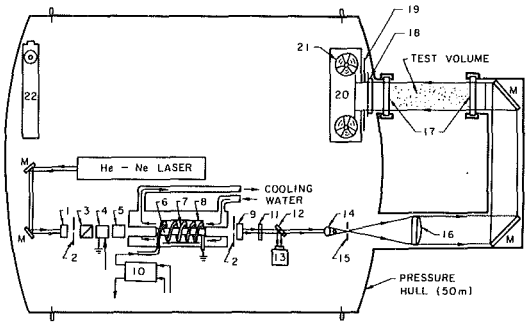

1. BACK MIRROR
2. IRIS APERTURE
3. POLARIZER
4. POCKELS CELL
5. POLARIZER (OPTIONAL)
6. RUBY ROD
7. XENON FLASH LAMP
8. REFLECTOR
9. FRONT MIRROR-SAPPHIRE ETALON
10. TRIGGER TRANSFORMER
11. NEUTRAL DENSITY FILTER
12. BEAM SPLITTER (4% REFLECTIVITY)
13. PIN DIODE
14. MICROSCOPE OBJECTIVE
15. SPATIAL FILTER-10μ PINHOLE
16. COLLIMATING LENS
17. GLASS WINDOWS
18. INTERFERENCE FILTER
19. SHUTTER
20. AUTOMATIC FILM DRIVE
21. HOLOGRAPHIC FILM SPOOLS
22. AUTO COLLIMATOR
M. MIRROR

Fig. 1 Line drawing of the holographic camera system mounted inside the submersible hull

agents as well as many others of organic origin. These waters represent a very interesting environment for cavitation research because of their great technical importance in various fields of applied sciences such as, for example, naval hydrodynamics, ship propulsion, underwater acoustics and optics. Detailed knowledge of the sea water liquid quality is essential for the simulation of marine conditions in the laboratory and for the scaling of model tests to prototype operation. However, relatively little is known about nuclei in marine environments because, due to the inherent experimental difficulties, there are not many reported studies in the literature on this subject. The various types of nuclei found in the ocean are of interdisciplinary interest far beyond cavitation, leading previous researchers to separately explore bubbles (Medwin, 1977; Thorpe, 1982), particles (Carder et al., 1982) and organisms (Pieper and Holliday, 1984). A review of the work on nuclei detection in ocean waters pertaining to cavitation is included in Billet, 1985. In this paper we report the application and compare the results of two of these methods, namely holographic and Coulter Counter detection, to the monitoring and sizing of cavitation nuclei in the ocean.

2 Holographic Experimental Apparatus

The holographic investigation involves in situ optical recording of ocean water samples for later analysis and derivation of the size and concentration of both microbubbles and particulate matter. A sketch of the system used for recording Fraunhofer holograms of ocean water samples is depicted in Fig. 1, which shows a modified version of the system first described by Katz et al., 1984. Detailed descriptions of the Fraunhofer holographic process are available in several texts and articles (see for example Collier et al., 1971 and De Velis et al., 1966) so only an elementary description will be given here. A pulsed ruby laser is used as the coherent light source for hologram recording. The laser is mounted inside a submersible hull with windows through which the expanded laser beam passes to illuminate an external water sample. Particles in the illuminated sample scatter a portion of the laser beam, while the remaining portion passes undiffracted through the sample. The hologram is a record of the pattern formed by interference of the diffracted and undiffracted laser light on a high resolution film. Maximum submersion is presently limited to 33.5 m by the electrical cables controlling and monitoring the laser and associated equipment.

Holographic reconstruction is accomplished by illuminating the developed hologram with a collimated continuous wave He-Ne laser beam. The hologram acts as a diffraction grating to produce three-dimensional real and virtual images of the original volume. Measurements are made by using a closed circuit vidicon system to examine a highly magnified portion of the real image. The resolution is approximately 5 μm. Discrimination of bubbles from solid particulates is important in monitoring cavitation nuclei and is made by visually examining the focused bubble image for roundness, brightness, and presence of a dark central spot due to the focusing effect of the bubble geometry. No attempt is made to establish the nature of nuclei with radii smaller than 10 μm.

Holographic determination of nuclei size is made by focusing a 220X magnified image of each nucleus on the reconstruction system monitor. At the focused plane, a major and minor diameter can be directly measured for non-circular objects. For purposes of comparison with the Coulter Counter results, the volume of the holographically detected particles is computed by assuming an ellipsoidal shape with the length of the third axis taken as the geometric mean of the two measured values, or, in cases of long thin objects, by assuming a cylindrical shape. The radius of a sphere of equal volume is then calculated.

3 Coulter Counter Experimental Apparatus

The measurement of particulate matter in the sea water was carried out using the particle sizing and counting instrumentation of the Department of Environmental Engineering of the

Nomenclature

a = particle cross-sectional area
A = Coulter Counter orifice cross-sectional area
c = MCA channel index corresponding to calibration radius R_c
i, j = MCA channel index
l = particle length
L = Coulter Counter orifice length
$n(R)$ = nuclei number concentration density distribution function
$N(R)$ = concentration of nuclei with radius smaller than R
N_g = number of nuclei counts in each radius group
N_{tot} = total particle concentration in the measured radius range
p_o = bubble equilibrium external pressure
p_v = liquid vapor pressure
$(p_v - p)_{\text{cr}}$ = bubble critical tension
R = particle radius
R_c = radius of Coulter Counter calibration particles
R_i, R_j = particle radius corresponding to channel i, j of MCA
R_o = bubble equilibrium radius
ΔR_{or} = change of Coulter Counter orifice electrical resistance
S = bubble surface tension
T = liquid temperature
V_p = particle volume
V_s = liquid sample volume
α, β = PSA calibration constants
σ = liquid electrical conductivity
σ' = particle electrical conductivity

California Institute of Technology. This system includes a Model B Coulter Counter shielded in a grounded Faraday cage, a Hewlett Packard 1208B oscilloscope, a Nuclear Data Particle Sizing Amplifier (PSA), a Multi-Channel Analyzer (MCA) for sorting of the signal amplitudes and a Teletype for output of the data. The apparatus has been developed for monitoring the particulate content of natural and laboratory waters and is described in detail by Hunt, 1980. Here the principles of operation of the system and the procedure used for computing the particle size distributions are briefly reviewed to the extent needed for the interpretation of the results presented in this paper.

In the Coulter Counter a known volume of the sampled liquid is forced through a small orifice in an electrically insulating medium. When an electric field is established in the conducting liquid across the orifice, inhomogeneities (here generally called particles regardless of their true nature) whose electrical resistivity is different from that of the surrounding liquid can be detected, counted and sized by the perturbation they induce in the electrical resistance across the orifice. The amplitude of the electrical signal is approximately proportional to the volume of the particle as long as its dimensions are less than about 40 percent of the orifice diameter. The signal amplitude also depends on the orifice diameter, electrical excitation, signal amplification and on the conductivities of the liquid and of the particle. Due to finite lower resolution, different electronic settings and orifice diameters are needed to measure relatively wide size distributions.

In the present apparatus the Coulter Counter pulse signal is amplified by the PSA, whose output is proportional to the logarithm of the volume of the sampled particle through two adjustable gain constants. The MCA then sizes the incoming pulses according to their amplitude and stores the corresponding counts in 128 separate channels. At the same time the MCA data are also displayed on the oscilloscope. During each run a preset volume of liquid is sampled. Data from multiple consecutive runs can be summed in the MCA in order to reach the required number of counts for a statistically significant measurement of the particle population. Because of the logarithmic response of the PSA, particles of radius R are counted in the channel of index $i = \alpha + \log_\beta R^3$. The calibration constants α and β are determined by sampling two or more suspensions of monodisperse particles of known size and electrical conductivity. Ideally in this case all the counts should be concentrated in just one channel, but in practice the distribution is broader and the channel corresponding to the mode of the distribution is used for calibration purposes. In this process care must be taken to correctly isolate the mode, since aggregation of two or more particles is possible and can cause misleading results. Then, if R_c is the radius of the calibration particles and c the corresponding channel index, the radius corresponding to any channel i is:

$$R_i = R_c \beta^{(i-c)/3}$$

The system was initially calibrated with monodisperse suspensions of electrically non-conductive ($\sigma' < 10^{-16}$ mho/cm) polystyrene latex spheres (Duke Scientific Corporation) in filtered sea water at room temperature ($\sigma \simeq 0.0463$ mho/cm) for given electronic settings (current excitation and signal amplification) and orifice diameter. The size distribution of the calibration particles reported by the manufacturer is very nearly Gaussian, with modal diameters of 19.1 μm, 49.4 μm and 99.1 μm and standard deviations 1.4 μm, 2.5 μm and 4.8 μm respectively. Only one orifice of 140 μm diameter was used with two different electronic settings to cover the particle radius range from about 10 μm to about 50 μm. This choice ensures adequate sensitivity and linearity of the instrument over the particle size range of interest and reduces the danger of disintegration of aggregate particles during their transit through the orifice (see Section 6) or of frequent orifice clogging. The calculated logarithmic bases of the PSA agreed within the achievable experimental accuracy with the values obtained with the same apparatus by previous investigators. At high amplification levels the electronic noise determines the maximum useful sensitivity and, together with the characteristics of the MCA, limits the measurement range to a maximum to minimum radius ratio of about 4.

4 Data Reduction

In cavitation research literature the liquid quality is usually expressed in terms of the nuclei number concentration density distribution function:

$$n(R) = \frac{dN}{dR} \tag{1}$$

where $N(R)$ is the concentration (in counts per volume) of nuclei with radius smaller than R. In practice $n(R)$ is measured by grouping together adjacent radii counts until a predetermined number of counts N_g is reached. This value is then divided by the corresponding radius range and sampled volume, V_s. Thus, if the nuclei radii are ordered by decreasing size and R_j is the maximum radius of the group:

$$n(R) \simeq \frac{N_g}{V_s(R_j - R_{j+N_g})} \tag{2}$$

The statistical error associated with this procedure is uniform and depends only on the size of the groups, N_g. Assuming that the occurrence of nuclei in the sample volume is a Poisson process, as it would be if the nuclei were randomly distributed and spatially uncorrelated, the estimate of the relative r.m.s. error in the computation of the concentration density distribution is equal to $1/\sqrt{N_g}$. The nominal radius R of each group is defined as the geometric mean of the minimum and maximum values of the radii of the group. This choice usually minimizes the difference between the observed total concentration of particles and the value calculated by integrating the measured nuclei number distribution.

The above reduction procedure differs slightly from the more common way of computing the concentration distribution density based on the number of counts observed in each prefixed interval subdividing the size range. First, it assures that the statistical error due to the finite number of counts of the sampled population is uniform for all the computed data points. Furthermore, by adjusting the size interval to the occurrence of the observed data, it avoids the upward bias which occurs when sparse data are assigned to fixed size intervals and zero counts are neglected, instead of being averaged with the neighboring ones over a wider size range. Finally, it preserves the information on the relative density of the distribution of the available data as a function of size, which would otherwise be lost.

5 Ocean Tests

Ocean tests were performed in late August 1985 at two locations near Santa Catalina Island, southwest of Los Angeles (see Fig. 2) using the 65 foot R/V Seawatch operated by the Institute for Marine and Coastal Studies of the University of Southern California. At each site holograms were recorded at various depths and sea water samples were collected with Nansen bottles for later Coulter Counter analysis. At approximately the same time standard oceanographic measurements were made, including Secchi disk casts together with transmissometer and salinity-temperature-depth (STD) profiles. Holographic data were collected only while anchored or drifting to avoid recording of artifact boat-generated bubbles. The water samples for Coulter Counter analysis were trans-

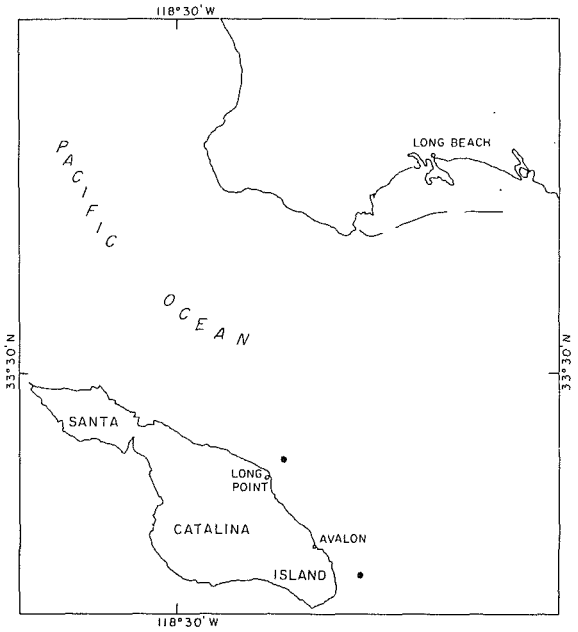

Fig. 2 Map of the Los Angeles coastal area indicating the two test sites, off Long Point at 33°24′47″ N, 118°21′45″ W and east of Santa Catalina Island at 33°18′30″ N, 118°17′12″ W

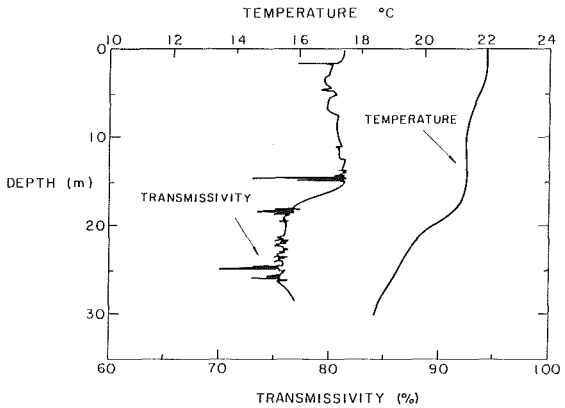

Fig. 3 Temperature and tranmissivity profiles for the test site off Long Point, Santa Catalina Island

ferred to opaque polyethylene bottles, kept refrigerated while on board in order to reduce biologic alteration as much as possible, stored overnight at ambient conditions to reach room temperature and processed within 24 hours. All samples appeared extremely clear, with no visible deposits in the bottles. Each water sample was stirred with a magnetic agitator for a few minutes immediately prior to analysis in order to eliminate any stratification effects and to restore the sample uniformity, taking care not to entrain bubbles in the process. Since excessive agitation may disrupt existing particulates and thus be itself a source of error, no reliable information is available on the effect of the degree of stirring on the nuclei concentration measured by the Coulter Counter.

The first test location was off Long Point, Santa Catalina Island. The boat drifted in waters ranging from 132 to 228 m depth during the two hours while holograms were being recorded. The water was quite clear, with the Secchi disk visible to 17 m. Sea state was 0 to 1, with less than 0.3 m swells, and no wind. Temperature and transmissivity profiles are presented in Fig. 3. Thirty holograms were recorded, sampling the water column from the surface to 32 m. The second test location was off the eastern point of Santa Catalina Island.

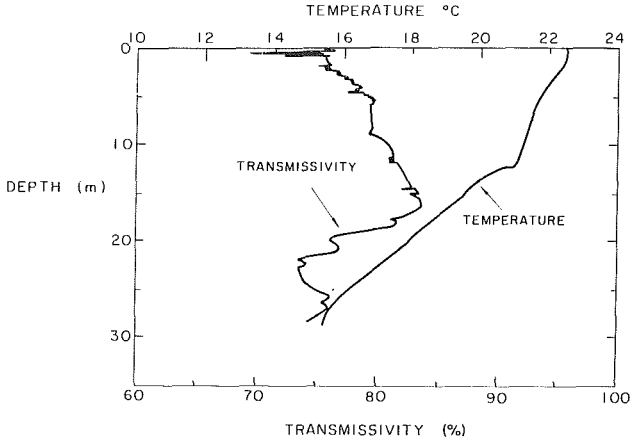

Fig. 4 Temperature and transmissivity profiles for the test site off east Santa Catalina Island

The sea floor depth was 92.7 m, Secchi disk visibility was 19 m, with sea state and wave activity the same as at the first test location. Temperature and transmissivity profiles are presented in Fig. 4. Fourteen holograms were recorded at this station, all at either 27.4 or 32 m.

6 Experimental Results and Discussion

For the purpose of cavitation research the most important nuclei are the largest ones which usually have smaller critical tensions and whose effects in cavitating flows therefore tend to dominate those of the smaller, generally less susceptible nuclei. For this reason the present paper focuses on nuclei of relatively large radius (more than 10 μm), unlike most previous investigations of particulate content of the ocean which used similar optical or electrical detection techniques.

(a) **Observations of Particulates.** Some results of particulate concentrations in the ocean obtained by holographic and Coulter Counter analysis of sea water from the same locations and at comparable depths and time are shown in Figs. 5 through 8. Data are expressed in terms of the concentration density distribution, $n(R)$, as a function of the particle radius, R, obtained as explained in Section 4. Here the number of radius counts per group is chosen as $N_g = 4$ in order to reduce both the maximum size range of each data group and the statistical error of the computed values of the concentration density distribution. The corresponding estimate of the relative r.m.s. error of the data is 50 percent. The Coulter Counter analysis was carried out on 20 ml water samples using two electronic settings of different sensitivity in order to extend as much as possible the radius range of the measurement. In the computation of the concentration density distribution from holographic records the sample volumes examined were on the order of 1 ml for nuclei from 10 to 25 μm radius and 100 ml for larger sizes. Since the sea water samples were maintained at atmospheric pressure for about 24 hours before being processed with the Coulter Counter, any existing bubbles had ample time to grow to their new equilibrium size and rise to the surface or dissolve. Indeed, no bubbles with radii larger than 10 μm were observed at the time of examination. On the other hand, the decompression effect on solid particulates both of mineral and organic origin is expected to be small in consideration of their low compressibility. Therefore, for better comparison of the results obtained with the two methods, the bubble population determined holographically has not been included in the data of Figs. 5 through 8, but will be discussed separately below.

The holographic results are consistently higher than the

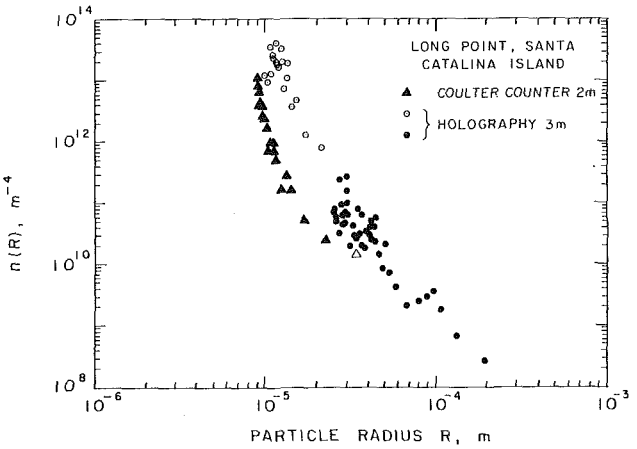

Fig. 5 Number concentration density distributions of particulates, *n(R)*, in the waters off Long Point, Santa Catalina Island, as a function of the particle radius, *R*. The number of radius counts per group is $N_g = 4$ and the expected r.m.s. error is 50 percent. Holographic data (circles) were recorded at 3 m depth with sampling volumes: 1 (open symbols) and 150 ml (solid symbols). Coulter Counter data (triangles) were obtained analyzing 20 ml water samples from 2 m depth with different sensitivity: high (solid symbols) and low (open symbols).

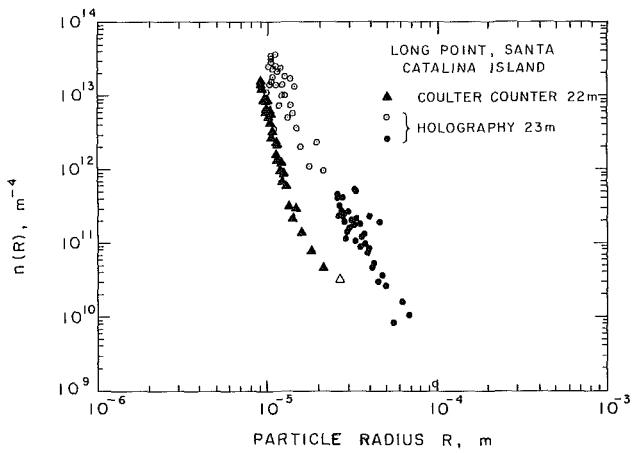

Fig. 6 Number concentration density distributions of particulates, *n(R)*, in the waters off Long Point, Santa Catalina Island, as a function of the particle radius, *R*. The number of radius counts per group is $N_g = 4$ and the expected r.m.s. error is 50 percent. Holographic data (circles) were recorded at 23 m depth with sampling volumes: 1.6 (solid symbols) and 54 ml (open symbols). Coulter Counter data (triangles) were obtained analyzing 20 ml water samples from 22 m depth with different sensitivity: high (solid symbols) and low (open symbols).

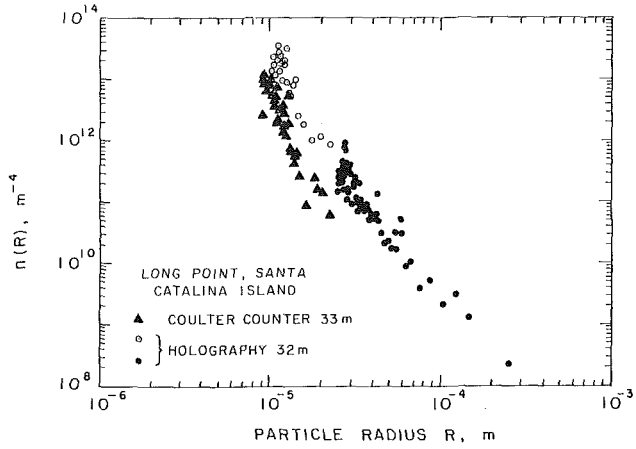

Fig. 7 Number concentration density distributions of particulates, *n(R)*, in the waters off Long Point, Santa Catalina Island, as a function of the particle radius, *R*. The number of radius counts per group is $N_g = 4$ and the expected r.m.s. error is 50 percent. Holographic data (circles) were recorded at 32 m depth with sampling volumes: 1.6 (open symbols) and 79 ml (solid symbols). Coulter Counter data (triangles) were obtained analyzing 20 ml water samples from 33 m depth with different sensitivity: high (solid symbols) and low (open symbols).

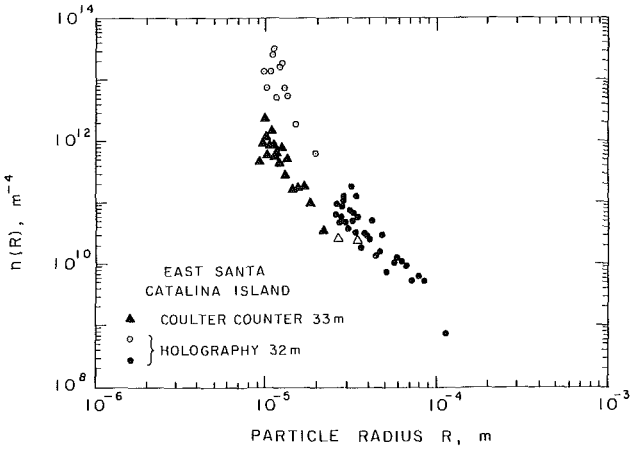

Fig. 8 Number concentration density distributions of particulates, *n(R)*, in the waters off east Santa Catalina Island as a function of the particle radius, *R*. The number of radius counts per group is $N_g = 4$ and the expected r.m.s. error is 50 percent. Holographic data (circles) were recorded at 32 m depth with sampling volumes: 0.9 (open symbols) and 100 ml (open symbols). Coulter Counter data (triangles) were obtained analyzing 20 ml water samples from 33 m depth with different sensitivity: high (solid symbols) and low (open symbols).

ones deduced using the Coulter Counter by as much as one order of magnitude. This fact is not surprising in view of the following considerations. First, the sizing procedure of the holographic detection method may tend to slightly overestimate the equivalent volume radius of particles with highly irregular shapes. However, apart from this small effect, since the holographic results are determined by visual inspection of a magnified image recorded in situ and no calibration is involved in the measurement process, there is little reason to doubt their validity. Second, the sampling of the Nansen bottles for Coulter Counter analysis differs from the recording of holographic data in both depth (within one meter), horizontal location (within five meters, neglecting drift) and time (less than one hour). Fluctuations of the particle population over relatively small distances are known to exist in ocean waters (Pieper and Holliday, 1984). These fluctuations do not introduce a systematic error, yet they may have contributed to some of the observed differences between the Coulter Counter and holographic data. However, in our opinion the most likely and important reason for the observed discrepancy in the results of the two detection techniques is the fundamental difference between the unknown electrical conductivity of the measured particles in the sea water samples and the nonconductive particles used to calibrate the Coulter Counter. In order to estimate the importance of this effect, let us consider a small cylindrical particle of cross-sectional area a, length l and electrical conductivity σ' suspended in a liquid of electrical conductivity σ at the center of a cylindrical orifice of cross-sectional area $A \gg a$ and length $L \gg l$. Then, from a simplified one-dimensional electrical model where the resistance of the particle, $l/a\sigma'$, is in parallel with that of the surrounding liquid, $l/(A-a)\sigma$, the total change of the electrical resistance across the orifice due to the presence of the particle can be expressed by:

$$\Delta R_{or} = \frac{(1-\sigma'/\sigma)V_p/A^2\sigma}{1-(1-\sigma'/\sigma)a/A} \tag{3}$$

where $V_p = al$ is the particle volume. For small particles the Coulter Counter signal is therefore proportional to

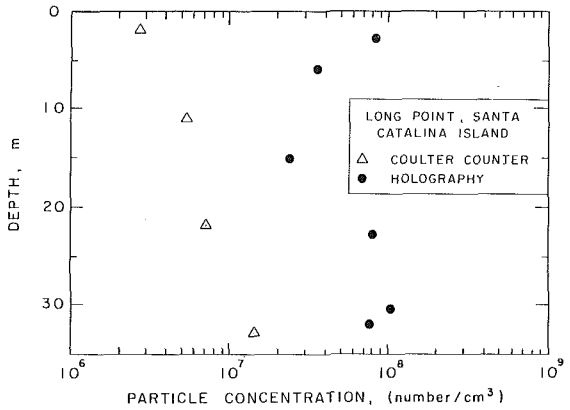

Fig. 9 Particle number concentration depth profiles off Long Point, Santa Catalina Island from holographic (circles) and Coulter Counter data (triangles) in the radius range from 10 to 50 μm

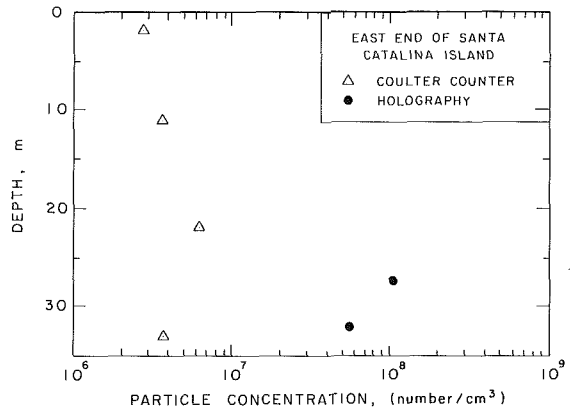

Fig. 10 Particle number concentration depth profiles off east Santa Catalina Island from holographic (circles) and Coulter Counter data (triangles) in the radius range from 10 to 50 μm

$V_p(1-\sigma'/\sigma)$. Then, for example, the size of particles whose electrical conductivity is equal to 90 percent of the conductivity of the suspending liquid would be underestimated by one order of magnitude. Indeed relatively high values of the electrical conductivity are not unrealistic in our case since most of the particles suspended in unpolluted oceans are of organic origin (Sheldon et al., 1972) and therefore their electrical conductivity is likely to be of the same order of magnitude as that of the surrounding waters (Carder et al., 1974).

The concentration density distributions determined using the Coulter Counter are steeper than those determined holographically, as indicated by Figs. 5 through 8. A possible reason for this difference is the rupture of the aggregate particles due to the shearing and elongational strains in the collection of the samples and in their flow through the Coulter Counter orifice (Gibbs, 1982; Hunt, 1980). The rupture of aggregate particles would increase the number of counts at smaller size ranges and therefore steepen the concentration density distribution. Aggregate particles were indeed observed in the holographic images of the sample. Since recognition could only be made for relatively large aggregate particles, we cannot estimate their total concentration and therefore the importance of their potential contribution to this effect.

The Coulter Counter also displays the general tendency to produce slightly concave concentration density distribution curves, unlike the holographic data. We believe that this is the consequence of the change of relative importance of the electronic noise with particle size. The results from blank samples of filtered sea water provided a statistical estimate of the electronic noise and indicated that its effects are significant only in the higher radius range where the number of spurious, noise induced counts becomes comparable to the original particle signal. However, no correction could be made due to the extreme sparsity of the data in this region of the size spectrum.

The particle concentration density distributions deduced from holographic data decrease approximately with the fourth power of the particle radius in the observed size range. Similar dependence has been reported in the literature for the population of particles in many natural environments including sea waters (Bader, 1970), as well as for the population of comparable size bubbles in the ocean (Mulhearn, 1981; Medwin, 1977).

The holographic and Coulter Counter determinations of total concentration of particles for various depths at the two test sites are presented in Figs. 9 and 10. Only particles in the 10 to 50 μm radius range are used in the calculation of the total concentration, as the holographic and Coulter Counter data directly overlap only over this radius range. Results are based on the analysis of eight holograms (six from the Long Point site and two from off east Santa Catalina Island) and eight Coulter Counter water samples (four from each site). The holographic data in Figs. 9 and 10 indicate higher total particulate concentrations in the 10 to 50 μm radius range than those reported in the literature for either ocean or laboratory waters. They also clearly reflect the previously noted discrepancy between the concentrations measured using the two methods. Both sets of data in Fig. 9 from the Long Point test site seem to indicate an increase in particle concentration near the bottom of the thermocline and to correlate well with the transmissometer trace of Fig. 3, which shows a drop in transmissivity near the thermocline depth. Similar behavior at the test site off east Santa Catalina Island is displayed by the Coulter Counter data of Fig. 10, as well as by the transmissometer trace of Fig. 4. The holographic results at this site are too sparse to indicate any trend with depth.

The observation of particle concentration increase near the bottom of the thermocline is supported by the data of Pieper and Holliday, 1984, who measured peak zooplankton concentrations near the bottom of the thermocline at a location, depths and thermocline conditions very close to the Long Point test site examined in this study. The present holographic results support this finding, clearly showing that a large percentage of the "particles" observed, especially below the thermocline, were living organisms. The finding of high zooplankton counts in deeper waters should be of interest in cavitation studies since zooplankton, with their metabolic gases, can presumably act as cavitation nuclei.

***(b)* Observations of Bubbles.** Since bubbles are known to be primary cavitation nuclei, results of the holographic study of bubbles will be included and briefly discussed here although, as mentioned earlier, the sea water samples were handled in such a way that no bubbles were expected nor observed at the time of the Coulter Counter analysis. Table 1 presents bubble concentrations and, in brackets, total number of bubbles counted in various radius ranges for several depths at the two test sites. No bubbles larger than 50 μm radius were seen in any of the holographic samples. Recall that no attempt was made to distinguish bubbles from particulates in the smallest size range, about 2.5 to 10 μm radius, so these data are not presented here.

Several observations can be made based on the small number of bubbles seen in the holographic images. The concentration of small bubbles (10 to 25 μm radius) at the test site off Long Point seems to be very high near the surface, then to decrease with depth until the thermocline is reached, at which point the concentration increases. Larger bubbles (25 to 50 μm radius) are found only below the thermocline. The bubble data for the test site off east Santa Catalina Island are sparse and

Table 1 Holographic results of bubble concentration in number per ml. The total number of bubbles counted in each radius range, N_g, is indicated in brackets. The estimated relative r.m.s. error of the bubble number concentration is $1/\sqrt{N_g}$.

NUMBER CONCENTRATION (Number per ml) [TOTAL NUMBER COUNTED]							
Test Location	Depth (m)	Radius Range (μm) 10–15	15–20	20–25	25–30	30–40	40–50
off Long Point	3	15 [15]	–	–	–	–	–
off Long Point	6	3.3 [7]	–	–	–	–	–
off Long Point	15	1.6 [5]	–	–	–	–	–
off Long Point	23	0.6 [1]	–	0.6 [1]	–	–	–
off Long Point	30	8.3 [10]	–	–	–	–	–
off Long Point	32	2.5 [4]	0.6 [1]	0.6 [1]	–	–	–
off East Catalina	27	1.1 [1]	–	1.1 [1]	–	–	–
off East Catalina	32	2.2 [2]	–	–	0.03 [3]	–	0.01 [1]

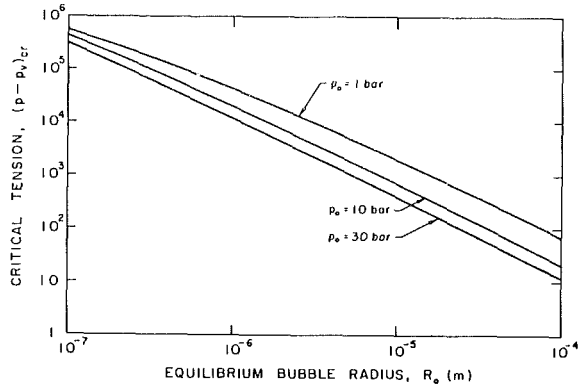

Fig. 11 Critical tension, $(p_v - p)_{cr}$, of an isolated air bubble in unbounded water as a function of its static equilibrium radius, R_o, at various external pressures: p_o = 1 bar (upper curve), p_o = 10 bar (intermediate curve) and p_o = 30 bar (lower curve) with T = 20°C (surface tension S = 0.073 N/m and vapor pressure p_v = 1919 Pa).

represent water below the thermocline only, indicating a fairly high concentration of larger bubbles at the 32 m depth. The expected relative r.m.s error for each bubble size interval is equal to $1/\sqrt{N_g}$, where N_g is the corresponding number of counts, shown in brackets in Table 1. This error is often large, especially for those size ranges with sparse bubble observations. The overall high bubble concentrations, particularly near the surface at the Long Point site, are surprising in view of the calm windless conditions at the time these holograms were recorded, as well as for several days earlier. Strong dependence of ocean bubble concentrations on wind speed have been reported by Medwin, 1977 and Thorpe, 1982. The existence of microbubbles down to 32 m and the apparent population inversion below the thermocline are also surprising. Shen et al., 1984, detected microbubbles to 25 m depth, with decreasing bubble concentration as a function of depth, although sampling below the deep thermocline at their subtropical test sites was not reported (Zsolnay et al., 1986). Medwin, 1977, observed bubbles as deep as 36 m, and under a windrow observed peak bubble concentrations at that depth. He speculates that the Langmuir cells under the windrow acted to deplete the upper waters without affecting the deep water bubbles, which are postulated to be of biological origin. Windrows were not present at the stations holographically examined in the present study but, as discussed above, there seemed to be a peak in biological activity below the thermocline, so bubbles of organic origin may play a role here. Several hypotheses have been formulated to explain the presence of bubbles at depth (Johnson and Cooke, 1981; Medwin, 1977; Mulhearn, 1981).

The relationship between the nuclei concentration density distribution and the tensile strength of the suspending liquid is still an elusive problem in cavitation research due to the many complexities and uncertainties involved. Little can be said about the role of particulates as cavitation nuclei from their holographic observation or from the Coulter Counter sizing, apart from the obvious consideration that larger concentrations of particulates are likely to lead to higher active cavitation nuclei populations. This difficulty can only be overcome by direct observation of cavitation induced by the liquid particulates under controlled circumstances, for example by means of cavitation susceptibility meters (Oldenziel, 1982; d'Agostino and Acosta, 1987). On the other hand, the dynamic properties of gas bubbles are indirectly related to their size by the Rayleigh-Plesset equation (Knapp et al., 1970). However, even in this case cavitation results from the combination of the dynamic and interference effects among developing cavities with the statistical occurrence of bubble nuclei and depends significantly on the specific flow conditions. Therefore a universal relation between the tensile strength of liquids and their bubble population can only be established in the idealized situation where the above effects are neglected, i.e., by considering the static equilibrium of individual bubbles. Then a lower bound for the tension required to cause cavitation is given by the critical tension of a spherical gas bubble which, in the absence of viscosity, mass diffusion and thermal effects, is expressed by (Knapp et al., 1970):

$$(p_v - p)_{cr} = \frac{4S}{3R_o}\left[3\left(1+\frac{p_o - p_v}{2S/R_o}\right)\right]^{-1/2} \tag{4}$$

where R_o and p_o are the equilibrium radius and external pressure of the bubble and S is the surface tension. This relation is plotted in Fig. 11 for the case of an air bubble in water at a temperature of 20°C and for several equilibrium pressures. In practice the surface tension in ocean bubbles is fairly uncertain due to the possible presence of surfactants, whose effects are not measured by the nuclei detection techniques considered here. Although the sparse bubble measurements are insufficient to determine a statistically significant value of the tensile strength for each water sample examined, Table 1 shows that all samples contained some bubbles with radius larger than 10 μm and in some cases as large as 50 μm. So, if the effect of surfactants is neglected, Fig. 11 indicates that the ocean waters tested in this investigation are expected to cavitate under an applied tension not larger than about 2000 Pa and, at least occasionally, as low as about 100 Pa.

7 Conclusions

Holographic detection clearly is the more reliable of the two methods considered in this paper for measuring the nuclei concentration density distributions. The unique capability of holography to provide discrimination between bubbles, particles and organisms is also of great value for in situ sea water analysis. However, the reconstruction and detailed visual analysis of holographic images is extremely time-consuming.

The comparison of the two techniques indicates that Coulter Counter analysis may underestimate the particulate content by up to an order of magnitude, most likely as a consequence of the assumption of electrically nonconducting particles implicit in the calibration procedure. It is conceivably possible to introduce empirical corrections to compensate for the latter phenomenon when the general nature of the particulate population in the sampled water is known. The apparent distortions of the concentration density distributions obtained from the Coulter Counter also suggest that rupture of particle aggregates might take place during the analysis of

the sample due to the strain produced by the flow of the liquid through the orifice, and that electronic noise is likely to be important only in the upper radius range where particle counts tend to become very sparse. These problems can be limited by using large aperture orifices and increasing the signal to noise ratio of the Coulter Counter electronics. The observation that the Coulter Counter may consistently underestimate the size of organic particles could be an important one, as this device is commonly used for sea water analysis (see for example Carder et al., 1971, and Sheldon et al., 1972).

The population of particulates obtained with the two techniques examined here are in agreement with previous comparable data from the literature within the expected experimental and statistical errors. They also confirm that the concentration density distribution of particulates in the range covered by our investigation decreases approximately with the fourth power of the particle size, as often reported in the literature. Both the holographic and Coulter Counter results indicate an increase in particle concentration near the bottom of the thermocline, in agreement with the zooplankton population measurements made by Pieper and Holliday, 1984. The holographic data also indicate similar behavior for the bubble concentration, although their relatively large statistical indetermination makes them less conclusive.

Further study is necessary to better clarify the dependence of the tensile strength of liquids on their nuclei content, especially in the case of particles, whose effect on the liquid susceptibility is not yet fully understood. However, the concentration of particles and bubbles in a liquid still provides an upper bound for the number of potentially active cavitation nuclei. Much higher concentrations of particles were detected in the ocean, according to the holographic analysis, than in typical cavitation test facilities (Billet, 1985). These differences should be taken into consideration in trying to relate laboratory results to prototype operation. Finally, the bubble concentration density distributions indicate that the average tensile strength of the ocean waters examined in this study is expected to be not larger than about 2000 Pa, and, at least occasionally, as low as about 100 Pa.

Acknowledgments

A field experiment must necessarily rely on the assistance and cooperation of many parties. In particular we would like to acknowledge the contributions of: Prof. J. Katz of Purdue University, Elton Daly and the staff of Caltech's W. M. Keck Laboratory of Hydraulics and Water Resources, the Captain and crew of the R/V Seawatch, and Raymond Moberly, Doug Gray, Sheldon Green, Esther (Cindy) Morss, Richard Arrieta and Cecilia Lin of Caltech. This work has been supported by the Office of Naval Research under Contract No. N00014-83-K-0506 and by a Fellowship for Technological Research administered by the North Atlantic Treaty Organization – Consiglio Nazionale delle Ricerche, Italy, Competition No. 215.18/11 of 9.24.1984. Their support is gratefully acknowledged. We are also grateful to our reviewers for their constructive comments.

References

Bader, H., 1970, "The Hyperbolic Distribution of Particle Sizes," *J. Geophysical Research*, Vol. 75, No. 15, pp. 2822–2830.

Billet, M. L., 1985, "Cavitation Nuclei Measurements – A Review," ASME Cavitation and Multiphase Flow Forum, Albuquerque, N.M.

Carder, K. L., Beardsley, G. F., Jr., and Pak, H., 1971, "Particle Size Distributions in the Eastern Equatorial Pacific," *J. Geophysical Research*, Vol. 76, No. 21, pp. 5070–5077.

Carder, K. L., Betzer, P. R., and Eggiman, D. W., 1974, "Physical, Chemical and Optical Measures of Suspended Particle Concentrations: Their Intercomparison and Application to the West African Shelf," Marine Science 4, *Suspended Solids in Water*, R. J. Gibbs, Ed., Plenum Press, pp. 173–193.

Carder, K. L., Steward, R. G., and Betzer, P. R., 1982, "In Situ Holographic Measurement of the Size and Settling Rates of Oceanic Particulates," *J. Geophysical Research*, Vol. 87, No. C8, pp. 5681–5685.

Collier, R. J., Burckhardt, C. B., and Lin, L. H., 1971, *Optical Holography*, Academic Press Inc., New York.

d'Agostino, L., and Acosta, A. J., 1987, "A Cavitation Susceptibility Meter with Optical Cavitation Monitoring," to be presented at the 1987 International Towing Tank Conference, Tokyo, Japan.

De Velis, J. B., Parrent, G. B., Jr., and Thompson, B. J., 1966, "Image Reconstruction with Fraunhofer Holograms," *J. Optical Society of America*, Vol. 56, No. 4, pp. 423–427.

Gibbs, R. J., 1982, "Floc Stability during Coulter Counter Size Analysis," *J. Sedimentary Petrology*, Vol. 52, pp. 657–660.

Hunt, J. R., 1980, "Coagulation in Continuous Particle Size Distributions: Theory and Experimental Verification," Ph.D. thesis, California Institute of Technology.

Johnson, B. D., and Cooke, R. C., 1981, "Generation of Stabilized Microbubbles in Seawater," *Science*, Vol. 213, pp. 209–211.

Katz, J., O'Hern, T. J., and Acosta, A. J., 1984, "An Underwater Holographic Camera System for Detection of Microparticulates," ASME Cavitation and Multiphase Flow Forum, New Orleans, LA.

Knapp, R. T., Daily, J. W., and Hammitt, F. G., 1970, *Cavitation*, McGraw-Hill, New York.

Medwin, H., 1977, "In Situ Acoustic Measurements of Microbubbles at Sea," *J. Geophysical Research*, Vol. 82, No. 6, pp. 971–976.

Mulhearn, P. J., 1981, "Distribution of Microbubbles in Coastal Waters," *J. Geophysical Research*, Vol. 86, No. C7, pp. 6429–6434.

Oldenziel, D. M., 1982, "A New Instrument in Cavitation Research: the Cavitation Susceptibility Meter," ASME JOURNAL OF FLUIDS ENGINEERING, Vol. 104, pp. 136–142.

Pieper, R. E., and Holliday, D. V., 1984, "Acoustic Measurements of Zooplankton Distributions in the Sea," *J. Cons. Int. Explor. Mer*, Vol. 41, pp. 226–238.

Sheldon, R. W., Prakash, A., and Sutcliffe, W. H., Jr., 1972, "The Size Distribution of Particles in the Ocean," *Limnology and Oceanography*, Vol. XVII, No. 3, pp. 327–340.

Shen, Y. T., Gowing, S., and Pierce, R., 1984, "Cavitation Susceptibility Measurements by a Venturi," ASME International Symposium on Cavitation Inception – 1984, New Orleans, LA.

Thorpe, S. A., 1982, "On the Clouds of Bubbles Formed by Breaking Wind-Waves in Deep Water, and Their Role in Air-Sea Gas Transfer," *Phil. Trans. R. Soc.*, London, Series A, Vol. 304, pp. 155–210.

Zsolnay, A., et al., 1986, "Environmental Parameters in Exuma Sound and the Straits of Florida," Naval Ocean Research and Development Activity Technical Note 252.

Observations on the Development of a Tip Vortex on a Rectangular Hydrofoil

T. B. Francis

J. Katz[1]

Hydromechanics Laboratory,
School of Civil Engineering,
Purdue University,
West Lafayette, IN 47907

The present paper describes a flow visualization study that focuses the development of a tip vortex on a rectangular NACA-66 hydrofoil. The experiments have been performed in a towing tank. Illumination with a thin laser sheet together with distribution of dye have been utilized as a means of observation. The results demonstrate the growth of the vortex along the chord, the increase in its dimensions with increasing incidence angle and decreasing Reynolds number. They also show that the center of the vortex moves inward towards the root with increasing incidence angle, increasing chordwise location, and decreasing velocity. Empirical relations for these trends have been computed. The observations also demonstrate that the flow around the tip is dominated by muliple vortex structures that include the primary vortex, a counter rotating structure, shear layer eddies, and several other secondary vortices.

1 Introduction

Trailing and tip vortices are responsible for many adverse phenomena associated with finite span lifting surfaces. Few examples are the occurrence of tip vortex cavitation on marine propellers, the hazard to small planes while passing through a trailing vortex of a large aircraft, particularly in an airport, and the effect of the flow structure behind the blade of a helicopter's rotor on the blade that follows. However, as summarized in two reviews, the first one by Platzer and Sounders (1979), and the second by Donaldson and Bilanin (1975), most of the research effort has focused on the wake structure behind the foil. Near field experimental studies, particularly on the roll-up region on the foil's surface, such as the hot wire measurements of Francis and Kennedy (1979) on a rectangular foil, and the LDV measurements close to the tip of an elliptical foil by Higuchi et al. (1986) are scarce. As a result, very little is known about the intricate details of the flow structure around the wing tip. Unlike the lack of experimental information, there has been a substantial theoretical and numerical effort. The original inviscid concentrated vortex modle has been developed by Lamb (1932). This model has been modified by Batchelor (1964) who introduced the axial velocity to the analysis, and by Moore and Saffman (1973) who incorporated the effects of viscosity. The effects of wing load distribution have been brought into consideration firstly by Betz (1933) and then by Donaldson et al. (1974). The latter has demonstrated that a single rolled-up vortex could not exist in the vicinity of a lifting surface and developed a criterion for the number of trailing vortices based on the wing load distribution. This criterion has been used extensively since then and has proven to be a reliable predictive scheme (see Yates (1974), for example). Numerical studies have been performed by Bilanin et al. (1977), Shamroth (1979), Chen and Wu (1983), Mansour (1984) Lin et al. (1986), and many others. The latter have computed the development of the tip vortex on the surface of a rectangular foils. Their results predict the development of several secondary flows, which agreed only qualitatively with the measurements of Francis and Kennedy (1979). We'll return to these results following the presentation of the current data.

Cavitation studies with stationary hydrofoils have been performed by McCormick (1962), Crimi (1970), Billet (1975), Arndt et al. (1985) and Sounders and Platzer (1981)). One of the most important conclusions from these studies is the increase in the cavitation inception index with the Reynolds number. This trend has led McCormick (1962) to hypothesize that the tip vortex core radius depends on the boundary layer of the foil's pressure side close to the wing tip. Moore and Saffman, on the other hand, claim that boundary layer thickness has very little effect on the core radius, but depends on the distance from the trailing edge. Both theories deal with the flow field donwstream of the trailing edge, and not on the rollup region on the foil itself. Of special importance, however, is the trend stated by McCormick, namely a reduction in the core radius as the Reynolds number is increased. Some support to this theory has been provided by Grow (1969) who noticed, by velocity measurements, that boundary layer tripping has caused a substantial increase in the radius of the tip vortex core. Francis and Kennedy's (1979) velocity measurements provide additional evidence to the role of boundary layer on the pressure side of the foil. They even argue

[1]Current Address: Department of Mechanical Engineering, The Johns Hopkins University, Baltimore, MD 21218.

Contributed by the Fluids Engineering Division for publication in the JOURNAL OF FLUIDS ENGINEERING. Manuscript received by the Fluids Engineering Division May 19, 1987.

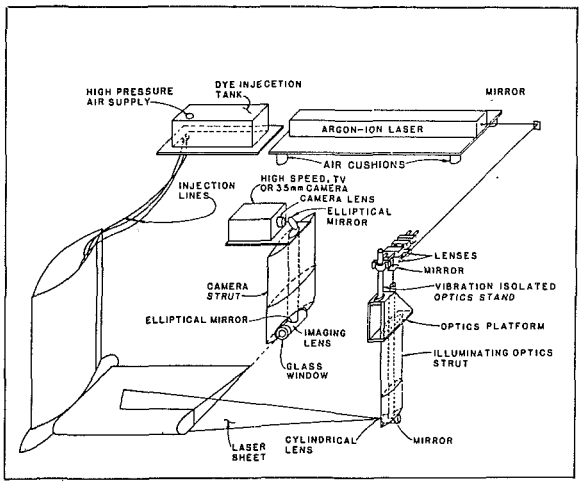

Fig. 1(*a*) A sketch of the flow visualization system

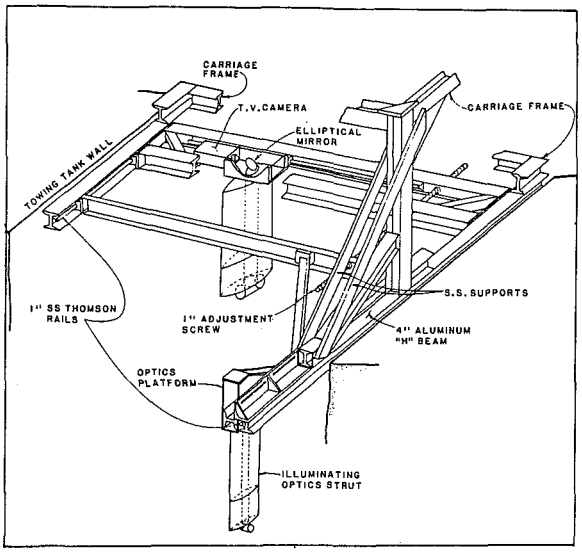

Fig. 1(*b*) A schematic description of the support system of the illuminating and recording struts

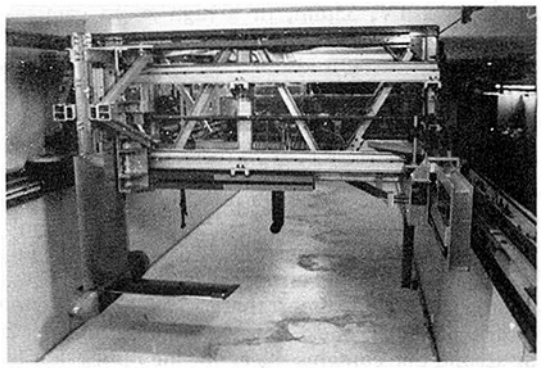

Fig. 2 A photograph of the towing tank test facility (with no water in the tank)

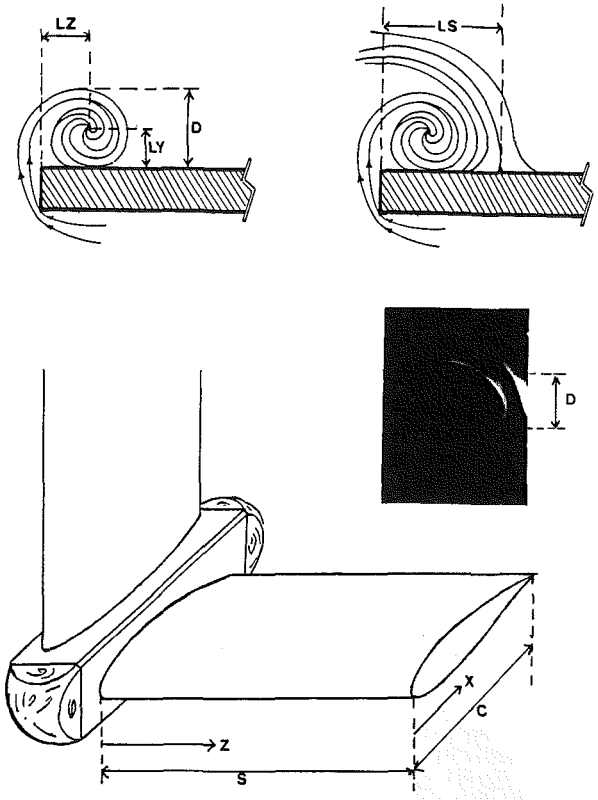

Fig. 3 Sketches illustrating D, LZ, LY, LS, X, Z, C, S, used in the present study

that the pressure side boundary layer vorticity migrates around the tip to the suction side. According to them, and as is also stated by Freymuth et al. (1986), who recently used smoke flow visualization to observe the development of tip vortices, very little is known about the vortical structures around the tip of rectangular wings. The present study focuses on this rollup region along the tip of a rectangular wing, particularly on the effect of the incidence angle and the Reynolds number on the development of the vortex along the chord. A brief description of the test facility and experimental procedures is provided in the following section. The results, developed empirical relationships, and discussions are described in the chapters that follow.

2 Description of the Apparatus

The model tested during the present study is a rectangular planform NACA-66 hydrofoil with a 10 percent thickness ratio and an 0.8 mean camber line. The chord-length of this foil is 0.61 m, its semi-span is 0.9 m and it has a flat tip. A layout of the flow visualization system is presented in Fig. 1(*a*), an additional sketch is provided in Fig. 1(*b*) and a photograph of the test facility is presented in Fig. 2. The experiments have been performed in the Purdue University towing tank (156 feet long and 11 × 5 feet test section), whose maximum carriage speed is 12.5 ft/s. In the present setup, an 8 watt Argon Ion laser (out of which 3 watts are emitted at 514.5 nanometers) is located on the towing tank carriage, inside a cooled, dust free, vibration isolated container. The ouput beam is directed by several mirrors into the illuminating foil, expanded to a thin sheet by a cylindrical lens, while its thickness is reduced to about 0.5 mm with long focal length spherical lens. Rhodamine dye can either be injected from a large number of ports located on the surface of the model, or distributed in the water in the tank shortly before each run. Besides few trial runs, due to the suspected effect of injection on the flow structure, all the actual experiments have been performed with distributed free stream dye. Intricate details associated with the flow structure at the illuminated cross section become visible due to the fluorescing property of the dye. This technique has become popular recently and several researchers, such as Dewey (1976) and Gad el Hak (1986), have already adapted it to their experiments. The resulting image is focused by a series of high resolution lenses and recor-

ded either by a TV, 35mm, or a high speed camera. The magnification and resolution of the image is controlled by a proper choice of lenses, and the details in each frame can be varied by changing the concentration of the dye. In the present configuration the magnification can be changed so that the area shown on the entire screen of the TV monitor ranges from 0.025×0.025 to 0.5×0.5 meters. The output of the video camera is stored on a high resolution video recorder.

A special mounting system has been designed and constructed for the flow visualization studies to allow for maximum flexibility in testing various types of models. This setup consists of a main strut support that carries the model and two smaller struts, the first one directs the illuminating laser beam, and the second one contains the collecting optics that lead to the camera. All three components are shown schematically in Fig. 1(*a*), and the details of the smaller struts are presented in Fig. 1(*b*). The model support can be moved vertically and laterally, and once the proper location is reached, the entire system can be locked rigidly to a particular position. The entire structure is heavily supported and extremely rugged to minimize the vibrations. The illuminating strut is located 0.15 meters from the wall of the towing tank and can be moved axially (motionwise) so that any desired section on and behind the model can be illuminated. The strut containing the periscope that leads to the camera usually trails about 3 meters behind the model. It is mounted on a transport system that allows motion both in the axial and lateral direction. The axial movement of this periscope can be coupled with the illuminating foil by a lead screw in order to keep the illuminated section focused on the camera when the light sheet is shifted.

3 Flow Visualization Results

The trends observed while analyzing the flow visualization records are documented in this section. Four dimensions have been measured off the video records. A sketch describing these terms is given in Fig. 3. The first term, D, is a chosen characteristic size for the tip vortex. Note that D is not the diameter of the vortex core, whose size can be determined only through velocity measurements. It is defined as the inner oval region, which is demonstrated in the sketch and illustrated in the attached photograph. The other terms are LZ and LY which denote the lateral and vertical location of the vortex center, respectively. Also shown is LS, the horizontal location of the attachment line separting between the primary and secondary structures on the surface of the hydrofoil. The primary cause for the uncertainty in the results of the flow visualization analysis is variations in the size and the location of the tip vortex from one image to the other. To determine the error, repeated measurements of D, LZ, and LY have been performed, both from several video frames of the same run, and by repeating the experiment. The resulting computed standard deviation of the data which is presented in this paper is 0.004 for D/C, and 0.003 for LZ/C, and 0.002 for LY/C.

3.1 Changes Along the Chord. Figure 4 contains a series of sample photographs that demonstrate the growth of the vortex as it progresses down the chord length of the foil. A graphic representation of this trend is given in Fig. 8. It can be seen, for example, that at 12 degrees incidence and a velocity of 0.30 m/s, the size of the vortex, D, increases from $D/C = 0.028$ to 0.067 and to 0.074 as the chordwise position increases from $X/C = 0.50$ to 0.75 and to 0.80, respectively. Similarly, at the same velocity and location, but at a 5 deg incidence, the respective vortex sizes are 0.011, 0.038, and 0.050. This trend is evident allthrough the entire range of velocities, and in many cases, this growth rate approaches a linear relationship.

Figures 9 and 10, which display the values of LZ and LY, respectively, demonstrate that the vortex center line shifts as the chordwise position increases. For example, at a velocity of 0.30 m/s, the horizontal location of the vortex center moves inward (toward the root of the foil) from $LZ/C = 0.027$ to 0.042 and to 0.053 at 8 degrees, and from 0.013 to 0.027 and to 0.040 at 5 degrees as X/C increases from 0.50, to 0.70, and

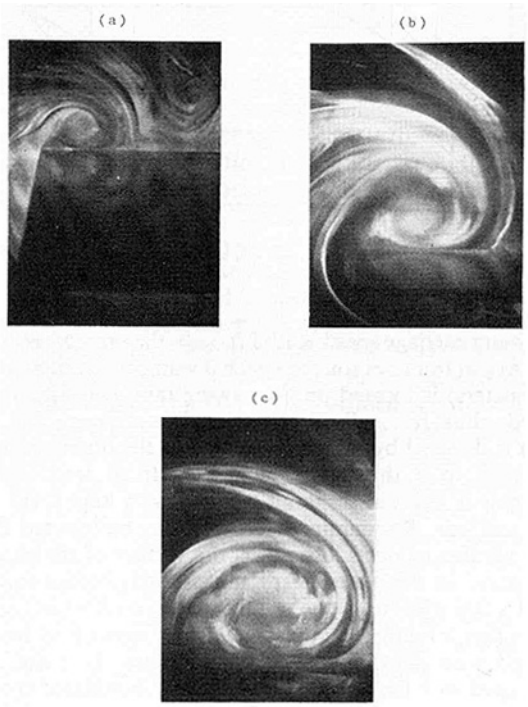

Fig. 4 A sequence of photographs demonstrating the development of the tip vortex along the chord. The incidence angle is 5 deg, and the velocity is 0.46 m/s.
(a) $X/C = 0.69$ (b) $X/C = 0.92$ (c) $X/C = 1.02$
The actual size of the image shown in each photograph is 10.4 cm.

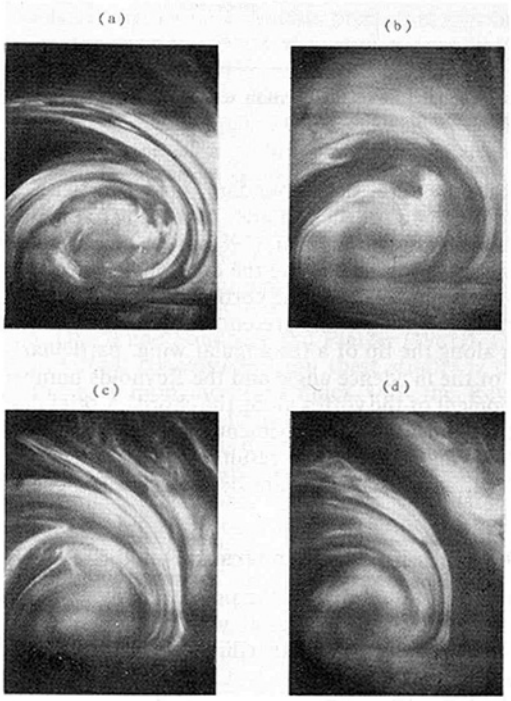

Fig. 5 A sequence of photographs demonstrating the dependence of the tip vortex size on the free stream velocity just downstream of the trailing edge. The incidence angle is 5 deg.
(a) $V = 0.46$ m/s (b) $V = 0.91$ m/s (c) $V = 1.83$ m/s (d) $V = 2.44$ m/s
The actual size of the image shown in each photograph is 10.4 cm.

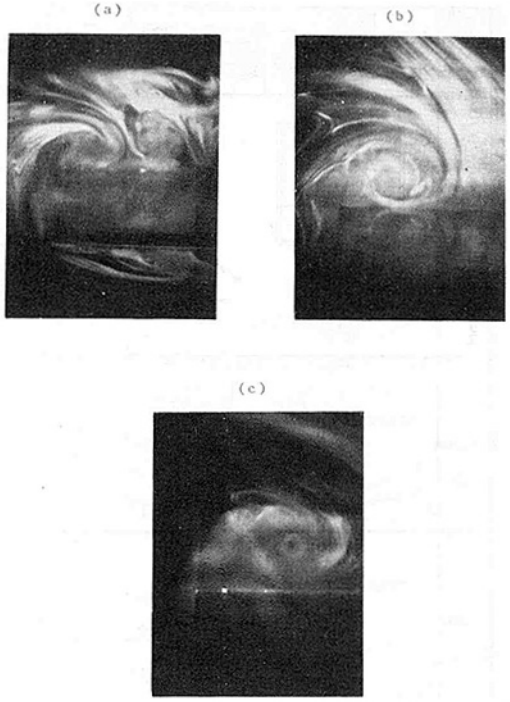

Fig. 6 A sequence of photographs demonstrating the dependence of the tip vortex size on the incidence angle. The free stream velocity is 0.79 m/s and $x/c = 0.82$.
(a) $\alpha = 2$ deg, (b) $\alpha = 5$ deg, (c) $\alpha = 12$ deg
The actual size of the image shown in each photograph is 10.4 cm.

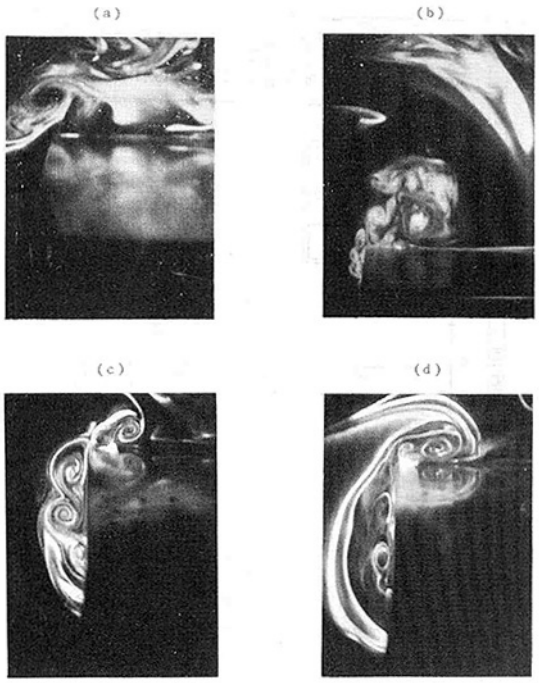

Fig. 7 A series of photographs of the primary and several secondary vortex structures around the tip of the hydrofoil.
(a) $V = 0.46$ m/s, $\alpha = 2$ deg, $X/C = 0.70$
(b) $V = 0.12$ m/s, $\alpha = 5$ deg, $X/C = 0.92$
(c) $V = 0.05$ m/s, $\alpha = 12$ deg, $X/C = 0.46$
(d) $V = 0.46$ m/s, $\alpha = 2$ deg, $X/C = 0.70$
The actual size of the image shown in each photograph is 10.4 cm. The primary structure is the clockwise rotating vortex which is located above the foil.

to 1.00, respectively. The vertical location of the vortex center rises from $LY/C = 0.017$ to 0.024 and to 0.048 at 8 degrees and from 0.004 to 0.015 and to 0.035 at 5 degrees at X/C increases from 0.50 to 0.70 and to 1.00, respectively. Similar trends are presented in Fig. 11, which displays the horizontal location of the attachment line, LS. For example, at an angle of 8 degrees and a velocity of 0.030 m/s, LS/C moves toward the root of the foil from 0.061 to 0.167 as X/C increases from 0.50 to 1.00. Expirical expressions for the trends evident from these results will be presented later.

3.2 Changes With Increasing Velocity. The velocity (and therefore the Reynolds number) also plays a role in determining vortex growth and location. Figure 5 contains photographs that demonstrate the tendency of the vortex size to decrease with increasing velocity. This trend becomes more evident as the incidence angle is increased. From the graphs (Fig. 8) one can see that at 8 degrees incidence and at $X/C = 1.0$, for example, D/C decreases from 0.075 to 0.063 as the velocity increases from 0.30 to 1.52 m/s, respectively. At the same speed, but at 5 degrees, and at $X/C = 0.90$, D/C decreases from 0.057 to 0.039. Increasing the velocity also results in an outward shift of the vortex center line. For example, at an incidence angle of 8 degrees and $X/C = 1.0$, Figs. 9 and 10 indicate that LZ/C decreases from 0.053 to 0.032 and LY/C decreases from 0.048 to 0.042 as the velocity increases from 0.30 to 1.52 m/s. This trend is also clearer at higher incidence angles. Note also that the growth rates of D/C, LZ/C, and LY/C are different, as will be discussed shortly. Similar to LZ/C, the location of the attachment line (FIg. 11) also moves outward (toward the tip of the wing) as the velocity increases. For example, for the same velocity change, at an angle of 8 degrees, and at $X/C = 1.0$, LS/C decreases from 0.167 to 0.125.

3.3 Changes With Increasing Incidence Angle. As is evident from the photographs in Fig. 6, as well as the data in Fig. 8, the tip vortex size increases as the incidence angle is increased. At the same time the center of this vortex moves inward and upward. For example, Figs. 9 and 10 show that at $X/C = 0.8$ and a velocity of 0.30 m/s, LZ/C increases from 0.034 to 0.048 and LY/C changes form 0.018 to 0.029 as the angle increases from 5 to 12 degrees. Under the same angle changes but at 1.52 m/s, LZ/C increases from 0.034 to 0.046, and LY/C increases from 0.016 to 0.028. The location of attachment also moves inward as the incidence increases (Fig. 11). For example, at 0.91 m/s and $X/C = 1.0$, LS/C increases from 0.081 to 0.125 as the angle changes from 2 to 8 degrees. Note also that changing the angle of attack has a stronger affect (in regards to location shifts and size changes) than variations in velocity (compare Figs. 8, 9, 10, and 11). It appears that the amount of liquid flowing into the tip vortex is highly dependent on the angle of attack. This observation agrees with the results of Arndt et al. (1985) who measured the velocity distribution in a tip vortex generated by an elliptical foil.

3.4 Secondary Structures. Secondary vortex structures have been visible throughout the flow visualization records. Figure 7 contains sample photographs of the commonly encountered phenomena, which include counter-rotating vortices, secondary vortices to the left of the wing tip, and shear layer eddies. The counter-rotating vortex, shown in Figs. 4(a) and 7(a), first appears at mid-chord beyond the wing's tip and then wraps around the main vortex as it progresses down the chord. As the trailing edge is approached, this structure reaches the surface on the inner (closer to the root) side to the right of the tip vortex. It is interesting to note that this secondary structure seems to be larger than the main tip vortex at upstream regions and low incidence angles (0 and 2 degrees). However, its existence has been evident throughout the entire range of meaasurements. We will return to these structures during the discussion.

In addition to the counter-rotating vortices, the mid chord

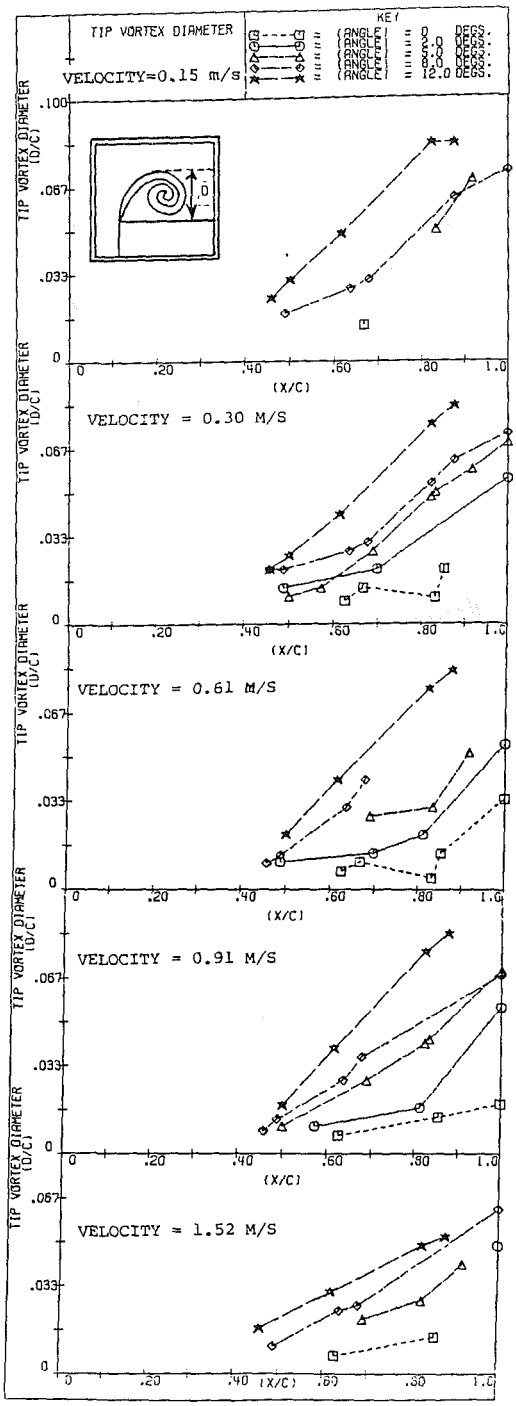

Fig. 8 The tip vortex characteristic siz as measured from the flow visualization images

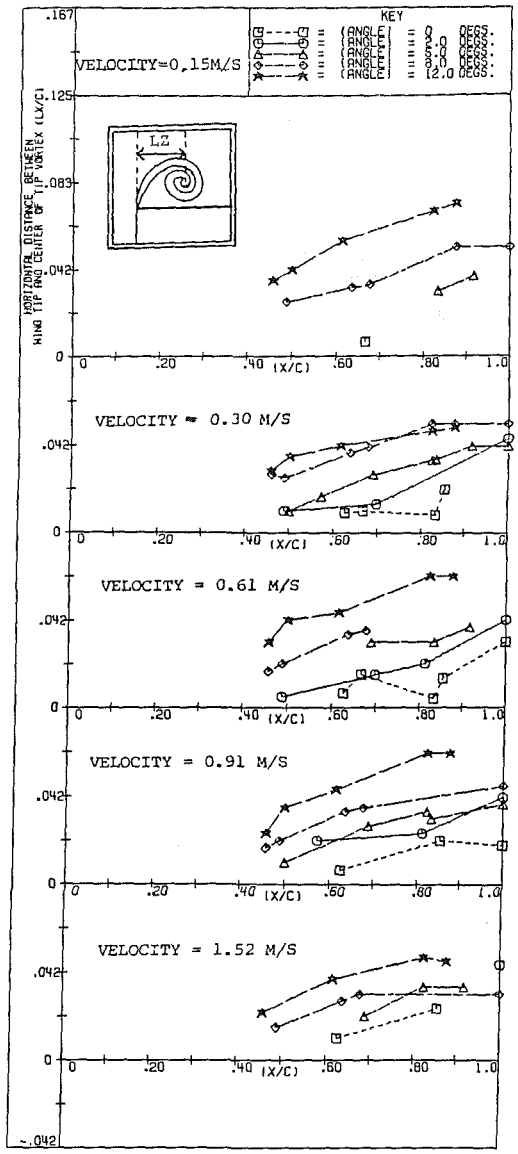

Fig. 9 The horizontal location of the tip vortex center as measured from the flow visualization images

sections contain several secondary structures on the side of the wingtip, as is evident from Figs. 7(*c*, *d*). Close to the trailing edge, as the foil becomes thinner, the secondary vortices take the form of shear layer eddies (Fig. 7(*b*)) which appear as soon as the flow separates at the edge of the wing's pressure side. Further downstream these secondary structures are eventually entrained by the main tip vortex. Obviously, modifications to the tip's shape can modify and may even eliminate these secondary flows. Future studies with modified geometry would determine their effect on the tip vortex size and growth.

3.5 Empirical Equations. The results in Figs. 8, 9, and 10 have been incorporated into empirical relationship for D/C, LZ/C, and LY/C, respectively. The equations are functions of three parameters: the Reynolds number, the incidence angle, and the chordwise position. They are designed to give acceptable estimates of the vortex size and location when the operating parameters of the foil are within the following ranges: a Reynolds number, (Re_c), between 10^5 and 5×10^6, an incidence angle, (α), between 0 and 12 degrees, and a chordwise location, (X/C), between 0.48 and 1.00. It should be reemphasized that these formulae are empirical equations developed to match data gathered under these specific test conditions.

The empirical expression developed for the tip vortex characteristic size (defined in Fig. 3) is as follows:

$$D/C = F(X/C,\alpha,\mathrm{Re}_c) = G(\alpha,X/C)H(\mathrm{Re}_c,X/C) \qquad (1)$$

where

$$G(\alpha,X/C) = 0.0378(X/C)\{2.1-2(\alpha+1)^{0.5}(X/C)^{-1}\}$$

$$H(\mathrm{Re}_c,X/C) = \{0.75+1.45*10^3(X/C)^{0.6}(\mathrm{Re}_c)^{-0.6}\}.$$

A plot comparing measured values of the tip vortex diameter and those calculated by equation (1) is presented in Fig. 12.

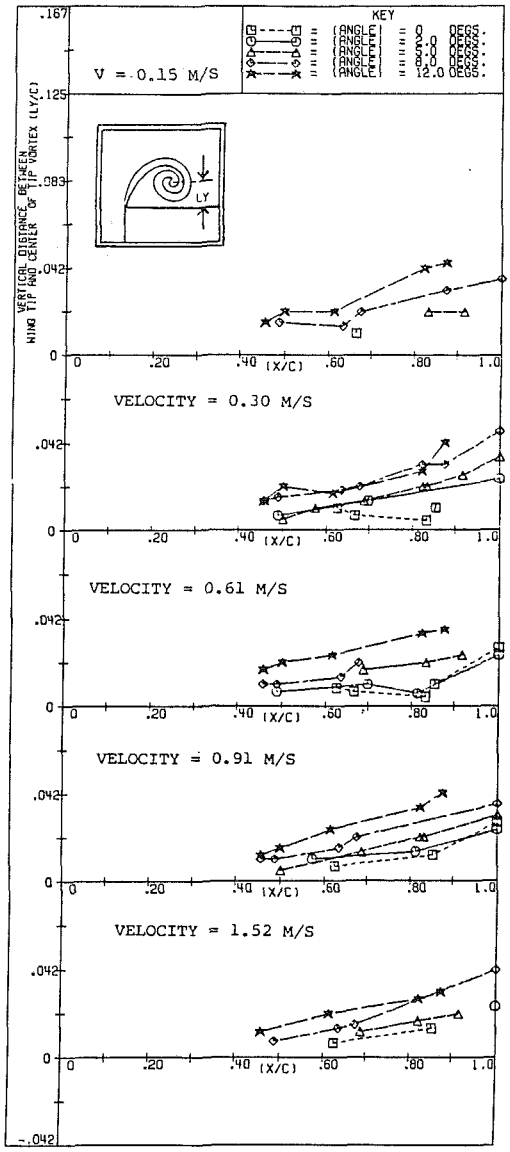

Fig. 10 The vertical location of the tip vortex center as measured from the flow visualization images

Note that equation (1) is divided into two parts. The first one, G, is a function of the chordwise position and the incidence angle. The second one, H, is a function of the chordwise position and the Reynolds number. As is evident from these equations, the characteristic vortex size is proportional to $\mathrm{Re}_c^{-0.6}$. This power is not far from the characteristic value, $\mathrm{Re}_c^{-0.5}$, which is typical to the growth rate of laminar boundary layer parameters. The scatter in the experimental results is higher in the upper region of the graph (for values which correspond to low speeds) than the data in the lower region (at higher velocities). The standard deviation of the experimental data from the empirical expression is 0.003.

The empirical expression for the horizontal location of the tip vortex center line (defined in Fig. 3) is as follows:

$$LZ/C = J(X/C,\alpha,\mathrm{Re}_c) = \{K(\alpha,X/C)L(\mathrm{Re}_c,X/C\}^{0.9} \quad (2)$$

where

$$K(\alpha,X/C) = 0.0295(X/C)\{0.28(\alpha+1)^{0.6} - 0.25\}$$

$$L(\mathrm{Re}_c,\ X/C) = \{0.75 + 1.74{*}10^3\ (X/C)^{0.6}\ (\mathrm{Re}_c)^{-0.6}\}.$$

A plot comparing measured values of LZ/C to those

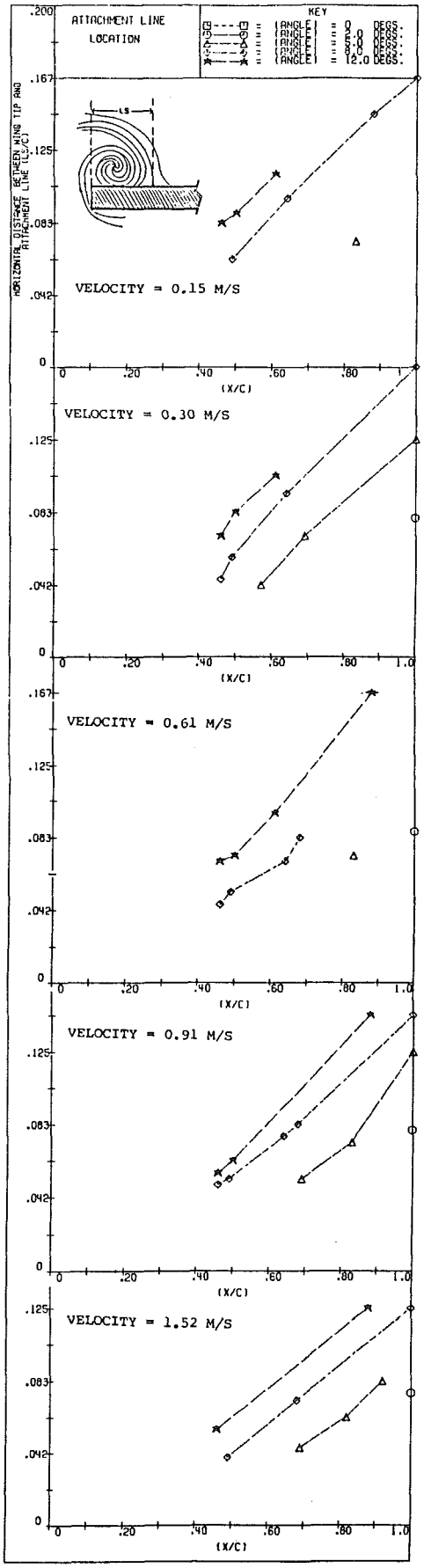

Fig. 11 The location of the attachment line as measured from the flow visualization images

calculated by equation 2 is presented in Fig. 13. The results show that the horizontal location is proportional to $(\mathrm{Re}_c^{-0.6})^{0.9}$ and to $((\alpha+1)^{0.6})^{0.9}$. Examinations of Fig. 13 reveals that the results are also more scattered in the upper part of the graph, which corresponds to lower speed conditions. The standard deviation in this figure is 0.004.

The empirical expression for the vertical location of the tip vortex center line (defined in Fig. 3) is as follows:

$$LY/C = N(X/C,\alpha,\mathrm{Re}_c) = Q(\alpha,X/C)P(\mathrm{Re}_c,X/C) \qquad (3)$$

where

$$Q(\alpha,X/C) = 0.0231\,\frac{0.35(\alpha+1)(X/C)^{1.1}-0.22}{(\alpha+1)^{0.5}}$$

$$P(\mathrm{Re}_c,X/C) = \{0.75+13.6(X/C)^{0.6}(\mathrm{Re}_c)^{-0.2}\}.$$

A plot comparing measured values of LY/C to those calculated by equation 3 is presented in Fig. 14. This equation demonstrates that the Reynolds Number does not affect the vertical location of the tip vortex center as much as it affects the horizontal location. The values of LY/C are proportional to $\mathrm{Re}_c^{-0.2}$, a much smaller power than the results in Figs. 12 and 13, but are still proportional to the square root of the incidence angle. The agreement between this equation and the data are also fairly good. Besides the upper region of the graph (low velocities), the scatter appears to be relatively uniform, and the standard deviation is 0.003. As a general statement, it should be noted that the coefficients in equations (1)–(3) may also be dependent on the geometry of the test facility, the shape of the hydrofoil's tip (being flat), the surface roughness etc. Thus, we do not claim here that these empirical expressions represent universal relationships. They do, however, match the current results.

4 Discussion

The first step in discussing the data in this paper is to compare the present results to the x wire measurements of Francis and Kennedy (1979). Although their study has been performed in a wind tunnel and on a different foil (their model is a NACA 64009 at a $\mathrm{Re}_c = 2.45/10^5$) some characteristics of the flow described by them, particularly the existence of secondary flows have been evident in both studies. However, some of the tip flow structures differ from each other. Firstly, due to the averaged results of the hot wire probes, their data do not display the existence of the shear layer eddies. They do state, however, that large fluctuations exist at mid chord which may be an indicator for vortex shedding. Secondly, their data do not contain any trace of the counter rotating structure either at mid chord, or on the model's surface close to the trailing edge. However, they do notice that for $x/c \geq 0.6$ the circulation on the wing suction size, computed between $Z/S = 0.917$ to 1.00, is smaller than the results computed for the region extending between $Z/S = 0.958$ and 1.00. Thus, a circulation with an opposite sign exists between $Z/S = 0.917$ and 0.958. This phenomenon may be a result of a counter rotating vortex structure. Their contours of the streamlines at $x/c \leq 0.6$ is quite similar to Fig. 7(*b*), and their result for $x/c = 0.9$ resembles the image shown in Fig. 5. Unfortunately, they do not provide information about trends with increasing freestream velocity and incidence angles. One of the most important conclusions from their results is that fact that most of the vorticity production until about mid-chord occurs below

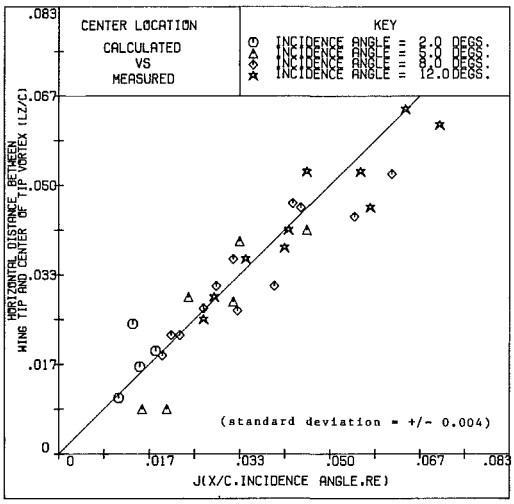

Fig. 13 A comparison between the empirical expression for the horizontal location of the tip vortex center and the measured results. Where:
$LZ/C = J(X/C,\alpha,\mathrm{Re}_c) = \{K[\alpha,X/C)L(\mathrm{Re}_c,X/C)\}^{0.9}$
$K(\alpha,X/C) = 0.0295(X/C)\{0.28(\alpha+1)^{0.6}-0.25\}$
$L(\mathrm{Re}_c,X/C\} = \{0.75+1.74{*}10^3(X/C)^{0.6}(\mathrm{Re}_c)^{-0.6}\}$

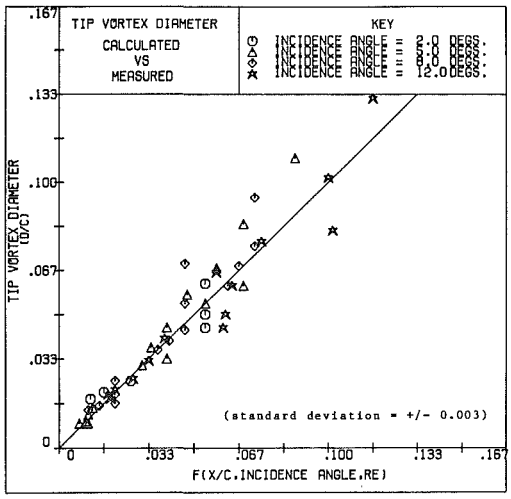

Fig. 12 A comparison between the empirical expression for the tip vortex diameter and the measured results. Where:
$D/C = F(X/C,\alpha,\mathrm{Re}_c) = G[\alpha,X/C)H(\mathrm{Re}_c,X/C)$
$G\alpha,X/C) = 0.0378(X/C)\{2.1-2(\alpha+1)^{0.5}(X/C)^{-1}\}$
$H(\mathrm{Re}_c,X/C\} = \{0.75+1.45{*}10^3(X/C)^{0.6}(\mathrm{Re}_c)^{-0.6}\}$

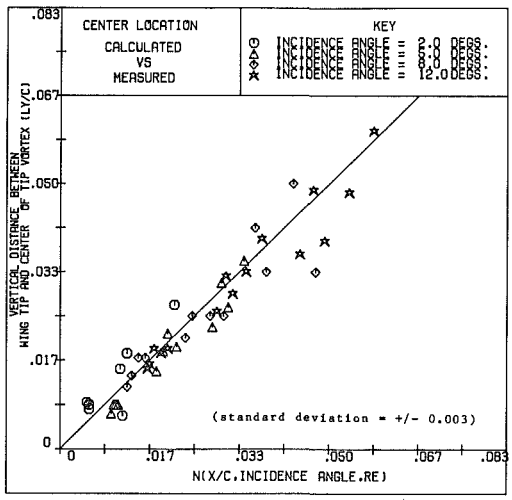

Fig. 14 A comparison between the empirical expression for the vertical location of the tip vortex center and the measured results. Where:
$LY/C = N(X/C,\alpha,\mathrm{Re}_c) = Q(\alpha,X/C)P(\mathrm{Re}_c,X/C)$
$Q(\alpha,X/C) = 0.0231\{0.35(\alpha+1)(X/C)^{1.1}-0.22\}/(\alpha+1)^{0.5}$
$P(\mathrm{Re}_c,X/C\} = \{0.75+13.6(X/C)^{0.6}(\mathrm{Re}_c)^{-0.2}\}$

the wing and as a result, no trace of a tip vortex can be seen on the upper surface prior to $x/c = 0.6$. This observation is in agreement with the data in Figs. 8–11. Finally, their image for $x/c = 0.05$ demonstrates the existence of an outward flow on the upper surface. This phenomenon may result in the shedding of counter vorticity, which is probably the origin of the counter rotating structure shown in Fig. 7. Note also that development of a tip vortex from the tip leading edge have been observed also by Freymuth et al. (1986) during smoke flow visualization studies, and by Green and Acosta (private communication) during cavitation studies on a similar NACA-66 foil. The currently observed trends with the Reynolds Number agree also with the postulations of McCormick (1962), and similar trends measured by Higuchi et al. (1986) on an elliptical foil. Continued studies, which are currently in progress, indicate also that boundary layer tripping with surface roughness also changes the vortex size and location. In fact, the vortex dimensions are even sensitive to the height of the roughness elements. These observations confirm the results of Grow (1969).

5 Summary and Conclusions

The development of tip vortices on a rectangular NACA-66 hydrofoil have been studied in a towing tank. The observations made have been used to demonstrate the trends of the tip vortex size and location with the incidence angle, chordwise location and the free stream velocity. Empirical relations for these trends have also been computed. These expressions demonstrate that under the current range of measurements the vortex size is proportional to $Re_c^{-0.6}$ and to $(\alpha+1)^{0.5}$. The horizontal distance from the tip is proportional to $Re_c^{-0.54}$ and $(\alpha+1)^{0.54}$. The vertical distance between the vortex center and the surface is proportional to $Re_c^{-0.2}$ and $(\alpha+1)^{0.5}$. The observations indicate that the flow is dominated by multiple vortex structures, including the main counter rotating vortex structure, shear layer eddies and several other secondary flows. As noted before, the present report is a summary of an initial series of observations. Future experiments will include observations on the effects of surface roughness, and modifications to the tip geometry on the development of tip vortices. The effects of rounding the edges of the tip to reduce the effect of some of the secondary structures, gradual variations in the chord length, the effect of the sweep angle, and the addition of various devices to modify the flow will also be studied in detail.

Acknowledgment

This work was supported by the Naval Sea Systems Command, General Hydrodynamic Research Program, administered by the David Taylor Naval Ship Research and Development Center under contract number N00014-85-K-0106.

The authors would like to thank Jim Craig for his help in constructing the test body, Tom Cooper and Ken Ward for their help in constructing the test facility.

References

Arndt, R. E. A., Higuchi, H., Quadrelli, C. S., 1985, "Tip Vortex Cavitation," ASME Cavitation and Multi-Phase Flow Forum, FED-Vol. 23.

Batchelor, G. R., 1964, "Axial Flow in Trailing Line Vortices," *Journal of Fluid Mechanics*, Vol. 20, Part 4, pp. 654–658.

Betz, A., 1933, "Behavior of Vortex Systems," NACA TM 713, (Translated from *ZAMM*, Vol. XII, 3, June 1932).

Bilanin, A. J., Teske, M. E., Williamson, G. G., 1977, "Vortex Interactions and Decay of Aircraft Wakes," *AIAA Journal*, Vol. 15, No. 2, pp. 250–260.

Billet, M. L., 1975, "Surface and Tip Vortex Cavitation on a Family of Rectangular Foils," Applied Research Laboratory, Pennsylvania State University.

Crimi, P., 1976, "Experimental Study of the Effects of Span Loading and Cavitation," *Journal of Hydronautics*, Vol. 4, No. 1.

Dewey, F. C., 1976, "Qualitative and Quantitative Flow Field Visualization Utilizing Laser Induced Fluorescence," AGARD-CP-193, No. 17.

Donaldson, D. du P., Snedeler, R. S., Sullivan, R. D., 1974, "A Method of Calculating Aircraft Wake Velocity Profiles and Comparison with Full-Scale Experimental Measurements," *J. Aircraft*, Vol. 11, No. 9, pp. 547–555.

Donaldson, C. Du P., Bilanin, A., 1975, "Vortex Wakes of Conventional Aircraft," AGARD ograph 204.

Francis, M. S., Kennedy, D. A. 1979, "Formation of a Trailing Vortex," *J. Aircraft*, Vol. 15, No. 3, pp. 148–154.

Freymuth, P. Finaish, F., Bank, W., 1986, "Visualization of Wing Tip Vortices in Unsteady and Steady Wings," AIAA-86-1096.

Gad-el-Hak, M., 1986, "The Use of the Dye Layer Technique for Unsteady Flow Visualization," ASME JOURNAL OF FLUIDS ENGINEERING, Vol. 108, pp. 34–48.

Grow, T. L., 1969, "Effects of a Wing on Its Vortex," *Journal of Aircraft*, Vol. 6, No. 1.

Higuchi, H., Quadrell, J. C., Farell, C., 1986, "Vortex Roll-up for an Elliptical-Loaded Wing at Moderately Low Reynolds Number," AIAA-86-0562.

Lamb, H., 1932, Hydrodynamics, Cambridge, also Dover ed., New York, 1945, pp. 591–592.

Lin, S. J., Levy, R., Shamroth, S. J., 1986, "A Three Dimensional Viscous Flow Analysis for the Helicopter Tip Vortex Generation Process about Square and Round Tipped Blades," AIAA-86-0560.

Mansour, N. N., 1984, "Numerical Simulations of the Tip Vortex off a Low Aspect Ratio Wing at Transonic Speed," AIAA-84-522.

McCormick, B. W., Jr., 1962, "On Cavitation Produced by a Vortex Trailing from a Lifting Surface," ASME *Journal of Basic Engineering*, pp. 369–379.

Moore, D. W., Saffman, P. G., 1973, "Axial Flow in Laminar Trailing Vortices," *Proc. Royal Soc.* (London), Series A 333, pp. 481–508.

Platzer, G. P., Sounders, W. G., 1979, "Tip Vortex Cavitation Delay with Application to Marine Lifting Surfaces, A Literature Survey," STNSRDC, Rep. No. 79/051.

Shamroth, S. J., 1979, "A Viscous Flow Analysis for the Tip Vortex Generation Process," NASA CR 318.

Sounders, W. G., Platzer, G. P., 1981, "Tip Vortex Cavitation Characteristics and Delay of Inception on a Three Dimensional Hydrofoil," DTNSRDC, Rep. No. 81/007.

Yates, J. E., 1974, "Cavitation of Initial Vortex Roll up in Aircraft Wakes," *Journal of Aircraft*, Vol. 11, No. 7, pp. 397–400.

A Comparison of Algebraic and Differential Second-Moment Closures for Axisymmetric Turbulent Shear Flows With and Without Swirl

S. Fu

P. G. Huang

B. E. Launder

M. A. Leschziner

Department of Mechanical Engineering,
University of Manchester Institute of Science
and Technology,
Manchester, U.K.

Computations are reported for three axisymmetric turbulent jets, two of which are swirling and one containing swirl-induced recirculation, obtained with two models of turbulence: a differential second-moment (DSM) closure and an algebraic derivative thereof (ASM). The models are identical in respect of all turbulent processes except that, in the ASM scheme, stress transport is represented algebraically in terms of the transport of turbulence energy. The comparison of the results thus provides a direct test of how well the model of stress transport adopted in ASM schemes simulates that of the full second-moment closure. The comparison indicates that the ASM hypothesis seriously misrepresents the diffusive transport of the shear stress in nonswirling axisymmetric flows, while in the presence of swirl the defects extend to all stress components and are aggravated by a failure to account for influential (additive) swirl-related stress-transport terms in the algebraic modelling process. The principal conclusion thus drawn is that in free shear flows where transport effects are significant, it is advisable to adopt a full second-moment closure if turbulence modelling needs to proceed beyond the eddy-viscosity level.

1 Introduction

In the 1970's, most applied computational studies on the fluid dynamics of turbulent shear flows adopted eddy-viscosity models for the effective turbulent stresses. The k–ϵ model, in which extra transport equations are solved for the turbulent kinetic energy (k) and its rate of viscous dissipation (ϵ) to obtain the local turbulent viscosity (proportional to k^2/ϵ), was (and indeed still is) a particularly popular route, because for many situations it combined relative simplicity with satisfactory physical realism [1]. The present decade has seen a marked shift, however, towards a more complicated modelling strategy – one offering greater width of applicability, particularly in complex shear flows or where external force fields modify the turbulence structure. These second-moment closures take the exact equations for the transport of the Reynolds stresses ($\overline{u_i u_j}$) as their starting point and devise approximations for the unknown turbulent correlations appearing in them. In a three-dimensional flow, or even in an axisymmetric swirling flow, all six components of the Reynolds-stress tensor are nonzero. With a full second-moment closure, therefore, differential transport equations need to be solved over the solution domain for each of these components. This represents a very considerable increase in the task of numerical solution compared with the situation where the k–ϵ eddy-viscosity model is adopted, for then only one Reynolds-stress-related equation (for the turbulence energy) is solved. It is for this reason that an intermediate level of modelling has been evolved [2, 3], known as *algebraic* second-moment closure (ASM), with the aim of retaining the greater physical realism of second-moment treatments while achieving computational times closer to that of an eddy-viscosity model.[1] The simplification is achieved by approximating the convective and diffusive transport of the Reynolds stresses in terms of the corresponding transport of turbulence energy. This simplification allows the erstwhile transport equations for the stresses to be expressed as a set of algebraic formulae containing the turbulence energy and its rate of dissipation as unknowns.

ASM schemes have been extensively and successfully applied in recent years to a wide range of flows and phenomena, e.g., references [4, 5]. Very few applications have considered axisymmetric flows, however. It is this class of free shear flow to which attention is given here, initially for the case of a nonswirling jet in stagnant surroundings and subsequently for two swirling flows, one of which contains a region of recir-

Contributed by the Fluids Engineering Division for publication in the JOURNAL OF FLUIDS ENGINEERING. Manuscript received by the Fluids Engineering Division September, 20, 1986.

[1] The increase in magnitude of the computational task is greater than a count of the number of dependent variables would suggest, because the Reynolds-stress equations are more complicated than that for the turbulence energy and are strongly intercoupled.

culation. Our aim is to compare the computed behaviour for both the algebraic and differential second-moment treatments (ASM and DSM, respectively) to allow conclusions to be drawn on how well the transport approximations in the former approach account for the convection and diffusion of the Reynolds stresses.

2 The Models Compared

The second-moment closure adopted for these comparisons is the simpler of the two forms proposed in reference [6], namely:

$$\frac{D\overline{u_iu_j}}{Dt}-\frac{\partial}{\partial x_k}\left(c_s\overline{u_ku_l}\,\frac{k}{\epsilon}\,\frac{\partial\overline{u_iu_j}}{\partial x_l}\right)=P_{ij}-\frac{2}{3}\,\delta_{ij}\epsilon$$
$$-c_1\epsilon\left(\frac{\overline{u_iu_j}-\frac{2}{3}\,\delta_{ij}k}{k}\right)-c_2\left(P_{ij}-\frac{1}{3}\,\delta_{ij}\,P_{kk}\right) \qquad (1)$$

where

$$P_{ij}\equiv-\overline{u_iu_k}\,\frac{\partial U_j}{\partial x_k}-\overline{u_ju_k}\,\frac{\partial U_i}{\partial x_k}$$

and where the coefficients c_s, c_1, and c_2 take their usual values 0.22, 1.8, and 0.6, respectively.

In the ASM treatment, the left side of equation (1) is replaced by way of Rodi's [3] ASM transport hypothesis,

$$\frac{D\overline{u_iu_j}}{Dt}-\frac{\partial}{\partial x_k}\left(c_s\overline{u_ku_l}\,\frac{k}{\epsilon}\,\frac{\partial\overline{u_iu_j}}{\partial x_l}\right)=\frac{\overline{u_iu_j}}{k}\left[\frac{Dk}{Dt}-\frac{\partial}{\partial x_k}\right.$$
$$\left.\left(c_s\overline{u_ku_l}\,\frac{k}{\epsilon}\,\frac{\partial k}{\partial x_l}\right)\right]=\frac{\overline{u_iu_j}}{k}\left(\frac{1}{2}\,P_{kk}-\epsilon\right) \qquad (2)$$

Other approximations have been proposed, e.g., [7], but our experiences suggest that their use would not materially affect the conclusions drawn herein. For both ASM and DSM calculations, the energy dissipation rate ϵ is obtained from:

$$\frac{D\epsilon}{Dt}=\frac{\partial}{\partial x_k}\left(c_\epsilon\,\overline{u_ku_l}\,\frac{k}{\epsilon}\,\frac{\partial\epsilon}{\partial x_l}\right)+\frac{c_{\epsilon1}}{2}\,\frac{P_{kk}\epsilon}{k}-c_{\epsilon2}\,\frac{\epsilon^2}{k} \qquad (3)$$

where c_ϵ, $c_{\epsilon1}$, and $c_{\epsilon2}$ take the standard values 0.18, 1.44, and 1.92, respectively.

3 The Numerical Solvers

The numerical solutions were obtained using adaptions of two finite-volume solvers developed at UMIST. The nonswirling jet was computed with the PASSABLE code of Leschziner [8], an axisymmetric (or plane two-dimensional) solver for parabolic equations employing a self-regulating expanding grid in the streamwise direction. Normally, 50 cross-stream nodes were prescribed with a forward step equal to 5 percent of the local domain width. Check runs with 30, 50 and 100 nodes and a forward step as low as 2 percent showed a variation in $\overline{uv}/U_\ell^2$ of less than 2 percent.

The strongly swirling jet flow of Sislian and Cusworth [9] was simulated with the elliptic solver TEAM (Huang and Leschziner [10]) which employs primitive variables on a staggered U, V, P mesh. The Reynolds stresses are also staggered so that they lie on the surfaces of the momentum control volumes on which they act. The procedure adopts quadratic upstream-weighted differencing for convective transport, and this choice allows the Reynolds stresses to be determined with a numerical accuracy of within 5 percent on a 40 × 35 grid, as verified from test runs with grids ranging from 28 × 28 to 60 × 60. Since the numerical errors are, in any case, essentially the same for the ASM and DSM solutions, the question of numerical accuracy is not of central importance in comparing the relative behaviour produced by the two types of models.

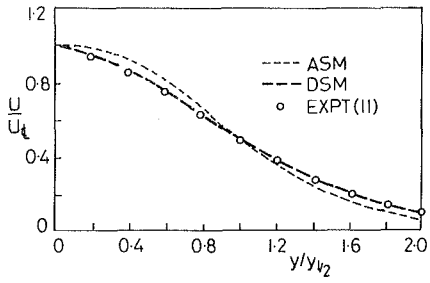

Fig. 1(a) Velocity profiles

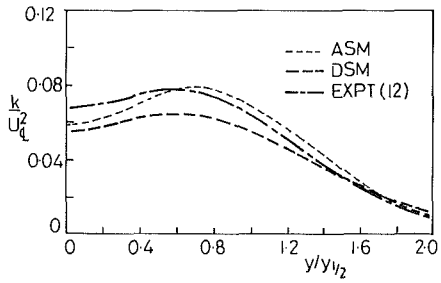

Fig. 1(b) Turbulence-energy profiles

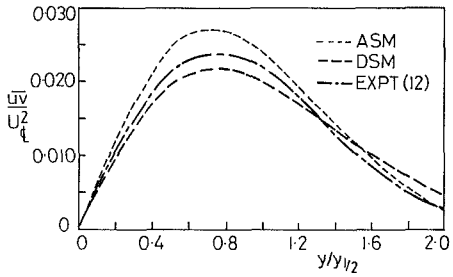

Fig. 1(c) Shear-stress profiles

Fig. 1 Fully developed plane jet

4 Comparison of Performance

As a preliminary to considering the axisymmetric flows, Fig. 1 shows the development of the plane turbulent jet in stagnant surroundings computed with the ASM and DSM schemes. This brings out a known – though, in practice, fairly minor – weakness of ASM's in plane flows, namely that excessive levels of "effective viscosity" are generated near the symmetry plane, giving rise to an overly full mean-velocity profile. Turbulence energy and shear-stress levels are increased relative to the DSM results, and the rate of spread, $dy_{½}/dx$, is 0.114 which is 5 percent higher than given by the full second-moment closure. These differences are fairly typical of those that can be expected in plane free shear flows in which transport effects are significantly larger than in wall-bounded flows; in the latter, closer correspondence between ASM and DSM computations usually results.

Computations of the round jet in stagnant surroundings are presented in Fig. 2. In this case, there is a more pronounced distortion of the mean-velocity profile than for the plane jet, with corresponding differences in the turbulence-energy profiles for the two models. It is in respct of the shear-stress profiles, however, that the most serious differences emerge: the peak level of uv is 45 percent higher for the ASM computation than for the DSM, which directly leads to a rate of spread 23 percent greater for the former.

This serious deterioration in the ability of the ASM to mimic the behaviour of the full second-moment closure merits

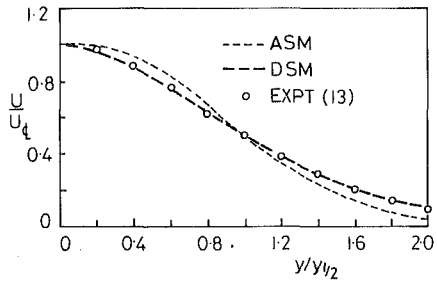

Fig. 2(a) Velocity profiles

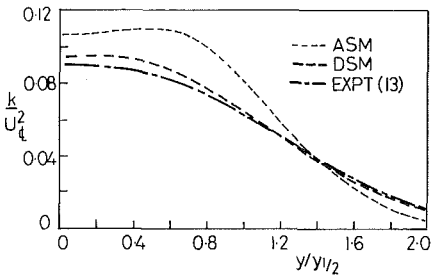

Fig. 2(b) Turbulence-energy profiles

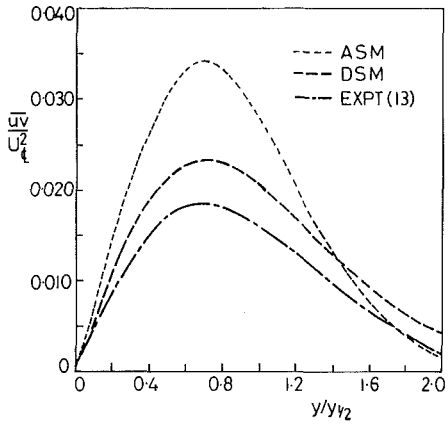

Fig. 2(c) Shear-stress profiles

Fig. 2 Fully developed round jet

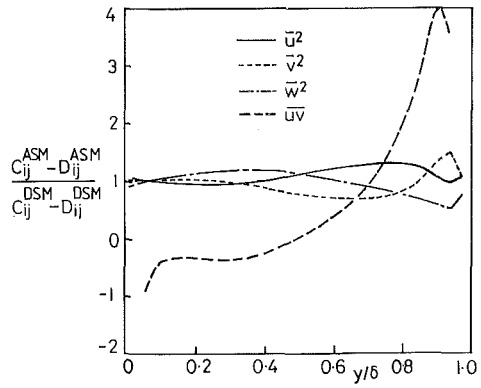

Fig. 3 Ratio of ASM-to-DSM stress transport evaluated from DSM prediction for fully developed round jet

closer attention. Fig. 3 examines, for the nonzero Reynolds stresses, how well the ASM hypothesis succeeds in representing the transport terms in the Reynolds-stress equations. For each component, the ASM-indicated transport has been evaluated from the DSM computations and compared with that resulting from the DSM computation itself. The ordinate shows the ASM transport divided by the DSM transport; so, if the ASM model were perfect, a value of unity would be returned for each component all the way across the shear flow. In fact, for the normal-stress components a value quite close to unity *is* obtained. For the shear stress, however, the ASM transport is of the wrong sign over much of the shear flow and takes on large negative values at the axis.

Although this defect is serious in its own right, when considered in the context of transport alone, the extent to which it modifies the flow and turbulence fields is initially surprising, for transport is generally held to make a insignificant contribution to the stress budget. That this is indeed so can be seen by focusing on the two curves closest to the zero ordinate line in Fig. 4. The solid curve represents the ASM approximation $\overline{uv}/k\ (0.5P_{kk}-\epsilon)$ evaluated from the DSM solution, while the chain-dotted line reflects the same approximation but obtained from the ASM solution actually generated with that form.

While the levels of both transport representations, as well as the differences between them, are low (relative to other processes), it is evident that the principal damage arises through a serious distortion of the production process which then results in a significant alteration in the stress level. The nature of this interaction is somewhat obscured by the complexity of inter-stress coupling and nonlinearity, but may essentially be understood by noting first that a descrease in transport (which is here negative) tends to increase $\overline{uv}$ and its production, the latter via an increase in the level of $\overline{u^2}$-generation leading to an increase in $\overline{v^2}$ which is proportional to the production of shear stress. An increase in uv and its production results, however, in larger (negative) levels of redistribution, through both the return-to-isotropy and the mean-strain contributions (respectively, the terms with coefficients c_1 and c_2 in equation (1)). This, in turn, tends to push the production still higher, since a balance between production, transport and redistribution must be maintained.

We proceed to show that the principal root for the misrepresentation of transport is the diffusion of the shear stress. Transformation of the diffusion term in equation (1) to cylindrical polar coordinates gives:

$$D_{uv}^{\mathrm{DSM}} = \frac{c_s}{r}\frac{\partial}{\partial r}\left(r\frac{k\overline{v^2}}{\epsilon}\frac{\partial \overline{uv}}{\partial r}\right) - \frac{c_s}{r}\frac{k\overline{w^2}}{\epsilon}\frac{\overline{uv}}{r} \tag{4}$$

where $\overline{v^2}$ and $\overline{w^2}$ are, respectively, the radial and tangential normal stresses. The ASM hypothesis approximates this process as:

$$D_{uv}^{\mathrm{ASM}} = \frac{c_s}{r}\frac{\overline{uv}}{k}\frac{\partial}{\partial r}\left(r\frac{k\overline{v^2}}{\epsilon}\frac{\partial k}{\partial r}\right) \tag{5}$$

Now, it is tempting to conclude from the above that expression (5) is merely an approximation of the first term in (4) and that a serious error may thus arise from the apparent neglect of the second term in (4), particularly near the axis when r tends to zero. Such a formalistic argument cannot be sustained, however, in view of the fact that both approximation (5) and the difference (4) must tend to zero, the latter because $\overline{uv}$ declines approximately linearly toward zero as the axis is approached, while $\overline{w^2}$ tends to $\overline{v^2}$. Indeed, if expressions (4) and (5) are evaluated from the DSM solution, both are found to vary in a qualitatively similar manner, as can be seen from Fig. 5. However, if (5) is actually used to generate the ASM solution, Fig. 5 shows that a seriously aberrant behaviour is returned, with diffusion strongly depressed in the region $0.05 < y/\delta < 0.35$ and strongly over-estimated very close to the axis – the reversal in sign being associated with the reversal in the curvature of k evident in Fig. 2 and brought about by excessive

k-generation in the highly sheared region. It thus appears that the erroneous behaviour stems from relatively mild distortions in the k-variations in the inner jet region, which result, however, in a radical alteration of the curvature of k and hence its diffusional behaviour.

We turn next to the case where swirl is present. It is particularly for such complex strain fields that the use of a second-moment closure should bring benefits over an eddy-viscosity model. The presence of swirl adds numerous additional terms to the DSM form of the transport processes. The convection terms for components involving radial or tangential velocity fluctuations are:

$$c_{rr}=\rho U\frac{\partial\overline{v^2}}{\partial x}+\rho V\frac{\partial\overline{v^2}}{\partial r}-2\rho\overline{vw}\frac{W}{r}$$

$$c_{\theta\theta}=\rho U\frac{\partial\overline{w^2}}{\partial x}+\rho V\frac{\partial\overline{w^2}}{\partial r}+2\rho\overline{vw}\frac{W}{r}$$

$$c_{rx}=\rho U\frac{\partial\overline{uv}}{\partial x}+\rho V\frac{\partial\overline{uv}}{\partial r}-\rho\overline{uw}\frac{W}{r} \tag{6}$$

$$c_{\theta r}=\rho U\frac{\partial\overline{vw}}{\partial x}+\rho V\frac{\partial\overline{vw}}{\partial r}+\rho(\overline{v^2}-\overline{w^2})\frac{W}{r}$$

$$c_{x\theta}=\rho U\frac{\partial\overline{uw}}{\partial x}+\rho V\frac{\partial\overline{uw}}{\partial r}+\rho\overline{uv}\frac{W}{r}$$

According to the ASM hypothesis, however, all convective transport terms are approximated as:

$$c_{ij}=\frac{\overline{u_iu_j}}{k}\left(\rho U\frac{\partial k}{\partial x}+\rho V\frac{\partial k}{\partial r}\right) \tag{7}$$

Thus, to take a particular example, c_{rx} given by equation (7) is entirely independent of the swirl velocity, whereas the exact version is not.

There are analogous problems with the diffusion term, which may be illustrated by considering just the diffusive transport of $\overline{v^2}$, D_{rr}. In the DSM computations this process is represented by:

$$D_{rr}^{\mathrm{DSM}}=\frac{\partial}{\partial x}\left[c_s\frac{k}{\epsilon}\left(\overline{u^2}\frac{\partial\overline{v^2}}{\partial x}+\overline{uv}\frac{\partial\overline{v^2}}{\partial r}-\boxed{2\overline{uw}\frac{\overline{vw}}{r}}\right)\right]$$

$$+\frac{\partial}{r\partial r}\left[rc_s\frac{k}{\epsilon}\left[\overline{uv}\frac{\partial\overline{v^2}}{\partial x}+\overline{v^2}\frac{\partial\overline{v^2}}{\partial r}-\boxed{2\overline{vw}\frac{\overline{vw}}{r}}\right]\right] \tag{8}$$

$$-2\frac{c_s}{r}\frac{k}{\epsilon}\left[\overline{uw}\frac{\partial\overline{vw}}{\partial x}+\overline{vw}\frac{\partial\overline{vw}}{\partial r}+\boxed{\frac{\overline{w^2}}{r}(\overline{v^2}-\overline{w^2})}\right]$$

whereas in the ASM scheme it is simply:

$$D_{rr}^{\mathrm{ASM}}=\frac{\overline{v^2}}{k}\frac{\partial}{\partial x}\left[c_s\frac{k}{\epsilon}\left(\overline{u^2}\frac{\partial k}{\partial x}+\overline{uv}\frac{\partial k}{\partial r}\right)\right]$$

$$+\frac{\partial}{r\partial r}\left[rc_s\frac{k}{\epsilon}\left(\overline{uv}\frac{\partial k}{\partial x}+\overline{v^2}\frac{\partial k}{\partial r}\right)\right] \tag{9}$$

The last term in the DSM representation of D_{rr} corresponds with that considered above where the diffusion of $\overline{uv}$ in a nonswirling jet was discussed. The boxed terms arise from the presence of swirl and, as is evident from equation (9), these have no counterpart in the ASM representation.

The consequences of these simplifications in the modelling of transport in a weakly-swirling free jet are brought out in Fig. 6. This shows comparisons between calculated values of all Reynolds stresses and distributions measured by Ribeiro and Whitelaw [14] at three axial stations. Differences between ASM- and DSM-computed normal stresses are not dramatic,

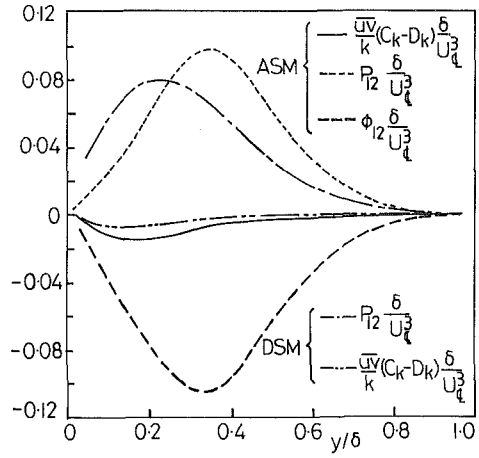

Fig. 4 Shear-stress budget from ASM computation compared to production and ASM approximation of transport extracted from DSM computation for round jet

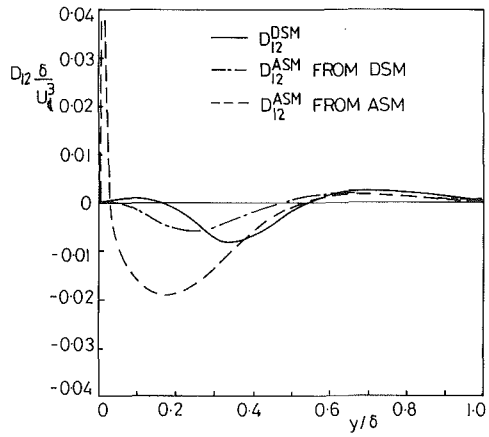

Fig. 5 Comparison of diffusive transport of shear stress for fully developed round jet extracted from the ASM and DSM computations and from the ASM approximation of the DSM solution

though it is observed that, in common with the nonswirling case considered earlier, higher k-levels are predicted, which, consistently, give rise to higher levels of shear stress. An important new feature here is the marked inequality between values of $\overline{v^2}$ and $\overline{w^2}$ at the axis – a physical impossibility. In the DSM scheme, this eventuality is avoided by "source" or "sink"-type contributions in the DSM-diffusion terms that become large, should $\overline{v^2}$ be different from $\overline{w^2}$ (see, for example, equation (8)).

As this flow is considerably more complex than the swirl-free case, it is difficult to isolate and identify specific causal connections responsible for the differences between the two models. It appears, however, that it is principally the influence of changes in normal-stress levels on shear-stress production which is the key mechanism. It is observed, for example, that model-induced differences in $\overline{u^2}$ go hand-in-hand with those in $\overline{uv}$, with $\overline{u^2}$ being generated by $\overline{uv}$, and the same may be said about the linkage between $\overline{w^2}$ and $\overline{vw}$.

One interaction through which swirl influences the stress level, via diffusion, has already been considered. A second, convection-related, mechanism may be identified upon comparing model-induced differences in the distributions of $\overline{v^2}$ and $\overline{w^2}$, particularly at $x/D=3$. At this station, DSM-values of $\overline{v^2}$ lie generally above those returned by the ASM, while the reverse occurs in relation to $\overline{w^2}$. This behaviour is consistent with the negative swirl-containing algebraic contributions in

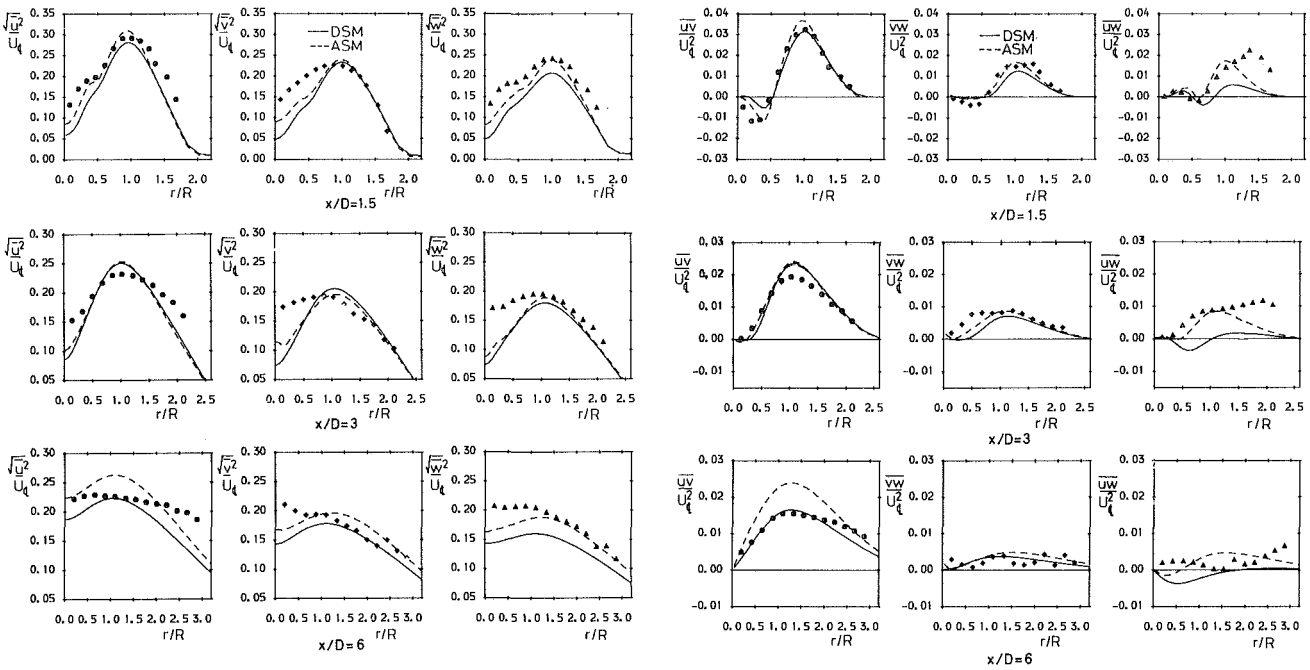

Fig. 6 Reynolds-stress profiles for weakly swirling jet of Ribeiro and Whitelaw [14], $S = 0.26$, $x/D = 1.5, 3, 6$

the normal-stress convection term c_{rr} and with the positive contribution in $c_{\theta\theta}$. The effect is weak but seems to be real. The interaction is less clear in the case of shear, for here approximation (7) cannot be said to be closely related to the first two terms of c_{rx}, $c_{\theta r}$ or $c_{x\theta}$. Since the swirl-related contributions to shear-stress convection are similar to those arising in normal-stress convection, there is reason to believe that the shear-stress levels will also be directly affected by these contributions.

The final comparison presented here relates to a strongly swirling recirculating free jet measured by Sislian and Cusworth [9]. Distributions of all normal and shear stresses are shown in Fig. 7 for one axial station. Here, differences between predicted distributions are large, but qualitatively similar to those observed in the weakly swirling case. Again, there is a serious discrepancy between ASM-calculated $\overline{v^2}$ and $\overline{w^2}$ values at the axis, and k, as well as shear-stress levels predicted by the ASM, significantly exceed corresponding DSM levels. Although the question of agreement with experiment is not one of the central issues here[2] (and while experimental defects are reflected by observed lack of conservation of swirl and axial momentum), it is interesting to note that the DSM computations of $\overline{u^2}$, $\overline{v^2}$ $\overline{w^2}$, and $\overline{uv}$ (which can be determined with much higher accuracy than $\overline{uw}$ and $\overline{vw}$) are in reasonable agreement with measurements.

5 Concluding Remarks

The comparison of ASM and DSM computations of swirling and nonswirling axisymmetric jets has shown that the most popular of the stress-transport hypotheses used to simplify differential second-moment closures (DSM) to the ASM form introduces serious errors in these types of flow. A detailed comparison of the different transport terms in the different models brings out the origin of these defects. The nature of the terms responsible for the defects is such that none of the more complicated ASM-transport hypotheses proposed so far can be expected to fare any better. In the case of the convection process, part of the problem stems from the fact that $U_k \partial \overline{u_i u_j}/\partial x_k$ is not an objective tensor (Eringen [15]), while, in an ASM scheme, it is being approximated in terms of a quantity that *is*. Although objective forms of convection tensors are known (reference [15], p. 111), none of these appear to provide a suitable basis for approximating the convective transport of $\overline{u_i u_j}$ in terms of that of turbulence energy. Moreover, the approximation of diffusion causes major and unavoidable differences between ASM and DSM forms, especially in swirling flows where all six Reynolds-stress components are active.

The conclusion drawn from these findings is that, despite the significant time savings, ASM schemes ought not to be used in axisymmetric swirling flows where stress-transport processes give rise to significant terms in the overall Reynolds-stress budget. In these cases, either a full second-moment closure should be employed or one should adopt a simpler eddy-viscosity model.

To end on a slightly less negative note, in *internal* flows it is often the case that the region in the vicinity of the duct axis is not very important: most of the stress generation occurs near the wall where the mean velocity gradients and the stresses themselves are largest. For such flows, axisymmetric and three-dimensional ASM schemes have been applied successfully, and there is no reason that they should not continue to be so used.

Acknowledgments

Different aspects of the research have been supported by the USAFOSR under grant F49620-82-C-0031, by the UK Science and Engineering Research Council (SERC) through a scholarship to one of the authors (S. Fu) and jointly by the SERC and Rolls Royce PLC through grant GR/C58010. Dr. B. A. Younis contributed substantially to the adaptation and development of the software employed in the study. Ms. L. Huxley has prepared the manuscript for publication. Authors' names appear alphabetically.

[2] Comparisons of the performance of different DSM models in predicting this flow are reported in reference [16].

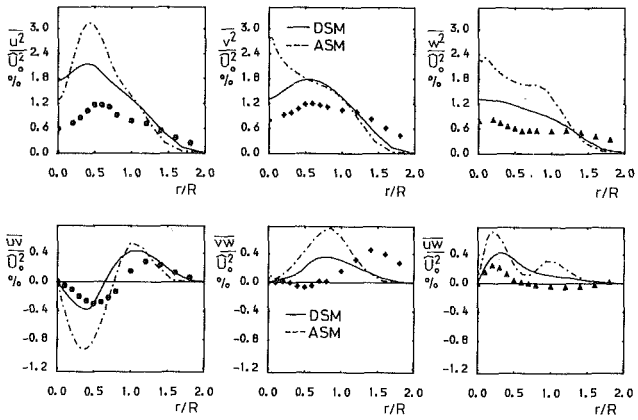

Fig. 7 Reynolds-stress profiles for strongly swirling jet of Sislian and Cusworth [9], $S = 0.8$, $x/D = 3$

References

1 Launder, B. E., and Spalding, D. B., "The Numerical Computation of Turbulent Flow," *Comp, Meth. Appl. Mech. and Eng.*, Vol. 3, 1977, p. 269.

2 Launder, B. E., "An Improved Algebraic Stress Model of Turbulence," Imperial College, Mechanical Engineering Department Report No. TM/TN/A/9, 1971.

3 Rodi, W., "A New Algebraic Stress Relation for Calculating the Reynolds Stresses," *Z. Ang. Math. und Mech.*, Vol. 56, 1976, p. 219.

4 Scheuerer, G., and Rodi, W., "Calculation of Curved Shear Layers with Two-Equation Turbulence Models," *Phys. Fluids*, Vol. 26, 1983, p. 1422.

5 Hossain, M. S., and Rodi, W., "A Turbulence Model for Buoyant Flow and Its Application to Vertical Buoyant Jets," in *Turbulent Buoyant Jets and Plumes*, ed. W. Rodi, HMT Series, Pergamon Press, 1982.

6 Launder, B. E., Reece, G. J., and Rodi, W., "Progress in the Development of a Reynolds-Stress Turbulence Closure," *JFM*, Vol. 68, 1975, p. 537.

7 Launder, B. E., "A Generalized Algebraic Stress-Transport Hypothesis, *AIAA Journal*, Vol. 20, 1983, p. 436.

8 Leschziner, M. A., "An Introduction and Guide to the Computer Code PASSABLE," Department of Mechanical Engineering, UMIST, 1982.

9 Sislian, J. P., and Cusworth, R. A., "Laser Doppler Velocimetry Measurements in a Free Isothermal Swirling Jet," University of Toronto Institute of Applied Science Report No. 281, CN ISSN, 0082-5255, 1984.

10 Huang, P. G., and Leschziner, M. A., "An Introduction and Guide to the Computer Code TEAM," Report TFD/83/9(R), Department of Mechanical Engineering, UMIST, 1983.

11 Robins, A., "The Structure and Development of a Plane Turbulent Free Jet," Ph.D. thesis, University of London, 1971.

12 Bradbury, L. J. S., "The Structure of Self-Preserving Turbulent Plane Jet," *JFM*, Vol. 23, 1965, p. 31.

13 Rodi, W., "The Prediction of Free Boundary Layers by Use of a Two-Equation Model of Turbulence, Ph.D. thesis, University of London, 1972.

14 Ribeiro, M. M., and Whitelaw, J. H., "Coaxial Jets With and Without Swirl," *JFM*, Vol. 96, 1980, p. 769.

15 Eringen, A. C., *Nonlinear Theory of Continuous Media*, McGraw-Hill, 1962, p. 110.

16 Fu, S., Launder, B. E., and Leschziner, M. A., "Modelling Strongly Swirling Recirculating Jet Flow with Reynolds-Stress Transport Closures," *Proc. 6th Symposium on Turbulent Shear Flows*, Toulouse, 1987, p. 6.17.1

Journal of Fluids Engineering

Technical Briefs

The Effect of Particle Shape on Pressure Drop in Turbulent Pipe Flow of a Gas-Solid Suspension[1]

M. T. Coughran[2]

The pressure drop was measured for air suspensions of spherical particles and two types of fibrous particles, all having mean diameters of between 8 and 20 μm, in the same apparatus and at the same operating conditions. The pipe diameter was 50.42 mm. A Reynolds number range of 61,000 to 114,000 and loading ratio range of 0.06 to 0.30 were investigated. Air-sphere suspensions showed drag reduction, in agreement with published results. Fairly uniform fibers of aspect ratio = 75 gave no drag change and drag increases resulted with "random cut" fibers of mean aspect ratio = 31, contrary to the published results for water-fiber suspensions. A relative humidity effect was also shown for fibrous particles. The flocculation of the fibers may be an important variable to address in future experiments.

Nomenclature

- D = pipe diameter
- f = friction factor
- Re = pipe Reynolds number
- $1/d$ = length/diameter, particle aspect ratio
- L = length of pipe over which ΔP is measured
- V = mass-average velocity in pipe
- ΔP = pressure drop
- μ = air viscosity
- η = loading ratio (kg flowing solids/kg flowing air)
- ρ = air density
- ϕ = relative humidity
- σ = standard deviation

Subscripts

- g = clean gas (air)
- $s+g$ = gas-solid suspension, at gas Reynolds number

1 Introduction

The pressure drop for a given fluid-particle combination in pipe flow is an important criterion in designing gas-solid flow systems. A number of empirical correlations are available for some simple flows, e.g., the correlation of Yang (1978) for spherical particles greater than 100 μm in vertical dilute gas-solid suspensions. Much work has also been done to model the fluid-particle flows. Some of the models show promise for predicting pressure drop in the simplest kinds of suspension flow. However, the important conditions of horizontal flow, elongated (and entangled) particles, and polydisperse particle size have not been included. Furthermore, models which include these and other effects are designed to predict particle concentration and velocity profiles, and cannot presently be extended to predict pressure drop. The modeling problem has been further complicated by the experimental discovery of anomalous effects such as the drag reduction phenomenon, which occurs in liquid-fiber suspensions and in gaseous suspensions of spherical particles of approximately 100 μm or less.

Previous studies by Vaseleski (1973) and Radin et al. (1975) have shown that the pressure drop in liquid-solid suspensions is highly dependent on particle shape. In the experiment of Vaseleski, nylon fibers with aspect ratio ($1/d$) on the order of 100 caused a 10 percent drag reduction in water at a loading ratio (η) of 0.01, while asbestos fibers with $1/d = 10{,}000$ gave 70 percent drag reduction at $\eta = 0.005$. The operating conditions included $60{,}000 \leq \mathrm{Re} \leq 400{,}000$. Radin et al. tested nylon and rayon fibers with $37 \leq 1/d \leq 105$ in water at $7{,}000 \leq \mathrm{Re} \leq 200{,}000$. They observed drag reduction of up to 25 percent over $0.002 \leq \eta \leq 0.04$ and also noted that drag reduction increased with fiber $1/d$. No drag reduction was obtained for any of the several types of spherical particles tested in their experiments.

Previous experimental and theoretical works on drag reduction in gas-solid suspensions have been reviewed by Pfeffer and Kane (1974) and Radin (1974). Drag reduction has been obtained for fine spherical particles at $10{,}000 \leq \mathrm{Re} \leq 300{,}000$. Rossetti and Pfeffer (1972) reported a 75 percent drag reduction for one combination of the variables in a vertical tube. On the other hand, Garner and Kerekes (1980), in their study of an air suspension of wood pulp fibers, reported a 6 percent drag reduction over $150{,}000 \leq \mathrm{Re} \leq 300{,}000$ and $\eta = 0.21$. At present the mechanism by which drag reduction occurs in the gas-solid suspensions has not been proven. Reference is usually made (e.g., Kolansky, 1976) to the hypothesis of Boothroyd (1966) that spherical particles of a certain size are unable to follow rapidly moving eddies near the wall, hence causing damping of the turbulence. However, no experiment has yet been devised to prove this. Also, there appears to be no published model by which the pressure drop may be predicted (even for spherical particles) over a wide range of variables, including the drag reduction regime. Choi and Chung (1983) reported some success in prediction of Boothroyd's spherical

[1]The work described in this paper was performed at Texas A&M University, College Station, Texas.

[2]Mechanical Engineer, Ship Hydromechanics Department, David Taylor Research Center, Bethesda, MD 20084. Assoc. Mem. ASME

Contributed by the Fluids Engineering Division and presented at the Symposium on Gas-Solid Flows, Atlanta, Ga., May 1986 of The American Society of Mechanical Engineers. Manuscript received by the Fluids Engineering Division January 21, 1987.

particle results with a modified mixing length model. The suspensions of elongated and entangled fibrous particles are probably far more complicated. One notable aspect of the many published studies on liquid-fiber drag reduction is the absence of any analytical work.

An additional variable known to be important in gas-solids flow is the electrostatic charging. The exact relationship between the electrostatic charge, relative humidity, and pressure drop has been the subject of some debate, especially for drag-reducing systems (Radin; Pfeffer and Kane). Smeltzer et al. (1982) showed that low relative humidities can cause increases of up to 70 percent in the suspension pressure drop. Tardos et al. (1983) measured and controlled the electrostatic charge in an experiment which indicated a drag increase with charge increase for horizontal tubes. Both of these experiments used spherical glass particles of diameter ≤ 150 μm. Radin suggested that different flow behavior may be occurring in various experiments due to the electrostatic effects on different materials used for the bulk solids and conveying pipes.

The mechanisms of drag reduction in gas-solid and liquid-solid flows may well be different, due to the greater relative importance of particle density and electrostatic charging in the gas-solid flows. However, the possibility of a relationship between particle shape and pressure drop in a gas-solid suspension has yet to be thoroughly investigated. This problem is not likely to yield to theory in the near future. The objective of this research was therefore to obtain more experimental information on the effects due to particle shape.

2 Experimental Program

The shape parameters for the 3 types of particles chosen for this study are given in Table 1. Spherical particles established the "baseline" for the experiment since they have previously been investigated over a wide range of variables. The silica glass from which the spheres were made had a specific gravity of 2.50. Fibers with a smooth surface and a specified diameter of 3 denier were obtained. The term "random cut" follows from the more irregular shape and size of the third type of particle. Both types of fibers were made from nylon with a specific gravity of 1.14. For the purposes of this study, all three types of particles had comparable diameters. Details of the particle origin and the experimental apparatus and procedures described below were given in the thesis by Coughran (1984).

Table 1 Particle dimensions

Particle type	Diameter (μm) mean	σ	Length (μm) mean	σ	Mean aspect ratio
Spheres	8.4	1.6	----------		1
3 Denier fibers	21.0	1.6	1,580	180	75
Random cut fibers	17.0	3.7	530	310	31

The apparatus, shown in Fig. 1, was an open-loop system with continuous particle feeding and removal. The system included two fans, a psychrometer, a specially designed particle feeder, a differential pressure transducer with micromanometer for calibration, a cyclone separator, and a flow-nozzle-type flowmeter. Two high-efficiency filters removed ambient particles prior to the feeder and particles which escaped the cyclone prior to the flowmeter. The particle feeder provided a steady feed for all particle types. It was calibrated at operating conditions by catching and weighing the solids at the cyclone over a measured time period. Loading ratios of 0.01 to 0.30 could be achieved. Run times ranged from 1 to 4 minutes. The electrostatic effects were minimized in the particle shape tests by obtaining data over narrow ranges of relative humidity (ϕ) as measured by the wet-and-dry-bulb psychrometer.

The horizontal test, entrance, and exit sections were constructed of one 6.096 m (20 ft) long piece of drawn copper tubing with an inside diameter of 50.42 mm (1.985 in). Five stations of static pressure taps, labeled A through E in Fig. 1, were installed in the test section so that fully developed flow could be verified. Station A was located 3.05 m (10 ft) from the entrance to the pipe. The subsequent taps were spaced at 0.61 m (2 ft). The pressure transducer was a Validyne variable reluctance type with a sensitivity of 0.0254 mm (0.001 in) of water and a range of 50.8 mm (2.0 in) of water. A well-type manometer was used to measure the static pressure in the test section for calculation of air density.

The review by Radin (1974) indicated that, in addition to problems with insufficient development length, several previous investigators measured clean air friction factors in error by 8 to 17 percent. In the present apparatus the series of pressure taps was used to verify that fully developed flow existed for air and for each type of gas-solid suspension. The friction factor (f) for clean air (subscript g) values were also compared with published data. Figure 2 shows f_g plotted against the formula of Techo et al. (1965), which is an explicit form of Prandtl's friction law. Each of these data points was acquired immediately prior to a particle run to establish a "control" condition. This figure shows that the measured friction factor differs from the correlation value by a maximum of 3 percent at the highest test Reynolds number of 114,000. The good agreement indicates proper drilling of the pressure taps and accurate measurement of the pressure drop

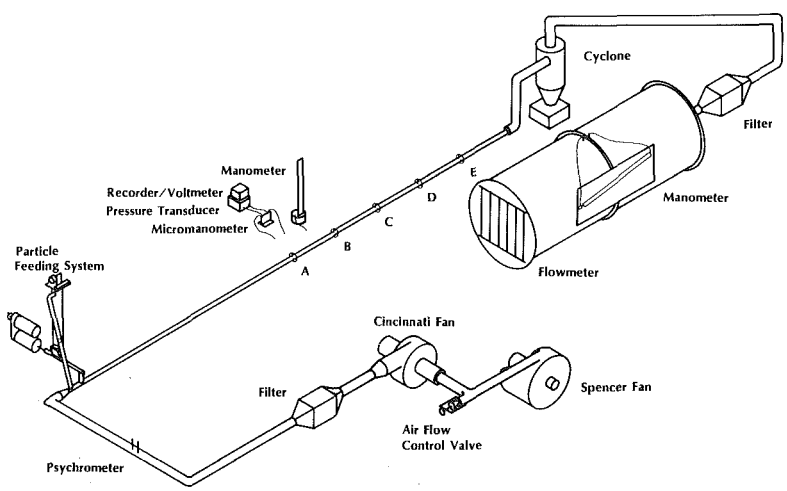

Fig. 1 Experimental apparatus

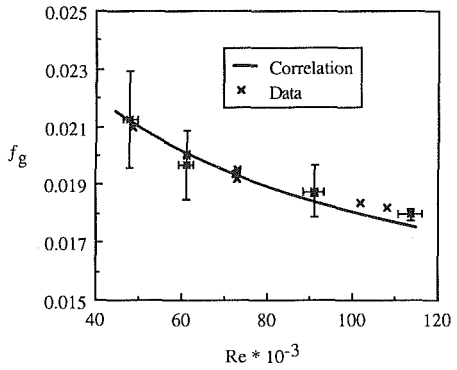

Fig. 2 System performance with clean air

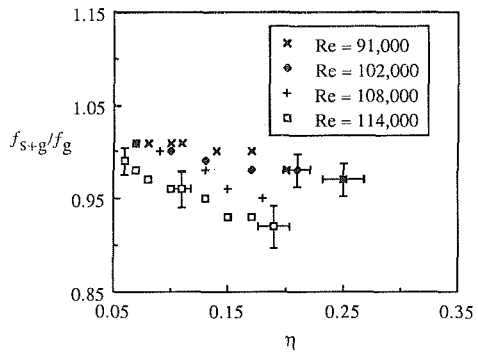

Fig. 3 Drag reduction with spheres at higher Re, 23 percent $\leq \phi \leq$ 28 percent

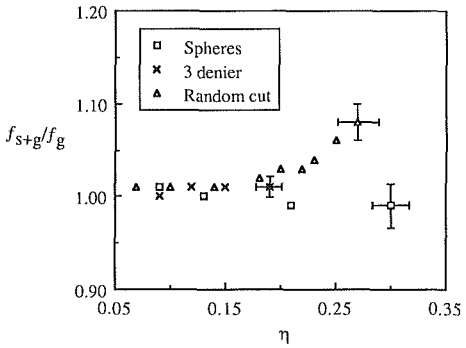

Fig. 4 Particle shape effect at Re = 61,000, 38 percent $\leq \phi \leq$ 40 percent

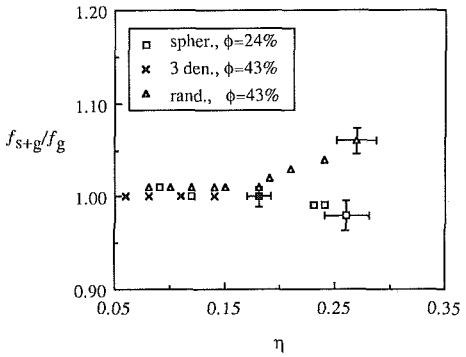

Fig. 5 Particle shape effect at Re = 73,000

and flowrate. The friction factor and pipe Reynolds number follow the usual definitions:

$$f = 2\Delta PD/\rho V^2 L \quad (1)$$

$$\mathrm{Re} = \rho VD/\mu \quad (2)$$

The uncertainties were computed based on 20:1 odds (Kline and McClintock, 1953) by the following procedure. Standard propagation-of-uncertainty gives the uncertainty of f and Re based on uncertainties of all the measured and computed quantities on the right-hand-sides of the equations. One source of uncertainty is the small fluctuations in ΔP which occur. The pressure transducer was connected to a strip chart recorder, from which the mean and rms of ΔP were obtained. These give the nominal value and uncertainty respectively. The other major souce of uncertainty is the velocity calculation. The velocity is obtained from the pressure drop across the flownozzle by a computer program which computes the air density and iterates for the discharge coefficient. This calculation was 'perturbed' using the input uncertainties, such as the fluctuation in the flow nozzle manometer readings, temperatures, etc. As shown in Fig. 2, the resulting uncertainty of f increases as the Reynolds number is decreased, reflecting a greater ratio of fluctuations to mean value at the lower speeds. However the good repeatability shown at several Re values indicates that the precision uncertainty estimates are generous.

The minimum Reynolds number achievable in the system for air-particle tests was 61,000 due to deposition of the spheres at lower air velocities. The gas-solid pressure drop was calculated in terms of f_{s+g}/f_g, the suspension-to-clean-air friction factor ratio, where f_{s+g} and f_g are measured at the same air Reynolds number. Note that the uncertainty of this quantity has a different structure; by its definition,

$$f_{s+g}/f_g = \Delta P_{s+g}/\Delta P_g \quad (3)$$

Hence there is no significant uncertainty contribution from the velocity calculation, and the uncertainty is due only to the small fluctuations in ΔP discussed above. This explains why the worst-case uncertainty bars on Fig. 2 can be larger than those which follow.

3 Results and Discussion

The data for air-sphere suspensions are shown in Fig. 3. The lower Reynolds number data, which are included in later figures, would be superimposed on the Re = 91,000 data if shown on this plot. The uncertainty trends for Re = 114,000 are typical of all particle tests. For the sake of clarity, the uncertainty bars are shown only at points of maximum uncertainty and points of comparison. Figure 3 shows that, in the range Re = 91,000 to 114,000, drag reduction increases with increasing Re and η to a maximum value of 8 percent. Rossetti and Pfeffer (1972) reported similar trends for loading ratio with similar particle size, although they used a 25.4 mm (1 in) tube at Re = 10,000 to 25,000. These results cannot be attributed to any acceleration effects. The check for fully developed flow was made for all 3 types of particles at Re = 73,000 and $\eta = 0.15$. The pressure drop was the same, within uncertainty of the measurements, across spans AB, BC, CD, and DE for each case. The Reynolds number effect in Fig. 3 may be due to an increased tendency toward stratification in horizontal tubes as the velocity decreases.

Figures 4, 5, 6, and 7 show the air-sphere and air-fiber data at Re = 61,000, 73,000, 91,000, and 114,000, respectively. For both types of fibers tested, no drag reduction was encountered at any combination of Re, η, and ϕ. In fact the 3 denier fibers showed practically no measureable changes in pressure drop from the clean air case over the range of loading ratios possible in the apparatus. The random cut fibers, on the other hand, demonstrated significant pressure drop increases—up to 17 percent at the highest loading ratio. The lack of agreement with the results of Garner and Kerekes (1980) must be attributed to differences in fiber type and Reynolds number range, since they used a similar pipe and a loading ratio within

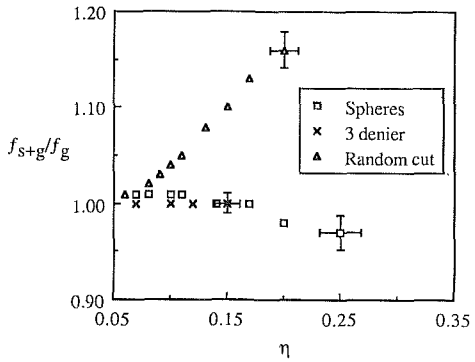

Fig. 6 Particle shape effect at Re = 91,000, 19 percent $\leq \phi \leq$ 23 percent

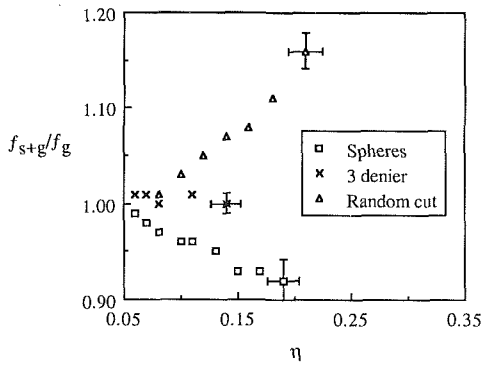

Fig. 7 Particle shape effect at Re = 114,000, 20 percent $\leq \phi \leq$ 23 percent

the range of the present data. The figures show that differences between the particle types increase with Reynolds number and loading ratio. The maximum particle shape effect was observed at Re = 114,000 and $\eta = 0.19$, where the spheres gave 8 percent drag reduction and the random cut fibers gave a 12 percent drag increase.

The previous figures also show the attempt made to match relative humidities between particle tests at each Reynolds number. In this range of relative humidities (20–40 percent) Smeltzer et al. (1982) measured a pressure drop increase corresponding to a decrease in relative humidity for an air-sphere suspension. They assumed this effect was due to greater electrostatic charging at the lower ϕ. The final plot, Fig. 8, shows that a similar effect exists in the present experiment for nonspherical particles, i.e., the random cut fibers. The range of humidities was obtained by making use of temporary changes in the ambient conditions and by using the Spencer blower, which heats the air, for the $\phi = 16$ percent case.

The new results for air-solid suspensions differ from the published results for water-solid suspensions, in that no drag reduction was obtained with high-aspect-ratio solids (although the longer fibers gave *less pressure drop*). The difference may be due to the different scales of turbulence in the two fluids, relative to the particle size. Sharma et al. (1979) postulated that liquid-fiber drag reduction is a result of fiber entanglements which cause a decrease of momentum transport in the core region. Garner and Kerekes (1980) concluded that there is no correlation between the degree of fiber flocculation in air and the pressure drop. It was not possible to quantify the degree of flocculation in the present experiments, beyond noting that the 3 denier fibers appeared to be in smaller flocs upon striking the cyclone walls.

4 Conclusions

Differences in pressure drop behavior in gas-solid suspensions due to differences in particle shape have been

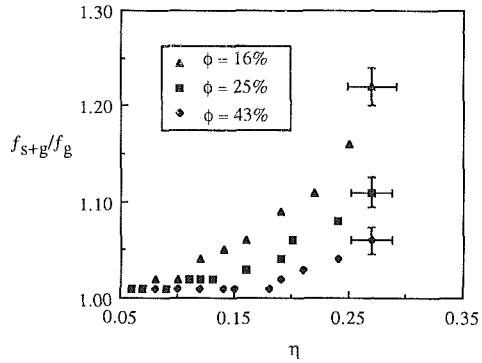

Fig. 8 Relative humidity (ϕ) effect for random cut fibers at Re = 73,000

demonstrated. Air-sphere suspensions showed drag reduction, as expected from previous investigations. Uniform fibers with an aspect ratio of 75 gave no drag change, while irregular or random cut fibers with a mean aspect ratio of 31 caused drag or pressure drop increases. These results are contrary to the published results for water-fiber experiments. A maximum difference in f_{s+g}/f_g of 20 percent was observed between sphere and random cut fiber suspensions. A relative humidity effect in which the pressure drop increased as relative humidity decreased was demonstrated with the random cut fibers, similar to that shown by previous authors for spherical particles. This effect is probably related to electrostatic charging. Future experiments should use some technique of controlling the degree of flocculation and measuring its effect.

Acknowledgments

This research was supported by the Department of Mechanical Engineering at Texas A&M University and by the General Electric Co. Some helpful comments concerning interpretation of the data were provided by D. G. Bogard of the University of Texas.

References

Boothroyd, R. G., 1966, "Pressure Drop in Duct Flow of Gaseous Suspensions of Fine Particles," *Trans. Instn. Chem. Engrs.*, Vol. 44, pp. T306–313.

Choi, Y. D., and Chung, M. K., "Analysis of Turbulent Gas-Solid Suspension Flow in a Pipe," ASME Paper 83-FE-6.

Coughran, M. T., 1984, "The Effect of Particle Shape on Pressure Drop in a Turbulent Gas-Solid Suspension," M.S. thesis, Texas A&M University, College Station, Texas.

Garner, R. G., and Kerekes, R. J., 1980, "Flow Regimes of Wood Pulp Fibers in Air Suspensions," *Tappi*, Vol. 63, No. 6, pp. 103–107.

Kline, S. J., and McClintock, F. A., 1953, "Describing Uncertainties in Single-Sample Experiments," *Mech. Engr.*, pp. 3–8.

Kolansky, M. S., 1976, "Studies in Fluid Mechanics," Ph.D. dissertation, City University of New York.

Pfeffer, R., and Kane, R. S., 1974, "A Review of Drag Reduction in Dilute Gas-Solids Suspension Flow in Tubes," Paper F1 and Discussion, *International Conference on Drag Reduction*, BHRA Fluid Engineering.

Radin, I., 1974, "Solid-Fluid Drag Reduction," Ph.D. dissertation, University of Missouri-Rolla.

Radin, I., Zakin, J. L., and Patterson, G. K., 1975, "Drag Reduction in Solid-Fluid Systems," *AIChE Journal*, Vol. 21, No. 2, pp. 358–371.

Rossetti, S. J., and Pfeffer, R., 1972, "Drag Reduction in Dilute Flowing Gas-Solid Suspensions," *AIChE Journal*, Vol. 18, No. 1, pp. 31–39.

Sharma, P. S., Seshadri, V., and Malhotra, R. C., 1979, "Drag Reduction in Dilute Fibre Suspensions: Some Mechanistic Aspects," *Chemical Engineering Science*, Vol. 34, pp. 703–713.

Smeltzer, E. E., Weaver, M. L., and Klinzing, G. E., 1982, "Pressure Drop Losses Due to Electrostatic Generation in Pneumatic Transport," *Industrial & Engineering Chemistry Process Design and Development*, Vol. 21, pp. 390–394.

Tardos, G., Yen, B., and Pfeffer, R., 1983, "The Effect of Static Charges on Drag Reduction in Dilute Gas-Particle Suspension Flow," *Chemical Engineering Communications*, Vol. 19, pp. 205–219.

Techo, R., Tickner, R. R., and James, R. E., 1965, "An Accurate Equation for the Computation of the Friction Factor for Smooth Pipes from the Reynolds Number," ASME *Journal of Applied Mechanics*, Vol. 32, p. 443.

Vaseleski, R. C., 1973, "Drag Reduction in the Turbulent Flow of Fiber Suspensions," M.S. thesis, University of Delaware-Newark.

Yang, W. C., 1978, "A Correlation for Solid Friction Factor in Vertical Pneumatic Conveying Lines," *AIChE Journal*, Vol. 24, No. 3, pp. 548–551.